Springer Theses
Recognizing Outstanding Ph.D. Research

Daniel Linnemann

Quantum-Enhanced Sensing Based on Time Reversal of Entangling Interactions

Springer

Springer Theses

Recognizing Outstanding Ph.D. Research

Aims and Scope

The series "Springer Theses" brings together a selection of the very best Ph.D. theses from around the world and across the physical sciences. Nominated and endorsed by two recognized specialists, each published volume has been selected for its scientific excellence and the high impact of its contents for the pertinent field of research. For greater accessibility to non-specialists, the published versions include an extended introduction, as well as a foreword by the student's supervisor explaining the special relevance of the work for the field. As a whole, the series will provide a valuable resource both for newcomers to the research fields described, and for other scientists seeking detailed background information on special questions. Finally, it provides an accredited documentation of the valuable contributions made by today's younger generation of scientists.

Theses are accepted into the series by invited nomination only and must fulfill all of the following criteria

- They must be written in good English.
- The topic should fall within the confines of Chemistry, Physics, Earth Sciences, Engineering and related interdisciplinary fields such as Materials, Nanoscience, Chemical Engineering, Complex Systems and Biophysics.
- The work reported in the thesis must represent a significant scientific advance.
- If the thesis includes previously published material, permission to reproduce this must be gained from the respective copyright holder.
- They must have been examined and passed during the 12 months prior to nomination.
- Each thesis should include a foreword by the supervisor outlining the significance of its content.
- The theses should have a clearly defined structure including an introduction accessible to scientists not expert in that particular field.

More information about this series at http://www.springer.com/series/8790

Daniel Linnemann

Quantum-Enhanced Sensing Based on Time Reversal of Entangling Interactions

Doctoral Thesis accepted by
the University of Heidelberg, Heidelberg, Germany

Springer

Author
Dr. Daniel Linnemann
Kirchhoff-Institut für Physik
Universität Heidelberg
Heidelberg, Germany

Supervisor
Prof. Markus K. Oberthaler
Kirchhoff-Institut für Physik
Universität Heidelberg
Heidelberg, Germany

ISSN 2190-5053 ISSN 2190-5061 (electronic)
Springer Theses
ISBN 978-3-319-96007-4 ISBN 978-3-319-96008-1 (eBook)
https://doi.org/10.1007/978-3-319-96008-1

Library of Congress Control Number: 2018948584

This Springer imprint is published by the registered company Springer Nature Switzerland AG
The registered company address is: Gewerbestrasse 11, 6330 Cham, Switzerland

All of old. Nothing else ever.
Ever tried. Ever failed. No matter.
Try again. Fail again. Fail better.

—Worstward Ho, Samuel Beckett

For my parents, Herbert and Renate, and siblings, Christian and Alexandra

Supervisor's Foreword

Quantum mechanics is the current theoretical framework to describe our world and is one of the best tested theoretical concepts we have at hand. Nevertheless there are still many aspects to be explored and understood, reaching from extending our fundamental understanding of dynamics and structure of interacting many-body systems to developing tools and strategies for the exploitation of the powerful resources for applications available in quantum systems. While the precise understanding of nature has been the strength behind the success of quantum mechanics from the very beginning, the aspect of usefulness for overcoming limitations of the classical world was only identified in the 1980s. Since then it has been an experimental challenge to implement the basic building blocks for demonstrating the proposed theoretical ideas on quantum cryptography, quantum computation and quantum metrology.

The experimental platforms of correlated photons realized with nonlinear optical techniques have been the workhorse for implementing quantum communication protocols going as far as quantum cryptography between earth and a satellite. The experimental systems of ions in traps and superconducting qubits in circuit QED have turned out to be the best choices for demonstrating many aspects in quantum information processing. This part of quantum technology has seen a significant boost in recent years and is now part of the portfolio of companies such as Google and Microsoft. Compared to these enterprises, quantum metrology is still in its infancy but real applications are emerging at an increasing pace. Here, the choice of system is determined by the properties one wants to detect. For gravitational waves, light interferometers are the current choice and there the realization of non-classical light is already pushing the performance of the devices beyond the classical limit. For detection of magnetic properties, atomic systems in the form of vacancies in diamond or cold and ultracold gases are the most suitable systems.

For the experimental platform of ultracold gases, Daniel Linnemann has significantly extended the possibilities for quantum limited detection by building on novel interferometric strategies. He has shown for the first time that *active* atom interferometry is possible and that the performance indeed beats the classical detection limit. Although the basic concept has already been discussed theoretically

in the 1980s in the context of quantum optics with photons, Daniel Linnemann realized it for the first time with atoms. He also developed a more general point of view of the interferometer, namely the controlled time-reversed running of entangling nonlinear dynamics—entangling–sensing–disentangling detection. The experimental results reveal that this new strategy comes very close to the fundamental detection limit given by quantum mechanics known as Heisenberg limit. This thesis not only summarizes these results but also puts them into a broader and well-founded context with the many activities in the field of quantum metrology. Furthermore, the experimental observations are directly compared to theoretical expectations showing that direct interplay between theoretical and experimental activities provides the ideal approach for pushing quantum metrology yet further.

Summarizing, Daniel Linnemann's Springer Thesis represents a valuable resource not only for experts in the field, who will find here important details and explanations, but also for newcomers and non-experts, who will benefit from an excellent introduction in the field of quantum optics with atoms.

Heidelberg, Germany
April 2018

Prof. Markus K. Oberthaler

Abstract

We experimentally study a nonlinear detection scheme in which entangling interactions are time reversed. In this way, non-classical many-particle states are disentangled in order to enable their feasible readout. In the context of quantum-enhanced sensing, such nonlinear readout techniques extend the class of entangled probe states that can be leveraged for interrogation without being limited by finite detector resolution.

As the underlying nonlinear mechanism, we employ spin exchange in a Bose–Einstein condensate. The scattering process among spins can be controlled experimentally to not only generate an entangled state, but also the corresponding time-reversed dynamics.

We explicitly demonstrate a quantum-enhanced measurement by constructing an atomic SU (1, 1) interferometer. Herein, spin exchange acts as an amplifier which spontaneously populates initially empty spin states. The nascent entangled two-mode squeezed vacuum state enables sensitive phase measurements. Checking whether or not the initial state is recovered after time reversal reveals phase imprints. This scheme is capable of exhausting the quantum resource by detecting solely average atom numbers, in principle, up to the fundamental Heisenberg limit of phase estimation.

The intrinsic amplification of this interferometry scheme provides benefits for weak signals. We experimentally explore the regime of an extended nonlinear readout in which noiseless amplification permits to maintain quantum-enhanced phase sensitivity even for large magnifications. Integrating nonlinear dynamics into the detection strategy is widely applicable. We provide additional examples by using it as an autonomous building block which maps subtle quantum correlations onto readily detectable quantities.

Acknowledgements

The work presented in this doctoral thesis would not have been possible without the tremendous support I received. Here, I want to take the opportunity to thank those who proved indispensable. It is a pleasure for me, to first and foremost thank Markus for his enduring support and the trust he put in me. His creative and trendsetting attitude is truly unique. He also gave me the opportunity to pursue our initial ideas with the help of an international cooperation and within the Heidelberg fast-track Ph.D. programme.

I would like to thank Karen Kheruntsyan and his group for the exceptional hospitality I received during my two stays at the University of Queensland in Brisbane. In discussions with him and his student, I learnt lots of new aspects about the theoretical description of our experiments.

I had the pleasure to present this and related work at international conferences and workshops. In particular, the discussions following the main talk turned out to be extremely rewarding. Those comments, questions but also concerns and objections raised led to a constant revision and advancement of our original ideas.

I thank the University of Heidelberg for awarding me with a generous Ph.D. stipend.

Finally, a big thank you goes out to all the members of our SynQS group. This thesis would not have been successful without their valuable suggestions and ideas. I could also always rely on their hands-on support; many thanks also for the thorough proofreading of this thesis. It was an exciting and intense time, I would not want to miss.

Detached from all subject-specific aspects, my family made the most significant contribution to this thesis. My parents, Herbert and Renate, and siblings, Christian and Alexandra, therefore, deserve the greatest credit. I dedicate this thesis to them.

Contents

Part IV Experimental Results

Chapter 1
Introduction

1.1 Quantum Technologies

Quantum mechanics entails effects like superpositions and entanglement that have no classical counterpart. Harnessing these counterintuitive aspects for technological advance is the goal of quantum technology. It is a thriving research field with some scholars [1] even seeing a third quantum revolution approaching. Here, the so-called first quantum revolution refers to the discovery or invention of the fundamental laws governing quantum physics such as the Schrödinger equation; proof-of-principle experiments on single particles have then led to the second quantum revolution [2]. Nowadays, quantum technologies harnessing many-body effects come of age and leave the realm of blue skies research as they find applications and progressively become a subject of engineering.

Most recently, arguing that more than half of the scientific papers on quantum technology are written by European authors, a call on the European Commission was started to secure this ascendancy. Following the proposal, grandiosely called quantum manifesto [3], one billion Euro will be spent on quantum technology starting next year [4, 5].

Meanwhile, all around the globe efforts to exploit quantum effects for technology are undertaken. The most prominent endeavour is the quest for quantum computers [6]. While the most innovative global players like Google, IBM, Microsoft, and Intel already entered the stage, yet they find themselves challenged as an era of startups and university spinoffs begins [7–9]. The basic question of what platform (or combination [10]) might be suited best is still open but first cross-platform comparisons are undertaken [11]. Google aims at building a programmable quantum computer with 7×7 superconducting qubits by the end of this year. IBM, with similar long term goals, recently realized a 17 qubit system. Knowing how to develop such devices in principle, researchers face similar problems as in early days conventional computing, namely the so-called Tyranny of numbers, that is the wiring-up of an ever increasing number of (qu-)bits.

D. Linnemann, *Quantum-Enhanced Sensing Based on Time Reversal of Entangling Interactions*, Springer Theses,
https://doi.org/10.1007/978-3-319-96008-1_1

In part relying on superpositions and not necessarily entanglement, quantum cryptography [12, 13] promises security based on the laws of quantum mechanics. This is different from the usage of one-way functions in conventional asymmetric cryptography, where the non-reversibility is generally believed but not mathematically proved [14]. Furthermore, considering post-quantum cryptography, those hard problems that asymmetric cryptography relies on can efficiently be solved using quantum algorithms [15]. While quantum computation is still in its infancy, quantum cryptography has already found its way into practical applications [16].

The third major field of quantum technologies is metrology. Often, quantum metrology is referred to as the science behind devising and performing measurements which involve individual quanta [17, 18]. For instance, redefinitions of units in terms of fundamental constants at single particle level are subsumed under this name. A recent example is the so-called quantum metrological triangle, which aims at probing Ohm's law at the level of well-defined individual quanta [19].

Within this thesis we adopt the term in a stricter sense. Here, quantum metrology refers to techniques which make use of quantum correlations such as entanglement to improve measurements [20–22]. Usually one aims at achieving higher precision, but other benefits, such as longer coherence times or a larger dynamic range, might also exist [23].

Most precision experiments map the quantity in question onto frequency or phase such that interferometric techniques can be used for readout. The prime example is timekeeping. Nowadays, atomic clocks [24] that use transitions in the optical domain reach accuracy levels of 10^{-18} [25, 26]. Such fractional uncertainties are achieved in two tour de force experiments: an ensemble of neutral strontium atoms that is trapped in an optical lattice, or a single Aluminium ion held in a quadrupole Paul-trap [27–29]. Both contenders plan to improve their accuracy by exploiting entanglement [30]. History teaches that the importance of ever increasing precision cannot be undervalued; often, new developments were only triggered by the unexpected result of a precision experiment. Famous examples in the field of quantum mechanics are the determination of the Lamb-shift, and the anomalous electron dipole moment for which Lamb and Kusch shared the Nobel prize. Both precision experiments can be considered the incentive of quantum electrodynamics. Today, precise clocks could determine whether or not fundamental constants change over time in a lab measurement [31–33]. Dirac advocated such drifts [34, 35].

The second major example of precision interferometry is gravitational wave detection [36, 37]. This year the third gravitational wave has been observed directly [38, 39]. However, all detected events were caused by rare black hole mergers. To start a new era of (multimessenger) astronomy that builds on detecting gravitational waves as a tool, the sensitivity has to be improved to extend the astrophysical reach. The implications of this so-called gravitational-wave astronomy are often compared to the advent of radio telescopes in the 1930 s which opened up the complementary rf spectrum for investigations of the universe. The strain sensitivity could be improved using quantum mechanically entangled (squeezed) light [40–43].

One could really argue that these are interesting times to live in—if this were not a Chinese curse.

1.2 Quantum-Enhanced Measurements

Let us start start by considering how a generic measurement task can be improved. We have an atom interferometry application in mind—but the arguments put forward in this section are of general nature and do not depend on a specific measurement apparatus [44].

Our aim is to determine a quantity precisely. This is routinely achieved by repeating measurements and averaging the individual outcomes: when performing a measurement N times, the error of the quantity to be measured, i.e. the error of its estimated mean value, averages down with the square-root of measurements. This is the fundamental $\sqrt{N}$ law of statistics which holds for independent sampling [21]. Often, the single measurements are not done sequentially in time but simultaneously. An example would be an atom interferometer in which an entire cloud of N atoms is used in parallel for interrogation [45]. As long as the probes are uncorrelated, the $\sqrt{N}$ law keeps valid [20]. Such a technique is shown schematically in Fig. 1.1a.

This limit, however, is by no means fundamental. It can be surpassed by not using *independent* particles but by introducing nonclassical correlations among them [21]. For this, a nonlinear mechanism is needed, i.e. a nonlinear Hamiltonian $\mathcal{H}$ which generates these correlations (red box in panel b). Then a quantum mechanically entangled probe state emerges (indicated as the intertwined atom cloud). If such a nonclassical probe state is used for interrogation, uncertainties smaller than the square root limit can be achieved in principle. Therefore, the same overall precision can be reached while using less atoms—or, with the same atom resource at hand smaller errors are attainable.

As a quid pro quo, however, the entangled state and its subtle correlations need to be measured at the final detection stage. For highly entangled states, this requires measurements of the full particle correlations with high fidelity, i.e. at single particle level. We indicate this by $\langle x^n \rangle$ to emphasize the need of higher moments like $\langle x^2 \rangle$ and $\langle x^3 \rangle$ instead of a simple average $\langle x \rangle$. For neutral particles, such single-particle resolved detection with high dynamic range remains challenging [46, 47]. To summarise, in order to have a highly sensitive probe state, one needs to have entanglement—but at the same time, entanglement at the readout stage is hard to deal with because of the need for sophisticated detection techniques not yet available.

One way to circumvent this detection problem is to use a nonlinear process right before detection. At this stage—after interrogation—it cannot improve the phase sensitivity any further. But instead, it eases detection as it is able to disentangle the state. To this end a similar process which generated the entangled state in the first place is applied right before detection. Then the effect of the first nonlinear process can be reversed and a classical state reemerges. For this the sign of the nonlinearity needs to be inverted. Inverting the sign of the governing Hamiltonian amounts to time reversal. We call such a scheme (depicted in panel c) therefore quantum-enhanced sensing based on time reversal. Since the state at the detection stage is disentangled standard averaging can be used to extract the information gained during interrogation (indicated by $\langle x \rangle$). In this thesis we present the experimental realization of such a

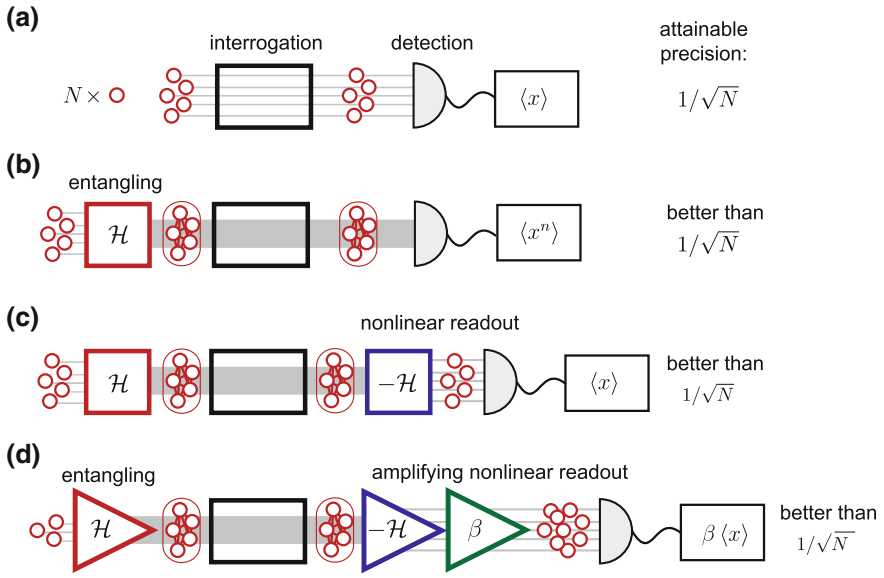

Fig. 1.1 Overview of detection strategies for quantum metrology. In panel **a** an ensemble of N independent probes is used to interrogate the black box. At the detection stage the individual measurement outcomes are averaged as indicated by $\langle x \rangle$. The error of the quantity to be measured averages down with the square root of probes—a direct consequence of the independent probing. The measurement's error can be reduced by introducing nonclassical correlations among the probes as shown in (**b**). Here, interactions described by a nonlinear Hamiltonian $\mathcal{H}$ generate an entangled state (intertwined cloud) which is used for subsequent interrogation. By measuring subtle correlation functions (indicated by $\langle x^n \rangle$) a higher precision is attainable. Panel **c** shows a nonlinear readout scheme where an additional nonlinear process is added before detection. While the entangled state is generated by $\mathcal{H}$ the time reversed process $(-\mathcal{H})$ is used to disentangle the state for feasible readout. Consequently, simple averaging at the output $(\langle x \rangle)$ suffices to exhaust the quantum resource of the entangled state and reach high precision. Panel **d** depicts the amplifying nonlinear readout. Here, entangling and subsequent disentangling are performed by nonlinear amplifiers. A posteriori amplification can be used to magnify the output signal (gain indicated by β) while maintaining improved precision

scheme. In particular, the entanglement generation and subsequent time reversal will be realized by nonlinear amplifiers. This arrangement that is indicated in panel (d) offers the unique possibility to further facilitate detection by a posteriori amplification. This additional amplification stage does not deteriorate the achievable phase sensitivity. We call such an arrangement amplifying nonlinear readout. It therefore serves two purposes: first, the quantum state's entire information is accessible by standard averaging; and secondly, the output signal is amplified (amplification factor denoted by β) for feasible detection. One mechanism which allows for experimental control over the sign of the nonlinearity is spin exchange which we introduce in the next sections. Before that, however, we detail the potential gain when using entangled probe states for phase estimation.

1.3 Quantum Mechanical Limits on Phase Sensitivity

We now address the question of how large the potential room for improvement is when using nonclassical probe states. Entanglement cannot enhance sensitivity ad infinitum. In fact there is a fundamental bound on how efficiently a phase can be measured in principle. Relying on the notion of efficiency, this so-called Heisenberg limit requires a common sense of a cost function. In quantum technologies, one conventionally aims at minimising the number of interrogations[1] [48, 49]. In the previous overview of quantum-enhanced atom interferometry we implicitly treated the total number of atoms as a resource count. This applies to the most common interferometry schemes in which all N employed atoms interrogate the phase shift once. Under such circumstance the fundamental Heisenberg limit reads $\Delta\varphi = N^{-1}$ which—for large atom numbers—is a major improvement over $\Delta\varphi = N^{-1/2}$ with the latter applying for unentangled states.

In other interferometry schemes, however, the total atom number does not agree with the number of phase interrogations. An important example is phase estimation with one atom traversing the interrogation stage many times. If in such a situation the atom number rather than the number of interrogations is inaccurately taken as a resource it seems that the Heisenberg limit could be surpassed—even without using entanglement at all [50]. Such and similar inconsistencies are caused by a wrong accounting of the resource [48, 49]. In this thesis we implement an interferometric sequence that relies on amplifying nonlinear readout. Generally, the ability to amplify requires holding back particles in a reservoir. For proper benchmarking of such interferometry schemes, only those atoms that experience the phase shift are counted as an expensive resource [51]. If we allow for fluctuations of this atom number ($\langle N\rangle$ denotes its average value) the associated Heisenberg limit is slightly adjusted and reads $\Delta\varphi = [\langle N\rangle(\langle N\rangle + 2)]^{-1/2}$ [52, 53].

This bound applies to linear phase estimation. This means that the phase imprint is identical for each employed atom. A popular counterexample in quantum optics is phase estimation exploiting the Kerr-effect [54]. For such nonlinear interferometers, that is interferometers with nonlinear phase evolution, the Heisenberg limit as stated above does not apply [55–58]. Within these two contexts the attribute nonlinear is routinely used. In this thesis we use the term nonlinear to account for processes which are able to generate entanglement among the probes [59]. Therefore, it is justified to call the readout technique nonlinear. In contrast, transformations which cannot generate particle entanglement are called linear. While this concerns the initial state preparation and the subsequent readout, the actual phase interrogation in between is linear as defined above.

[1] This argumentation is not restricted to interferometers. Grovers algorithm, for instance, exploits quantum effects to learn about an unknown function (the so-called oracle) by performing fewer operations (interrogations) on that function than classically necessary [15].

1.4 Tailorable Nonlinear Amplifier for Entanglement Generation

We implement the nonlinear readout scheme within the well isolated atomic spin degree of freedom. Crucially, this scheme relies on a customizable amplification process where the sign of the governing Hamiltonian can be inverted. We use spin exchange to experimentally realize such an amplifier [60, 61]. This very process is used for entangled state generation, the nonlinear readout, and a posteriori amplification.

Here, we present the conceptual idea and first show how an entangled probe state is generated by amplification. Let us consider a spin-1 system whose three magnetic sublevels are shown in Fig. 1.2a. In such a system, spin exchange describes a scattering process during which two atoms of the $|0\rangle$ state are transferred to states $|\uparrow\rangle$ and $|\downarrow\rangle$ each as indicated. In our experiments we start with empty modes $|\uparrow\rangle$ and $|\downarrow\rangle$—only the mode $|0\rangle$ is highly populated. Within the appropriate limits, this elementary process is then governed by a Hamiltonian of the form

$$\mathcal{H} = \hbar\kappa\ \hat{a}_{\uparrow}^{\dagger}\hat{a}_{\downarrow}^{\dagger} + \text{h.c.} \tag{1.1}$$

Here, the pairwise process is described by creation operators $\hat{a}_{\uparrow}^{\dagger}$ and $\hat{a}_{\downarrow}^{\dagger}$ for modes $|\uparrow\rangle$ and $|\downarrow\rangle$, respectively. This introduces nonclassical correlations among the atoms of both modes [62–64]. Such scattering processes realize an amplifier: the atoms in state $|0\rangle$ provide a particle reservoir which is used to reinforce the population of the two remaining spin states. With initially empty spin states $|\uparrow\rangle$ and $|\downarrow\rangle$ the amplification process is initially triggered by quantum fluctuations [65–67]. In this line of thinking, the reservoir atoms define the nonlinearity or gain κ—and thus the rate at which these collisions occur.

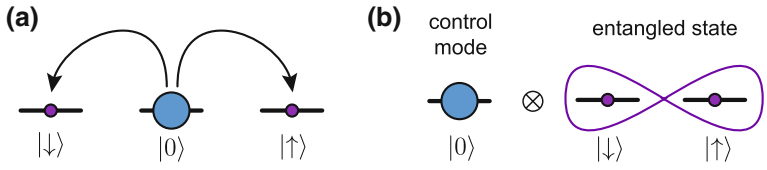

Fig. 1.2 Spin exchange as highly customizable nonlinear mechanism. **a** Spin exchange describes the pairwise scattering of two atoms residing in the pump mode ($|0\rangle$) into spin states $|\uparrow\rangle$ and $|\downarrow\rangle$ each. This process generates a particle entangled state in modes $|\uparrow\rangle$ and $|\downarrow\rangle$. Both, the magnitude as well as the phase of this nonlinear process can be tailored via the classically populated pump mode $|0\rangle$, which therefore acts as a control mode: by modifying the number of pump atoms, the nonlinear coupling κ is varied in strength. Similarly, by changing the phase of the pump mode the sign of the nonlinearity can be inverted. We therefore endorse the view of a classically populated mode that exerts comprehensive control over the quantum mechanically entangled sub system as illustrated in the cartoon of panel (**b**)

The key feature of this implementation is that the nonlinear coupling strength κ can be tailored by solely controlling the reservoir atoms in state $|0\rangle$. Both, the magnitude as well as the phase and thus the overall sign of κ can thereby be altered. We therefore take the point of view that the quantum mechanical subsystem formed by $|\uparrow\rangle$ and $|\downarrow\rangle$ with its nonclassical correlations can be controlled comprehensively by a third mode as sketched in Fig. 1.2b.

1.5 Quantum-Enhanced Interferometry with Linear Readout

In this section we detail how quantum-enhanced phase measurements are accomplished with linear interferometry. The arguments presented above in abstracto will be substantiated by considering specific cases in detail. With these examples we cover the most widely used states employed in quantum metrology and their discussion will showcase the characteristics of using highly entangled probe states. For reference we start our discussion with a separable (unentangled) state. Based on this we will present the peculiarities when dealing with highly entangled probe states.

A Mach-Zehnder interferometer as depicted in Fig. 1.3a can be considered prototypical for linear two-mode interferometry [68]. In order to estimate the differential phase shift φ the first beam splitter generates a phase sensitive probe state. It is a superposition of modes described by bosonic creation operators $\hat{c}^\dagger$ and $\hat{d}^\dagger$. The second beam splitter downstream maps the accumulated phase onto distinct mode populations measured at the detection stage, i.e. in modes described by $\hat{e}^\dagger$ and $\hat{f}^\dagger$. In such a scheme the last beam splitter taken together with subsequent intensity measurements constitutes a linear readout.

Before we investigate highly nonclassical states we consider a separable probe state which is shown in panel (b). The four histograms denote the mode population of the probe (top) and output state (lower three panels). The output distributions are shown for three distinct phase imprints as indicated. The state at all stages of the interferometric sequence can be described in the following way (each terms acts onto vacuum)

$$(\hat{b}^\dagger)^N \rightarrow (\hat{c}^\dagger + \mathrm{i}\hat{d}^\dagger)^N \rightarrow (\hat{c}^\dagger + \mathrm{i}\mathrm{e}^{\mathrm{i}\varphi}\hat{d}^\dagger)^N \rightarrow (\cos\varphi\hat{e}^\dagger + \sin\varphi\,\hat{f}^\dagger)^N \tag{1.2}$$

Here, we use mode operators as defined in Fig. 1.3. The first step describes the action of the (balanced) beam splitter when N (identical and bosonic) particles enter via one of its input ports. The resulting state is an equal superposition of modes described by $\hat{c}^\dagger$ and $\hat{d}^\dagger$. The population distribution of this probe state is shown in panel b (top). The two modes inside the interferometer get populated in a binomial fashion. Subsequent phase interrogation is described by modified mode operators, $\hat{d}^\dagger \rightarrow \mathrm{e}^{\mathrm{i}\varphi}\hat{d}^\dagger$. The accumulated differential phase is finally mapped onto the output

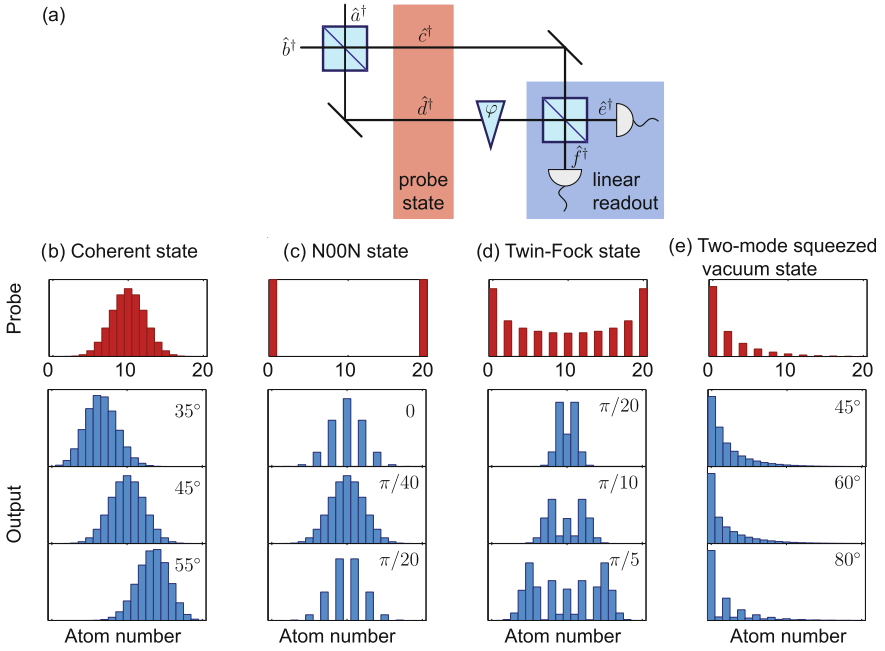

Fig. 1.3 Quantum-enhanced interferometry with linear readout. **a** A Mach-Zehnder interferometer is archetypical for linear two path interferometry. The last beam splitter in combination with subsequent intensity detection at its output can be considered a linear readout. The four panels **b–e** show the respective population distributions in each mode for different quantum states at the probe (top) and output stage (lower three histograms are for three different phase settings). **b** Separable (coherent) state. Starting with N particles at one input, the first beam splitter generates a phase sensitive equal superposition of the two modes. Each of the modes is populated in a binomial fashion (top histogram). A second beam splitter translates the accumulated phase difference φ between the modes into distinct output populations. The three histograms show the counting statistics of mode described by $\hat{e}^\dagger$ for the indicated phase. Tracking the shift of the average population allows estimating the accrued phase. **c** $N00N$ state injected into the interferometer *after* the first beam splitter. The probe state is described by a superposition of all $N = 20$ atoms either in mode described by $\hat{c}^\dagger$ or $\hat{d}^\dagger$ (top histogram). At the output of the interferometer fringes at the single atom level emerge. The broad envelope has the shape of a separable state but does not shift under phase imprints. To recover a phase sensitive signal, the underlying fine structure has to be resolved. **d** Twin-Fock state at input. The probe state is a comb consisting only of even atom numbers. At the output, both the envelope as well as the finer structure on top changes. **e** Two-mode squeezed vacuum state at input. Similar to case (**d**) the probe contains only even atom numbers. Depending on the phase accumulated, the odd atom numbers get filled up to different levels

mode population by the second beam splitter. The lower three histograms of panel (b) show the mode population recovered at one of the two outputs. Clearly, as the imprinted phase varies the centre of the output distribution shifts. Therefore, by measuring the average population at the output state, $\langle N \rangle = N \cos^2 \varphi$ the phase φ can be inferred. The corresponding phase sensitivity can be determined by applying error propagation, $(\Delta\varphi)^2 = (\Delta N)^2/|\mathrm{d}N/\mathrm{d}\varphi|^2$ which takes into account both, the fluctuations at the output, as well as the slope of the signal. As a consequence of the binomial output statistics the variance of the observable is $(\Delta N)^2 = 4N \cos^2 \varphi \sin^2 \varphi$. Therefore, the phase sensitivity reads $(\Delta\varphi)^2 = 1/N$ and is independent of the working point. We recognize the classical bound for phase estimation with independent probes.

We now detail the implications when employing entangled states for achieving higher phase precision [69]. Highest phase sensitivity is attained when using the so-called $N00N$ state at the probe stage [70]. Its name derives from the fact that its dual-rail representation reads $|N, 0\rangle + |0, N\rangle$. Therefore it is a coherent superposition of all N particles being in either mode with the respective other empty. For atomic states it is most often referred to as GHZ (Greenberger et al. [71]) state. For this interferometry scheme, the state after the first beam splitter, i.e. at the probe stage, reads $(\hat{c}^\dagger)^N + (\hat{d}^\dagger)^N$. Its population histogram for one of the involved modes is shown in panel (c) (top). The phase imprint and the final beam splitting is described by

$$(\hat{c}^\dagger)^N + (\hat{d}^\dagger)^N \rightarrow (\hat{c}^\dagger)^N + \mathrm{e}^{\mathrm{i}N\varphi}(\hat{d}^\dagger)^N \rightarrow (\hat{f}^\dagger + \mathrm{i}\hat{g}^\dagger)^N + \mathrm{e}^{\mathrm{i}N\varphi}(\hat{e}^\dagger - \mathrm{i}\hat{f}^\dagger)^N \quad (1.3)$$

This should be compared to Eq. 1.2. As a result of the final beam splitting the atom number distribution recovered at the output (panel c) has a binomial envelope identical to the separable state. However, as the phase inside the interferometer is changed this envelope remains unaltered. Instead the finer structure within changes [72]. This fine structure is on single-atom level and is described by modifying the probabilities for detecting an odd or even atom number by $\sin^2(N\varphi)$ and $\cos^2(N\varphi)$, respectively [73, 74]. Therefore, rather than being phase dependent to φ the phase winds N times faster, i.e. the phase dependence is with respect to $N\varphi$. This property, which is characteristic for entangled states is called super-resolving. As a side effect it reduces the dynamic range.

A different class of entangled states that allow for quantum-enhanced phase measurements are twin-Fock states [75]. Here the input state is given by $(\hat{a}^\dagger)^{N/2}(\hat{b}^\dagger)^{N/2}$ (panel d). The first beam splitter transforms this into a comb-like distribution with only even atom numbers of the probe state being populated, the so-called Holland-Burnett state [75]. For two atoms, the absence of the odd contribution corresponds to the famous Hong-Ou-Mandel dip. If no differential phase is accumulated ($\varphi = 0$) the twin-Fock state (input state) is recovered at the output. Instead, for a phase of $\pi/2$ the *probe* state is retained at the output. In between both of these phase settings the state grows rapidly in size with a fine structure at single-atom level on top. The fine structure is modulated with respect to 2φ. The average value vanishes for all phase settings [76].

Finally, building on the previous case, a superposition of twin-Fock states is considered. Such states are highly relevant because they are routinely generated by the process of parametric amplification. There, the emerging state (called two-mode squeezed vacuum state) is a superposition of twin-Fock states with weights p_k that decrease in a power-law fashion, $\sum_{k=0}^{\infty} \sqrt{p_k}(\hat{a}^\dagger \hat{b}^\dagger)^k$ [77]. Here, an important distinction to the previous examples is that this state involves arbitrary high twin-Fock states (albeit with ever-decreasing weights). Therefore the state's atom number is only defined by its average population. Because of the underlying twin-Fock character the probe state has only even atom numbers populated (panel e, top). The envelope which resembles a thermal state is characteristic for this two-mode squeezed vacuum state. At phase $\pi/2$ this probe state is recovered at the output. Phase changes around $\pi/2$ yield to a filling up of the (initially) absent odd population numbers while the envelope is barely changed [78].

The appearance of finer structures (at single particle level) amidst a broad pattern is a general feature connected to entangled states and their linear readout. In any case, the average mode population ceases to be phase dependent and one needs to determine higher moments of the underlying mode population. While for the twin-Fock state the second moment suffices [62, 75], the $N00N$ and twin-Fock state need much higher moments: the phase information can be retrieved by evaluating the parity signal of the output atom number distribution, $\Pi = \mathrm{e}^{\mathrm{i}\pi n}$ which assigns $+1$ (-1) to an even (odd) atom count n [73]. While it is prone to detection noise as it needs single-atom resolution, it is efficient in the sense that it contains all moments k of the probability distribution, $\Pi \sim \sum_k \langle n^k \rangle$ [73, 74].

1.6 Advantage of Amplifying Nonlinear Readout

Here we pick up on two examples provided in the previous section and exemplify how nonlinear readout eases detection. The prototypical scheme realising nonlinear readout is shown in Fig. 1.4a. The crucial feature of the nonlinear readout is its mapping of the accumulated phase onto first moments that are accessible via global measurements. This makes single-atom resolution unnecessary even when approaching the ultimate limit on phase sensitivity [79–86]. Additional to this mapping onto easily accessible observables the output signal can be amplified without signal degradation [87, 88].

Mapping onto global observables

As a probe state we specifically consider the $N00N$ (panel b) and the two-mode squeezed vacuum state (panel c). While the latter is the subject of this thesis, the $N00N$ state was treated in the seminal paper experimentally demonstrating nonlinear readouts to approach the Heisenberg limit of phase sensitivity [81]. We summarize the idea in panel (b). The first nonlinear process generates the entangled $N00N$ state for phase probing. The top histogram shows the atom number distribution in either of the two interferometry modes. To be consistent with the previous section

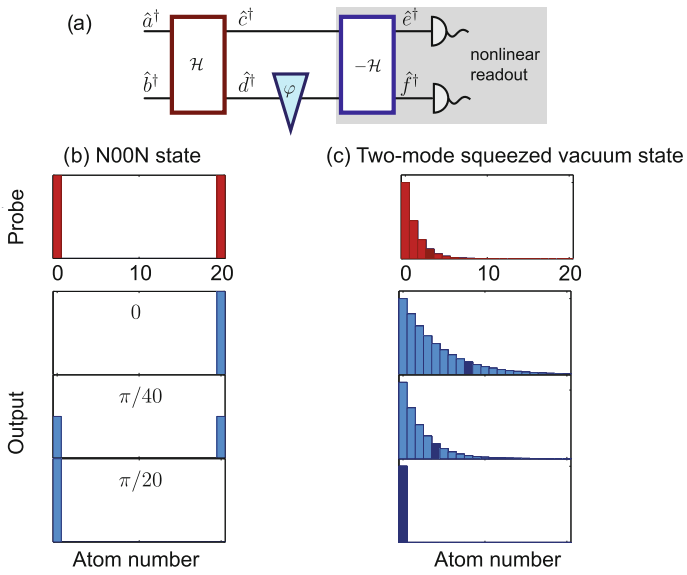

Fig. 1.4 Nonlinear readout. **a** Schematic representation of interferometry with nonlinear readout. Here, a nonlinear mechanism (blue) that is attuned to the initial entangling process (red) is used after phase interrogation. In panels **b** and **c** population distributions akin to Fig. 1.3 are shown. **b** Population distribution of mode described by $\hat{c}^\dagger$ when the first nonlinear process generates a $N00N$ state of 20 atoms as probe. Depending on the phase shift φ the subsequent nonlinear process generates population distributions of the mode described by $\hat{e}^\dagger$ as indicated in the three lower histograms. **c** Two-mode squeezed vacuum state as probe (top). Depending on the phase imprint the second nonlinear process enhances or diminishes the average atom number (indicated by dark coloured bin) found in mode described by $\hat{e}^\dagger$. In both cases, the full phase information contained in the entangled state is mapped onto the first moment of the output population distribution

we choose a total atom number of 20 (the pioneering experiment was performed with three beryllium ions). After differential phase accumulation the same nonlinear process that produced the entangled state in the first place is reapplied before readout. It maps the phase dependence onto only two possible outcome states: all atoms identically leave either of the two output ports. Such an output signal is maximally robust towards detection inefficiencies. The three lower histograms show the output statistics of mode described by $\hat{e}$ for different phase settings. Compared to the linear readout scheme, no single-atom resolved measurements are necessary. Instead, a global measurement suffices and the super-resolving phase signal can be recovered by determining the average mode population.

The nonlinear readout harnessing the two-mode squeezed vacuum state works in a similar fashion. However, as emphasized above, while the $N00N$ state has a fixed number of particles the generation of the two-mode squeezed vacuum state involves superpositions of twin-Fock states with different total atom numbers. Therefore, the atom number of the two-mode squeezed vacuum state is defined only by an average. The two-mode squeezed vacuum state is shown in panel (c). The population

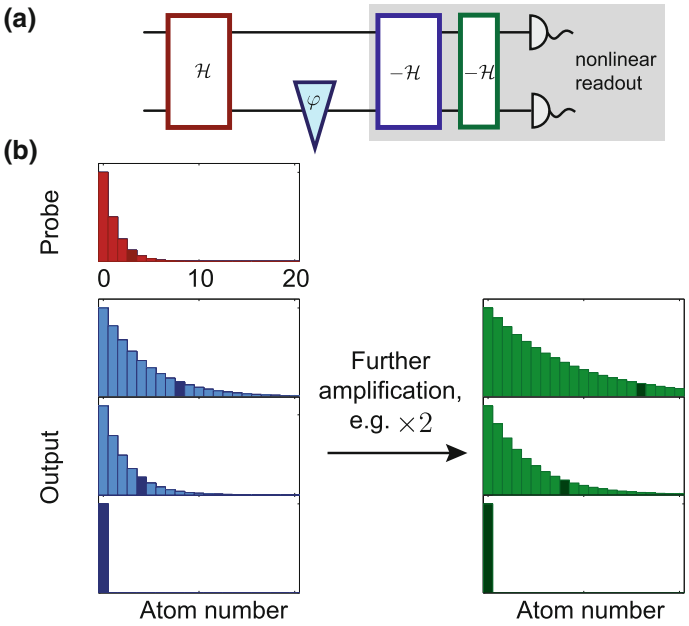

Fig. 1.5 Amplifying nonlinear readout. **a** The intrinsic amplification of the nonlinear readout can be enlarged by extending the scheme with an additional period under nonlinear dynamics (green). This extra amplification is noiseless in the sense that it does not degrade the phase sensitivity. Regardless of the amplification factor a phase sensitivity at the Heisenberg limit can be retained. **b** Counting statistics at three different stages (indicated by colour) of the interferometer similar to Fig. 1.4. The dark coloured bins indicate the average value

distribution at both, the probe stage (top) as well as the readout stage (lower panels) follow a distinctive thermal-like skewed distribution. Their average value (indicated by the dark coloured bin) constitutes the phase sensitive signal. Measurements of this average value suffice to fully exhaust the quantum resource up to the fundamental Heisenberg limit [89].

Sensitivity-maintaining amplification of the output signal

Furthermore to the mapping onto global observables the two-mode squeezed vacuum state is amplified during the nonlinear readout. This intrinsic amplification of the output signal facilitates additionally the detection. This stands in contrast to the $N00N$ state whose passive scheme redistributes an ever-fixed number of atoms for readout. Apart from the inherent amplification when using the two-mode squeezed vacuum state in the symmetric arrangement of Fig. 1.4 the output signal can be amplified even further. For this the nonlinear readout is extended by an additional period of nonlinear evolution as illustrated in Fig. 1.5a. Panel (b) shows the atom number distribution at the probe stage (red), after (symmetric) time-reversal (blue) and after additional amplification (green). During the final amplification stage the output signal is magnified nonlinearly once more. Remarkably, the phase sensitivity

of the interferometer is not degraded by the additional amplification and Heisenberg limited phase sensitivity can still be retained. This counterintuitive behaviour is the consequence of the entanglement present during amplification [87, 88].

Therefore, the resource entanglement is harnessed twice in this scheme: first, it enables a nonclassical phase measurement which surpasses the classical precision bound. For this purpose, entanglement has to be present at the probe stage [21]. Secondly, during nonlinear readout the entanglement enables the amplification of the output without signal degradation. The ability to amplify the output signal allows for detection noise resilient phase estimation approaching the ultimate Heisenberg limit [90]. This is because, in principle, any amount of technical noise that is added during the detection process can be rendered negligible by choosing sufficiently large amplification.

1.7 Organisation of this Thesis

To experimentally realize the nonlinear readout scheme we use spin exchange among three states which altogether form an effective spin-1 system. We therefore devote the first chapter to the theoretical description of quantum mechanical spins. We begin with the conceptually simplest case of a spin-1/2 object before presenting the peculiarities of spin-1 systems on that basis. Next, we detail the collisional interactions that arise in ultracold spinor systems which eventually leads to the Hamiltonian description of spin exchange. Before discussing the inherent quantum features of this Hamiltonian we provide an intuitive picture based on classical approximations. In Chap. 4 we reexamine the Hamiltonian description in view of parametric amplification. This analogy is based on an approximation that is central to this work—a highly populated spin mode which acts akin a undepleted reservoir. The comprehensive possibilities of control promote the process of parametric amplification to the central building block of the nonlinear readout scheme—which will be described in depth. Chapter 5 provides a more formal treatment that builds on the so-called SU(1,1) framework. In this mathematical framework the common and distinctive features of the nonlinear readout when comparing it to routinely employed interferometers are especially evident. With this we conclude the conceptual part of the thesis.

Our experimental apparatus to study spinor Bose-Einstein condensates is presented in Chap. 6. In particular we detail the techniques employed to control spin exchange reliably. The experimental results are the subject of the chapters that follow: we characterize the process of spin exchange in Chap. 7. For this the essential parameters, i.e. nonlinear coupling strength, detuning, and spin relaxation rates are determined. Special attention is paid to the nascent spin state and its distinguishing features—chiefly its coherent spin fluctuations. Finally, we probe the conditions that have to be met in order to achieve prototypical parametric amplification.

In Chap. 8 we present the results of time reversal interferometry. Here, the nonlinear readout is matched to the initial preparation of an entangled state. We explicitly

show that the phase sensitivity is better than classically allowed. Subsequently—in Chap. 9—we extend the scheme and characterize the amplifying nonlinear readout. Here an additional amplifier stage is added before detection. We show that quantum-enhanced phase sensitivity is not only preserved but made more robust.

We employ the nonlinear readout as an instrument in Chap. 10 and present two applications: first, motivated by theoretical studies of phase diffusion in Bose-Einstein condensates, the nonlinear readout is used to investigate the mechanisms of phase damping. In the second application the nonlinear readout is employed to characterize its input state. Specifically, it serves as a witness for Einstein-Podolsky-Rosen entanglement.

Finally—in the outlook—we present a method to extend the nonlinear readout such that time reversal is achieved even when going beyond the restrictive approximation of an undepleted reservoir. Recently, the study of out-of-time order correlations has attracted considerable interest. We show that the nonlinear readout in fact realizes such a measurement.

1.8 Publication List

(1) H. Strobel, W. Muessel, D. Linnemann, T. Zibold, D.B. Hume, L. Pezzé, A. Smerzi, M.K. Oberthaler, Fisher information and entanglement of non-Gaussian spin states. Science **345**, 424–427 (2014), http://dx.doi.org/10.1126/science.1250147.

(2) W. Muessel, H. Strobel, D. Linnemann, D.B. Hume, M.K. Oberthaler, Scalable spin squeezing for quantum-enhanced magnetometry with Bose-Einstein condensates. Phys. Rev. Lett. **113**, 103004 (2014), http://dx.doi.org/10.1103/PhysRevLett.113.103004.

(3) W. Muessel, H. Strobel, D. Linnemann, T. Zibold, B. Juliá-Díaz, M.K. Oberthaler, Twist-and-turn spin squeezing in Bose-Einstein condensates. Phys. Rev. A **92**, 023603 (2015), http://dx.doi.org/10.1103/PhysRevA.92.023603.

(4) D. Linnemann, H. Strobel, W. Muessel, J. Schulz, R.J. Lewis-Swan, K.V. Kheruntsyan, M.K. Oberthaler, Quantum-enhanced sensing based on time reversal of nonlinear dynamics. Phys. Rev. Lett. **117**, 013001 (2016), http://dx.doi.org/10.1103/PhysRevLett.117.013001.

(5) D. Linnemann, J. Schulz, W. Muessel, P. Kunkel, M. Prüfer, A. Frölian, H. Strobel, M.K. Oberthaler, active SU(1, 1) atom interferometry. Quantum Sci. Technol. **2**, 044009 (2017), http://stacks.iop.org/2058-9565/2/i=4/a=044009.

(6) P. Kunkel, M. Prüfer, H. Strobel, D. Linnemann, A. Frölian, T. Gasenzer, M. Gärttner, M.K. Oberthaler, Spatially distributed multipartite entanglement enables EPR steering of atomic clouds. Science **360**, 413–416 (2018), http://dx.doi.org/10.1126/science.aao2254.

This thesis' main result as described in Chap. 8—the realization of a quantum-enhanced phase measurement which is based on time reversal during nonlinear

readout—is published in reference (4). Furthermore, in reference (5) the amplifying nonlinear readout stage is treated in the framework of the so-called SU(1,1) interferometer. Therein we discuss the characterising features by comparing it to routinely used passive interferometry schemes. Parts of this thesis' Chaps. 5 and 7 are published in this paper.

1.9 Overview of Related Experiments

Here, we review related work to put this thesis' content into perspective and to provide a broader overview. With science being rarely disruptive, advances in diverse areas are made in parallel. The basic idea of using two nonlinear processes in sequence with a phase accumulation stage in between has been realized using different experimental platforms. In this section we present the most relevant experiments. We start with those that are dealing with photons. For these experiments the nonlinear mechanism is implemented by parametric amplification, a Hamiltonian that is formally equivalent to the one used in this thesis (Eq. 1.1). Therefore, from a procedural point of view, these photonic experiments bear greatest resemblance to the atomic spin exchange experiments of this thesis.

Quantum optics

Using parametric down-conversion in a nonlinear crystal, the authors of reference [91] retroreflected the signal and idler beam to traverse the nonlinear crystal once more. Depending on a phase imprint, the intensity of the signal and idler beams after passing the crystal twice is either enhanced or diminished. By systematically changing the phase of all three involved beams individually (pump, signal, and idler) the overall phase dependence was inferred. In our atomic spin system this phase is called spinor phase and will be introduced in Chap. 2.

With the bulk crystal being substituted by a photonic crystal fibre (to achieve larger nonlinearities) a similar experiment arrangement was studied in reference [92]. Special attention is paid to the fact that the second fibre passing comprises a detection which is sensitive only to biphotons [93]. The modulation depth of this biphotonic signal was used to study qualitatively the transition from classical to quantum nonlinear behaviour.

Parametric amplification can be realized by three (four) wave mixing in alkali vapour gases. For this one exploits the strongly nonlinear response to light being close to two-photon resonance of an atomic three level system. In references [94, 95] vapour cells filled with Rubidium-85 operated at thermal temperatures are used. Using two such vapour cells in sequence, an interferometer was realized in [96, 97]. Using a bright seed for parametric amplification, quantum-enhanced phase sensitivity could be inferred [98]. In a similar setup the authors of reference [88] surpassed the quantum noise limit for amplification by using an entangled state. We will elaborate on this aspect of noiseless amplification and interferometry in Chap. 8. Similar to our atomic experiments which start with vacuum initially, quantum-enhanced per-

formance was recently observed for unseeded optical parametric amplification [99]. This operation regime where amplification is not predetermined by classical seeds is more challenging. Subsequent additional amplification is employed additionally which we detail in Chap. 9.

Superconducting qubits

In a cryogenic environment, a Josephson mixer is used to realize the parametric amplification Hamiltonian for microwave photons [100]. The emerging entangled state is distributed over two transmission lines. Reversibility under a second Josephson mixer was used as an entanglement witness. We will detail the procedure in Chap. 10 and extend it such that a particular strong form of Einstein-Podolsky-Rosen entanglement is witnessed [101].

In reference [102] entangled microwave photons are employed to interrogate an ensemble of electronic spins via their magnetic resonance. Entangling and readout are both implemented by Josephson mixers. Quantum-enhanced performance was demonstrated.

Trapped ions

Beyond question cooled and trapped ions offer the highest degree of experimental control with impressive single gate fidelities surpassing 'six nines' [103] and entangling gates at the 'three nines' level [104, 105]. Additionally, their high fidelity readout makes them ideally suited for quantum information processing tasks [106, 107]. As detailed in the previous section a nonlinear readout scheme harnessing a $N00N$ state for quantum-enhanced interferometry was realized with three beryllium ions. In this pioneering work [81], the authors directly compare the outcome obtained under linear and nonlinear readout. They stress the advantage of the latter if detection infidelities were present. While the previous photonic experiments leveraged parametric amplification, here a different nonlinear mechanism is employed which generates an $N00N$ state in the spin degree of freedom [108]. Charged ions, however, suffer one drawback: the two-gate interactions (among two specific ions) are (usually) mediated via collective vibrational modes which become narrowly spaced as more and more ions are used. Therefore, the extension to large arrays of many ions while maintaining the high speed of gate operations remains challenging [109–111].

Giving up the individual addressability a large two-dimensional crystal of more than 100 ions with collective interactions among them was realized recently [112, 113]. In this system a time reversal sequence was implemented to study out-of-time-ordered correlators [114]. With the ability to accurately determine the overlap of the final and initial state, the multiple quantum coherence spectrum could be extracted.

Cold gases in optical cavities

The authors of reference [115] use nonlinear interactions to magnify a quantum state before readout. A similar nonlinear process is employed to, first, generate an entangled spin-squeezed state, which is subsequently magnified to ease detection. An ensemble containing half a million laser cooled Rubidium atoms is used. The collective nonlinear interactions are mediated by an optical cavity [116]. Comprehensive theoretical studies are focussed on similar experimental setups [84, 117].

Ultracold gases

The collisional interactions inherent to degenerate quantum gases provide a strong nonlinear mechanism which promotes them to an ideal testing bed for nonlinear quantum atom optics [118]. Early on phase-sensitive amplification of matter waves was observed [119, 120]. In these experiments Raman scattering is used to couple out atoms of the condensate spatially.

More recently, experiments conducted within the spin degree of freedom reach the quantum noise limit of amplification. The authors of reference [121] studied how spin exchange is inhibited by imprinting phase shifts stroboscopically. To this end the sequence contains periods of nonlinear evolution with subsequent quasi-instantaneous phase imprints. The authors investigate the results in the context of stabilization theory.

References

1. A. Celi, A. Sanpera, V. Ahufinger, M. Lewenstein, Quantum optics and frontiers of physics: the third quantum revolution. Phys. Scr. **92**, 013003 (2016)
2. J.P. Dowling, G.J. Milburn, Quantum technology: the second quantum revolution. Phil. Trans. R. Soc. Lond. A **361**, 1655–1674 (2003)
3. A. de Touzalin, C. Marcus, F. Heijman, I. Cirac, R. Murray, T. Calarco, Quantum manifesto. A new era of technology (2016). http://qurope.eu/manifesto
4. E. Gibney et al., Billion-euro boost for quantum tech. Nature **532**, 426 (2016)
5. J. Mlynek, Quantum technologies flagship, intermediate report (2017). http://ec.europa.eu/newsroom/document.cfm?doc_id=42721
6. T.D. Ladd, F. Jelezko, R. Laflamme, Y. Nakamura, C. Monroe, J.L. O'Brien, Quantum computers. Nature **464**, 45 (2010). https://doi.org/10.1038/nature08812
7. E. Cartlidge, Quantum computing: How Close Are We? Opt. Photon. News **27**, 30–37 (2016). https://doi.org/10.1364/OPN.27.10.000030
8. G. Popkin, Scientists are close to building a quantum computer that can beat a conventional one. Science (2016)
9. D. Castelvecchi, Quantum computers ready to leap out of the lab in 2017. Nature **541**, 9 (2017)
10. G. Kurizki, P. Bertet, Y. Kubo, K. Molmer, D. Petrosyan, P. Rabl, J. Schmiedmayer, Quantum technologies with hybrid systems. PNAS **112**, 3866–3873 (2015). https://doi.org/10.1073/pnas.1419326112
11. N.M. Linke, D. Maslov, M. Roetteler, S. Debnath, C. Figgatt, K.A. Landsman, K. Wright, C. Monroe, Experimental comparison of two quantum computing architectures. PNAS **114**, 3305–3310 (2017). https://doi.org/10.1073/pnas.1618020114
12. N. Gisin, G. Ribordy, W. Tittel, H. Zbinden, Quantum cryptography. Rev. Mod. Phys. **74**, 145–195 (2002). https://doi.org/10.1103/RevModPhys.74.145
13. N. Gisin, R. Thew, Quantum communication. Nat. Photon. **1**, 165–171 (2007). https://doi.org/10.1038/nphoton.2007.22
14. L. Fortnow, The status of the P versus NP problem. Commun. ACM **52**, 78–86 (2009)
15. M. Nielsen, I. Chuang, *Quantum Computation and Quantum Information* (Cambridge University Press, 2000). https://books.google.de/books?id=-s4DEy7o-a0C
16. J.L. O'Brien, A. Furusawa, J. Vuckovic, Photonic quantum technologies. Nat. Photon. **3**, 687–695 (2009). https://doi.org/10.1038/nphoton.2009.229

17. W. Nawrocki, *Introduction to Quantum Metrology: Quantum Standards and Instrumentation* (Springer, 2015). https://books.google.de/books?id=7VSzBwAAQBAJ
18. E. Goebel, U. Siegner, *Quantum Metrology: Foundation of Units and Measurements* (Wiley, 2015). https://books.google.de/books?id=NCCPCQAAQBAJ
19. J. Brun-Picard, S. Djordjevic, D. Leprat, F. Schopfer, W. Poirier, Practical quantum realization of the ampere from the elementary charge. Phys. Rev. X **6**, 041051 (2016). https://doi.org/10.1103/PhysRevX.6.041051
20. V. Giovannetti, S. Lloyd, L. Maccone, Quantum-enhanced measurements: beating the standard quantum limit. Science **306**, 1330–1336 (2004). https://doi.org/10.1126/science.1104149
21. V. Giovannetti, S. Lloyd, L. Maccone, Quantum metrology. Phys. Rev. Lett. **96**, 010401 (2006). https://doi.org/10.1103/PhysRevLett.96.010401
22. V. Giovannetti, S. Lloyd, L. Maccone, Advances in quantum metrology. Nat. Photon. **5**, 222–229 (2011). https://doi.org/10.1038/nphoton.2011.35
23. C.F. Roos, M. Chwalla, K. Kim, M. Riebe, R. Blatt, Designer atoms' for quantum metrology. Nature **443**, 316–319 (2006). https://doi.org/10.1038/nature05101
24. A.D. Ludlow, M.M. Boyd, J. Ye, E. Peik, P.O. Schmidt, Optical atomic clocks. Rev. Mod. Phys. **87**, 637–701 (2015). https://doi.org/10.1103/RevModPhys.87.637
25. N. Huntemann, C. Sanner, B. Lipphardt, C. Tamm, E. Peik, Single-Ion atomic clock with 3×10^{-18} systematic uncertainty. Phys. Rev. Lett. **116**, 063001 (2016). https://doi.org/10.1103/PhysRevLett.116.063001
26. I. Ushijima, M. Takamoto, M. Das, T. Ohkubo, H. Katori, Cryogenic optical lattice clocks. Nat.Photon. **9**, 185–189 (2015). https://doi.org/10.1038/nphoton.2015.5
27. B.J. Bloom, T.L. Nicholson, J.R. Williams, S.L. Campbell, M. Bishof, X. Zhang, W. Zhang, S.L. Bromley, J. Ye, An optical lattice clock with accuracy and stability at the 10^{-18} level. Nature **506**, 71–75 (2014). https://doi.org/10.1038/nature12941
28. T.L. Nicholson, S.L. Campbell, R.B. Hutson, G.E. Marti, B.J. Bloom, R.L. McNally, W. Zhang, M.D. Barrett, M.S. Safronova, G.F. Strouse, W.L. Tew, J. Ye, Systematic evaluation of an atomic clock at 2×10^{-18} total uncertainty. Nat. Commun. **6**, 6896 (2015). https://doi.org/10.1038/ncomms7896
29. C.W. Chou, D.B. Hume, J.C.J. Koelemeij, D.J. Wineland, T. Rosenband, Frequency comparison of two high-accuracy Al^+ optical clocks. Phys. Rev. Lett. **104**, 070802 (2010). https://doi.org/10.1103/PhysRevLett.104.070802
30. E.M. Kessler, P. Kómár, M. Bishof, L. Jiang, A.S. Sørensen, J. Ye, M.D. Lukin, Heisenberg-limited atom clocks based on entangled qubits. Phys. Rev. Lett. **112**, 190403 (2014). https://doi.org/10.1103/PhysRevLett.112.190403
31. N. Huntemann, B. Lipphardt, C. Tamm, V. Gerginov, S. Weyers, E. Peik, Improved limit on a temporal variation of m_p/m_e from comparisons of yb^+ and cs atomic clocks. Phys. Rev. Lett. **113**, 210802 (2014). https://doi.org/10.1103/PhysRevLett.113.210802
32. R.M. Godun, P.B.R. Nisbet-Jones, J.M. Jones, S.A. King, L.A.M. Johnson, H.S. Margolis, K. Szymaniec, S.N. Lea, K. Bongs, P. Gill, Frequency ratio of two optical clock transitions in $^{171}Yb^+$ and constraints on the time variation of fundamental constants. Phys. Rev. Lett. **113**, 210801 (2014). https://doi.org/10.1103/PhysRevLett.113.210801
33. N. Nemitz, T. Ohkubo, M. Takamoto, I. Ushijima, M. Das, N. Ohmae, H. Katori, Frequency ratio of Yb and Sr clocks with 5×10^{-17} uncertainty at 150 seconds averaging time. Nat. Photon. **10**, 258–261 (2016). https://doi.org/10.1038/nphoton.2016.20
34. P.A. Dirac, The cosmological constants. Nature **139**, 323 (1937)
35. J.-P. Uzan, The fundamental constants and their variation: observational and theoretical status. Rev. Mod. Phys. **75**, 403–455 (2003). https://doi.org/10.1103/RevModPhys.75.403
36. R. Schnabel, N. Mavalvala, D.E. McClelland, P.K. Lam, Quantum metrology for gravitational wave astronomy. Nat. Commun. **1**, 121 (2010). https://doi.org/10.1038/ncomms1122
37. R.X. Adhikari, Gravitational radiation detection with laser interferometry. Rev. Mod. Phys. **86**, 121–151 (2014). https://doi.org/10.1103/RevModPhys.86.121
38. B.P. Abbott et al., (LIGO Scientific Collaboration and Virgo Collaboration), GW150914: The advanced LIGO detectors in the era of first discoveries. Phys. Rev. Lett. **116**, 131103 (2016). https://doi.org/10.1103/PhysRevLett.116.131103

39. B.P. Abbott et al., (LIGO Scientific and Virgo Collaboration), GW170104: observation of a 50-solar-mass binary black hole coalescence at redshift 0.2. Phys. Rev. Lett. **118**, 221101 (2017). https://doi.org/10.1103/PhysRevLett.118.221101
40. J. Aasi et al., (The LIGO Scientific Collaboration), Enhanced sensitivity of the LIGO gravitational wave detector by using squeezed states of light. Nat. Photon. **7**, 613–619 (2013). https://doi.org/10.1038/nphoton.2013.177
41. J. Miller, L. Barsotti, S. Vitale, P. Fritschel, M. Evans, D. Sigg, Prospects for doubling the range of advanced LIGO. Phys. Rev. D **91**, 062005 (2015). https://doi.org/10.1103/PhysRevD.91.062005
42. Y. Ma, H. Miao, B.H. Pang, M. Evans, C. Zhao, J. Harms, R. Schnabel, Y. Chen, Proposal for gravitational-wave detection beyond the standard quantum limit through EPR entanglement. Nat. Phys. **13**, 776–780 (2017). https://doi.org/10.1038/nphys4118
43. R. Schnabel, Squeezed states of light and their applications in laser interferometers. Phys. Rep. **684**, 1–51 (2017). https://doi.org/10.1016/j.physrep.2017.04.001
44. C.L. Degen, F. Reinhard, P. Cappellaro, Quantum sensing. Rev. Mod. Phys. **89**, 035002 (2017). https://doi.org/10.1103/RevModPhys.89.035002
45. A.D. Cronin, J. Schmiedmayer, D.E. Pritchard, Optics and interferometry with atoms and molecules. Rev. Mod. Phys. **81**, 1051–1129 (2009). https://doi.org/10.1103/RevModPhys.81.1051
46. H. Zhang, R. McConnell, S. Cuk, Q. Lin, M.H. Schleier-Smith, I.D. Leroux, V. Vuletic, Collective state measurement of mesoscopic ensembles with single-atom resolution. Phys. Rev. Lett. **109**, 133603 (2012). https://doi.org/10.1103/PhysRevLett.109.133603
47. D.B. Hume, I. Stroescu, M. Joos, W. Muessel, H. Strobel, M.K. Oberthaler, Accurate atom counting in mesoscopic ensembles. Phys. Rev. Lett. **111**, 253001 (2013). https://doi.org/10.1103/PhysRevLett.111.253001
48. M. Zwierz, C.A. Pérez-Delgado, P. Kok, General optimality of the Heisenberg limit for quantum metrology. Phys. Rev. Lett. **105**, 180402 (2010). https://doi.org/10.1103/PhysRevLett.105.180402
49. M. Zwierz, C.A. Pérez-Delgado, P. Kok, Ultimate limits to quantum metrology and the meaning of the Heisenberg limit. Phys. Rev. A **85**, 042112 (2012). https://doi.org/10.1103/PhysRevA.85.042112
50. B.L. Higgins, D.W. Berry, S.D. Bartlett, H.M. Wiseman, G.J. Pryde, Entanglement-free Heisenberg-limited phase estimation. Nature **450**, 393–396 (2007). https://doi.org/10.1038/nature06257
51. M.W. Mitchell, Number-unconstrained quantum sensing. Quantum Sci. Technol. **2**, 044005 (2017). http://stacks.iop.org/2058-9565/2/i=4/a=044005
52. H.F. Hofmann, All path-symmetric pure states achieve their maximal phase sensitivity in conventional two-path interferometry. Phys. Rev. A **79**, 033822 (2009). https://doi.org/10.1103/PhysRevA.79.033822
53. L. Pezzè, P. Hyllus, A. Smerzi, Phase-sensitivity bounds for two-mode interferometers. Phys. Rev. A **91**, 032103 (2015). https://doi.org/10.1103/PhysRevA.91.032103
54. M. Kitagawa, Y. Yamamoto, Number-phase minimum-uncertainty state with reduced number uncertainty in a kerr nonlinear interferometer. Phys. Rev. A **34**, 3974–3988 (1986). https://doi.org/10.1103/PhysRevA.34.3974
55. A. Luis, Nonlinear transformations and the Heisenberg limit. Phys. Rev. A **329**, 8–13 (2004). https://doi.org/10.1016/j.physleta.2004.06.080
56. M. Napolitano, M. Koschorreck, B. Dubost, N. Behbood, R.J. Sewell, M.W. Mitchell, Interaction-based quantum metrology showing scaling beyond the Heisenberg limit. Nature **471**, 486–489 (2011). https://doi.org/10.1038/nature09778
57. R.J. Sewell, M. Napolitano, N. Behbood, G. Colangelo, F. Martin Ciurana, M.W. Mitchell, Ultrasensitive atomic spin measurements with a nonlinear interferometer. Phys. Rev. X **4**, 021045 (2014). https://doi.org/10.1103/PhysRevX.4.021045
58. D. Braun, G. Adesso, F. Benatti, R. Floreanini, U. Marzolino, M.W. Mitchell, S. Pirandola, Quantum enhanced measurements without entanglement (2017). arXiv:1701.05152

59. L. Pezzé, A. Smerzi, Entanglement, nonlinear dynamics, and the Heisenberg limit. Phys. Rev. Lett. **102**, 100401 (2009). https://doi.org/10.1103/PhysRevLett.102.100401
60. Y. Kawaguchi, M. Ueda, Spinor Bose-Einstein condensates. Phys. Rep. **520**, 253–381 (2012). https://doi.org/10.1016/j.physrep.2012.07.005
61. D.M. Stamper-Kurn, M. Ueda, Spinor Bose gases: symmetries, magnetism, and quantum dynamics. Rev. Mod. Phys. **85**, 1191 (2013). https://doi.org/10.1103/RevModPhys.85.1191
62. B. Lücke, M. Scherer, J. Kruse, L. Pezzè, F. Deuretzbacher, P. Hyllus, O. Topic, J. Peise, W. Ertmer, J. Arlt, L. Santos, A. Smerzi, C. Klempt, Twin matter waves for interferometry beyond the classical limit. Science **334**, 773–776 (2011). https://doi.org/10.1126/science.1208798
63. C. Gross, H. Strobel, E. Nicklas, T. Zibold, N. Bar-Gill, G. Kurizki, M.K. Oberthaler, Atomic homodyne detection of continuous-variable entangled twin-atom states. Nature **480**, 219 (2011). https://doi.org/10.1038/nature10654
64. C.D. Hamley, C.S. Gerving, T.M. Hoang, E.M. Bookjans, M.S. Chapman, Spin-nematic squeezed vacuum in a quantum gas. Nat. Phys. **8**, 305 (2012). https://doi.org/10.1038/nphys2245
65. S.R. Leslie, J. Guzman, M. Vengalattore, J.D. Sau, M.L. Cohen, D.M. Stamper-Kurn, Amplification of fluctuations in a spinor Bose-Einstein condensate. Phys. Rev. A **79**, 043631 (2009). https://doi.org/10.1103/PhysRevA.79.043631
66. C. Klempt, O. Topic, G. Gebreyesus, M. Scherer, T. Henninger, P. Hyllus, W. Ertmer, L. Santos, J.J. Arlt, Parametric amplification of vacuum fluctuations in a spinor condensate. Phys. Rev. Lett. **104**, 195303 (2010). https://doi.org/10.1103/PhysRevLett.104.195303
67. P.D. Nation, J.R. Johansson, M.P. Blencowe, F. Nori, Colloquium: stimulating uncertainty: amplifying the quantum vacuum with superconducting circuits. Rev. Mod. Phys. **84**, 1–24 (2012). https://doi.org/10.1103/RevModPhys.84.1
68. H. Lee, P. Kok, J.P. Dowling, A quantum Rosetta stone for interferometry. J. Mod. Opt. **49**, 2325–2338 (2002). https://doi.org/10.1080/0950034021000011536
69. J.-W. Pan, Z.-B. Chen, C.-Y. Lu, H. Weinfurter, A. Zeilinger, M. Zukowski, Multiphoton entanglement and interferometry. Rev. Mod. Phys. **84**, 777 (2012). https://doi.org/10.1103/RevModPhys.84.777
70. J.P. Dowling, Quantum optical metrology-the lowdown on high-N00N states. Contemp. Phys. **49**, 125–143 (2008)
71. D.M. Greenberger, M.A. Horne, A. Zeilinger, Going beyond Bell's theorem, in *Bell's Theorem, Quantum Theory and Conceptions of the Universe* (Springer, 1989) pp. 69–72
72. N.D. Mermin, Extreme quantum entanglement in a superposition of macroscopically distinct states. Phys. Rev. Lett. **65**, 1838–1840 (1990). https://doi.org/10.1103/PhysRevLett.65.1838
73. J.J. Bollinger, W.M. Itano, D.J. Wineland, D.J. Heinzen, Optimal frequency measurements with maximally correlated states. Phys. Rev. A **54**, R4649–R4652 (1996). https://doi.org/10.1103/PhysRevA.54.R4649
74. C.C. Gerry, J. Mimih, The parity operator in quantum optical metrology. Contemp. Phys. **51**, 497–511 (2010). https://doi.org/10.1080/00107514.2010.509995
75. M.J. Holland, K. Burnett, Interferometric detection of optical phase shifts at the Heisenberg limit. Phys. Rev. Lett. **71**, 1355–1358 (1993). https://doi.org/10.1103/PhysRevLett.71.1355
76. R.A. Campos, C.C. Gerry, A. Benmoussa, Optical interferometry at the Heisenberg limit with twin Fock states and parity measurements. Phys. Rev. A **68**, 023810 (2003). https://doi.org/10.1103/PhysRevA.68.023810
77. S.L. Braunstein, P. van Loock, Quantum information with continuous variables. Rev. Mod. Phys. **77**, 513–577 (2005). https://doi.org/10.1103/RevModPhys.77.513
78. P.M. Anisimov, G.M. Raterman, A. Chiruvelli, W.N. Plick, S.D. Huver, H. Lee, J.P. Dowling, Quantum metrology with two-mode squeezed vacuum: parity detection beats the Heisenberg limit. Phys. Rev. Lett. **104**, 103602 (2010). https://doi.org/10.1103/PhysRevLett.104.103602
79. T. Kim, J. Dunningham, K. Burnett, Precision measurement scheme using a quantum interferometer. Phys. Rev. A **72**, 055801 (2005). https://doi.org/10.1103/PhysRevA.72.055801
80. J. Dunningham, T. Kim, Using quantum interferometers to make measurements at the Heisenberg limit. J. Mod. Opt. **53**, 557–571 (2006). https://doi.org/10.1080/09500340500443268

81. D. Leibfried, M.D. Barrett, T. Schaetz, J. Britton, J. Chiaverini, W.M. Itano, J.D. Jost, C. Langer, D.J. Wineland, Toward Heisenberg-limited spectroscopy with multiparticle entangled states. Science **304**, 1476 (2004). https://doi.org/10.1126/science.1097576
82. F. Fröwis, P. Sekatski, W. Dür, Detecting large quantum fisher information with finite measurement precision. Phys. Rev. Lett. **116**, 090801 (2016). https://doi.org/10.1103/PhysRevLett.116.090801
83. T. Macri, L. Pezzè, A. Smerzi, Loschmidt Echo for quantum metrology (2016). arXiv:1604.04246
84. E. Davis, G. Bentsen, M. Schleier-Smith, Approaching the Heisenberg limit without single-particle detection. Phys. Rev. Lett. **116**, 053601 (2016). https://doi.org/10.1103/PhysRevLett.116.053601
85. E. Davis, G. Bentsen, T. Li, M. Schleier-Smith, Advantages of interaction- based readout for quantum sensing, in *Proceedings of SPIE*, vol. 10118 (2017)
86. S.P. Nolan, S.S. Szigeti, S.A. Haine, Optimal and Robust quantum etrology using interaction-based readouts (2017). arXiv:1703.10417 [quant-ph]
87. A.A. Clerk, M.H. Devoret, S.M. Girvin, F. Marquardt, R.J. Schoelkopf, Introduction to quantum noise, measurement, and amplification. Rev. Mod. Phys. **82**, 1155–1208 (2010). https://doi.org/10.1103/RevModPhys.82.1155
88. J. Kong, F. Hudelist, Z.Y. Ou, W. Zhang, Cancellation of internal quantum noise of an amplifier by quantum correlation. Phys. Rev. Lett. **111**, 033608 (2013). https://doi.org/10.1103/PhysRevLett.111.033608
89. B. Yurke, S.L. McCall, J.R. Klauder, SU(2) and SU(1,1) interferometers. Phys. Rev. A **33**, 4033 (1986). https://doi.org/10.1103/PhysRevA.33.4033
90. C. Sparaciari, S. Olivares, M.G.A. Paris, Gaussian-state interferometry with passive and active elements. Phys. Rev. A **93**, 023810 (2016). https://doi.org/10.1103/PhysRevA.93.023810
91. T.J. Herzog, J.G. Rarity, H. Weinfurter, A. Zeilinger, Frustrated two-photon creation via interference. Phys. Rev. Lett. **72**, 629–632 (1994). https://doi.org/10.1103/PhysRevLett.72.629
92. R.Z. Vered, Y. Shaked, Y. Ben-Or, M. Rosenbluh, A. Peer, Classical-to-quantum transition with broadband four-wave mixing. Phys. Rev. Lett. **114**, 063902 (2015). https://doi.org/10.1103/PhysRevLett.114.063902
93. Y. Shaked, R. Pomerantz, R.Z. Vered, A. Peer, Observing the nonclassical nature of ultra-broadband bi-photons at ultrafast speed. New J. Phys. **16**, 053012 (2014). http://stacks.iop.org/1367-2630/16/i=5/a=053012
94. V. Boyer, A.M. Marino, R.C. Pooser, P.D. Lett, Entangled images from four-wave mixing. Science **321**, 544–547 (2008)
95. C.F. McCormick, A.M. Marino, V. Boyer, P.D. Lett, Strong low-frequency quantum correlations from a four-wave-mixing amplifier. Phys. Rev. A **78**, 043816 (2008). https://doi.org/10.1103/PhysRevA.78.043816
96. R.C. Pooser, A.M. Marino, V. Boyer, K.M. Jones, P.D. Lett, Low-noise amplification of a continuous-variable quantum state. Phys. Rev. Lett. **103**, 010501 (2009). https://doi.org/10.1103/PhysRevLett.103.010501
97. J. Jing, C. Liu, Z. Zhou, Z. Y. Ou, W. Zhang, Realization of a nonlinear interferometer with parametric amplifiers. Appl. Phys. Lett. **99** (2011)
98. F. Hudelist, J. Kong, C. Liu, J. Jing, Z. Ou, W. Zhang, Quantum metrology with parametric amplifier-based photon correlation interferometers. Nat. Commun. **5**, 3049 (2014). https://doi.org/10.1038/ncomms4049
99. M. Manceau, G. Leuchs, F. Khalili, M. Chekhova, Detection loss tolerant supersensitive phase measurement with an SU (1, 1) interferometer (2017). arXiv:1705.02662
100. E. Flurin, N. Roch, F. Mallet, M.H. Devoret, B. Huard, Generating entangled microwave radiation over two transmission lines. Phys. Rev. Lett. **109**, 183901 (2012). https://doi.org/10.1103/PhysRevLett.109.183901
101. E. Flurin, The Josephson Mixer, a Swiss army knife for microwave quantum optics, Ph.D. thesis, Ecole Normale Supérieure, Paris (2014). https://tel.archives-ouvertes.fr/tel-01241123

102. A. Bienfait, P. Campagne-Ibarcq, A. Holm-Kiilerich, X. Zhou, S. Probst, J. Pla, T. Schenkel, D. Vion, D. Esteve, J. Morton, et al., Magnetic resonance with squeezed microwaves (2016). arXiv:1610.03329
103. T.P. Harty, D.T.C. Allcock, C.J. Ballance, L. Guidoni, H.A. Janacek, N.M. Linke, D.N. Stacey, D.M. Lucas, High-fidelity preparation, gates, memory, and readout of a trapped-ion quantum bit. Phys. Rev. Lett. **113**, 220501 (2014). https://doi.org/10.1103/PhysRevLett.113.220501
104. J.P. Gaebler, T.R. Tan, Y. Lin, Y. Wan, R. Bowler, A.C. Keith, S. Glancy, K. Coakley, E. Knill, D. Leibfried, D.J. Wineland, High-fidelity universal gate set for $^{9}Be^{+}$ ion qubits. Phys. Rev. Lett. **117**, 060505 (2016). https://doi.org/10.1103/PhysRevLett.117.060505
105. C.J. Ballance, T.P. Harty, N.M. Linke, M.A. Sepiol, D.M. Lucas, High-fidelity quantum logic gates using trapped-ion hyperfine qubits. Phys. Rev. Lett. **117**, 060504 (2016). https://doi.org/10.1103/PhysRevLett.117.060504
106. H. Häffner, C.F. Roos, R. Blatt, Quantum computing with trapped ions. Phys. Rep. **469**, 155–203 (2008)
107. R. Blatt, D. Wineland, Entangled states of trapped atomic ions. Nature **453**, 1008 (2008). https://doi.org/10.1038/nature07125
108. A. Sørensen, K. Mølmer, Quantum computation with ions in thermal motion. Phys. Rev. Lett. **82**, 1971–1974 (1999). https://doi.org/10.1103/PhysRevLett.82.1971
109. D. Kielpinski, C. Monroe, D.J. Wineland, Architecture for a large-scale ion-trap quantum computer. Nature **417**, 709 (2002)
110. C. Monroe, J. Kim, Scaling the ion trap quantum processor. Science **339**, 1164–1169 (2013). https://doi.org/10.1126/science.1231298
111. J.D. Siverns, Q. Quraishi, Ion trap architectures and new directions (2017). arXiv:1708.04689
112. J.W. Britton, B.C. Sawyer, A.C. Keith, C.-C.J. Wang, J.K. Freericks, H. Uys, M.J. Biercuk, J.J. Bollinger, Engineered two-dimensional ising interactions in a trapped-ion quantum simulator with hundreds of spins. Nature **484**, 489–492 (2012). https://doi.org/10.1038/nature10981
113. J.G. Bohnet, B.C. Sawyer, J.W. Britton, M.L. Wall, A.M. Rey, M. Foss-Feig, J.J. Bollinger, Quantum spin dynamics and entanglement generation with hundreds of trapped ions. Science **352**, 1297–1301 (2016). https://doi.org/10.1126/science.aad9958
114. M. Gärttner, J.G. Bohnet, A. Safavi-Naini, M.L. Wall, J.J. Bollinger, A.M. Rey, Measuring out-of-time-order correlations and multiple quantum spectra in a trapped-ion quantum magnet. Nat. Phys. **13**, 781–786 (2017). https://doi.org/10.1038/nphys4119
115. O. Hosten, R. Krishnakumar, N.J. Engelsen, M.A. Kasevich, Quantum phase magnification. Science **352**, 1552–1555 (2016). https://doi.org/10.1126/science.aaf3397
116. O. Hosten, N.J. Engelsen, R. Krishnakumar, M.A. Kasevich, Measurement noise 100 times lower than the quantum-projection limit using entangled atoms. Nature (2016)
117. J. Borregaard, E.D. Davis, G.S. Bentsen, M.H. Schleier-Smith, A.S. Sørensen, One- and two-axis squeezing of atomic ensembles in optical cavities (2017). arXiv:1706.01650
118. S.L. Rolston, W.D. Phillips, Nonlinear and quantum atom optics. Nature **416**, 219–224 (2002). https://doi.org/10.1038/416219a
119. S. Inouye, T. Pfau, S. Gupta, A.P. Chikkatur, A. Gorlitz, D.E. Pritchard, W. Ketterle, Phase-coherent amplification of atomic matter waves. Nature **402**, 641–644 (1999). https://doi.org/10.1038/45194
120. M. Kozuma, Y. Suzuki, Y. Torii, T. Sugiura, T. Kuga, E.W. Hagley, L. Deng, Phase-coherent amplification of matter waves. Science **286**, 2309–2312 (1999)
121. T.M. Hoang, C.S. Gerving, B.J. Land, M. Anquez, C.D. Hamley, M.S. Chapman, Dynamic stabilization of a quantum many-body spin system. Phys. Rev. Lett. **111**, 090403 (2013). https://doi.org/10.1103/PhysRevLett.111.090403

Part I
Theoretical Basics

Chapter 2
Quantum Mechanical Spin

We start our theoretical treatment with one of quantum mechanics most paradigmatic systems, the spin-1/2. To this end we introduce a set of spin operators that exhaustively describe such elementary systems and detail the Bloch sphere representation. Characteristic features of three level systems are developed on that basis.

2.1 A Spin-1/2 System

Following a reductionism approach we first introduce the most fundamental entity, the quantum bit (qubit). Such a qubit describes the quantum mechanical state of a two level system. In particular a spin-1/2 particle falls into this category where two basis states might be identified with spin-up ($|\uparrow\rangle$) and spin-down ($|\downarrow\rangle$). To characterize its wave function we introduce the following set of spin operators

$$\hat{\boldsymbol{J}} = \begin{pmatrix} \hat{J}_x \\ \hat{J}_y \\ \hat{J}_z \end{pmatrix} = \frac{1}{2} \begin{pmatrix} \hat{a}_\uparrow^\dagger \hat{a}_\downarrow + \hat{a}_\downarrow^\dagger \hat{a}_\uparrow \\ (\hat{a}_\uparrow^\dagger \hat{a}_\downarrow - \hat{a}_\downarrow^\dagger \hat{a}_\uparrow)/\mathrm{i} \\ \hat{a}_\uparrow^\dagger \hat{a}_\uparrow - \hat{a}_\downarrow^\dagger \hat{a}_\downarrow \end{pmatrix} . \tag{2.1}$$

Using the second quantisation formalism even for a single particle at this point, $\hat{a}_\uparrow^\dagger$ and $\hat{a}_\downarrow^\dagger$ denote the bosonic creation operators for mode $|\uparrow\rangle$ and $|\downarrow\rangle$, respectively. The operator $\hat{J}_z$ quantifies the population imbalance (magnetization) between both basis states while $\hat{J}_x$ and $\hat{J}_y$ contain the coherences. Because of the rotational symmetry retained by angular momenta these spin operators satisfy the defining commutation relations of SU(2), i.e. $[\hat{J}_x, \hat{J}_y] = \mathrm{i}\hat{J}_z$ and cyclic permutations thereof.

Every spin-1/2 wave function $|\vartheta, \varphi_L\rangle$ can be associated with a unit vector $2\mathbf{r}$ via the identity

D. Linnemann, *Quantum-Enhanced Sensing Based on Time Reversal of Entangling Interactions*, Springer Theses,
https://doi.org/10.1007/978-3-319-96008-1_2

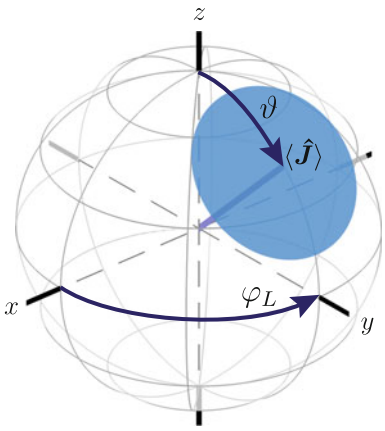

Fig. 2.1 Bloch sphere representation of a spin-1/2 system. The state space spanned by the two states spin-up $|\uparrow\rangle$ and spin-down $|\downarrow\rangle$ can be visualized on the surface of a sphere. In this Bloch sphere representation, the orthogonal states $|\uparrow\rangle$ and $|\downarrow\rangle$ are identified with the north and south pole, respectively. Any pure state describing a coherent superposition can be represented by the direction of its mean spin $\langle\hat{\boldsymbol{J}}\rangle$, often parametrized through two angles as indicated. The blue area denotes the intrinsic indetermination imposed by the uncertainty principle

$$\langle\vartheta, \varphi_L|\,\hat{\mathbf{J}}\cdot\mathbf{r}\,|\vartheta, \varphi_L\rangle = 1/2\,. \tag{2.2}$$

This visualisation of wave functions in terms of points spanning the surface of a unit ball is called Bloch sphere representation; it is shown in Fig. 2.1. A pure spin-1/2 system is characterized completely by the direction into which its mean spin $\langle\hat{\mathbf{J}}\rangle$ points. Often this orientation is parametrized by two angles: while the polar angle ϑ encodes the population imbalance, the azimuthal angle is given by the Larmor phase φ_L. This Larmor phase is the dynamic phase associated to the energy difference between the two basis states $|\uparrow\rangle$ and $|\downarrow\rangle$ and is therefore responsible for spin precession. Advancing the Larmor phase by $\varphi_L = \pi/2$ rotates $\hat{J}_x$ into $\hat{J}_y$, which in terms of individual mode operators is described by the substitution $\hat{a}_\uparrow \to \hat{a}_\uparrow \exp \mathrm{i}\varphi_L$. Transformation of this form will become important later on. The inner volume within the Bloch sphere becomes accessible only for mixed states.

According to Heisenberg's uncertainty relation there is a fundamental lower bound on how well two non-commuting spin components can be determined. This bound is indicated by the blue shaded area in Fig. 2.1. It follows from

$$(\Delta\hat{J}_x)^2(\Delta\hat{J}_y)^2 \geq |\langle\hat{J}_z\rangle|^2/4 \tag{2.3}$$

which holds similarly for the other spin components. Here, $(\Delta\cdot)^2$ denotes variance.

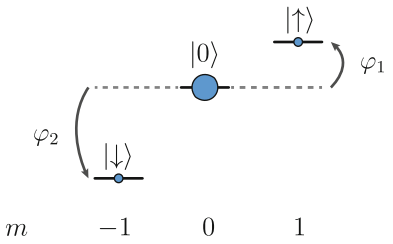

Fig. 2.2 Phases of a spin-1 system. As a three level system, a spin-1 accommodates two distinct phases, e.g. $\varphi_1 = \varphi_0 - \varphi_\uparrow$ and $\varphi_2 = \varphi_0 - \varphi_\downarrow$ as indicated. The decomposition into a Larmor phase contribution, $\varphi_L = \varphi_2 - \varphi_1$, and spinor phase, $\varphi = \varphi_1 + \varphi_2$, is particularly insightful. This is because each phase is responsible for qualitatively different dynamics of the three level system. Similar to the situation encountered in a spin-1/2 system, the Larmor phase rotates an oriented spin. In contrast, the spinor phase drives orientation-to-alignments oscillations

2.2 A Spin-1 System

The wave function of a spin-1 object involves three states, for instance the three Zeeman levels. In direct analogy to the spin-1/2 case we first introduce spin operators which characterize the spin's orientation. However, in contrast to the two-level system more operators are needed to completely describe spin-1 states. We motivate this by considering composite wave functions made up by two antipodal spin-1/2 particles. The additional operators characterize the alignment of spin fluctuations.

Spin operators—orientation

We treat the spin-1 object in the Zeeman basis consisting of the three states $|m = 1\rangle \equiv |\uparrow\rangle$, $|m = 0\rangle \equiv |0\rangle$, and $|m = -1\rangle \equiv |\downarrow\rangle$. These three levels might have an unequal energy spacing. The possible two independent energy differences call for two distinct (dynamic) phases, $\varphi_1 = \varphi_0 - \varphi_\uparrow$ and $\varphi_2 = \varphi_0 - \varphi_\downarrow$ as indicated in Fig. 2.2. Here $\varphi_\uparrow$ denotes the phase of state $|\uparrow\rangle$ with a similar notation for the other states. The Larmor phase of this three level system is given by $\varphi_L = \varphi_2 - \varphi_1$. Similar to the spin-1/2 case it is related to the energy difference between states $|\uparrow\rangle$ and $|\downarrow\rangle$ and generates rotations of the mean spin direction. The additional phase, called spinor phase $\varphi = \varphi_2 + \varphi_1$, is in turn related to the energy difference with respect to state $|0\rangle$. It is given by

$$\varphi = 2\varphi_0 - \varphi_\uparrow - \varphi_\downarrow \,. \tag{2.4}$$

It is useful to introduce the shorthand notation for the symmetric and antisymmetric combination of spin-up and spin-down annihilation operators,

$$\hat{s}_+ = (\hat{a}_\uparrow + \hat{a}_\downarrow)/\sqrt{2} \qquad \hat{s}_- = (\hat{a}_\uparrow - \hat{a}_\downarrow)/\sqrt{2} \,. \tag{2.5}$$

These definitions allow constructing the spin operators of a three level system in a manner mnemonic to the spin-1/2 case [1], namely

$$\hat{\boldsymbol{S}} = \begin{pmatrix} \hat{S}_x \\ \hat{S}_y \\ \hat{S}_z \end{pmatrix} = \begin{pmatrix} \hat{a}_0^\dagger \hat{s}_+ + \hat{a}_0 \hat{s}_+^\dagger \\ (\hat{a}_0^\dagger \hat{s}_- - \hat{a}_0 \hat{s}_-^\dagger)/\mathrm{i} \\ \hat{a}_\uparrow^\dagger \hat{a}_\uparrow - \hat{a}_\downarrow^\dagger \hat{a}_\downarrow \end{pmatrix} . \tag{2.6}$$

Here, the definition of $\hat{S}_y$ involves the operators of $\hat{s}_-$ rather than $\hat{s}_+$. This is because the spin operators $\hat{S}_x$ and $\hat{S}_y$ need to be connected via a rotation of the Larmor phase which transforms $\hat{s}_+$ into $\mathrm{i}\hat{s}_-$. By such a construction these operators automatically fulfil the rotational SU(2) commutator relations. However, a spin-1 object is not exhaustively described by its mean spin direction $\langle \hat{\boldsymbol{S}} \rangle$. We motivate the need for further operators by an example in the following section.

Quadrupole operators—alignment

Let us imagine, cum grano salis, that the spin-1 is composed of two fictitious fundamental spin-1/2 particles. Due to bosonic exchange symmetry we can explicitly construct the wave function out of two spin-1/2 wave functions in the following way, $\Psi = \frac{1}{\sqrt{2}}(|\vartheta_1, \phi_1\rangle_1 |\vartheta_2, \phi_2\rangle_2 + |\vartheta_2, \phi_2\rangle_1 |\vartheta_1, \phi_1\rangle_2)$ [2, 3]. Here the state's subscript labels the individual spins. These two spin-1/2 can point into arbitrary direction, in particular into diametrically opposite ones. Such a case is shown in Fig. 2.3 where one spin-1/2 points to the north pole and the other to the south pole. The combined state is then given by $\Psi = (|\uparrow\rangle_1 |\downarrow\rangle_2 + |\downarrow\rangle_1 |\uparrow\rangle_2)/\sqrt{2}$. This is the state with total spin $S = 1, m = 0$. It thus corresponds to the situation with only the $m = 0$ component populated. Such a state is the starting point for all experiments reported on in this thesis. As the superposition of two antipodal states its mean spin length vanishes. However, its spin fluctuations are anisotropic as shown in the right panel where the Bloch sphere representation of the spin $\hat{\boldsymbol{S}}$ is shown. The fluctuations amount to

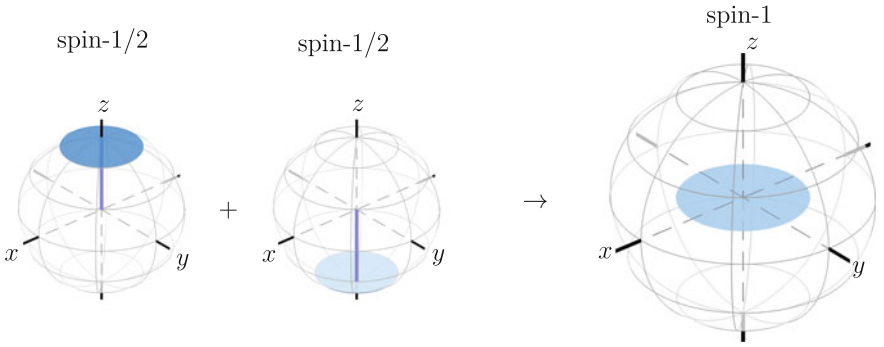

Fig. 2.3 Majorana representation. A spin-1 object can be thought of as being composed of two fundamental spin-1/2. A particular interesting case arises when two antipodal spins are combined. Shown are the Bloch sphere representations of a spin-1/2 in state $|\uparrow\rangle$ and $|\downarrow\rangle$ with associated uncertainties indicated as blue shading. The resulting spin-1 has no orientation, however its fluctuations (blue area) have the shape of a disc and are thus anisotropic

$$(\Delta\hat{S}_x)^2 = (\Delta\hat{S}_y)^2 = 1, \quad (\Delta\hat{S}_z)^2 = 0\,. \tag{2.7}$$

Similarly, the resulting state of two antipodal spins lying on the equator, say along the x and $-x$ direction, gives anisotropic spin fluctuations with $(\Delta\hat{S}_y)^2 = (\Delta\hat{S}_z)^2 = 1$ and $(\Delta\hat{S}_x)^2 = 0$ which can be understood as a rotation of the previous spin-up and spin-down case. Therefore both states have vanishing mean spin length $\langle\hat{\mathbf{S}}\rangle = 0$ but describe different states as witnessed by their coherent fluctuations. Such states are known under different names: in spinor condensates, they are predominantly called polar states, in solid state physics spin-nematic, in nuclear physics quadrupolar, and in atomic physics aligned. The contrastive pair of orientation versus alignment is particularly illustrative. Here, orientation describes an object having one direction. In contrast, alignment describes objects having an axis.

The previously introduced spin-1/2 operators can be regarded as a consequence of transformations under Larmor phase rotations. In a similar manner we can construct additional sets of operators that satisfy SU(2) symmetry by construction. For this we impose a rotation with the spinor phase: starting with the operator $\hat{S}_x$ and substituting $\hat{a}_0 \to \hat{a}_0 \exp \mathrm{i}\varphi$ we obtain:

$$\hat{\boldsymbol{F}} = \begin{pmatrix} \hat{F}_x \\ \hat{F}_y \\ \hat{F}_z \end{pmatrix} = \begin{pmatrix} \hat{a}_0^\dagger \hat{s}_+ + \hat{a}_0 \hat{s}_+^\dagger \\ (\hat{a}_0^\dagger \hat{s}_+ - \hat{a}_0 \hat{s}_+^\dagger)/\mathrm{i} \\ \hat{a}_0^\dagger \hat{a}_0 - \hat{s}_+^\dagger \hat{s}_+ \end{pmatrix}. \tag{2.8}$$

A similar procedure can be done by starting with $\hat{S}_y$:

$$\hat{\boldsymbol{G}} = \begin{pmatrix} \hat{G}_x \\ \hat{G}_y \\ \hat{G}_z \end{pmatrix} = \begin{pmatrix} \hat{a}_0^\dagger \hat{s}_- + \hat{a}_0 \hat{s}_-^\dagger \\ (\hat{a}_0^\dagger \hat{s}_- - \hat{a}_0 \hat{s}_-^\dagger)/\mathrm{i} \\ \hat{a}_0^\dagger \hat{a}_0 - \hat{s}_-^\dagger \hat{s}_- \end{pmatrix}. \tag{2.9}$$

With the help of these operators, a spin-1 wave function is completely characterized. The additional operators measure the anisotropy of spin fluctuations. Expressed in terms of spin orientation operators they take the form of anticommutators $\{S_i, S_j\}$. Therefore the name quadrupole operators is justified [4]. For a spin-1/2 these products of spin operators vanish as a consequence of the Pauli matrices satisfying $\{\sigma_i, \sigma_j\} = 0$ for $i \neq j$, see appendix (Sect. C.1). This is in accordance with the Wigner-Eckhart theorem stating that a wave function describing an angular momentum J object has vanishing expectation values for all moments of the multipole expansion greater than $2J$. Turning the argument around shows that the spin-1 is fully characterized by $\hat{\boldsymbol{S}}$ and the alignment operators $\hat{\boldsymbol{F}}$ and $\hat{\boldsymbol{G}}$, respectively.

In the language of atomic physics, the operators $\hat{F}_y$ and $\hat{G}_y$ measure the alignment of the spin. This is opposed to the orientation which is characterized by the operators belonging to $\hat{\boldsymbol{S}}$: the spinor phase φ drives alignment-to-orientation oscillations while the Larmor phase rotates an oriented spin. Because of the rotational symmetry the alignment operators can be visualized on a Bloch sphere in exactly the same manner

as the oriented spin. In such a representation the aforementioned state $S = 1, m = 0$ (as shown in Fig. 2.3) corresponds to the north pole of the Bloch sphere belonging to $\hat{\boldsymbol{F}}$ and $\hat{\boldsymbol{G}}$, respectively. We will come back to this representation in the next chapter.

References

1. L. Pezzè, A. Smerzi, M. K. Oberthaler, R. Schmied, P. Treutlein, Non-lassical states of atomic ensembles: fundamentals and applications in quantum metrology (2016). arXiv:1609.01609
2. A.R.U. Devi, Sudha, A. K. Rajagopal, Majorana representation of symmetric multiqubit states. Quantum Inf. Process. **11**, 685–710 (2012)
3. D.M. Stamper-Kurn, M. Ueda, Spinor Bose gases: symmetries, magnetism, and quantum dynamics. Rev. Mod. Phys. **85**, 1191 (2013). https://doi.org/10.1103/RevModPhys.85.1191
4. C.D. Hamley, C.S. Gerving, T.M. Hoang, E.M. Bookjans, M.S. Chapman, Spin-nematic squeezed vacuum in a quantum gas. Nat Phys **8**, 305 (2012). https://doi.org/10.1038/nphys2245

Chapter 3
Hamiltonian of a Spin-1 Bose-Einstein Condensate

In this section we present the Hamiltonian description of a spinor Bose-Einstein condensate. With the motional degrees of freedom frozen out, the dynamics are within the spin. We detail the collisional interactions that lead to spin exchange among three modes. For developing intuition about the dynamics induced by spin exchange the classical phase space is discussed before the quantum mechanical treatment follows. Finally, we give an overview of the employed semi-classical simulation methods.

3.1 Spinor BEC in a Single Spatial Mode

In our experiments we employ mesoscopic Bose-Einstein condensates (BEC) containing about 400 atoms that are tightly trapped in an optical lattice potential. In such a situation the external degrees of freedom are frozen out and the ensuing dynamics is restricted to the spin. Furthermore, the trapping potential treats all spin components equally. Under these conditions the spatial wave function of the condensate $\phi(\mathbf{r})$ is common to all spin states. Formally, this means that the three spin components j have wave functions given by

$$\hat{\Psi}_j(\mathbf{r}) = \phi(\mathbf{r})\hat{a}_j \,. \tag{3.1}$$

The shared mode function $\phi(\mathbf{r})$ can be determined by solving the Gross-Pitaevski equation in the external potential. Depending on the atomic density two qualitatively different regimes arise. For very low atomic densities interactions among the particles can be neglected and the BEC wave function is given by the corresponding single-particle wave function. In the opposite case of high density and thus

D. Linnemann, *Quantum-Enhanced Sensing Based on Time Reversal of Entangling Interactions*, Springer Theses,
https://doi.org/10.1007/978-3-319-96008-1_3

dominant interactions the kinetic energy contribution can be neglected. In this Thomas-Fermi approximation the chemical potential takes the shape of the (inverted) trappin potential [1, 2].

3.2 Collisional Interactions

Due to the diluteness of atomic gases it suffices to only treat two-body collisions. To describe the interactions of any general three component BEC all pairwise scattering processes need to be considered. This amounts to three inter- and three intra-component scattering channels. However, in our case the three components are not independent of each other but constitute a physical spin. As such it has well defined properties upon rotation. By exploiting symmetries, in particular the conservation of angular momentum, the treatment of interactions can be greatly simplified [3].

Within the ultracold temperature regime, only head-on collisions occur. This is because two low energy atoms with finite orbital angular momentum $l \neq 0$ in their centre-of-mass reference frame cannot overcome the centrifugal barrier to probe the short range interatomic potential. Therefore, only s-wave collisions with $l = 0$ need to be considered. This s-wave entrance channel cannot be left (by interconversion of internal angular momentum) because the scattering potential is assumed to be spherically symmetric. Here, we explicitly exclude effects due to dipole-dipole interaction[1] which is anisotropic. Under these conditions, the conservation of total angular momentum (external and internal) stipulates the conservation of spin alone. Two indistinguishable bosonic atoms with spin $F = 1$ can couple to a combined spin of either $F = 2$ or $F = 0$. Each of these channels is associated with a scattering length a_F. Therefore, the interaction takes the form

$$V = a_0 \mathcal{P}_0 + a_2 \mathcal{P}_2 \tag{3.2}$$

where $\mathcal{P}_F$ are projectors onto the coupled spin, i.e. $\mathcal{P}_F = \sum_{m=-F}^{F} |F, m\rangle \langle F, m|$.

Analogy to solid state magnetism

To gain insight into the microscopic interaction between two spins, we express the interaction potential (Eq. 3.2) in terms of the two individual spins $\mathbf{F}_1$ and $\mathbf{F}_2$. For this we note that the operator $\mathbf{F}_1 \cdot \mathbf{F}_2$ has eigenvalue 1 if the two spins $\mathbf{F}_1$ and $\mathbf{F}_2$ are coupled to $F = 2$ and eigenvalue -2 correspondingly for $F = 0$. Therefore, we

[1] We estimate the importance of dipolar interactions by comparison to the collisional interactions. For this purpose we assume a uniform particle density and integrate both contributions over a sphere. The ratio of dipolar energy E_d to collisional energy E_s reads $E_d/E_s = \mu_0 \mu^2 m/12\pi a\hbar^2$ [4]. Here μ_0 denotes the vacuum permeability, μ is the magnetic moment, m the mass and a the s-wave scattering length. For the background scattering length of Rubidium-87 the ratio is 2‰. Having said that, spin exchange is driven by smaller scattering length *differences* such that the weak dipolar effects can become important [5, 6]. However, in our case the relevant scattering length amounts to 6 Bohr radii such that the ratio is 2% which we neglect.

have $\mathbf{F}_1 \cdot \mathbf{F}_2 = \mathcal{P}_2 - 2\mathcal{P}_0$. Together with the resolution of identity the interaction potential can then be written as

$$V = c_0 + c_1 \mathbf{F}_1 \cdot \mathbf{F}_2 \,. \tag{3.3}$$

Here the coefficient c_0 quantifies the spin-independent interactions. In terms of s-wave scattering lengths the coefficients are given by $c_0 \propto a_0 + 2a_2$ and $c_1 \propto a_2 - a_0$. Therefore, the spin-dependent interaction is mediated by the scattering length difference between singlet and triplet channel. The above scattering potential emphasises that the underlying interaction is of pairwise nature and has the form of (anti-) ferromagnetic spin exchange. For $c_1 < 0$ aligned spins are favoured (ferromagnetic) while for $c_1 > 0$ energy is minimized for an antiparallel spin configuration [7]. While this resembles the interaction in solid state magnetism, one has to keep in mind that the indistinguishability of identical particles is crucial. In a Bose-Einstein condensate the particles, being delocalized, are described by a spatial mode. In solid state physics one often considers the interactions among spins localized to specific lattice sites.

3.3 Hamiltonian

The projection operators onto the coupled spin (Eq. 3.2) can be expressed in terms of the individual spin components. We call $N_\uparrow$ the population of state $|\uparrow\rangle$ with a similar notation for the other states. We assume a fixed number of N atoms in total. Considering only the spin-dependent terms as quantified by c_1 we obtain the Hamiltonian

$$\mathcal{H} = \mathcal{H}_{\mathrm{SCC}} + \mathcal{H}_{\mathrm{el}} \qquad \begin{aligned} \mathcal{H}_{\mathrm{SCC}} &= \hbar g(\hat{a}_0 \hat{a}_0 \hat{a}_\downarrow^\dagger \hat{a}_\uparrow^\dagger + \text{h.c.}) \\ \mathcal{H}_{\mathrm{el}} &= \hbar g(N_0 - 1/2)(N_\uparrow + N_\downarrow) \end{aligned} \tag{3.4}$$

Here, $\mathcal{H}_{\mathrm{SCC}}$ describes the spin exchange process by which a pair of atoms in the pump mode $|0\rangle$ scatters coherently into the side modes, i.e. $|\uparrow\rangle$ and $|\downarrow\rangle$, such that the magnetization $(N_\uparrow - N_\downarrow)$ remains conserved. As a coherent process the reversible effect of two atoms scattering into the pump mode is allowed on equal footing. We call g the microscopic nonlinear coupling strength. It quantifies the rate at which atoms undergo these spin-changing collisions. In terms of s-wave scattering lengths it is given by $g \propto c_1$. Additionally, this nonlinear coupling strength depends on the overlap of the external wave function $g \propto \int \mathrm{d}^3x |\phi(\boldsymbol{x})|^4$, as defined above in Eq. 3.1.

Generally, Hamiltonian terms of the form $\Delta E(N_\uparrow + N_\downarrow) = -\Delta E N_0$ describe energy shifts of the pump mode by ΔE with respect to the side modes. The previous equality holds because a constant term—in this case $\Delta E N$—can be added or subtracted from the Hamiltonian. The second part, $\mathcal{H}_{\mathrm{el}}$, is of this kind and describe collisional energy shifts. Notably, the size of these shifts is given by $\hbar g$, the same quantity which characterizes the spin exchange coupling strength.

Altogether, these two terms result directly from the scattering potential, Eq. 3.2. Additionally, energy shifts arise due to externally applied fields. Most importantly, we have to consider magnetic bias fields and the thereby caused Zeeman shifts. For alkali atoms these energy shifts are described by the Breit-Rabi formula. Its predominant contribution is linear in magnetic field strength and shifts the levels proportional to their magnetic quantum number, $\Delta E \propto m$. It therefore treats the two $m = \pm 1$ asymmetrically: while one of the levels is raised in energy, the other is lowered by the same amount. Level shifts of this kind play no rôle for the spin exchange dynamics because both levels are populated in a pairwise fashion. Therefore, the Larmor phase is inconsequential for the ensuing dynamics. However, expanding the Breit-Rabi formula to higher orders in magnetic field strength B yields the quadratic Zeeman shift. To capture this energy shift we supplement the Hamiltonian with the following term $\mathcal{H}_B = \hbar q_B B^2 (N_\uparrow + N_\downarrow)$ where q_B quantifies the strength of the quadratic shifts. Any additional level shifts are included in a similar manner. In particular we use dispersive microwave dressing which predominantly shifts the $m = 0$ level in energy. As such it acts in a similar fashion as the applied magnetic bias field. We describe the total energy shift by

$$\mathcal{H}_q = -\hbar q (N_\uparrow + N_\downarrow) \tag{3.5}$$

and call q the spin exchange detuning. It incorporates all external level shifts. Since the Hamiltonian cannot build up or change magnetization, we restrict our discussion to the case of vanishing magnetization throughout the unitary evolution. This is appropriate because in our experiments the initial populations of $m = \pm 1$ are carefully emptied.

Hamiltonian in collective spin representation

The Hamiltonian $\mathcal{H}$ can be expressed in terms of the spin-1 operators. Although these operators have been introduced before for a single particle they retain their form for many particles. This is a consequence of the indistinguishability of identical Bosons (see Sect. C.1). Within this Schwinger Boson representation, the spin operators describe a collective spin made up by N individual spin-1 particles: for instance, the collective spin operator S_x is obtained by summing up all single-particle spin operators of each individual particle. Therefore the resulting spin has a size of $S = 0 \ldots N$. Similar expressions hold for the alignment operators $\hat{\boldsymbol{F}}$ and $\hat{\boldsymbol{G}}$ [3].

Taking the following combinations of collective spin operators we recognize the distinctive terms of the spin exchange Hamiltonian,

$$F_x^2 + G_y^2 \equiv S_x^2 + S_y^2 = \frac{1}{2}(\hat{a}_0 \hat{a}_0 \hat{a}_\downarrow^\dagger \hat{a}_\uparrow^\dagger + \text{h.c.} + 2N_0(N_\uparrow + N_\downarrow) + N_0 + N) \tag{3.6}$$

and

$$F_z + G_z = N_0 - (N_\uparrow + N_\downarrow)/2\,. \tag{3.7}$$

The first describes the spin exchange process and the associated collisional shifts, while the latter contains the detuning terms due to externally applied fields, e.g. a magnetic bias field. Therefore the Hamiltonian can be cast into

$$\mathcal{H}/2\hbar = g\left(\hat{F}_x^2 + \hat{G}_y^2\right) + \frac{q}{3}\left(\hat{F}_z + \hat{G}_z\right). \tag{3.8}$$

Rearranging the terms such that the operators belonging to one common SU(2) space stand together we arrive at

$$\mathcal{H}/2\hbar = \left(g\hat{F}_x^2 + \frac{q}{3}\hat{F}_z\right) + \left(g\hat{G}_y^2 + \frac{q}{3}\hat{G}_z\right). \tag{3.9}$$

This can be understood as nonlinear dynamics within the SU(2) space of $\{F_x, F_y, F_z\}$ and similar dynamics in the space of $\{G_x, G_y, G_z\}$. These two SU(2) spaces are connected by a fixed Larmor phase rotation such that it suffices to discuss the dynamics in one of the two spaces [8, 9]. In the following we thus treat the following Hamiltonian

$$\mathcal{H}/2\hbar = g\hat{F}_x^2 + \frac{q}{3}\hat{F}_z\,. \tag{3.10}$$

When deriving the Hamiltonian we assumed a vanishing magnetization and neglected terms of the form $(N_\uparrow - N_\downarrow)$. As a side remark: when keeping these terms, the Hamiltonian in absence of any external fields can be written in the elegant form of $\mathcal{H}/2\hbar = g\hat{\mathbf{S}}^2$. Such a formulation is beneficial for discussing the quantum mechanical ground state [10]: for ferromagnetic interactions $g > 0$ the ground state has maximal spin length, $S = N$; all $2N + 1$ sub states are degenerate. In contrast, for antiferromagnetic interactions $g < 0$ the ground state is unique and has $S = 0$. Here pairs of atoms (for N even) form spin singlets [3, 11].

3.4 Mean-Field Description and Classical Phase Space

Before discussing the Hamiltonian and its peculiarities in a quantum mechanical framework we first present its classical approximation. For this we consider the mean-field limit which is valid for large particle numbers, $N \to \infty$ and all of them share an identical *single*-particle state. Then no quantum mechanical correlations among them can exist. Additionally, the quantum nature of any single particle, which might for instance show up in fluctuations, becomes unimportant due to the infinitely large ensemble. Therefore, the mean-field limit essentially amounts to a classical approximation. Formally we substitute the mode operators by complex numbers. Motivated by the previous discussion we anticipate the importance of the spinor phase and only consider states with vanishing magnetization such that the Larmor phase is rendered unimportant:

$$\begin{aligned}\hat{a}_\uparrow &\to \sqrt{N_\uparrow} = \sqrt{(N - N_0)/2} \\ \hat{a}_0 &\to \sqrt{N_0}\exp \mathrm{i}\varphi \\ \hat{a}_\downarrow &\to \sqrt{N_\downarrow} = \sqrt{(N - N_0)/2}\,.\end{aligned} \tag{3.11}$$

Conventionally, the phase space is expressed in the cylindrically symmetric space of N_0/N and spinor phase φ. Then, the mean-field energy per particle reads

$$\frac{E}{N} = \hbar g N \frac{N_0}{N}\left(1 - \frac{N_0}{N}\right)(\cos\varphi + 1) + \hbar q\left(1 - \frac{N_0}{N}\right). \tag{3.12}$$

The shape of the energy landscape depends on the relative strength of the spin exchange detuning q compared to the effective nonlinear coupling strength given by gN. Phase space portraits for different choices of parameters are shown in the right column of Fig. 3.1. For parameters $0 < q < 2gN$ the phase space portrait shows running phase solutions as well as confined orbits. Both structurally different regions are divided by a separatrix which is indicated as the bold trajectory. For a vanishing spin exchange detuning $q = 0$ only confined orbits occur as shown at the top. In contrast, for a detuning exceeding $q > 2gN$ as depicted at the bottom only running (spinor) phase trajectories exist.

The two variables N_0/N and spinor phase φ are given by projections of the Bloch sphere representation of $\hat{\boldsymbol{F}}$. In the language of spins the substitutions of Eq. 3.11 amount to

$$\boldsymbol{F} \to N\begin{pmatrix}\sin\vartheta\cos\varphi \\ \sin\vartheta\sin\varphi \\ \cos\vartheta\end{pmatrix} \tag{3.13}$$

where $\cos\vartheta = N_0/N$ parametrizes the fractional population in the pump mode. The mean-field solutions in terms of these spin variables are shown on a Bloch sphere in the first two columns of Fig. 3.1. In this representation the angle ϑ corresponds to the polar angle while the spinor phase φ defines the azimuthal position on the Bloch sphere. Evidently, the cylindrical phase space, Eq. 3.12 is a projection of this Bloch sphere representation.

At large spin exchange detuning $q > 2gN$ as shown exemplary at the bottom, the north and south pole of the Bloch sphere host a (neutrally) stable fixed point. These two fixed points are enclosed by phase running trajectories. This structure of the phase space changes once the spin exchange detuning is reduced. At $q = 2gN$ the system undergoes a (supercritical) pitchfork bifurcation. Thereby, the formerly stable fixed point located at the Bloch sphere's north pole splits up into two stable and one unstable fixed point. The latter remains at the north pole while the two stable fixed points as enclosed by the separatrix move towards the equatorial plane which they asymptotically reach at vanishing detuning $q \to 0$. The unstable fixed point at the north pole corresponds to a saddle point (hyperbolic fixed point) at which the stable and unstable manifold of the separatrix meet. At $q = gN$ the separatrix'

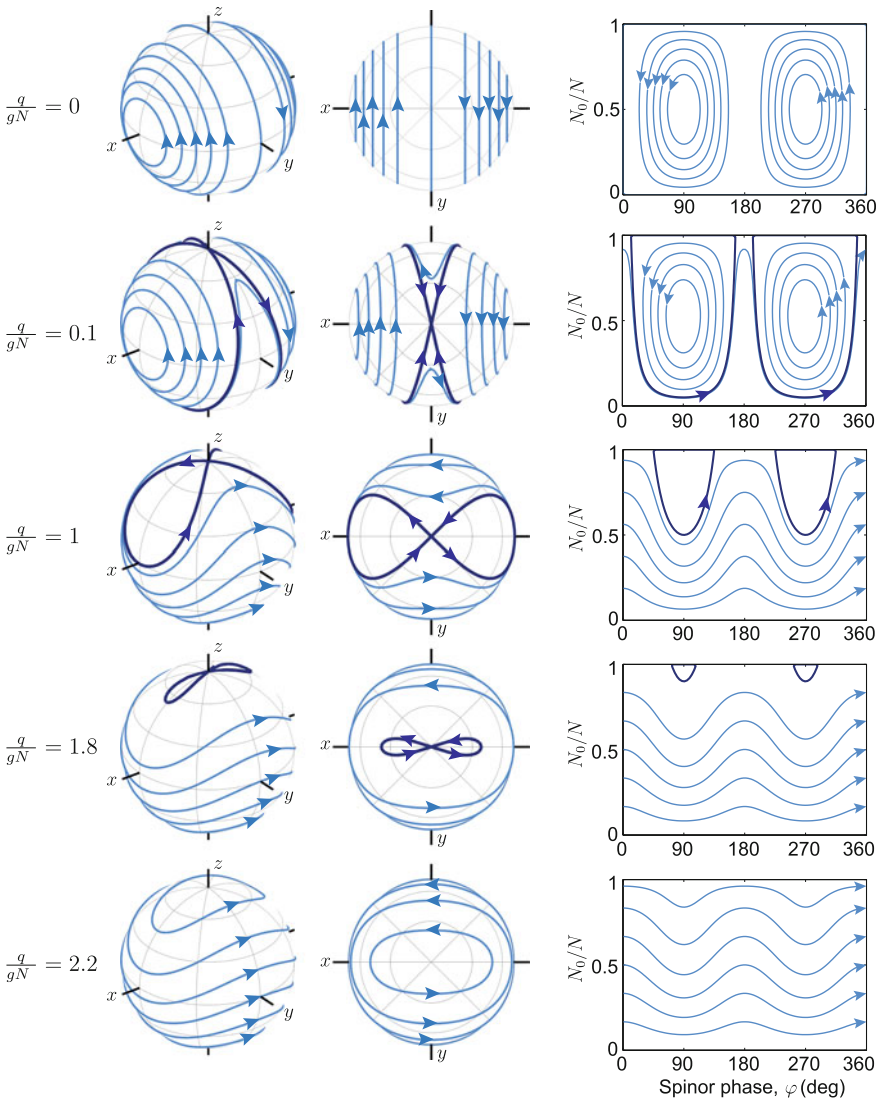

Fig. 3.1 Classical phase space of the spin operators $\boldsymbol{F}$. Mean-field trajectories for different ratios between spin exchange detuning q and effective coupling strength gN (from top to bottom). The right column shows the dynamics in the cylindrical phase space spanned by N_0/N and the spinor phase φ (see Eq. 3.12). It is a projection of the Bloch sphere representation with $N_0 = N$ and $N_0 = 0$ corresponding to the north and south pole, respectively. For spin exchange detuning $q = 0$ (top row) the mean-field trajectories are confined (oscillatory) orbits. In contrast, for a spin exchange detuning exceeding $q = 2gN$, only running phase solutions exist as exemplified in the row at the bottom. At this point, the phase space gets bifurcated for smaller detuning. Henceforth, a separatrix (thick line) divides the running phase solutions from oscillatory trajectories. At $q = gN$ the branches of the separatrix encloses an angle of 90° (middle row)

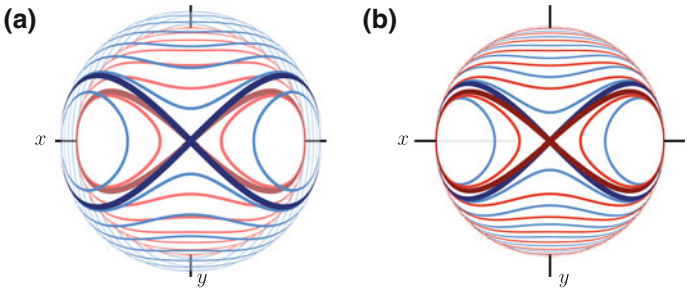

Fig. 3.2 Structural stability of the phase space. **a** The mean-field phase space is shown for two different atom numbers, $N = 400$ (blue) and $N = 350$ (red), respectively with otherwise identical parameters. Each phase space is drawn on the correspondingly sized Bloch sphere. To directly compare both phase space portraits the Bloch spheres are rescaled to a common size in panel **b** While the angle enclosed by the separatrix (bold) changes, the position of the hyperbolic fixed point remains unaltered at the corresponding north pole

two branches enclose an angle of 90°. At this point the bifurcated phase space is structurally particularly stable.

Let us investigate this structural stability when considering different total atom numbers. Such considerations are important in view of particle loss which is inevitable in experimental realizations. Figure 3.2a shows the classical phase space for total atom numbers of $N = 400$ and $N = 350$ in blue and red, respectively. Here the phase space of $N = 400$ atoms corresponds to the parameter setting $q = gN$. As the atom number is reduced the associated Bloch sphere shrinks. For clarification, panel (b) shows both phase spaces on a fixed-size Bloch sphere. While the angle enclosed by the separatrix changes, the position of the hyperbolic fixed point remains at the north pole. Therefore, starting at parameters for which $q \approx gN$ mild particle loss will not lead to structural changes of the classical phase space. Of course such an approach to particle loss is greatly oversimplified. However, it highlights two aspects: the topological structure is described by a single parameter, q/gN, and, within the bifurcated phase space the position of the hyperbolic fixed point does not change. The latter point is particularly important for the experiments reported on in this thesis. All experiments start with only the $m = 0$ spin state populated which corresponds to the Bloch sphere's north pole. Such a state can experimentally be generated reliably. In the associated classical system this amounts to a preparation precisely onto an unstable fixed point.

A bifurcation occurring in the classical dynamics is often connected to a quantum phase transition of the corresponding Hamiltonian. One should keep in mind that while within mean-field theory the bifurcated regime extends from $q = 0 \ldots 2gN$ a quantum calculation (under conserved magnetization) reveals that the region extends symmetrically, $-2gN < q < 2gN$ with a quantum phase transition at the respective edge [12, 13].

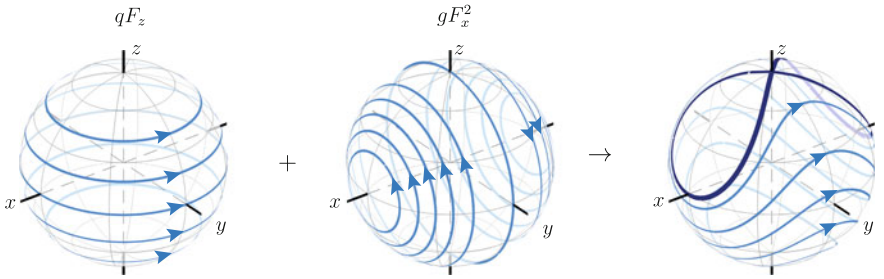

Fig. 3.3 Constitution of the phase space as the interplay of rotation and shearing dynamics. Expressing the Hamiltonian in terms of spin operators allows for an elegant interpretations of the dynamics on the Bloch-sphere. The spin operators are the generators of rotations. Therefore the term $\hat{F}_z$ describe rotations about the $z-$axis. Terms akin to F_x^2 yield a shearing which can be understood as a rotation with an angular velocity depending on the projection of F_x itself. The combination of these two operators generates the dynamics shown on the right Bloch sphere

Structure of the phase space

The topological structure of the phase space is a consequence of the interplay between the two constituent terms $\hat{F}_z$ and $\hat{F}_x^2$, respectively. Such a combination of spin operators is often referred to as Lipkin-Meshkov-Glick Hamiltonian [14]. The action of both operators can intuitively be understood: very much like the momentum operator generates translations, angular momentum operators are generators of rotation. Therefore, when viewed on the Bloch sphere the term $q\hat{F}_z$ describes a rotation about the z-axis with angular velocity given by q. This is illustrated in Fig. 3.3. Similarly, the action of $\hat{F}_x^2$ can be understood as a rotation about the x-axis with an angular velocity given by $\hat{F}_x$ itself. Thus, the angular velocity increases when leaving the plane $x = 0$. Additionally the sense of rotation is different on the two hemispheres with $x < 0$ and $x > 0$, respectively as indicated by the arrows in Fig. 3.3.

Therefore, the spin exchange detuning q drives oscillations between $\hat{F}_x \equiv \hat{S}_x$ (orientation) and $\hat{F}_y$ (alignment). In contrast the quadratic spin term $\hat{F}_x^2$ is responsible for population transfer among the three involved modes.

3.5 Fluctuations

We can go one step further than the mean-field approximation by additionally considering quantum mechanical fluctuations. For this discussion we consider the Hamiltonian in terms of collective spin operators. By virtue of their angular momentum nature these operators satisfy the SU(2) commutator relations which in turn imposes a Heisenberg uncertainty relation for the individual spin components, e.g.

$$(\Delta\hat{F}_x)^2(\Delta\hat{F}_y)^2 > |\langle\hat{F}_z\rangle|^2 \tag{3.14}$$

Therefore there is an inherent uncertainty associated to the spin as well as the alignment operators. Starting point of all experiments is a state in which all N atoms are prepared in $m = 0$. As stated above, such a state has $\langle \hat{F}_z \rangle = N$ (and similarly $\langle \hat{G}_z \rangle = N$) as it is fully aligned. In the absence of quantum mechanical correlations among the individual atoms the uncertainty imposed by Eq. 3.14 is shared equally between F_x and F_y. Therefore, $(\Delta F_x)^2 = (\Delta F_y)^2 = N$.

In a microscopic point of view these fluctuation can be traced back to the quantum fluctuations of a single spin-1. For uncorrelated particles the variances of these individual spins add up to give the total uncertainty of the collective spin. Since a single spin-1 has uncertainty 1 the uncertainty of the collective spin is $\sqrt{N}$. However, one has to keep in mind that the associated Bloch sphere has a radius of size N. Therefore the relative fluctuations become smaller $\propto 1/\sqrt{N}$ as more particles constitute the spin. In the mean-field limit these fluctuations vanish.

Equation 3.14 is often compared to the canonical uncertainty relation for one individual spin. In this case, the right hand side reads $\hbar/4$. Therefore, one might argue that the collective spin system features an effective Planck constant that depends on the number of atoms, $\hbar_{\text{eff}} = \sqrt{2/N}$. Then the mean-field limit formally corresponds to $\hbar_{\text{eff}} = 0$ which is the limiting case that is routinely used to recover the laws of classical mechanics out of the more fundamental laws of quantum physics.

3.6 The Wigner Function as a Quasiprobability Distribution

To simulate and visualize the quantum dynamics we make use of phase space methods [15]. A central object is the representation of a state using the Wigner quasiprobability function [16]. This is the generalization of classical probability distributions into the realm of quantum mechanics. For simplicity we first consider the single mode case, before discussing the multimode extension in the next section. The mode is described by creation operator $\hat{a}^\dagger$. Starting point is the definition of a characteristic function; these functions are widely used in stochastics as they provide means to generate the moments of a probability distribution. The moments are then obtained as derivatives of the characteristic function. In quantum mechanics a characteristic function χ_W can be defined as the expectation value of the mode's displacement operator, i.e.

$$\chi_W(\lambda, \lambda^*) = \left\langle \mathrm{e}^{\lambda \hat{a}^\dagger - \lambda^* \hat{a}} \right\rangle . \tag{3.15}$$

Average values are then obtained formally by taking derivatives with respect to λ and λ^*, respectively, which are treated independently

$$\langle \hat{a}^k (\hat{a}^\dagger)^l \rangle_W = \left(\frac{\mathrm{d}}{\mathrm{d}\lambda} \right)^k \left(\frac{\mathrm{d}}{\mathrm{d}\lambda^*} \right)^l \chi_W(\lambda, \lambda^*) \Big|_{\lambda \to 0} . \tag{3.16}$$

Here $\langle\cdot\rangle_W$ denotes the expectation value of the *symmetrized* combination of destruction and creation operators. This symmetrisation occurs because the exponential of the characteristic function contains two non commuting operators. Then their ordering is important. The single exponential yields the symmetric ordering of $\hat{a}$ and $\hat{a}^\dagger$. Therefore the expectation values generated by χ_W are symmetrically ordered. For example $\langle\hat{a}^\dagger\hat{a}\rangle_W = \langle\hat{a}^\dagger\hat{a} + \hat{a}\hat{a}^\dagger\rangle/2$.

The Wigner quasiprobability function is defined as the Fourier transform of the symmetrically ordered characteristic function χ_W,

$$W(\alpha, \alpha^*) = \frac{1}{\pi^2}\int \mathrm{d}^2\lambda\, \mathrm{e}^{\lambda^*\alpha - \lambda\alpha^*}\chi_W(\lambda, \lambda^*)\,. \tag{3.17}$$

Symmetrically ordered operator averages are then given by the phase space averages over the Wigner function

$$\langle\hat{a}^k(\hat{a}^\dagger)^l\rangle_W = \int \mathrm{d}^2\alpha\, \alpha^k(\alpha^*)^l W(\alpha, \alpha^*)\,. \tag{3.18}$$

Another widely used characteristic function is the one corresponding to antinormal ordering. The difference between the symmetrically ordered characteristic function χ_W and the antinormal ordered one, i.e. $\chi_a = \left\langle \mathrm{e}^{-\lambda^*\hat{a}}\mathrm{e}^{\lambda\hat{a}^\dagger}\right\rangle$ is given by $\chi_a = \mathrm{e}^{-|\lambda|^2/2}\chi_W$. The Fourier transform of the antinormal ordered characteristic function gives the often employed Husimi representation. Therefore, the Husimi function can be obtained from the Wigner function by convolution with the Gaussian $\mathrm{e}^{-|\lambda|^2/2}$.

3.7 Simulation Method Based on the Wigner Function

We simulate the spin exchange dynamics semi-classically using phase space methods which make use of the Wigner representation [15]. At the core of this simulation method lies the correspondence between the action of mode operators and derivatives of the corresponding Wigner function. While this correspondence is exact, the resulting set of differential equations is often only tractable when applying the so-called truncated Wigner approximation. This restricts the method to Wigner functions that remain positive throughout the evolution. Vigorous nonclassical effects that lead to negativities of the associated Wigner function are therefore not captured.

From a practical point of view, the procedure is surprisingly simple and intuitive: the initial Wigner function is stochastically sampled; each sample is then propagated in time according to the classical mean-field trajectories and finally averaged to give the Wigner function at a later point in time. While the time evolution proceeds according to the deterministic classical equations of motion, quantum fluctuations are effectively taken into account by the uncertainty of the initial state [15, 17].

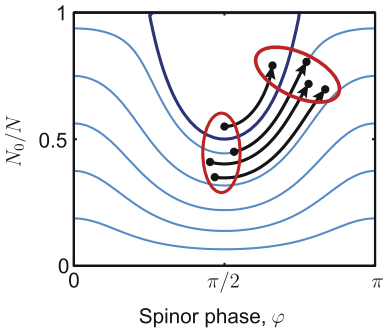

Fig. 3.4 Illustration of the simulation method within the truncated Wigner approximation. To simulate the quantum dynamics an initial Wigner function is sampled in phase space (indicated by the red ellipse). Each of these initial conditions is propagated in time using the classical equations of motion as shown by the black arrows. The resulting distribution coincides with the Wigner function. Although the time evolution of each trajectory is classical, beyond mean-field effects are included by the initial stochastic sampling. However, decisively nonclassical effects leading to negativities are not captured and the method is restricted to positive Wigner functions throughout the evolution

We now summarise the procedure in more detail. The von Neumann equation governs an operator's time evolution. For a density matrix ρ it reads $\mathrm{i}\hbar\,\mathrm{d}\rho/\mathrm{d}t = [\mathcal{H}, \rho]$ which can be reexpressed in terms of the Wigner function. In this framework the commutator terms like $\mathcal{H}\rho$ and $\rho\mathcal{H}$ correspond to derivatives of the corresponding Wigner function. For a single mode with annihilation operator $\hat{a}$ we have the correspondence of $\hat{a}\rho \leftrightarrow \left(\alpha + \frac{1}{2}\frac{\mathrm{d}}{\mathrm{d}\alpha^*}\right) W(\alpha, \alpha^*)$. In this manner, Hamiltonians bilinear in $\hat{a}$ and $\hat{a}^\dagger$ lead to a differential equation with first and second derivatives. As such they are similar to a drift and diffusion equation. If the initial Wigner function is positive, it remains so during the entire evolution. This, however, only holds in the Gaussian regime, i.e. for Hamiltonians bilinear in mode operators.

The spin exchange Hamiltonian is quartic in mode operators which gives rise to a third derivative in the differential equation. The truncated Wigner approximation consists in neglecting this third derivative. Within this approximation time evolution is governed by the deterministic trajectories according to mean-field. Effects that go beyond mean-field are captured by stochastically sampling the initial condition, i.e. the initial Wigner function. This is illustrated in Fig. 3.4. The experiments reported on in this thesis start with a single occupied spin component: all N atoms populate the $|0\rangle$ component. The Wigner function of each spin state is a Gaussian with width reflecting the quantum fluctuations—we detail the description in the space of quadrature at a later point. Our initial condition is constructed in the following manner; to sample the initial state, for each run and spin component, we draw phases β and γ from a normal distribution. The initial state for either mode $|i\rangle$ is then given by $\alpha_i = \sqrt{N_i} + \frac{1}{2}(\beta + \mathrm{i}\gamma)$ where N_i is the population of the mode in question ($N_0 = N$ and $N_\uparrow = N_\downarrow = 0$). After time propagation we calculate phase space averages of the desired observable. As detailed above, these phase space averages correspond to symmetrically ordered

operators. The average mode population therefore reads $\langle \hat{N}_i \rangle = \langle \alpha_i^* \alpha_i \rangle - 1/2$ while the corresponding variance is given by $(\Delta \hat{N}_i)^2 = (\Delta \alpha_i^* \alpha_i)^2 - 1/4$.

This procedure is often summarised in the following simplified terms: to take into account quantum effects, initially half a quantum of noise is added to each mode which—after classical time evolution—is again subtracted from the final result. One has to keep in mind though that single trajectories do not necessarily resemble experimental realizations [18].

This method's region of validity cannot easily be assessed in general. In the case of spin exchange, the authors of reference [19] compared the results obtained via the truncated Wigner approximation to solving the exact quantum dynamics. For sufficiently short durations, the predominant process is scattering from the highly populated pump mode into the sparsely populated side modes. Only for later times the pump mode might be emptied and repopulated by backscattering from the then increasingly populated side modes. Up to this point in time the truncated Wigner approximation seems to remains valid. All experiments reported on in this thesis are restricted to such short durations and we routinely use numerical simulations that are based on the truncated Wigner approximation.

3.8 Visualisation of the Quantum Dynamics

In this section we use the Wigner representation to illustrate the quantum dynamics on the Bloch sphere of spin $\boldsymbol{F}$. For this, the above single mode treatment of the Wigner function is extended to three levels by using vectors $\boldsymbol{\alpha} = (\alpha_\uparrow, \alpha_0, \alpha_\downarrow)^t$ and similarly for $\boldsymbol{\lambda} = (\lambda_\uparrow, \lambda_0, \lambda_\downarrow)^t$. Finally, we transform the phase space variables $\boldsymbol{\alpha}$ into spin variables, e.g. $F_x = \alpha_0(\alpha_\uparrow + \alpha_\downarrow) + \text{c.c.}$.

Figure 3.5 shows the corresponding Wigner functions for four different durations under spin exchange. For this purpose we simulate the dynamics with the experimentally extracted parameters. While the experimental characterisation of spin exchange is the subject of a later chapter, here we merely state that the parameters amount to a coupling strength of $gN = 2\pi \times 22\,\text{Hz}$ and a spin exchange detuning of $q = 2\pi \times 24\,\text{Hz}$ which corresponds to $q = 1.1gN$. The initial state contains $N = 400$ atoms that are prepared in state $|0\rangle$. The associated Wigner function is an isotropic Gaussian centred at the Bloch sphere's north pole. Subsequent nonlinear evolution deforms the state in a fashion which can intuitively be understood by following the mean-field solutions. These classical trajectories are drawn as grey lines. As the north pole corresponds to a hyperbolic fixed point, the state's centre of gravity remains unchanged during the ensuing nonlinear evolution. However, as the state's quantum uncertainty extends into the surrounding space, it is dynamically redistributed. For short durations this yields a squeezed state which is shown in the respective panels for 5 and 10 ms of spin exchange [8]. Clearly, the width along the squeezed direction is narrower than the extension of the original isotropic state. In a semiclassical description this redistribution is a consequence of the compression

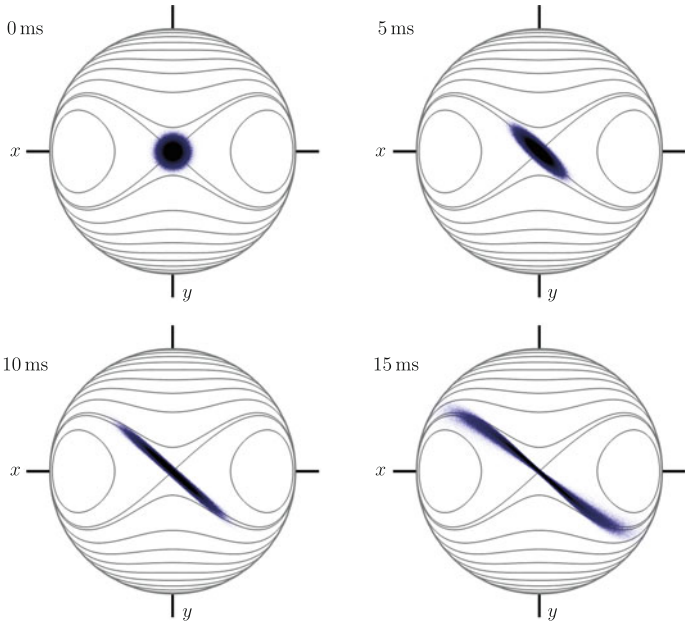

Fig. 3.5 Simulated Wigner functions for spin exchange. The initial state in which all $N = 400$ atoms are prepared in the $|0\rangle$ state has an isotropically extending Wigner function centred at the Bloch sphere's north pole (panel top left). The grey lines indicate the mean-field trajectories. Tracing these classical solution allows for an intuitive explanation of the ensuing dynamics: as the north pole corresponds to a hyperbolic fixed point the state's centre of gravity remains unchanged. However, the fluctuations extend into the surrounding area and are thus compressed or enlarged as described by the converging or diverging manifold of the separatrix. Consequently, after allowing for 5 ms of spin exchange a squeezed state emerges. For longer evolution times ($t = 10$ ms) this process is even more pronounced before the state eventually experiences the curvature of the underlying Bloch sphere. At evolution times exceeding $t > 15$ ms the state starts to bend around the sphere

along the converging manifold of the separatrix while at the same time the state is elongated along its diverging branch. For longer durations the state progressively wraps around the Bloch sphere as expected from the infinity-sign shaped mean-field trajectories [20]. The experiments reported in this thesis involve such extended states up to evolution times of $\approx$15 ms as exemplified in the last panel.

3.9 Mexican Hat Analogy of Increased Spin Fluctuations

Complementary, to the above Bloch sphere description based on the orientation and alignment operators belonging to $\hat{F}$, the spin exchange dynamics can be visualized in the space of spin $\hat{\boldsymbol{S}}$ alone. In this space there is no oriented spin since the mean

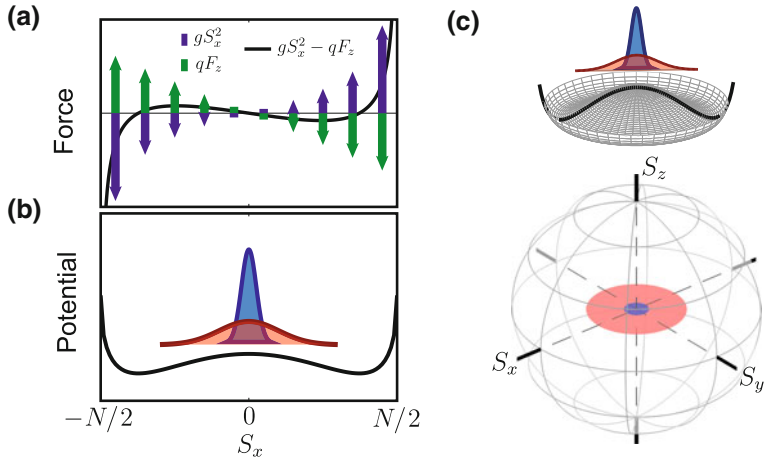

Fig. 3.6 Mexican hat potential analogy to spin exchange. **a** The forces arising due to the shearing interaction (purple) and rotation (green) are shown along the axis of S_x. Subtraction of both contributions results in the solid black line. **b** This interplay between shearing and rotation leads to a double-well potential. The uncorrelated initial state can be imagined as a narrow wave packet that dynamically expands in the potential of spin exchange. **c** As a consequence of the inconsequential Larmor phase the potential is rotationally symmetric in the space of S_x and S_y. The resulting potential therefore resembles a Mexican hat. **d** Within a Bloch sphere representation the initial state corresponds to the blue disc with diameter $\sqrt{N}$. Under spin exchange this diameter gets enlarged. Since the magnetization vanishes throughout the evolution, the disc has no corresponding extension in z-direction

spin length vanishes $\langle \hat{\boldsymbol{S}} \rangle = 0$. This corresponds to a state lying at the centre of the associated Bloch sphere. The spin exchange dynamics becomes manifest in the size of fluctuations. As shown for the oriented state these fluctuations take the form of a disc as depicted in Fig. 2.3.

During spin exchange, the radius of this disc increases which is detailed in Fig. 3.6. Here panel (a) shows an accounting of the forces that are exerted by, both, the nonlinear term $\hat{F}_x^2 \equiv \hat{S}_x^2$ (purple), and the rotation $\hat{F}_z$ (green) when plotted against $\hat{S}_x$. The resulting force is cubic (black line). This corresponds to a double-well potential that is drawn in panel (b). When preparing a wave packet (blue) in this double-well potential its width increases (red) as a result of dispersion while its average positions stays ideally fixed at $\langle \hat{S}_x \rangle = 0$. Because of the symmetry with respect to Larmor phase rotations this simple picture has to be generalized to the rotationally symmetric case (panel c). Dynamics under nonlinear spin exchange is then similar to preparing a narrow wave packet on the unstable fixed point of a Mexican hat-like potential. In a Bloch sphere representation the spin fluctuations take the shape of a disc whose diameter grows as nonlinear dynamics proceeds (panel d). The Mexican hat-like potential is prototypical for spontaneous symmetry breaking [21], it supports two excitations [22] which has been studied experimentally in reference [23].

3.10 Comparison to Spin Squeezing of a Two-Level System

The squeezing of spin-1 objects as described above occurs in the space spanned by both, orientation (spin) and alignment (quadrupole) operators [24]. As such it is markedly different from the corresponding squeezing exhibited in two-level systems. In this section we first review such two-level spin squeezing, before we compare its characteristics to the present spin-1 situation.

Atomic spin squeezing was first proposed for two-level systems [25, 26] and later generalized to larger spins [24]. For two-level systems, one studies the fluctuations of a collective spin which has total size $N/2$ as it is formed by N indistinguishable spin-1/2 objects. The constituent spin-1/2 can be made up by any two levels—often called a pseudo spin-system. The necessary nonlinear interactions have been engineered in a variety of experimental platforms. For ultracold atoms, two methods have proven successful: nonlinearities mediated via light matter interaction [27], or via collisional interactions of the atoms themselves [28]. The first uses the dispersive energy shift exerted on a two-level atom by the dipole force of off-resonant light. In spin language such energy shifts can be captured by a term akin to $\hat{J}_z$. By engineering an appropriate feedback mechanism the strength of this rotation term can be made to depend on $\hat{J}_z$ itself [29, 30]. For this a high finesse cavity is used and the nonlinear spin term of the form $\chi \hat{J}_z^2$ arises where χ describes the nonlinear coupling strength. The method building on collisional interactions relies on controlling the intra- or inter-component scattering rates to tune χ. These collisional rates can be manipulated by employing magnetic Feshbach resonances or by tuning the spatial overlap of both atomic spin states [31–33]. Either method has been used for spin squeezing in mesoscopic Rubidium Bose-Einstein condensates.

Additional to these spin-squeezing techniques that deterministically produce a squeezed state at an a priori known position in phase space, methods exist for so-called conditional spin squeezing. Such conditional spin squeezing arises in measurement based protocols, i.e. when performing quantum nondemolition measurements. This procedure is called conditional because it depends on the individual measurement outcome. Only by using feedback on the measurement outcome deterministic spin squeezing can be generated [34]. The nondemolition measurements can be performed by using the dispersive phase shift of off-resonant light when travelling through an atom cloud [35]. To enhance the effect a high finesse optical cavity can be used [36–38]. Similarly the polarization rotation of light via the Faraday effect can be employed [39]. In fact the strongest atomic spin squeezing which amounts to 20 dB was achieved using a combination of both, conditional and unconditional squeezing techniques that use a shearing interaction [40].

All these techniques lead to an effective Hamiltonian that contains a single squared spin operator. Therefore, the squeezing is generated under shearing dynamics. By adding linear coupling to these systems—characterized through its strength Ω and detuning δ—a Hamiltonian similar to the spin-1 system can be engineered: the interplay between the shearing interaction and the rotation yields a Hamiltonian of the form $\chi \hat{J}_z^2 - \Omega \hat{J}_x + \delta \hat{J}_z$ [41, 42]. If the linear coupling is resonant ($\delta = 0$) this system

structurally resembles the spin exchange Hamiltonian (Eq. 3.9) and thus leads to similar dynamics, in particular to squeezing. This method was realized in Bose-Einstein condensates where it was coined twist-and-turn spin squeezing [43]. Alternatively, a discretized way of repeated squeezing with subsequent rotation has been suggested [44]. For squeezing within optical cavities similar mechanisms are proposed [45]. Finally, in nuclear magnetic resonance, the interaction of the spin-quadrupole with intrinsic electric field gradients generate a similar Hamiltonian combining shearing interaction and linear coupling [46, 47].

For (pseudo) spin-1/2 systems spin squeezing occurs within the space of the collective spin $\hat{\boldsymbol{J}}$. As defined in Eq. 2.1 these are single-particle operators. Therefore each point of the associated Bloch sphere representing the spin $\boldsymbol{J}$ can be reached by routinely employed single-particle operations, e.g. linear coupling of the two constituent levels. For the above mentioned experiments this is typically achieved by rf-pulses which perform single-particle spin rotations.

In contrast, the squeezing of a spin-1 system occurs in the SU(2) space spanned by operators $\hat{\boldsymbol{F}}$ (or equivalently $\hat{\boldsymbol{G}}$). Here, only the $\hat{F}_x \equiv \hat{S}_x$ component is a single-particle operator. The operator $\hat{F}_y$ describes particle *pairs*. Therefore, the state space corresponding to the Bloch sphere of operators $\hat{\boldsymbol{F}}$ cannot be accessed via linear coupling. To experimentally explore this state space different control mechanism which involve particle-interactions are needed as demonstrated in reference [48]. Albeit, this state space which exhibits squeezing lacks the well-established control techniques, the pair character leads to an additional symmetry. The structural stability of the classical phase can be traced back to this symmetry; compared to the spin-1/2 Hamiltonian shown above, this symmetry enforces $\delta = 0$.

References

1. F. Dalfovo, S. Giorgini, L.P. Pitaevskii, S. Stringari, Theory of Bose-Einstein condensation in trapped gases. Rev. Mod. Phys. **71**, 463–512 (1999). https://doi.org/10.1103/RevModPhys.71.463
2. C. Pethick, H. Smith, *Bose-Einstein Condensation in Dilute Gases* (Cambridge University Press, 2008)
3. D.M. Stamper-Kurn, M. Ueda, Spinor Bose gases: Symmetries, magnetism, and quantum dynamics. Rev. Mod. Phys. **85**, 1191 (2013). https://doi.org/10.1103/RevModPhys.85.1191
4. G.E. Marti, D.M. Stamper-Kurn, Spinor Bose-Einstein gases (2015). arXiv:1511.01575
5. F. Deuretzbacher, G. Gebreyesus, O. Topic, M. Scherer, B. Lücke, W. Ertmer, J. Arlt, C. Klempt, L. Santos, Parametric amplification of matter waves in dipolar spinor Bose-Einstein condensates. Phys. Rev. A **82**, 053608 (2010). https://doi.org/10.1103/PhysRevA.82.053608
6. G.E. Marti, A. MacRae, R. Olf, S. Lourette, F. Fang, D.M. Stamper-Kurn, Coherent magnon optics in a ferromagnetic spinor Bose-Einstein condensate. Phys. Rev. Lett. **113**, 155302 (2014). https://doi.org/10.1103/PhysRevLett.113.155302
7. T.-L. Ho, Spinor bose condensates in optical traps. Phys. Rev. Lett. **81**, 742–745 (1998). https://doi.org/10.1103/PhysRevLett.81.742
8. C.D. Hamley, C.S. Gerving, T.M. Hoang, E.M. Bookjans, M.S. Chapman, Spin-nematic squeezed vacuum in a quantum gas. Nat. Phys. **8**, 305 (2012). https://doi.org/10.1038/nphys2245

9. I. Kruse, K. Lange, J. Peise, B. Lücke, L. Pezzè, J. Arlt, W. Ertmer, C. Lisdat, L. Santos, A. Smerzi, C. Klempt, Improvement of an atomic clock using squeezed vacuum. Phys. Rev. Lett. **117**, 143004 (2016). https://doi.org/10.1103/PhysRevLett.117.143004
10. C.K. Law, H. Pu, N.P. Bigelow, Quantum spins mixing in spinor Bose- Einstein condensates. Phys. Rev. Lett. **81**, 5257 (1998). https://doi.org/10.1103/PhysRevLett.81.5257
11. A. Chudnovskiy, V. Cheianov, Stable condensate of singlet pairs in spinor Bose gases (2017). arXiv:1706.08085
12. Z. Zhang, L.-M. Duan, Generation of massive entanglement through an adiabatic quantum phase transition in a spinor condensate. Phys. Rev. Lett. **111**, 180401 (2013). https://doi.org/10.1103/PhysRevLett.111.180401
13. X.-Y. Luo, Y.-Q. Zou, L.-N. Wu, Q. Liu, M.-F. Han, M.K. Tey, L. You, Deterministic entanglement generation from driving through quantum phase transitions. Science **355**, 620–623 (2017). https://doi.org/10.1126/science.aag1106
14. H.J. Lipkin, N. Meshkov, A. Glick, Validity of many-body approximation methods for a solvable model: (i). exact solutions and perturbation theory. Nucl. Phys. **62**, 188–198 (1965)
15. P.B. Blakie, A.S. Bradley, M.J. Davis, R.J. Ballagh, C.W. Gardiner, Dynamics and statistical mechanics of ultra-cold Bose gases using c-field techniques. Adv. Phys. **57**, 363–455 (2008). https://doi.org/10.1080/00018730802564254
16. S. Haroche, J.-M. Raimond, *Exploring the quantum: atoms, cavities, and photons* (Oxford University Press, 2006)
17. A. Sinatra, C. Lobo, Y. Castin, The truncated Wigner method for Bosecondensed gases: limits of validity and applications. J. Phys. B: At. Mol. Opt. Phys. **35**, 3599 (2002)
18. R.J. Lewis-Swan, M.K. Olsen, K.V. Kheruntsyan, Approximate particle number distribution from direct stochastic sampling of the Wigner function. Phys. Rev. A **94**, 033814 (2016). https://doi.org/10.1103/PhysRevA.94.033814
19. R. J. Lewis-Swan, *Ultracold atoms for foundational tests of quantum mechanics* (Springer, 2016)
20. C.S. Gerving, T.M. Hoang, B.J. Land, M. Anquez, C.D. Hamley, M.S. Chapman, Non-equilibrium dynamics of an unstable quantum pendulum explored in a spin-1 Bose-Einstein condensate. Nat. Commun. **3**, 1169 (2012). https://doi.org/10.1038/ncomms2179
21. A.J. Leggett, Bose-Einstein condensation in the alkali gases: some fundamental concepts. Rev. Mod. Phys. **73**, 307–356 (2001). https://doi.org/10.1103/RevModPhys.73.307
22. D. Pekker, C. Varma, Amplitude/Higgs modes in condensed matter physics. Ann. Rev. Condens. Matter Phys. **6**, 269–297 (2015). https://doi.org/10.1146/annurev-conmatphys-031214-014350
23. T.M. Hoang, H.M. Bharath, M.J. Boguslawski, M. Anquez, B.A. Robbins, M.S. Chapman, Adiabatic quenches and characterization of amplitude excitations in a continuous quantum phase transition. PNAS **113**, 9475–9479 (2016). https://doi.org/10.1073/pnas.1600267113
24. J.D. Sau, S.R. Leslie, M.L. Cohen, D.M. Stamper-Kurn, Spin squeezing of high-spin, spatially extended quantum fields. New J. Phys. **12**, 085011 (2010)
25. M. Kitagawa, M. Ueda, Squeezed spin states. Phys. Rev. A **47**, 5138 (1993)
26. D.J. Wineland, J.J. Bollinger, W.M. Itano, D.J. Heinzen, Squeezed atomic states and projection noise in spectroscopy. Phys. Rev. A **50**, 67–88 (1994). https://doi.org/10.1103/PhysRevA.50.67
27. K. Hammerer, A.S. Sørensen, E.S. Polzik, Quantum interface between light and atomic ensembles. Rev. Mod. Phys. **82**, 1041 (2010)
28. L. Pezzè, A. Smerzi, M.K. Oberthaler, R. Schmied, P. Treutlein, Non-lassical states of atomic ensembles: fundamentals and applications in quantum metrology (2016). arXiv:1609.01609
29. I.D. Leroux, M.H. Schleier-Smith, V. Vuletić, Implementation of cavity squeezing of a collective atomic spin. Phys. Rev. Lett. **104**, 073602 (2010)
30. M.H. Schleier-Smith, I.D. Leroux, V. Vuletić, Squeezing the collective spin of a dilute atomic ensemble by cavity feedback. Phys. Rev. A **81**, 021804 (2010)
31. C. Chin, R. Grimm, P. Julienne, E. Tiesinga, Feshbach resonances in ultracold gases. Rev. Mod. Phys. **82**, 1225–1286 (2010). https://doi.org/10.1103/RevModPhys.82.1225

32. C. Gross, T. Zibold, E. Nicklas, J. Esteve, M.K. Oberthaler, Nonlinear atom interferometer surpasses classical precision limit. Nature **464**, 1165–1169 (2010). https://doi.org/10.1038/nature08919
33. M.F. Riedel, P. Böhi, Y. Li, T.W. Hänsch, A. Sinatra, P. Treutlein, Atom-chipbased generation of entanglement for quantum metrology. Nature **464**, 1170–1173 (2010). https://doi.org/10.1038/nature08988
34. K.C. Cox, G.P. Greve, J.M. Weiner, J.K. Thompson, Deterministic squeezed states with collective measurements and feedback. Phys. Rev. Lett. **116**, 093602 (2016)
35. J. Appel, P.J. Windpassinger, D. Oblak, U.B. Hoff, N. Kjærgaard, E.S. Polzik, Mesoscopic atomic entanglement for precision measurements beyond the standard quantum limit. PNAS **106**, 10960–10965 (2009)
36. J.G. Bohnet, K.C. Cox, M.A. Norcia, J.M. Weiner, Z. Chen, J.K. Thompson, Reduced spin measurement back-action for a phase sensitivity ten times beyond the standard quantum limit. Nature **8**, 731–736 (2014)
37. Z. Chen, J.G. Bohnet, J.M. Weiner, K.C. Cox, J.K. Thompson, Cavity-aided nondemolition measurements for atom counting and spin squeezing. Phys. Rev. A **89**, 043837 (2014)
38. M.H. Schleier-Smith, I.D. Leroux, V. Vuletić, States of an ensemble of two-level atoms with reduced quantum uncertainty. Phys. Rev. Lett. **104**, 073604 (2010)
39. G. Colangelo, F.M. Ciurana, L.C. Bianchet, R.J. Sewell, M.W. Mitchell, Simultaneous tracking of spin angle and amplitude beyond classical limits. Nature **543**, 525–528 (2017)
40. O. Hosten, N.J. Engelsen, R. Krishnakumar, M.A. Kasevich, Measurement noise 100 times lower than the quantum-projection limit using entangled atoms. Nature (2016)
41. T. Zibold, E. Nicklas, C. Gross, M.K. Oberthaler, Classical bifurcation at the transition from Rabi to Josephson dynamics. Phys. Rev. Lett. **105**, 204101 (2010). https://doi.org/10.1103/PhysRevLett.105.204101
42. H. Strobel, W. Muessel, D. Linnemann, T. Zibold, D.B. Hume, L. Pezzé, A. Smerzi, M.K. Oberthaler, Fisher information and entanglement of non-Gaussian spin states. Science **345**, 424–427 (2014). https://doi.org/10.1126/science.1250147
43. W. Muessel, H. Strobel, D. Linnemann, T. Zibold, B. Juliá-Díaz, M.K. Oberthaler, Twist-and-turn spin squeezing in Bose-Einstein condensates. Phys. Rev. A **92**, 023603 (2015). https://doi.org/10.1103/PhysRevA.92.023603
44. Y. Liu, Z. Xu, G. Jin, L. You, Spin squeezing: transforming one-axis twisting into two-axis twisting. Phys. Rev. Lett. **107**, 013601 (2011)
45. J. Borregaard, E.D. Davis, G.S. Bentsen, M.H. Schleier-Smith, A.S. Sørensen, One- and two-axis squeezing of atomic ensembles in optical cavities (2017). arXiv:1706.01650
46. A.G. Araujo-Ferreira, R. Auccaise, R.S. Sarthour, I.S. Oliveira, T.J. Onagamba, I. Roditi, Classical bifurcation in a quadrupolar NMR system. Phys. Rev. A **87**, 053605 (2013). https://doi.org/10.1103/PhysRevA.87.053605
47. R. Auccaise, A.G. Araujo-Ferreira, R.S. Sarthour, I.S. Oliveira, T.J. Bonagamba, I. Roditi, Spin squeezing in a quadrupolar nuclei NMR system. Phys. Rev. Lett. **114**, 043604 (2015). https://doi.org/10.1103/PhysRevLett.114.043604
48. T.M. Hoang, M. Anquez, B.A. Robbins, X.Y. Yang, B.J. Land, C.D. Hamley, M.S. Chapman, Parametric excitation and squeezing in a many-body spinor condensate. Nat. Commun. **7**, 11233 (2016). https://doi.org/10.1038/ncomms11233

Part II
Concepts of Time Reversal Interferometry

Chapter 4
Spin Exchange as an Amplifier

In this chapter we describe how spin exchange can be employed as an amplifier. The nonlinear readout scheme is based upon such elementary amplification processes. In principle, one heavily populated spin component acts as a reservoir which enables the amplification of the two remaining. We detail which conditions have to be met in order to maintain and control the amplification process. Comprehensive control of both, the gain of the amplifier as well as the sign of the associated nonlinearity are crucial for realising the quantum-enhanced interferometry protocol.

First, we focus on the central approximation under which spin exchange transforms into the well-known Hamiltonian of parametric amplification. Being extensively studied especially in quantum optics we will draw on photonic analogues. Special attention is paid to the characteristic spin populations that arise during spin exchange. This description of spin exchange in terms of individual mode populations is connected to the complementary view of collective spins as developed in the previous section.

4.1 Undepleted Pump Approximation

The description of spin exchange in terms of collective spins is particularly enlightening as it uncovers the underlying rotational SU(2) symmetry. We will come back to this elegant representation at a later point. Now, we consider the spin exchange process in terms of the individual mode populations (Eq. 3.4): the Hamiltonian consists of three parts: the first, $\mathcal{H}_{\mathrm{SCC}}$ is responsible for the population transfer during the actual scattering process. This scattering is intrinsically connected to collisional shifts as embedded in $\mathcal{H}_{\mathrm{el}}$. Finally, exogenous energy shifts are described by $\mathcal{H}_q$.

D. Linnemann, *Quantum-Enhanced Sensing Based on Time Reversal of Entangling Interactions*, Springer Theses,
https://doi.org/10.1007/978-3-319-96008-1_4

If operated within the appropriate limits—which will be the subject of this section—the latter two contributions can be made to compensate each other. The ensuing dynamics is then fully governed by

$$\mathcal{H}_{\mathrm{SCC}} = \hbar g\, \hat{a}_0 \hat{a}_0 \hat{a}_\uparrow^\dagger \hat{a}_\downarrow^\dagger + \mathrm{h.c.} \tag{4.1}$$

As initial state we consider a large population residing in mode $|0\rangle$ and empty side modes. For sufficiently short evolution times only few atoms are scattered out of the largely populated pump mode. Then the undepleted pump approximation applies by which the operator $\hat{a}_0$ is approximated by a complex number, $\hat{a}_0 \to \sqrt{N_0}$ effectively treating the pump mode classically. The Hamiltonian $\mathcal{H}_{\mathrm{SCC}}$, from initially being quartic in mode operators then simplifies to the quadratic one describing parametric amplification,

$$\mathcal{H}_{\mathrm{PA}} = \hbar\kappa\, \hat{a}_\uparrow^\dagger \hat{a}_\downarrow^\dagger + \mathrm{h.c.} \tag{4.2}$$

Here $\kappa = gN_0$ quantifies the effective nonlinear coupling strength. It builds on the microscopic nonlinearity g and is enlarged by the number of pump atoms. Note, that a similar parameter proved already decisive in the mean-field treatment. In the undepleted pump approximation the pump mode merely provides an unlimited particle reservoir for parametric amplification of the side modes. In contrast to the mean-field approximation, the two side modes are treated quantum mechanically.

The action of any Hamiltonian that is at most quadratic in mode operators can be captured by linear mode transformations [1, 2]. For the parametric amplification Hamiltonian (Eq. 4.2) they read

$$\begin{pmatrix} a_\uparrow \\ a_\downarrow^\dagger \end{pmatrix} \to \begin{pmatrix} \cosh\kappa t & \sinh\kappa t \\ \sinh\kappa t & \cosh\kappa t \end{pmatrix} \begin{pmatrix} a_\uparrow \\ a_\downarrow^\dagger \end{pmatrix} \tag{4.3}$$

where t denotes the evolution time under spin exchange.

Parametric amplification in the quantum regime was first realized with photons and evolved quickly into an indispensable tool of quantum optics. First we give a short accounting of this process in the realm of quantum optics and detail how the emerging entangled state is characterized experimentally. The analogy between the atomic and photonic experiments will then be tightened by giving the appropriate formal limiting cases.

4.2 Parametric Amplification in Quantum Optics

Parametric amplification is the textbook example of a nonlinear process that generates an entangled state. Most prominently, it is realized in quantum optics by the process of parametric down conversion. Here, mediated by a nonlinear crystal a strong coherent

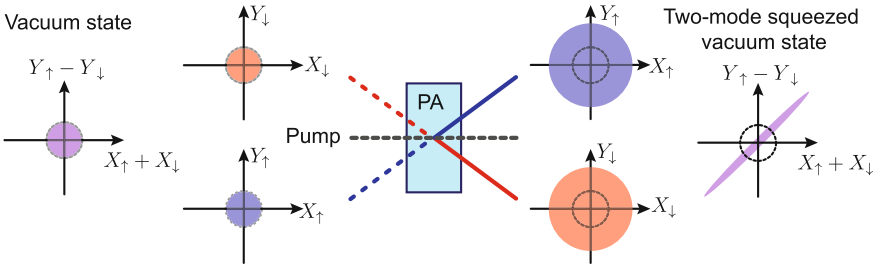

Fig. 4.1 Parametric amplification (PA) in quantum optics. By means of a nonlinear crystal photons of a strong pump beam are converted into signal and idler, respectively. Both of these modes are initially in the vacuum state (indicated by dashed circles), as shown by the quadrature diagrams (left). After parametric amplification (PA) both modes show excess fluctuations (right). The quantum mechanical correlations generated in the pairwise process show up in the two-mode quadratures as indicated in purple: a (vacuum) squeezed state emerges

pump beam is converted into signal and idler beam. The resulting state, called two-mode squeezed vacuum, is the archetype of continuous variable entanglement.

In quantum optics a mode is usually characterized by its quadratures, e.g. $X_\uparrow = (\hat{a}_\uparrow + \hat{a}_\uparrow^\dagger)/\sqrt{2}$ and $Y_\uparrow = (\hat{a}_\uparrow^\dagger - \hat{a}_\uparrow)\mathrm{i}/\sqrt{2}$ and similarly for mode $|\downarrow\rangle$. They fulfil the commutator relation $[X_\uparrow, Y_\uparrow] = \mathrm{i}$ and therefore have to satisfy a mutual uncertainty bound. This so-called vacuum noise limit is shown as a dashed circle in Fig. 4.1 which illustrates the characteristics of parametric amplification in the space of these quadratures drawn in blue and red, respectively. Measurements of the quadratures are a routine task which involve a technique dubbed balanced homodyne detection: here the mode in question is overlapped with a strong coherent light field at a beam splitter. Measuring the light intensity at both exit ports before subtracting them gives $I \propto \mathrm{e}^{\mathrm{i}\phi}\hat{a}_\uparrow + \mathrm{e}^{-\mathrm{i}\phi}\hat{a}_\uparrow^\dagger$. By scanning the phase ϕ of the coherent light field both quadratures $X_\uparrow$ and $Y_\uparrow$ can successively be measured. The two-mode squeezed vacuum state is characterized by $\langle X_\uparrow \rangle = \langle Y_\uparrow \rangle = 0$ from which the vacuum part in its name derives. However, although the mean quadratures vanish for both modes they exhibit excess fluctuations, which is shown in Fig. 4.1. The quadrature's variance is connected to the number of photons in that particular mode $(\Delta X_\uparrow)^2 = \langle N_\uparrow \rangle + 1/2$.

Due to the pairwise generation process, the large fluctuations of each mode are strongly correlated. This is witnessed by the so-called two-mode quadratures which are the sum and difference of the single mode quadratures, $\sqrt{2}X = X_\uparrow + X_\downarrow$, and $\sqrt{2}Y = Y_\uparrow - Y_\downarrow$. These two-mode quadratures satisfy a similar uncertainty relation, $[X, Y] = \mathrm{i}$ (dashed circle). The squeezed and enlarged fluctuations become visible only in the space of these two-mode quadratures as indicated in purple. The fact that a heavily fluctuating mode becomes quiet by adding another heavily fluctuating mode is the hallmark of entanglement. That is: entropy is reduced by taking into account an additional system.

In this context, the substitution of Eq. 2.5 introduced merely as a shorthand is well known in quantum optics and provides an alternative practical path to achieving two-mode squeezing. To see this, we rewrite the time evolution for parametric amplification in terms of these operators. One can show that the following identity holds [3],

$$\mathrm{e}^{-\mathrm{i}\mathcal{H}_{\mathrm{PA}}t/\hbar} = \mathrm{e}^{\mathrm{i}\frac{\kappa}{2}\left(s_+^{\dagger 2} - s_+^2\right)} \mathrm{e}^{-\mathrm{i}\frac{\kappa}{2}\left(s_-^{\dagger 2} - s_-^2\right)}. \tag{4.4}$$

The two *separate* exponentials on the right hand side describe single-mode squeezing of the modes $\hat{s}_-$ and $\hat{s}_+$, respectively. The operation of obtaining these modes in terms of the fundamental modes ($\hat{a}_\uparrow$ and $\hat{a}_\downarrow$) can be achieved by a beam splitter. Therefore, the two-mode squeezed vacuum state can also be generated by superimposing two single-mode squeezed states at a beam splitter. Indeed, this technique is used to generate the highest reported amount of optical squeezing (15 dB [4]).

Besides the generation of entangled states within the continuous-variable limit [5], the pairwise nature is routinely exploited for heralded single photon sources [6]. Similarly, using a cascade of down-conversion stages, heralded photon-pair sources can be realized. This technique is also employed to generate entangled photon pairs in one of the maximally entangled Bell states, which are the resource of digital quantum computation [7, 8]. For these applications the parametric down-conversion is operated in a regime for which the probability of creating twin-Fock states with populations exceeding a single pair of photons can be neglected.

4.3 Optical Phase Matching and Atomic Resonance Condition

For parametric down-conversion in optics care has to be taken to ensure the spatial overlap of the pump mode with the signal and idler beam, respectively. Above all, a fixed phase relation between these three beams has to be maintained, the so-called phase matching condition [9]. However, the emerging signal and idler beams typically have different frequency or polarizations. Due to dispersion and birefringence, respectively, the locked phase relation of these two beams with respect to the pump beam will eventually be lost.

An analogous situation is encountered in the atomic case where energy detunings of the three levels yield phase mismatches: the atomic Hamiltonian contains additional terms besides the sought-after parametric amplification part. Most importantly, these other parts include collisional energy shifts which depend on the exact partition of atoms among the three levels, as described by

$$\mathcal{H}_{\mathrm{el}} = \hbar g(N_0 - 1/2)(N_\uparrow + N_\downarrow). \tag{4.5}$$

As atoms are dynamically scattered from the pump into the side modes, these energy shifts become time dependent. In optical terms, such collisional shifts would corresponds to Kerr nonlinearities. For sufficiently short evolution times these energy shifts can approximately be compensated [10]. For this the collisional shifts have to match the external detuning

$$\mathcal{H}_q = -\hbar q(N_\uparrow + N_\downarrow). \tag{4.6}$$

Such a cancellation requires $q = g(N_0 - 1/2) \approx gN_0$ since the pump mode is largely occupied. When collisional shifts and external detuning exactly cancel each other, the energy difference driving spinor phase rotations vanishes. Therefore the spinor phase remains stable which corresponds to the phase matching condition in quantum optics. Referring to the classical phase space in terms of collective spins this situation corresponds to the separatrix having perpendicular branches.

4.4 Correspondence Between Atomic Spin Squeezing and Optical Two-Mode Squeezing

Within the undepleted pump approximation, the spin squeezing experienced in the space of $\hat{F}_x$, $\hat{F}_y$, and $\hat{F}_z$ (and, identically, also in the other alignment operators belonging to $\hat{\boldsymbol{G}}$) is equivalent to the two-mode squeezing encountered in quantum optics [11]. Indeed the curvature of the Bloch sphere describing the spin $\hat{\boldsymbol{F}}$ is inversely proportional to the number of atoms which compose this collective spin in the first place. Thus for a sufficiently large total atom number the phase space can be approximated to be locally flat, which is shown in Fig. 4.2. Furthermore, since only few atoms are scattered out of the pump mode only a small area of the surrounding phase space is explored.

Within this locally flat phase space the spin operators transform to $\hat{F}_x \to \sqrt{N_0}(s + s^\dagger)$ and $\hat{F}_y \to \sqrt{N_0}(s - s^\dagger)$, respectively. Formally, this substitution of $\hat{a}_0$ by a complex number can also be understood by truncating the Holstein-Primakoff transformation to first order. Then the spin operators $\hat{F}_x \propto X = X_\uparrow + X_\downarrow$ and $\hat{F}_y \propto Y = Y_\uparrow - Y_\downarrow$ directly transform into the two-mode quadrature operators from quantum optics. This analogy is shown in Fig. 4.2 panels (a) and (b). Within the undepleted pump approximation the squeezing observed in the spin corresponds to the mode populations shown in the histograms of panel (c). These distinctive mode populations are the subject of the next section.

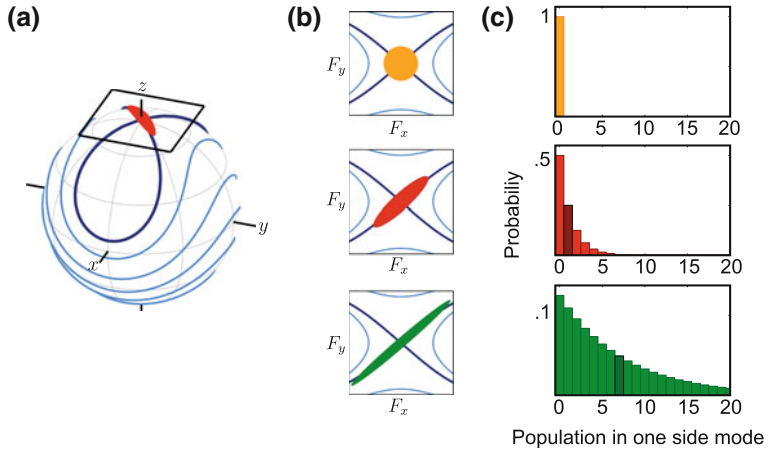

Fig. 4.2 Undepleted pump approximation. **a** For a largely populated pump mode which is only weakly depleted, the sphere can locally be approximated to be flat. Under this assumption spin exchange generates the two-mode squeezed vacuum state shown in **b** The space spanned by F_x and F_y corresponds to the two-mode quadratures in quantum optics. The uncorrelated initial state is isotropic (gold) which corresponds to a pure $m = 0$ population without any excitations of the side modes $m = \pm 1$. The side mode population is shown in the histograms of panel **c** As correlations build up the state is squeezed which is accompanied by a rising population of the side modes. This side mode population follows a thermal distribution with a distinctive slowly decaying power-law tail. The average side mode population is indicated by the dark coloured bin in the respective histogram

4.5 Population Statistics Generated by Parametric Amplification

In this section we discuss the process of parametric amplification in terms of mode populations. The squeezing observed in the space of spins is directly related to these populations of the two side modes. On the Bloch sphere, the mode populations of the two-mode squeezed vacuum correspond to the state's projection along the z-axis. However, we note that this direct relationship holds only if the coherences $\left\langle \hat{a}_\uparrow^\dagger \hat{a}_\downarrow \right\rangle$ vanish, which is fulfilled by the two-mode squeezed vacuum state. Then, the squeezed fluctuations exhibited in the space of $\hat{F}_x$ and $\hat{F}_y$ translate in orthogonal direction into atom number populations and their corresponding variances – these quantities are the main observable for the experiments described in this thesis.

Generally, spin squeezing requires excitations of particle pairs. Within the parametric amplification approximation, the average side mode population grows nonlinearly according to

$$\left\langle N_\uparrow \right\rangle = \left\langle N_\downarrow \right\rangle = \sinh^2(\kappa t) \tag{4.7}$$

when the states $|\uparrow\rangle$ and $|\downarrow\rangle$ are both empty initially. This nonlinear growth of the side mode population is accompanied by large fluctuations. The underlying atom number

distributions are shown in Fig. 4.2c. In these histograms, the corresponding average value is indicated by the dark coloured bin. Evidently, the distribution is not centred symmetrically at this average value and extends far into large atom numbers.

Due to the pairwise scattering into the side modes their emerging state can be expressed by $\sum_{n=0}^{\infty} \sqrt{p_n}\,|n\rangle_\uparrow\,|n\rangle_\downarrow$, i.e. a coherent sum of twin-Fock states. Within the undepleted pump approximation, the weights take the form of a thermal-like distribution $p_n = (1-\mathrm{e}^{-\beta})\mathrm{e}^{n\beta}$ in which β^{-1} stands for an effective temperature given by $\mathrm{e}^{-\beta} = \tanh^2(\kappa t)$. Expressed in terms of average mode populations these weights read $p_n = \langle N_\uparrow\rangle^n/(1+\langle N_\uparrow\rangle)^{n+1}$. These distributions are drawn in Fig. 4.2c: as characteristic for a thermal state, the vacuum state has the highest weight while a characteristically skewed distribution with a slowly decaying wing towards high atom number populations arises. Often the two-mode squeezed vacuum state is written as

$$\frac{1}{\cosh(\kappa t)}\sum_{n=0}^{\infty}\tanh^n(\kappa t)\,|n\rangle_\uparrow\,|n\rangle_\downarrow \tag{4.8}$$

for which the thermal weights are reexpressed as $\sqrt{p_n} = \tanh^n(\kappa t)/\cosh(\kappa t)$.

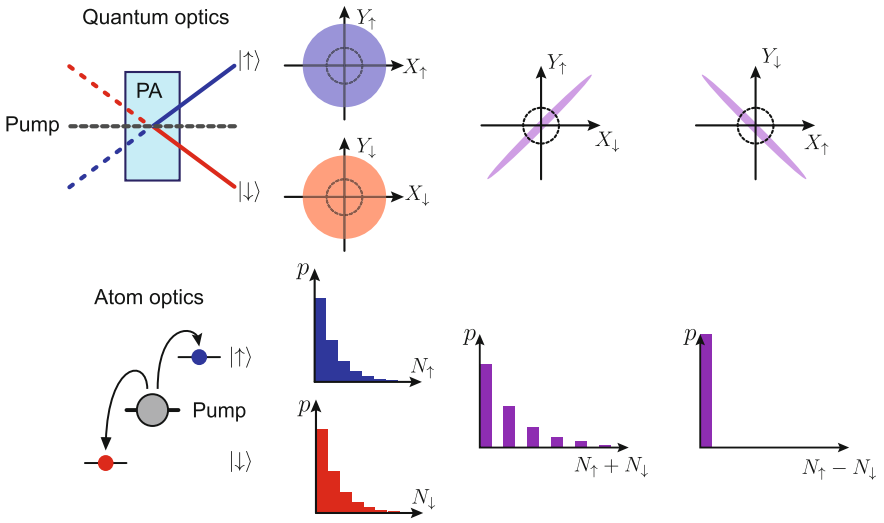

Fig. 4.3 Parametric amplification in quantum and atom optics. In quantum optics the process of parametric amplification is usually analysed in the space of quadratures. The individual modes $|\uparrow\rangle$ (blue) and $|\downarrow\rangle$ (red) exhibit excess thermal-like fluctuations (vacuum noise indicated as dashed line). The fluctuations are squeezed in the space of the two-mode quadratures (purple). Spin exchange furnishes an atom optics analogue. In this thesis we investigate this nonlinear process and the resulting state by measuring the spin populations. These individual spin populations show thermal-like fluctuations as witnessed by the broad and characteristically skewed histograms (red, blue). The strong correlations become apparent when considering the sum and difference spin populations shown in purple, respectively

As a result of the thermal-like distribution, the variance of each mode exhibits super-Poissonian fluctuations given by $(\Delta N_\uparrow)^2 = \langle N_\uparrow \rangle (\langle N_\uparrow \rangle + 1)$. This follows directly from noticing that Eq. 4.8 has the form of a Schmidt decomposition. Tracing out one mode leaves the other in the mixed state describing a thermal state, i.e. $\sum_n p_n |n\rangle \langle n|$. Thermal states have the largest possible entropy for a given mean population, yielding the characteristic variance stated above [3, 12]. In this sense, the two-mode squeezed vacuum state can be considered the purification of a thermal state. This thermal-like population of each side mode is a distinguishing feature of the two-mode squeezed vacuum state, as shown in Fig. 4.2c. Figure 4.3 shows the juxtaposition of parametric amplification investigated either in the space of quadratures (top) or via mode populations (bottom). The analogy between parametric down-conversion and spin exchange is shown additionally.

4.6 Amplification of Vacuum Fluctuations

Performing parametric amplification with initially empty side modes can be understood as amplifying vacuum fluctuations [13, 14]. When constructing the Heisenberg equations of motion for the side modes, e.g. $\hat{a}_\uparrow$, one arrives at the differential equation $\frac{\mathrm{d}}{\mathrm{d}t}\hat{a}_\uparrow \propto \hat{a}_\downarrow$. Therefore when starting with empty modes this process cannot grow in a purely classical framework. Instead, quantum mechanical fluctuations are necessary to trigger the amplification process initially [15]. In the Mexican-hat potential of Fig. 3.6, this situation corresponds to the classically unstable fixed point at $\hat{\boldsymbol{S}} = 0$. This analogy also elucidates that the quantum mechanical fluctuations which are the incentive for amplification are due to atomic projection noise of all atoms. As the name suggests, the fluctuations are due to the inherent quantum mechanical fluctuations that trace back to commutators being equal to $\hbar \neq 0$. In the atomic case, the size of these fluctuations corresponds to the effective Planck constant $\hbar_{\mathrm{eff}} = \sqrt{2/N}$.

Rather than being triggered by the quantum fluctuations, spin exchange can also be initiated by any initial population of the side modes [10]. This can most easily be seen by resorting to the input-output mode transformations, Eq. 4.3. The atom number in the side modes is given by $\langle N_\uparrow^{\mathrm{out}} \rangle = \cosh^2(\kappa t)\langle N_\downarrow^{\mathrm{in}} \rangle + \sinh^2(\kappa t)(\langle N_\uparrow^{\mathrm{in}} \rangle + 1)$ and similarly for the other mode. Here, $\langle N_\uparrow^{\mathrm{in}} \rangle$ corresponds to the average atom number in state $|\uparrow\rangle$ before parametric amplification took place with a similar definition for $|\downarrow\rangle$. The terms proportional to $\cosh^2(\kappa t)$ describe processes due to Bose stimulated emission while the $\sinh^2(\kappa t)$ part is the spontaneous contribution. In a symmetric situation, where both side modes are initially populated by $\langle N_\uparrow^{\mathrm{in}} \rangle = \langle N_\downarrow^{\mathrm{in}} \rangle = \langle N_+^{\mathrm{in}} \rangle /2$ the ensuing population growth during parametric amplification is described by

$$\langle N_+^{\mathrm{out}} \rangle = \langle N_+^{\mathrm{in}} \rangle + 2(1 + \langle N_+^{\mathrm{in}} \rangle) \sinh^2(\kappa t). \tag{4.9}$$

If the spin dynamics are triggered by such a classical seed ($\langle N_+^{\mathrm{in}} \rangle \neq 0$) rather than the spontaneous quantum mechanical fluctuations the spin exchange process is sped up.

4.7 Tailorable Hamiltonian

The mechanism of parametric amplification allows for substantial experimental control. Manipulations over the nonlinear dynamics can be achieved by solely affecting the pump mode. Since this mode is classically populated its control in terms of technical feasibility is routine. This exploits the fact that the pump mode defines the effective nonlinear coupling strength.

Magnitude of the Nonlinear Coupling

The magnitude of the effective nonlinear coupling strength $\kappa = gN_0$ can be adjusted by changing the number of pump atoms. In particular, the pump atoms can rapidly be transferred to an ancilla state which does not participate in the nonlinear process. This shelving technique allows quickly interrupting the nonlinear dynamics. A subsequent transfer back reinitiates the nonlinear dynamics.

Additionally, controlled phase imprints onto the pump mode allow to change the relative phase between the two constituent Hamiltonian terms $\hat{a}_\uparrow^\dagger \hat{a}_\downarrow^\dagger$ and $\hat{a}_\uparrow \hat{a}_\downarrow$. This phase regulates whether the side mode population is magnified or degraded in an ensuing period of parametric amplification. This phase imprint therefore gives experimental access to time reversal.

Time Reversal

As time and energy are intimately connected, time reversal is equivalent to evolution under an inverted Hamiltonian. This notion of time reversal is particularly evident when examining the quantum mechanical time evolution operator, $\mathrm{e}^{-\mathrm{i}\mathcal{H}t/\hbar}$. Therefore to experimentally realize a time reversal sequence, a system's energy spectrum has to be inverted. Inversion of the parametric amplification's nonlinear coupling strength has this effect. To maintain spin exchange the resonance condition has to be met such that the spinor phase remains locked [16]. Non-adiabatically changing this phase inverts the nonlinear coupling strength such that a subsequent period of spin exchange reverses the effect of the first. For this a controlled phase of $\varphi = \pi$ has to be imprinted such that $\kappa \to \mathrm{e}^{\mathrm{i}\varphi}\kappa = -\kappa$. This method inverts the sign of $\mathcal{H}_{\mathrm{PA}}$. In fact, this can most easily be seen from the complete spin exchange Hamiltonian which reads

$$\mathcal{H}_{\mathrm{SCC}} = \hbar g\, \hat{a}_0 \hat{a}_0 \hat{a}_\uparrow^\dagger \hat{a}_\downarrow^\dagger + \mathrm{h.c.} \tag{4.10}$$

Phase changes can be captured by modifying the individual mode operators in the following manner, $\hat{a}_\uparrow \to \hat{a}_\uparrow \mathrm{e}^{\mathrm{i}\varphi_\uparrow}$ and similarly for the remaining two modes. Evidently, to invert the entire Hamiltonian the decisive phase is $2\varphi_0 - \varphi_\uparrow - \varphi_\downarrow$ which amounts to the spinor phase. If the phase of the side modes remains unchanged, the phase of the pump mode gives control over the sign of κ. This mechanism can be extended to cover an interferometer which measures a phase imprint onto the side modes: by determining the pump phase φ_0 for which time reversal is achieved the phase $\varphi_\uparrow + \varphi_\downarrow$ can be inferred. We detail this interferometer scheme in the next section.

It might seem that the undepleted pump approximation merely guarantees the generation of the two-mode squeezed vacuum state but is not imperative for achieving

time reversal. This, however, is not the case. The reason being that the collisional shifts are unaffected by such phase imprints. Therefore, the method is limited to the undepleted pump regime in which cancellation of the collisional shifts is achieved.

The work presented in this thesis builds on this approximate time reversal. In the outlook we present a different approach of achieving time reversal by inverting the microscopic nonlinear coupling strength g. In contrast to the aforementioned method of changing the effective coupling via phase imprints, this extended time reversal does not rely on the undepleted pump approximation.

4.8 Interferometry Based on Time Reversal

The time reversal sequence achieved for a spinor phase imprint of π can be extended to cover a full interferometer. For this we consider the case of intermediate phase imprints between $\varphi = 0$ (which corresponds to forward time propagation) and π (backward time propagation). This is the essence of the so-called SU(1,1) interferometer. It was first proposed in the field of quantum optics [17]. Figure 4.4 shows the optical setup of such an interferometer. The atom optics analogy using spin exchange for parametric amplification is shown underneath [18]. At the interrogation stage, the energy mismatch ΔE is measured by its effect onto the spinor phase. Before we treat this interferometry concept in a more formal manner in Chap. 5, we visualize the working principle in the classical phase space.

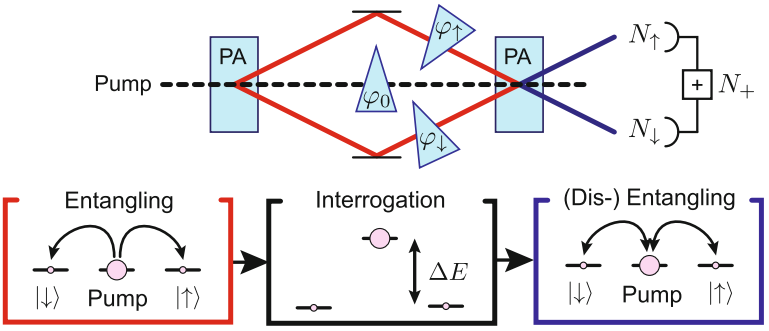

Fig. 4.4 Interferometry based on (dis-) entangling nonlinear dynamics. The interferometry scheme involves two cascaded periods of parametric amplification (PA), matched in length, with phase interrogation in between. The above cartoon shows an implementation in quantum optics. The analogue realization using spin exchange is shown underneath. Here, a first period under spin exchange generates the entangled state which is subsequently used to interrogate an energy mismatch ΔE. This energy mismatch corresponds to a spinor phase imprint which controls the action of the subsequent spin exchange. For an accumulated spinor phase of π the final period of spin exchange is time reversed and disentangles the probe state. Instead, for phases close to 2π the state gets further amplified. The readout is given by N_+

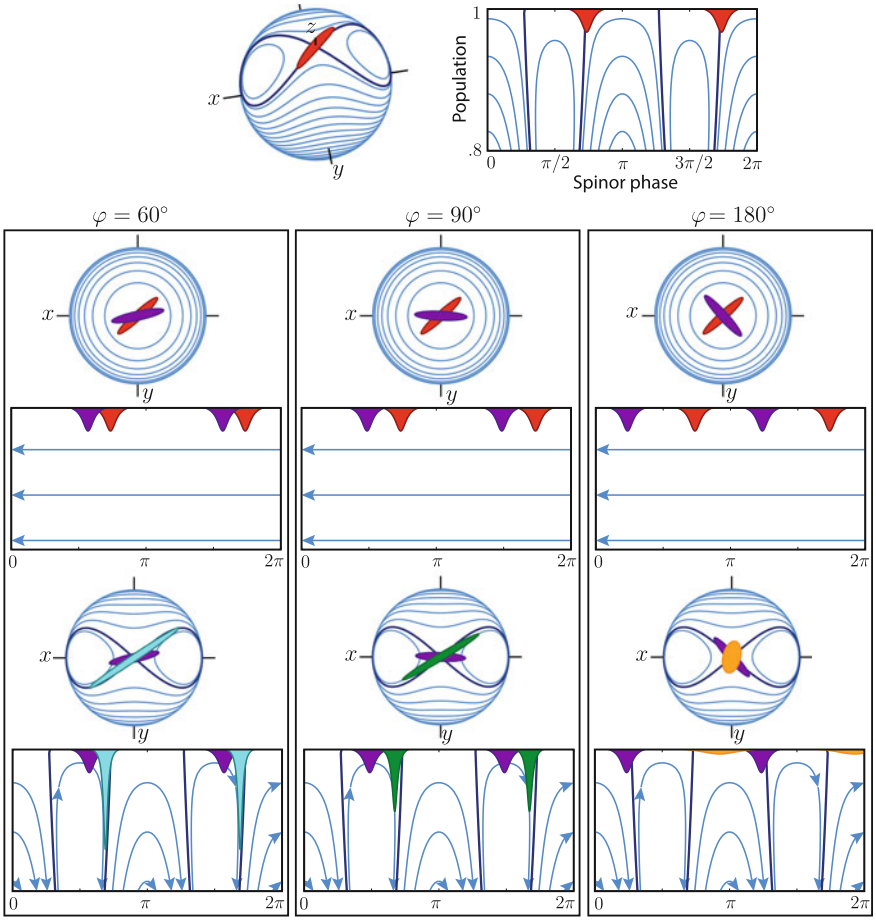

Fig. 4.5 Disentangling time reversal sequence in phase space. During a first period of spin exchange (not shown) an entangled two-mode squeezed vacuum state arises (top). The z-projection of the Bloch sphere reflects the side mode population. The state's projection onto this axis is shown together with the classical phase space (top right). Starting from this state, the ensuing spin exchange dynamics is shown in the triptychon-like lower panels for three different spinor phase imprints, $\varphi = 60°$, $\varphi = 90°$, and $\varphi = 180°$. This phase imprint is implemented by varying the holding time at a large spin exchange detuning $q \gg \kappa$. The phase space during this phase imprinting period is that of a pure rotation about the z-axis (Bloch sphere and classical phase space shown). Depending on the state's rotation, a second period of spin exchange squeezes further or unsqueezes the state. This process can be understood intuitively by following the trajectories of the underlying phase space, in particular the converging and diverging manifold of the separatrix shown in bold. The squeezing is reflected in the side mode population which is shown in the lower cylindrical phase space. For details see main text

Phase Space Illustration of the Interferometry Concept

Here, we provide an intuitive illustration of the interferometry scheme by resorting to the classical phase space [19]. The key steps are depicted in Fig. 4.5. At the top the initial two-mode squeezed vacuum state is shown on the Bloch sphere of $\boldsymbol{F}$. Measurements of the side mode population correspond to the state's projection along the z-axis. Therefore, a zoom-in into the cylindrical classical phase space that shows this projection is depicted additionally. Below, the three panels show the ensuing dynamics for three different spinor phase imprints.

On the left, a rotation of 60° is applied. For this the dynamical phase building up under a dominating spin exchange detuning $q \gg gN$ can be harnessed. At this stage, the classical phase space is that of a pure rotation about the z-axis. After this phase imprint (purple), spin exchange is performed that squeezes the state further and realigns it slightly towards the diverging manifold of the separatrix. The resulting state is shown in blue. Its side mode population is increased compared to the initial state as shown in the lowest phase space portrait. A phase imprint of 180° is shown in the outermost right panel. Here, the state after rotation (purple) is oriented almost perfectly with the converging manifold of the separatrix. Therefore, during the second period of spin exchange the state is unsqueezed (orange). Although a precise phase imprint of 180° has been applied this reversal back to an isotropic uncorrelated state is nonideal. This comes about because the classical phase space is shown for the experimentally extracted parameters which are $q \approx 1.1gN$. Thus, the angle enclosed by the separatrix is slightly smaller than 90° as exemplified in the classical phase space portraits of Fig. 3.1. In this setting, ideal time reversal is indeed reached at a slightly smaller phase imprint. Nonetheless, the side mode population of the resulting state is strongly reduced. The panel in the middle shows an intermediate phase imprint of 90°. Here, the state after rotation (purple) is aligned almost symmetrically between the diverging and converging manifold of the separatrix. Still, the subsequent spin exchange dynamics squeezes the state further (green) and the side mode population is enlarged. This exemplifies the intrinsic amplification of the nonlinear readout. In the next section we complement this illustrative description with a quantitative and more formal treatment. It is based on the so-called SU(1,1) framework.

References

1. S.L. Braunstein, P. van Loock, Quantum information with continuous variables. Rev. Mod. Phys. **77**, 513–577 (2005), https://doi.org/10.1103/RevModPhys.77.513
2. C. Weedbrook, S. Pirandola, R. García-Patrón, N.J. Cerf, T.C. Ralph, J.H. Shapiro, S. Lloyd, Gaussian quantum information. Rev. Mod. Phys. **84**, 621–669 (2012), https://doi.org/10.1103/RevModPhys.84.621
3. G. Agarwal, *Quantum Optics*, Quantum Optics (Cambridge University Press, 2012)
4. H. Vahlbruch, M. Mehmet, K. Danzmann, R. Schnabel, Detection of 15 dB squeezed states of light and their application for the absolute calibration of photoelectric quantum efficiency. Phys. Rev. Lett. **117**, 110801 (2016), https://doi.org/10.1103/PhysRevLett.117.110801

5. U.L. Andersen, J.S. Neergaard-Nielsen, P. van Loock, A. Furusawa, Hybrid discrete- and continuous-variable quantum information. Nat. Phys. **11**, 713–719 (2015). https://doi.org/10.1038/nphys3410
6. M.D. Eisaman, J. Fan, A. Migdall, S.V. Polyakov, Single-photon sources and detectors. Rev. Sci. Instrum. **82**, 071101 (2011), https://doi.org/10.1063/1.3610677
7. P. Kok, W.J. Munro, K. Nemoto, T.C. Ralph, J.P. Dowling, G.J. Milburn, Linear optical quantum computing with photonic qubits. Rev. Mod. Phys. **79**, 135–174 (2007), https://doi.org/10.1103/RevModPhys.79.135
8. J.L. O'Brien, A. Furusawa, J. Vuckovic, Photonic quantum technologies. Nat. Photon **3**, 687–695 (2009). https://doi.org/10.1038/nphoton.2009.229
9. W. Nagourney, *Quantum Electronics for Atomic Physics and Telecommunication* (Oxford University Press, 2014)
10. R.J. Lewis-Swan, K.V. Kheruntsyan, Sensitivity to thermal noise of atomic Einstein-Podolsky-Rosen entanglement. Phys. Rev. A **87**, 063635 (2013), https://doi.org/10.1103/PhysRevA.87.063635
11. L. Pezzè, A. Smerzi, M.K. Oberthaler, R. Schmied, P. Treutlein, Non-lassical states of atomic ensembles: fundamentals and applications in quantum metrology. arXiv:1609.01609 (2016)
12. U. Leonhardt, *Essential Quantum Optics: From Quantum Measurements to Black Holes* (Cambridge University Press, 2010)
13. S.R. Leslie, J. Guzman, M. Vengalattore, J.D. Sau, M.L. Cohen, D.M. Stamper-Kurn, Amplification of fluctuations in a spinor Bose-Einstein condensate. Phys. Rev. A **79**, 043631 (2009), https://doi.org/10.1103/PhysRevA.79.043631
14. C. Klempt, O. Topic, G. Gebreyesus, M. Scherer, T. Henninger, P. Hyllus, W. Ertmer, L. Santos, J.J. Arlt, Parametric amplification of vacuum fluctuations in a spinor condensate. Phys. Rev. Lett. **104**, 195303 (2010), https://doi.org/10.1103/PhysRevLett.104.195303
15. P.D. Nation, J.R. Johansson, M.P. Blencowe, F. Nori, Colloquium: Stimulating uncertainty: Amplifying the quantum vacuum with superconducting circuits. Rev. Mod. Phys. **84**, 1–24 (2012), https://doi.org/10.1103/RevModPhys.84.1
16. T. Zibold, V. Corre, C. Frapolli, A. Invernizzi, J. Dalibard, F. Gerbier, Spinnematic order in antiferromagnetic spinor condensates. Phys. Rev. A **93**, 023614 (2016), https://doi.org/10.1103/PhysRevA.93.023614
17. B. Yurke, S.L. McCall, J.R. Klauder, SU(2) and SU(1,1) interferometers. Phys. Rev. A **33**, 4033 (1986), https://doi.org/10.1103/PhysRevA.33.4033
18. A.M. Marino, N.V. Corzo, Trejo, P.D. Lett, Effect of losses on the performance of an SU(1,1) interferometer. Phys. Rev. A **86**, 023844 (2012), https://doi.org/10.1103/PhysRevA.86.023844
19. T.M. Hoang, C.S. Gerving, B.J. Land, M. Anquez, C.D. Hamley, M.S. Chapman, Dynamic stabilization of a quantum many-body spin system. Phys. Rev. Lett. **111**, 090403 (2013), https://doi.org/10.1103/PhysRevLett.111.090403

Chapter 5
Interferometry Concept Within the SU(1,1) Framework

In this section we analyse the nonlinear time reversal sequence quantitatively. To this end we introduce operators belonging to the SU(1,1) group which are used to describe spin exchange. This somewhat more formal treatment allows us to compare the nonlinear interferometry sequence to routinely employed schemes like Ramsey's atom interferometry. While the latter constitutes a passive device, the nonlinear readout is active since spin exchange is employed for parametric amplification. The content of this chapter is published in reference [1].

5.1 SU(1,1) Operators

To describe the interferometric sequence we assume that the pump mode remains undepleted and introduce the following three operators [2] which act onto the side modes

$$\begin{aligned}\hat{K}_x &= \frac{1}{2}(\hat{a}_\uparrow^\dagger \hat{a}_\downarrow^\dagger + \hat{a}_\uparrow \hat{a}_\downarrow)\\ \hat{K}_y &= \frac{1}{2\mathrm{i}}(\hat{a}_\uparrow^\dagger \hat{a}_\downarrow^\dagger - \hat{a}_\uparrow \hat{a}_\downarrow)\\ \hat{K}_z &= \frac{1}{2}(\hat{a}_\uparrow^\dagger \hat{a}_\uparrow + \hat{a}_\downarrow^\dagger \hat{a}_\downarrow + 1) = \frac{1}{2}(\hat{N}_\uparrow + \hat{N}_\downarrow + 1).\end{aligned} \tag{5.1}$$

The operators $\hat{K}_x$ and $\hat{K}_y$ include terms for the coherent and pairwise creation and destruction of particle pairs. Therefore, they describe the coherences (anomalous moments) $\langle \hat{a}_\uparrow \hat{a}_\downarrow \rangle$ and $\left\langle \hat{a}_\uparrow^\dagger \hat{a}_\downarrow^\dagger \right\rangle$. The number of atoms shared in both modes is entailed in the operator $\hat{K}_z$. Note that while this latter component resembles $\hat{F}_z$ the other

D. Linnemann, *Quantum-Enhanced Sensing Based on Time Reversal of Entangling Interactions*, Springer Theses,
https://doi.org/10.1007/978-3-319-96008-1_5

operators are fundamentally different. In fact, the operators satisfy the defining commutation relations of the SU(1,1) group:

$$[\hat{K}_x, \hat{K}_y] = -\mathrm{i}\hat{K}_z, \qquad [\hat{K}_y, \hat{K}_z] = \mathrm{i}\hat{K}_x, \qquad [\hat{K}_z, \hat{K}_x] = \mathrm{i}\hat{K}_y. \tag{5.2}$$

Here, the minus sign in the first equation distinguishes them from the cyclic commutators of the SU(2) group. The SU(1,1) group has a conserved quantity which is given by $\hat{K}_{\mathrm{tot}}^2 = \hat{K}_z^2 - \hat{K}_x^2 - \hat{K}_y^2$. This quantity, known as Casimir invariant, is given by the atom number imbalance $N_\uparrow - N_\downarrow$. For vanishing magnetization, we have $\hat{K}_{\mathrm{tot}}^2 = 1/2$. In a geometrical interpretation, this equation defines a hyperbolic surface that is spanned by the three operators $\hat{K}_i$.

Therefore, we can visualize the states that satisfy the SU(1,1) algebra on the surface of a cone. Such a visualisation—which corresponds to the Bloch sphere representation of the spin operators—is shown in Fig. 5.1. Similar to Fig. 3.5 where simulated Wigner functions are shown on the associated Bloch spheres, here we plot similar Wigner functions onto the hyperbolic surfaces of SU(1,1). Panel (a) shows the vacuum state which is represented at the bottom of the cone, $\langle \hat{K}_z \rangle = \frac{1}{2}$, and has isotropic uncertainty in the x and y-direction (see projection underneath the cone). Starting from this state, the operators $\hat{K}_x$ and $\hat{K}_y$ generate boosts along the x and y-direction, respectively. Here, we use the term boost in analogy to special relativity, whose description in terms of rapidity and Minkowski space resembles the SU(1,1) description of parametric amplification [3–5]. This boost moves the initial vacuum state upwards on the surface of the cone as shown in panel (b). A highly anisotropic and elongated Wigner distribution arises. Its average value is indicated in red. The projection underneath shows that the initial state is spread out in x-direction. For the SU(1,1) description to be valid we assumed that the pump mode remains undepleted and furnishes an unlimited particle reservoir. Within this idealisation, the cone is not

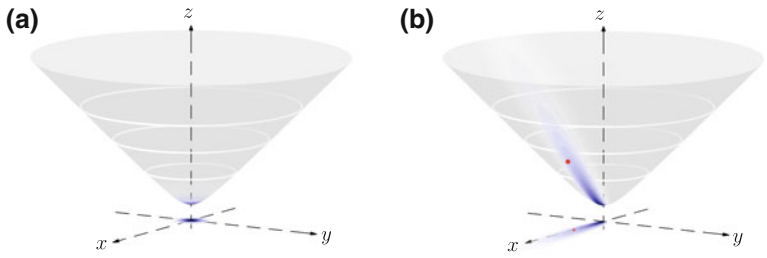

Fig. 5.1 Representation of parametric amplification on the SU(1,1) hyperbolic surface. **a** Simulated Wigner function of the initial state with empty side modes. The summed side mode population N_+ corresponds to the state's projection onto the z-axis. Consequently, the vacuum state is represented at the bottom of the cone. Its Wigner function extends isotropically in the projected space of $\hat{K}_x$ and $\hat{K}_y$ which is shown underneath the cone. Starting from this state parametric amplification is described by boosting the state along the x-direction. Panel **b** Shows the Wigner function of the resulting two-mode squeezed vacuum state. Its average value is indicated in red. The large extension in z-directions corresponds to the excess number fluctuations in N_+

terminated at some highest side mode population but remains open to the top. In this representation, the operator $\hat{K}_z$ generates rotations about the z-axis.

Interferometric Sequence

Within this framework the interferometric sequence is build up by two SU(1,1) boosts with a phase rotation in between. Such a scheme is shown in Fig. 5.2a. Additional to a sketch of an optical SU(1,1) interferometer the action of each of the elements is shown on a corresponding hyperbolic surface. From top to bottom, we start with empty side modes and only the pump mode (dashed) populated. During a first period of parametric amplification (PA) the side modes $|\uparrow\rangle$ and $|\downarrow\rangle$ get populated. On the hyperbolic surface this process is described by a state moving upwards on the cone. The atom number shared in both modes is given by $\hat{K}_z$. The trajectory's projection beneath the cone showcases that this is a boost along the x-direction. Subsequently, the side modes pass through an area of phase imprinting (grey dashed box). Here,

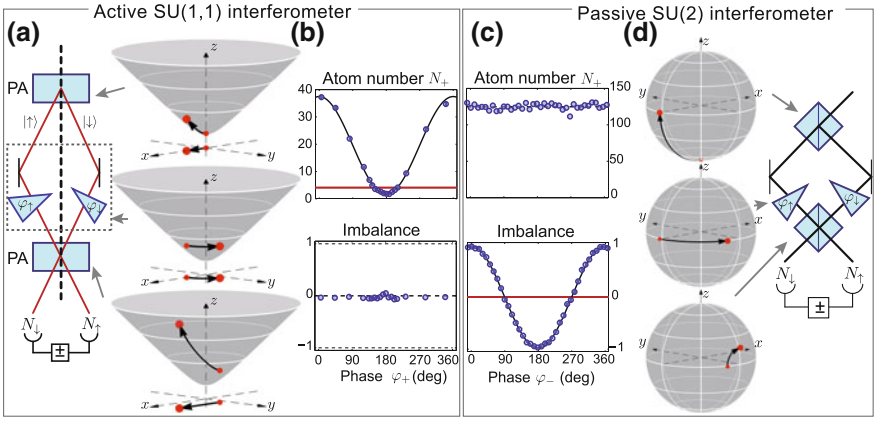

Fig. 5.2 Comparison of an active SU(1,1) interferometer to a passive one. **a** Schematic representation of an active interferometer in optics. The action of each component is described on an associated hyperbolic surface. From top to bottom, a first period of parametric amplification (PA) populates the initially empty side modes $|\uparrow\rangle$ and $|\downarrow\rangle$ (red). On the hyperbolic surface, this corresponds to a boost along the x-direction during which the initial vacuum state (small red pointer) located at the cone's bottom is displaced towards the top (large red pointer). Subsequently, both side modes pass an area of phase interrogation (grey dashed box). On the cone, such phase accumulation by $\varphi_+ = \varphi_\uparrow + \varphi_\downarrow$ is represented by a rotation about the z-axis. A final period of parametric amplification implements another boost along the x-direction. Hereby, the phase is mapped onto the average side mode population $\langle N_+ \rangle$ which corresponds to the state's projection along the z-axis. The resulting fringe is shown in panel (**b**). The horizontal red line denotes the probe state's average population. The atom number imbalance vanishes throughout all phase settings. **d** Schematic of a Mach-Zehnder interferometer representative of a passive SU(2) interferometer. From top to bottom the first beam splitter creates a phase sensitive superposition of both modes. On the Bloch sphere the beam splitter's action is described by a rotation about the y-axis. Subsequent phase interrogation of $\varphi_- = \varphi_\uparrow - \varphi_\downarrow$ is described by a rotation about the z-axis. The final beam splitter maps this differential phase onto the z-axis which corresponds to the atom number imbalance. The fringe is shown in panel (**c**). As a passive device the atom number N_+ remains constant

each side mode accumulates a phase $\varphi_\uparrow$ and $\varphi_\downarrow$, respectively. On the hyperbolic surface, this corresponds to a rotation about the z-axis by an angle of $\varphi_+ = \varphi_\uparrow + \varphi_\downarrow$. After phase accumulation the two side modes are parametrically amplified once more. This last pulse maps the accumulated phase onto a detectable atom number sum, i.e. different projections onto the z-axis. An interferometry fringe is obtained by measuring $\langle K_z \rangle$, i.e. the summed atom number of both side modes. The interferometry fringe is thus given by $\langle N_\uparrow + N_\downarrow \rangle \propto 1 + \cos(\varphi_+)$ which is shown in panel (c). For an accumulated phase of $\varphi_+ = \pi$ the two boosts act along diametrically opposite directions such that the second boost reverses the effect of the first. This corresponds to time reversal. Then the initial vacuum state is recovered at the output. In contrast for phase settings close to $\varphi_+ \approx 0$ the nonlinear character of two successive boosts along the same direction becomes visible: the state gets much further displaced than during the first nonlinear process. Therefore, the atom number detected at the fringe maximum is nonlinearly enhanced. This nonlinear amplification becomes striking when comparing the fringe height in panel c to the average side mode population after the first boost, that is within the interferometer which is shown as the red horizontal line. The atom number imbalance vanishes for all phase settings.

5.2 Comparison to Passive SU(2) Interferometers

Unquestionably, the most important technique for atom interferometry is Ramsey's method of separate oscillatory fields [6]. This can be considered the atomic analogue of an optical Mach-Zehnder interferometer. Archetypical for a passive two path interferometer it is best described in a SU(2) framework. We describe the interferometric sequence and put it into contrast to the SU(1,1) description of spin exchange interferometry.

Pseudospin Description

A passive two path interferometer can be described in terms of spin-1/2 operators. This is because every number conserving two state system can be mapped onto a (fictitious) spin-1/2 system as detailed in Chap. 2. We will resort to the operators of Eq. 2.1 to describe the interferometric sequence. In this pseudo-spin description, the atom number imbalance is given by $\hat{J}_z$. The coherences between both modes, i.e. $\left\langle a_\uparrow^\dagger a_\downarrow \right\rangle$ and $\left\langle a_\uparrow a_\downarrow^\dagger \right\rangle$, are described by $\hat{J}_x$ and $\hat{J}_y$, respectively. As a pseudo spin-1/2 the system can be illustrated on a Bloch sphere. For N indistinguishable Bosons the collective spin picture is adequate [7].

Interferometric Sequence

In Fig. 5.2d a Mach-Zehnder interferometer is depicted. Here the two paths $|\uparrow\rangle$ and $|\downarrow\rangle$ of the interferometer are identified with the north and south pole of the Bloch sphere, respectively. From top to bottom; starting in state $|\downarrow\rangle$ (south pole of Bloch sphere) a beam splitter populates both modes and creates a phase sensitive superposition. To

achieve highest phase sensitivity an equal superposition of $|\uparrow\rangle$ and $|\downarrow\rangle$ is desirable. On the Bloch sphere such a state is represented on the equator. The action of the beam splitter is akin to $\hat{J}_y$ and thus represented by a rotation of 90° about the y-axis on the Bloch sphere. In spin language such a rotation is called $\pi/2$ pulse. The following phase accumulation of both modes, $\varphi_\uparrow$ and $\varphi_\downarrow$, respectively is described by a rotation of the state about the z-axis. The angle of rotation is given by $\varphi_- = \varphi_\uparrow - \varphi_\downarrow$. Finally the phase difference between both modes is mapped onto the z-axis by the final beam splitter. By measuring the imbalance $2\langle \hat{J}_z \rangle / N = \langle N_\uparrow - N_\downarrow \rangle / N = \cos(\varphi_-)$ the accumulated phase difference φ_- can be inferred. As a passive device, the atom number sum remains constant (panel c). This ever-fixed atom number corresponds to the radius of the Bloch sphere.

5.3 Phase of the Coupling Mechanism

Interferometers compare the phase that is accumulated during the interrogation stage to a phase reference that is associated to the coupling mechanism. We explain this first for the passive interferometer: for the Ramsey interferometer beam splitting is often performed by microwave $\pi/2$ pulses. The prime example is the caesium-133 fountain clock whose hyperfine energy spacing of $2\pi \times 9.2\,\mathrm{GHz}$ acts as an international time standard. By changing the relative phase of the two Raman pulses with respect to each other Bloch sphere rotations about different axes are implemented. This allows for control of the interferometer's working point which can be adjusted independently of the interrogated phase. Then the first pulse defines the axis of rotation as no other phase reference is available. Let us choose the y-axis, that is the first rotation is performed by the action of $\hat{J}_y$. A subsequent non-adiabatic switching of the rf phase by φ_{ref} then amounts to the substitution $\hat{J}_y \to \cos\varphi_{\mathrm{ref}} \hat{J}_y + \sin\varphi_{\mathrm{ref}} \hat{J}_x$ for the subsequent rotation. Thereby rotations about any axis can be implemented. In particular, an interferometry fringe is obtained by scanning the relative phase of the coupling. To emphasize this connection, the output fringe is given by

$$\langle N_\uparrow - N_\downarrow \rangle \propto \cos(\varphi_{\mathrm{ref}} - \varphi_-) \tag{5.3}$$

which combines the phase accumulated during interrogation φ_- and the reference phase of the coupling φ_{ref}. This is a general statement: any interferometer compares the accumulated phase to the phase of the associated coupling mechanism. In particular, to realize an interferometric sequence at all the relative phase of the two successive pulses needs to be stable. For beam splitting using optical transitions this is challenging as slight variations of the light's wave front have large impacts.

For the nonlinear interferometer the pump atoms provide the common phase reference. Therefore, within the SU(1,1) framework phase changes of the pump mode can be used to implement boosts along different directions of the hyperbolic surface. When the first boosts acts along the x-direction (via the action of $\hat{K}_x$) a

nonadiabatic phase change of the pump mode corresponds to the substitution of $\hat{K}_x \rightarrow \cos\varphi_{\mathrm{ref}}\hat{K}_x + \sin\varphi_{\mathrm{ref}}\hat{K}_y$ for the second boost. Therefore, in a more complete picture the interferometry fringe is given in terms of

$$\left\langle N_\uparrow + N_\downarrow \right\rangle \propto 1 + \cos(\varphi_{\mathrm{ref}} - \varphi_+) \tag{5.4}$$

Since the reference phase is given by the pump phase, $\varphi_{\mathrm{ref}} = 2\varphi_0$ the complete phase dependence is given by the spinor phase $\varphi = 2\varphi_0 - \varphi_\uparrow - \varphi_\downarrow$ as expected from the previous considerations.

5.4 Hamiltonian in SU(1,1) Representation

Within the undepleted pump approximation the spin exchange Hamiltonian can be written in the form

$$\mathcal{H} = 2\hbar\kappa(\cos\varphi_{\mathrm{ref}}\hat{K}_x + \sin\varphi_{\mathrm{ref}}\hat{K}_y) + 2\hbar(\kappa - q)\hat{K}_z \tag{5.5}$$

using the SU(1,1) operators (Eq. 5.1) [2, 8]. Here, phase imprints onto the pump mode are included by φ_{ref} and decide whether a boost along the x- or y-direction is performed. With a phase reference missing, the first such pulse defines the phase relation for all subsequent pulses. When spin exchange resonance is achieved the last (detuning) term, $\propto \hat{K}_z$, vanishes and a pure boost without additional rotation is realized.

Note that the exemplary Wigner functions displayed in Fig. 5.1 are the result of a numerical simulation whose parameters match the experimentally extracted ones. While the experimental parameter characterization is the subject of a later chapter, here we remark that for $N = 400$ atoms the spin exchange detuning corresponds to $q = 1.1\kappa$. As a result the detuning term in the above equation is only partly compensated. In Fig. 5.1b this is witnessed by the slight rotation of the two-mode squeezed vacuum state away from the x-axis.

5.5 Coherent States of SU(1,1) and SU(2)

The two-mode squeezed vacuum state corresponds to the coherent state of the SU(1,1) theory. In general, coherent states are generated by applying linear combinations of the fundamental operators onto the energetically lowest lying state. In the SU(1,1) framework that is the action of the $\hat{K}$ operators acting onto vacuum. The coherent states are thus given by $|r,\varphi\rangle = \mathrm{e}^{-\mathrm{i}\varphi\hat{K}_z}\mathrm{e}^{-\mathrm{i}r\hat{K}_x}\,|0\rangle_\uparrow\,|0\rangle_\downarrow$. In terms of twin-Fock states this amounts to

$$|r,\varphi\rangle = \frac{1}{\cosh(r)} \sum_{n=0}^{\infty} e^{in\varphi} \tanh^n(r) \, |n\rangle_\uparrow \, |n\rangle_\downarrow \, . \tag{5.6}$$

Here, r is the magnitude of the boost which is tantamount to the squeezing factor characterising the two-mode squeezed vacuum state. Comparing this to the previous definition Eq. 4.8 the phase dependence with respect to the spinor phase φ is now explicitly included.

The SU(2) coherent states are generated similarly by the action of the (collective) pseudo-spin operators onto the lowest lying state. Therefore, $|\theta,\varphi_L\rangle = \mathrm{e}^{-\mathrm{i}\varphi_L \hat{J}_z} \mathrm{e}^{-\mathrm{i}\theta \hat{J}_y} \, |0\rangle_\uparrow \, |N\rangle_\downarrow$. Here the notation using two angles introduced in Fig. 2.1 is used. For a collective spin, each of the N individual atoms is independently put into an identical superposition state, $|\theta,\varphi_L\rangle = (\cos\theta/2\,|\downarrow\rangle + \mathrm{e}^{\mathrm{i}\varphi_L} \sin\theta/2\,|\uparrow\rangle)^{\otimes N}$. Upon measuring, this independent distribution of N atoms among two states yields outcome statistics that are equal to a Bernoulli trial [9]. Such a state can be represented in Fock states,

$$|\theta,\varphi_L\rangle = \sum_{n=0}^{N} e^{\mathrm{i}n\varphi_L} \sqrt{\binom{N}{n} p^n (1-p)^{N-n}} \, |n\rangle_\uparrow \, |N-n\rangle_\downarrow \, . \tag{5.7}$$

Here, $p = (\cos\theta + 1)/2$ denotes the success probability, i.e. the probability for being in state $|\uparrow\rangle$.

While the coherent states of SU(1,1) are characterized by a fluctuating total atom number $(N_\uparrow + N_\downarrow)$, the magnetization $(N_\uparrow - N_\downarrow)$ is constant. In contrast, the coherent states of SU(2) feature binomial fluctuations in population imbalance (magnetization) but have constant total atom number. This contraposition as exemplified in panels (c) and (d) of Fig. 5.2 is crucial and connected to the state's phase sensitivity with respect to φ_+ and φ_-, respectively. We will continue this discussion on the basis of experimental data in Chap. 7. Before that we first present our experimental setup.

References

1. D. Linnemann, J. Schulz, W. Muessel, P. Kunkel, M. Prüfer, A. Frölian, H. Strobel, M.K. Oberthaler, Active SU(1,1) atom interferometry. Quantum Sci. Technol. **2**, 044009 (2017)
2. B. Yurke, S.L. McCall, J.R. Klauder, SU(2) and SU(1,1) interferometers. Phys. Rev. A **33**, 4033 (1986), https://doi.org/10.1103/PhysRevA.33.4033
3. D. Han, Y.S. Kim, Special relativity and interferometers. Phys. Rev. A **37**, 4494–4496 (1988), https://doi.org/10.1103/PhysRevA.37.4494
4. S. Baskal, E. Georgieva, Y.S. Kim, M.E. Noz, Lorentz group in classical ray optics. J. Opt. B Quantum Semiclassical Opt. **6**, S455 (2004), http://stacks.iop.org/1464-4266/6/i=6/a=001
5. U. Leonhardt, *Essential Quantum Optics: From Quantum Measurements to Black Holes* (Cambridge University Press, 2010)
6. A.D. Cronin, J. Schmiedmayer, D.E. Pritchard, Optics and interferometry with atoms and molecules. Rev. Mod. Phys. **81**, 1051–1129 (2009), https://doi.org/10.1103/RevModPhys.81.1051

7. L. Pezzè, A. Smerzi, M.K. Oberthaler, R. Schmied, P. Treutlein, Non-lassical states of atomic ensembles: fundamentals and applications in quantum metrology (2016), arXiv:1609.01609
8. M. Gabbrielli, L. Pezzè, A. Smerzi, Spin-mixing interferometry with bose- einstein condensates. Phys. Rev. Lett. **115**, 163002 (2015), https://doi.org/10.1103/PhysRevLett.115.163002
9. W.M. Itano, J.C. Bergquist, J.J. Bollinger, J.M. Gilligan, D.J. Heinzen, F.L. Moore, M.G. Raizen, D.J. Wineland, Quantum projection noise: population fluctuations in two-level systems. Phys. Rev. A **47**, 3554–3570 (1993), https://doi.org/10.1103/PhysRevA.47.3554

Part III
Experimental Platform

Chapter 6
Experimental System and Manipulation Techniques

In this chapter we detail our experimental apparatus. First, we summarize the setup of the optical traps. Spin exchange among three hyperfine spin levels of Rubidium is achieved by the interplay of an applied magnetic bias field and dispersive microwave fields. Techniques to control the nonlinear coupling strength and to imprint spinor phase shifts are introduced. Finally, we give a description of our detection scheme.

6.1 Bose-Einstein Condensate

More than 20 years after the first observations of Bose-Einstein condensates in dilute alkali atoms, their robust generation is now routine to many labs. We will mention only a few crucial steps of our setup. We start by laser cooling and accumulating a sample of Rubidium-87 in a three-dimensional magneto-optical trap (mot). This trap is fed by an atom beam originating from a two-dimensional mot. After a short period of sub-Doppler cooling the atoms are optically pumped to the lower $F = 1$ hyperfine manifold and the molasses is reconfined in a magnetic trap. Majorana losses are avoided by using a time averaged potential technique. Reducing the radius of the time orbiting potential allows atoms at the edge to leave the magnetic trap. This circle-of-death evaporation takes about 25 s and leaves us with one million atoms slightly above the transition temperature for Bose-Einstein condensation.

6.2 Optical Trapping Setup

With the atomic cloud being still above the critical temperature to undergo Bose-Einstein condensation we transfer it into a crossed beams optical dipole trap. Both beams are derived from a Yb:YAG laser that operates at a wavelength of 1030 nm.

D. Linnemann, *Quantum-Enhanced Sensing Based on Time Reversal of Entangling Interactions*, Springer Theses,
https://doi.org/10.1007/978-3-319-96008-1_6

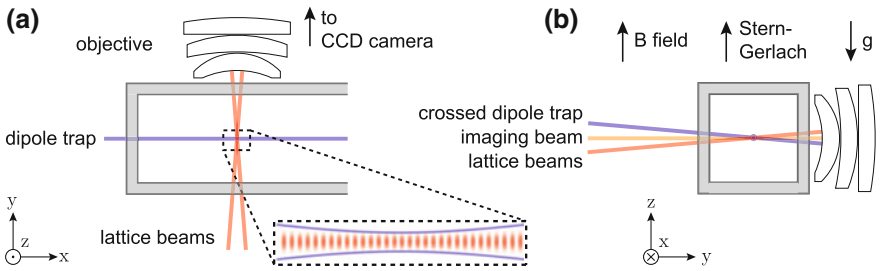

Fig. 6.1 Experimental setup. **a** Generation of the optical lattice potential. Experiments are performed in a glass cell (grey). In this bottom-top view the optical lattice is formed by two intersecting lattice beams. Their crossing angle is 9° giving a lattice spacing of 5.5 µm. For transversal confinement a waveguide like potential (blue) is superimposed. The combined optical potential is shown in the inset; its size corresponds to the field of view of our imaging system—the high-NA objective is indicated. **b** Additional optical beams used during the experimental sequence. In this front view we look along the waveguide beam. Evaporation to Bose-Einstein condensation is performed in the optical potential formed by the two crossing dipole trap beams. Resonant light (orange) is used for absorption imaging. State-selective detection is achieved by Stern-Gerlach splitting during time of flight. The direction of the magnetic field, its gradient, and gravity are indicated

Further forced evaporation is employed by reducing the optical trap depth. For this the intensity of one beam is lowered. Hereby a BEC of 10^4 Rubidium atoms without discernible thermal fraction is generated. After ramping down one of the beams, we let the BEC expand in the shallow potential of the remaining beam. With a large aspect ratio of 100 this potential acts like a waveguide. It provides transversal confinement with a trap frequency of $2\pi \times 440$ Hz but only very weak on-axis trapping. At the point at which the BEC is expanded to an extension of $\approx$150 µm along the waveguide, we adiabatically ramp up a one dimensional optical lattice potential that intersects the BEC. This optical lattice is formed by two additional beams crossing under an angle of $\approx 9°$. The lattice beams are generated by a Ti:Sa laser and have a wavelength of $\lambda = 810$ nm. This yields a lattice spacing of 5.5 µm and a longitudinal trap frequency of $2\pi \times 660$ Hz. The lattice beams are red detuned to both the D1 and D2 transition of Rubidium at 795 nm and 780 nm, respectively. Figure 6.1 shows the experimental setup with all laser beams indicated. Since quantum mechanical tunnelling between adjacent lattice sites can be neglected we use the $\approx$30 populated lattice sites to increase the statistical sample size of our experiments. For this each lattice site constitutes an independent experimental realization. Close to the centre of the cloud each site contains about 400–500 atoms. The extent of the on-site wave functions is smaller than the spin healing length. Thereby, dynamics in the internal degree of freedom are well isolated and the single spatial mode description is valid.

6.3 Effective Spin-1 System

In its electronic ground state, the hyperfine splitting of Rubidium-87 yields two manifolds with total spin $F = 1$ and $F = 2$, respectively, which are separated by 6.8 GHz in energy. We perform our experiments at a magnetic bias field of $B = 0.9\,\mathrm{G}$. The corresponding energy shifts, as described by the Breit-Rabi formula, are depicted in Fig. 6.2. Here, we draw the contributions caused by the linear (panel a), and the quadratic Zeeman shift (panel b) separately. The familiar linear Zeeman effect shifts adjacent m_F levels by $\mu B = 2\pi \times 630\,\mathrm{kHz}$ as indicated. In contrast, the level shifts due to the quadratic Zeeman effect are orders of magnitude smaller in size. They are described by $\Delta E = \binom{+}{-}(4 - m_F^2)\hbar q_B B^2$ where the upper (lower) sign is valid for the spin $F = 2$ ($F = 1$) hyperfine manifold and $q_B B^2 = 2\pi \times 60\,\mathrm{Hz}$.

Our experiments on spin exchange are performed within the upper $F = 2$ manifold. For this an effective three level system is formed by the states $|2, 0\rangle$ and $|2, \pm 1\rangle$ as indicated in the figure by the grey box. Because of its magnetization conserving nature spin exchange is unaffected by the level shifts caused by the linear Zeeman effect. Therefore only the quadratic Zeeman shifts need to be considered. The three level description is thus valid because the $|2, \pm 2\rangle$ states, not subjected to the quadratic Zeeman shift at all, are energetically sufficiently remote. Then the situation can be mapped onto the spin-1 Hamiltonian as developed in the theory section. The microscopic nonlinear coupling strength g depends on the underlying microscopic scattering details and is thus different for spin exchange within $F = 1$ and $F = 2$. In particular, if two $F = 2$ atoms collide an additional scattering channel with combined spin $F = 4$ arises which is absent in the aforementioned $F = 1$ case.

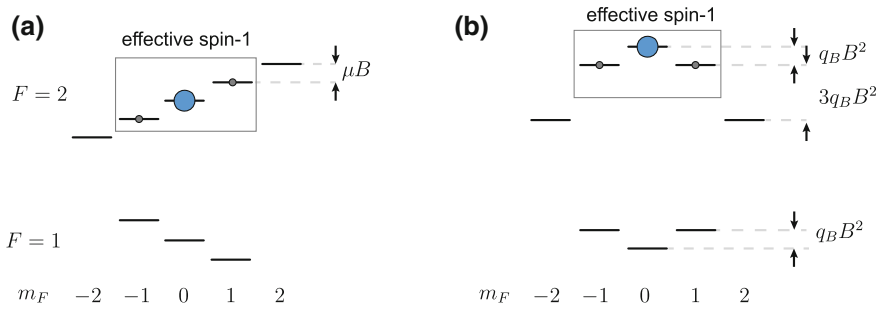

Fig. 6.2 Hyperfine structure of Rubidium-87 in a magnetic field. The two hyperfine manifolds, $F = 1$ and $F = 2$ are separated by 6.8 GHz in energy. The level shift caused by an externally applied magnetic field is described by the Breit-Rabi formula. These level shifts can be divided into a linear (panel a) and quadratic (panel b) contribution. The former splits adjacent magnetic sublevels by $\mu B = 2\pi \times 630\,\mathrm{kHz}$ at our magnetic bias field of $B = 0.9\,\mathrm{G}$. The quadratic Zeeman effect leads to level shifts such that the $m_F = 0$ state is separated from both $m_F = \pm 1$ states by an amount of $\pm q_B B^2 = 2\pi \times 60\,\mathrm{Hz}$. The $m_F = \pm 2$ states, not subjected to this level shift, are separated by $4q_B B^2$ from state $|2, 0\rangle$. Because this energy spacing is much larger than the spin exchange coupling strength, the remaining states form an effective spin-1 system as indicated by the grey box

As a result, the coupling strength for spin exchange within $F = 2$ is one order of magnitude larger than for $F = 1$. In our experiments it is of order $\kappa = 2\pi \times 20\,\mathrm{Hz}$. Details of this mapping can be found in Appendix A.

This effective description in terms of a three level system embedded in $F = 2$ remains valid as long as the $m_F = \pm 2$ states do not participate in the spin dynamics. We guarantee this by working at a sufficiently large magnetic bias field.[1] In fact, we chose the magnetic field strength in order to comply with two requirements: the closedness of the effective three level system—and a not too large energy barrier between $|2, 0\rangle$ and $|2, \pm 1\rangle$ such that the detuning of the spin exchange can be controlled reliably with dispersive microwave dressing. We will detail both aspects in the next sections.

6.4 Microwave Dressing

We use state selective microwave dressing to fulfil the spin exchange resonance condition [1]. In Fig. 6.3 we detail how individual level shifts make up the effective spin exchange detuning q. Starting point are the level shifts caused by the magnetic bias field as described in the previous section: the quadratic Zeeman shift elevates the pump mode in energy with respect to both side modes. This energy splitting is shown on the very left of each panel. We employ microwave dressing that predominantly shifts the state $|2, 0\rangle$, as depicted in the middle. Additionally, the collisional shifts reduce the energy of the pump mode, which is represented on the right of each panel. The effective spin exchange detuning $q = 0$ corresponds to the case where the energy shifts caused by microwave dressing and the quadratic Zeeman effect cancel each other (panel a). In contrast, spin exchange resonance, $q = \kappa$, is achieved when all *three* individual level shifts compensate each other as displayed in panel (c). One should keep in mind that only the shifts relevant for spin exchange are drawn. Because of the linear Zeeman shift, the three depicted levels are not energetically degenerate. In the complete picture this case corresponds to the pump mode being energetically exactly in the middle of both side modes. Starting with all atoms prepared in the pump mode, spin exchange leads to population transfer only within the parameter regime $q < 0 < 2\kappa$ which corresponds to the bifurcated classical phase space.

We now explain the dispersive microwave dressing in more detail. We apply microwave radiation $\delta = 2\pi \times 110\,\mathrm{kHz}$ blue detuned to the transition $|1, 0\rangle \leftrightarrow |2, 0\rangle$. If other transitions were absent, this would shift the two states in energy by $\pm\Omega^2/4\delta$ where Ω is the corresponding on-resonance Rabi frequency. However, such dispersive energy shifts decrease only slowly with the detuning δ from resonance. Therefore, for a precise accounting all possible microwave transitions should be considered. The employed loop antenna radiates microwaves of all three polarizations. Thus, the mutual energy shifts of all eight involved levels have to be taken into

[1] Yet small enough such that an interplay with external dynamics can be neglected. For details see Appendix A.

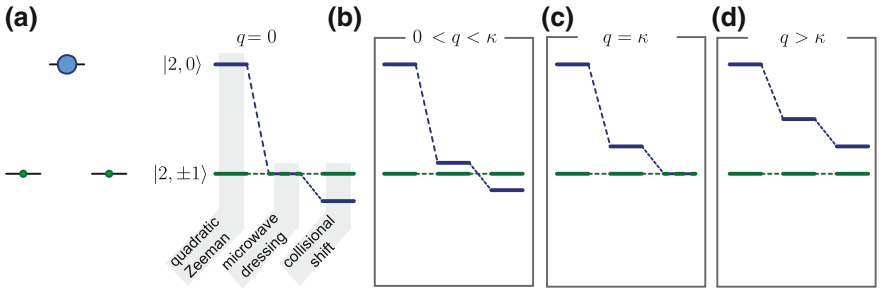

Fig. 6.3 Microscopic level shifts and their contribution to the spin exchange detuning q. Spin exchange is parametrized by the effective coupling strength κ and the overall spin exchange detuning q. The latter has three contributions that arise due to applied magnetic fields, microwave dressing fields, and collisional interactions of the atoms themselves. Each panel shows a different spin exchange detuning itemised into these three contributions. The quadratic Zeeman shift elevates the pump mode above the side modes (outermost left splitting). Microwave dressing is used to (partially) compensate this energy mismatch (middle). Finally, the collisional interactions lower the pump mode's energy by an amount of κ (right). The associated classical phase space of spin exchange is bifurcated for the parameter regime $0 < q < 2\kappa$, out of which we exemplify the microscopic energy shifts for four particular cases: $q = 0$, $0 < q < \kappa$, $\kappa = q$ which corresponds to the spin exchange resonance, and $\kappa < q < 2\kappa$

account. Such a procedure is outlined in Appendix B. Here, we shortly summarise the result: we find best agreement among several measurements if we assume that the three levels $(|2, -1\rangle, |2, 0\rangle, |2, 1\rangle)$ that constitute the effective spin-1 systems are shifted in energy by $2\pi \times (+4.5, 37, -6)$ Hz, respectively. In total, these microscopic shifts then lead to an effective spin exchange detuning of $q = 2\pi \times 24.5$ Hz.

Complementary to the microscopic considerations detailed above, we use the spin exchange itself as a probe to characterize the microwave dressing in an effective way. In Fig. 6.4 the interferometric sequence is performed for different detuning δ of the microwave dressing. We use such measurements to experimentally find the spin exchange resonance. Panel (a) shows two exemplary fringes for $\delta = 2\pi \times 155$ kHz and $\delta = 2\pi \times 95$ kHz, respectively, while the power and thus the on-resonance Rabi frequency remains fixed. While the amplitude of the fringes is almost identical the detuning shows up most prominently in a spinor phase advance. In panel (b) we plot the starting spinor phase of each interferometry fringes versus the microwave detuning δ. At the zero crossing, spin exchange resonance is fulfilled. On this basis we use the microwave detuning of $\delta = 2\pi \times 110$ kHz for the main experiments. The grey line shows the result of a numerical simulation. We use this simulation to collaborate and correct the calculation of the microscopic level shifts (see Appendix B). Panels (c) and (d) show the starting phase of the interferometry fringes versus the duration of spin exchange. For resonant spin exchange (panel c) the spinor phase remains close to 0. If weaker microwave dressing is employed, a spinor phase is dynamically built up.

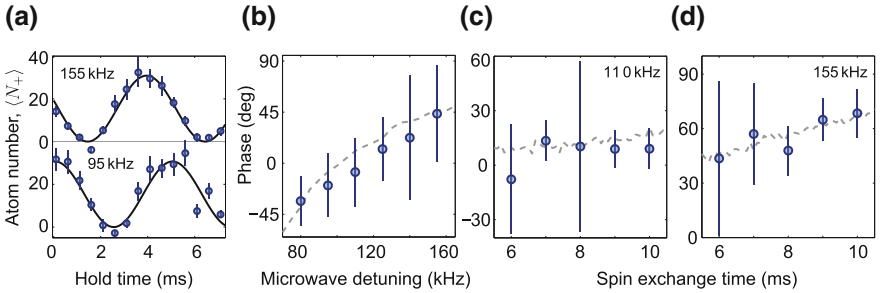

Fig. 6.4 SU(1,1) interferometry fringes for different microwave dressing. **a** Performing spin exchange detuned leads to an additional phase accumulation that shifts the interferometry fringe. Shown are two fringes that are obtained for different energy shifts. For this the microwave detuning (value indicated) to atomic resonance is changed. The resulting fringe's phase offset is plotted in panel (b) versus the microwave dressing detuning used to initiate and maintain spin exchange. Spin exchange for 6 ms was used. We deduce that a microwave detuning of $2\pi \times 110\,\mathrm{kHz}$ corresponds to spin exchange resonance. This is further collaborated by the fact that for this microwave detuning the phase stays flat versus spin exchange duration (panel c). For the non-resonant case a phase is dynamically accumulated. The grey dashed lines correspond to the result of a numerical simulation

6.5 Gradients

The microwave is radiated from a home built single-loop antenna. Its position is optimized such that gradients (of all three polarizations) over the atomic array are minimized while still being as close as possible to the glass cell in order to achieve sufficiently large on-resonance Rabi frequencies. To estimate spatial gradients of the microwave we perform resonant Rabi flopping. Eventually, the right and left part of the atomic cloud will start oscillating out of sync from which the power gradient is estimated. This procedure is repeated for all three microwave polarizations. As detailed in the previous section, microwave dressing yields a total energy shift that amounts to $\approx 2\pi \times 36\,\mathrm{Hz}$. This contribution is altered due to gradients of the microwaves by $2\pi \times 0.1\,\mathrm{Hz}$ over a spatial extent of 100 µm along the atomic cloud. Since the nonlinear coupling strength is of order $\kappa = 2\pi \times 20\,\mathrm{Hz}$ such minute energy shifts are negligible for the spin exchange dynamics. A more detailed accounting of the individual gradients can be found in Appendix B.

The magnetic field gradient over the atomic cloud is levelled by positioning small permanent magnets in vicinity of the glass cell. In order to characterize the magnetic field gradient we perform a Ramsey sequence on states $|1,-1\rangle$ and $|2,-2\rangle$ and extend the Ramsey time until the fringes run out of sync spatially. Over the full extent of the atomic cloud (150 µm) we find a magnetic field gradient that amounts to 0.1 mG. With spin exchange being magnetically insensitive to first order, these field changes of 0.1 mG translate into an spin exchange detuning of $2\pi \times 10\,\mathrm{mHz}$. Even an order of magnitude smaller than the microwave dressing gradients such an energy shift can safely be neglected.

6.6 Residual Couplings Out of the Effective Spin-1 System

For the spin-1 description to be valid the spin exchange dynamics needs to be restricted to the subspace formed by the three levels $|2, 0\rangle$ and $|2, \pm 1\rangle$. Besides the desired spin exchange process of the form $2 \times |2, 0\rangle \leftrightarrow |2, -1\rangle + |2, +1\rangle$, the five levels of $F = 2$ allow for additional channels [2, 3]. In principle, all processes that leave the total magnetization unaltered are admissible. Figure 6.5 shows these possible spin exchange channels. We choose the magnetic bias field of $B = 0.9\,\mathrm{G}$ such that these spurious spin exchange processes are energetically suppressed. We substantiate this by a numerical simulation (detailed in Appendix A) which shows the impact of leaving the three-level approximations at lower magnetic field strengths. Additional to this detuning, the spurious spin channels are weaker in coupling strength [3]. In Appendix A we derive the spin interactions of two $F = 2$ atoms and provide a thorough description of the full Hamiltonian with a detailed accounting of all allowed spin exchange channels.

Since only the pump mode is macroscopically populated, the bosonic enhancement is largest for those processes which include the pump mode. With the side modes $|2, \pm 1\rangle$ being only sparsely populated the associated coupling strength for the process $|2, -1\rangle + |2, 1\rangle \leftrightarrow |2, -2\rangle + |2, 2\rangle$ (depicted in orange, panel a) is therefore negligible. Here, we provide two further examples.

The most important channel is $2 \times |2, \pm 1\rangle \leftrightarrow |2, \pm 2\rangle + |2, 0\rangle$ because it has both, the smallest detuning and largest microscopic coupling strength. Panel (b) shows one of the two equivalent processes in green. For a simple estimation of the relevant detuning, we assume that microwave dressing shifts the energy of the pump exclusively. Additionally, we neglect collisional shifts such that during microwave dressing the levels $|2, 0\rangle$ and $|2, \pm 1\rangle$ have equal energies. Then, the spin exchange process in question is detuned by $1.5 q_B B^2 = 2\pi \times 90\,\mathrm{Hz}$. Microscopically, the nonlinear coupling strength of this process is similar to the one characterizing the desired process g. However, with only the pump mode being macroscopically populated the associated spin exchange channel is enhanced only by $\sqrt{N}$ rather than N. Even if

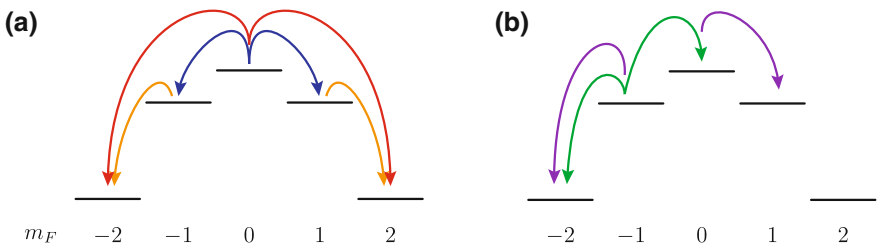

Fig. 6.5 Overview of all spin exchange channels in the $F = 2$ **manifold**. **a** Symmetric spin exchange couplings. **b** Asymmetric processes. For the sake of clarity only half of the allowed channels are shown. For a complete accounting, one has to consider the additional processes which arise under the interchange $m_F \rightarrow -m_F$

the microscopic nonlinearity were identical the effective coupling is still an order of magnitude smaller.

From the symmetric processes shown in panel a, $2 \times |2, 0\rangle \leftrightarrow |2, -2\rangle + |2, +2\rangle$ depicted in red is the most important. Proceeding from $|2, 0\rangle$ it experiences the full enhancement by the pump atoms. However, in this case the microscopic nonlinearity is only a twentieth of g, while the detuning is huge, $3q_B B^2 = 2\pi \times 180\,\text{Hz}$. Therefore, the states $m_F = \pm 2$ do not participate at spin exchange and the effective three level system remains closed.

6.7 Pump Mode Shelving

Our reason to choose an effective three level system within $F = 2$, rather than the direct $F = 1$ system are twofold: first of all, because of the larger coupling strength the spin exchange is faster and more robust. This being a mere technical reason there is also a more profound advantage: that is the possibility of having the pump atoms shelved in a spectator level that does not participate in the spin exchange. We use this technique to control the strength of the nonlinear coupling which is defined by the number of pump atoms. In particular, this enables us to abruptly start and stop the nonlinear process. As a side effect of the large coupling strength in $F = 2$, the detuning when deactivating the microwave dressing is not large enough to suppress residual off-resonant processes. Additionally, the side mode population generated via the nonlinear process itself acts as a seed to speed up further amplification once it is initiated. Therefore, the shelving technique is crucial for precise control over the nonlinear coupling. To this end we transfer the pump mode into the state $|1, 0\rangle$ via a fast microwave π-pulse as shown in Fig. 6.6. In contrast, within the $F = 1$ manifold already a small energy detuning suffices to efficiently stop spin exchange entirely.

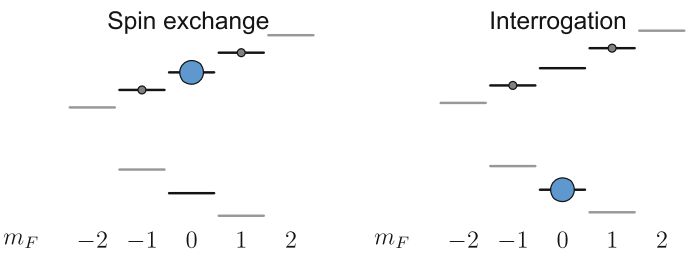

Fig. 6.6 Pump mode shelving technique. Spin exchange is performed within the upper $F = 2$ hyperfine manifold. For this the pump mode is prepared in state $|2, 0\rangle$ (left panel) and microwave dressing is applied to ensure energy matching (not shown). To interrupt spin exchange the microwave dressing is disabled. However, the resulting detuning is not sufficiently large to suppress spin exchange entirely. We rapidly transfer the pump atoms to the spectator state $|1, 0\rangle$ via a microwave π-pulse. With the pump mode shelved in $|1, 0\rangle$ the side mode's population remains frozen in $|2, \pm 1\rangle$ and can be used for phase interrogation (right panel)

This is in part because the $m_F = \pm 1$ states remain empty at all times and cannot act as a seed. This yields another advantage: to compare the phase sensitivity, the number of atoms shared in both side modes after the first period of spin exchange needs to be measured to assess the resource. Such a measurement is simplified when the off resonant spin exchange during phase interrogation is inhibited.

6.8 Phase Imprint

To realize different spinor phases we imprint a phase onto the pump mode while it is being shelved in $F = 1$. The protocol is explained in Fig. 6.7 where we make use of the Bloch sphere representation. As shown in the left panel, the sphere's north pole corresponds to all N_0 atoms prepared in state $|2, 0\rangle$ while the south pole is identified with $|1, 0\rangle$. We start with the pump mode being in state $|2, 0\rangle$. A red pointer is included to track the phase of the pump mode φ_0 during the sequence.

We perform the microwave π-pulse that is used for the pump transfer slightly detuned. With a on-resonance Rabi frequency of $2\pi \times 10\,\mathrm{kHz}$ the detuning of $\delta_{\mathrm{mw}} = 2\pi \times 90\,\mathrm{Hz}$ has a negligible effect on the transfer efficiency. On the Bloch sphere

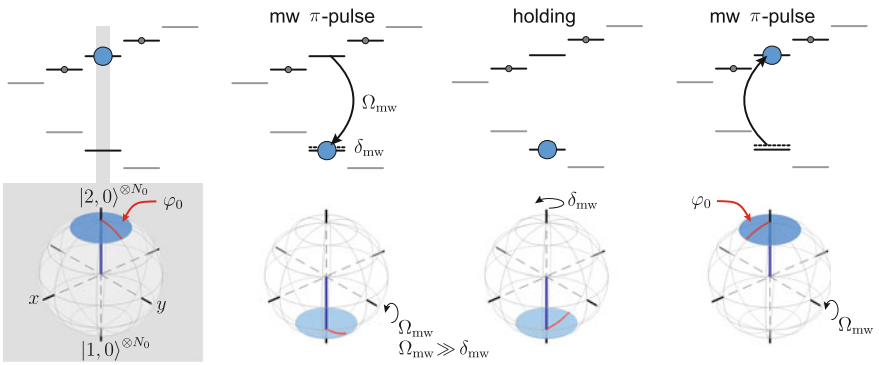

Fig. 6.7 Spinor phase imprint. The spinor phase of the three level system is scanned via phase imprints onto the pump mode. For this we perform the microwave π-pulses used for pump shelving slightly detuned. We detail the phase imprinting procedure with the help of the Bloch sphere representation. Here, the north and south pole correspond to state $|2, 0\rangle$ and $|1, 0\rangle$, respectively, as shown in the grey shaded left panel. The relative phase between these two states is indicated by the red pointer. The microwave π-pulse used for pump mode shelving is represented by a rotation of $\approx 180°$ about the y-axis. This mw pulse is detuned by δ_{mw} which is much smaller than the on-resonance Rabi frequency Ω_{mw}. Then, its effect on the population transfer is negligible and the state is almost perfectly rotated onto the Bloch sphere's south pole. During the subsequent holding time t_{hold} the phase evolves at a rate given by δ_{mw}. On the Bloch sphere this is represented by a rotation about the z-axis. Finally, a second mw π-pulse rotates the state back to the north pole. The phase φ_0 of the pump mode is thereby changed by $\delta_{\mathrm{mw}} t_{\mathrm{hold}}$. Additionally to this dynamical phase a geometrical phase arises. For a resonant 2π-pulse this geometric phase contribution amounts to $180°$ with a $1°$ correction due to the detuning

this π-pulse rotates the state from the north towards the south pole. During the time the pump mode is shelved in $F = 1$ the phase evolves at a rate given by the pulse detuning δ_{mw}. We exploit this dynamic phase that accumulates versus holding time t_{hold}. On the Bloch sphere this corresponds to a rotation of the state about the z-axis. Upon transfer back to $F = 2$ a spinor phase change of $\varphi_0 = 2\delta t_{\mathrm{hold}} + \tilde{\varphi}_0$ is realized. Here, $\tilde{\varphi}_0$ denotes the geometrical phase that arises during the 2π-pulse due to the detuning and amounts to 2°. As we scan the pump phase via the hold time, this geometric phase offset is inconsequential.

6.9 State Preparation

Initially the atoms are condensed in the state $|1, -1\rangle$ which is a consequence of the magnetic trapping. Figure 6.8 shows the experimental sequence in a timing diagram. The top row indicates microwave pulses used for either state transfers or dispersive energy shifts. The lower panel shows the atomic populations at the respective stage. For clarity, only the quadratic Zeeman shift is drawn.

First, by means of two consecutive π-pulses the atoms are transferred to state $|1, 0\rangle$ (via the intermediate state $|2, 0\rangle$). At this stage we apply a strong magnetic field gradient which expels spurious atoms in $m_F \neq 0$ states (Stern-Gerlach cleaning). In particular, atoms in the $|1, -1\rangle$ state are cleaned which might have remained from an imperfect microwave π-pulse. Application of the magnetic field gradient briefly

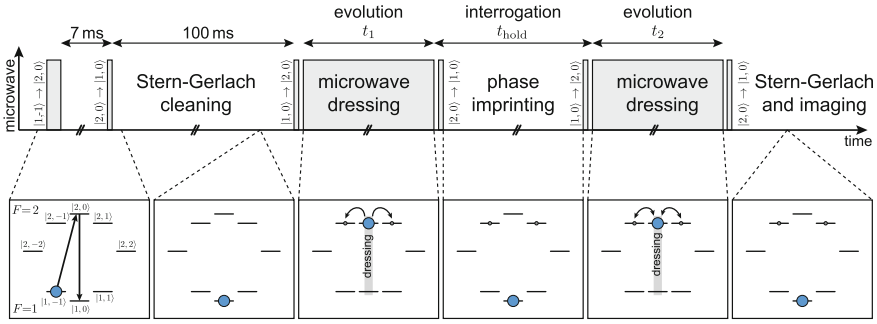

Fig. 6.8 Timing diagram of the experimental sequence. The top row indicates the microwave pulses used throughout the sequence for either state transfers or dispersive dressing. The lower panel indicates the action of the microwave pulses in a simplified level diagram. Here we only show the energetic level shifts due to the quadratic Zeeman effect. Starting point for our spin exchange experiments is a shelved pump mode in state $|1, 0\rangle$ with all other spin states empty. To achieve this a strong magnetic field gradient expels the atoms in sub states with $m_F \neq 0$ (Stern-Gerlach cleaning). Transfer of the pump mode into $|2, 0\rangle$ is done by fast resonant microwave pulses. Thereby the nonlinear coupling strength for the ensuing spin exchange is effectively quenched. During phase imprinting the pump mode is shelved in $|1, 0\rangle$. After a second period of spin exchange the atomic population is detected by absorption imaging

distorts the magnetic field stabilization servo loop. A holding time of 100 ms is added to allow the homogeneous magnetic bias field to settle.

At our magnetic bias field of $B = 0.9\,\mathrm{G}$ spin exchange within the $F = 1$ manifold is suppressed as the detuning of $q\,B^2 = 2\pi \times 60\,\mathrm{Hz}$ is much larger than the nonlinear coupling strength of $\approx 2\pi \times 2\,\mathrm{Hz}$ as detailed in the previous sections. This state $|1, 0\rangle$ is the starting point of all experiments. Spin exchange is subsequently performed by transferring the pump atoms to state $|2, 0\rangle$ via a fast microwave π-pulse that takes 46 µs thereby effectively quenching the nonlinear coupling strength in $F = 2$, $\kappa \to 20\,\mathrm{Hz}$. Immediately after state transfer microwave dressing is employed to shift the pump mode into spin exchange resonance. After a variable time of spin exchange, which is on the order of $t_1 = 6 - 10\,\mathrm{ms}$, microwave dressing is stopped and the pump mode is shelved in $F = 1$ for phase imprinting. The holding time in $F = 1$ is varied (typically between $t_{\mathrm{hold}} = 0 - 2\,\mathrm{ms}$) to imprint different spinor phases. After the final period of spin exchange we detect the atomic population by absorption imaging. We detail the imaging procedure in the next section.

6.10 Detection

After the final period of spin exchange we deactivate microwave dressing and immediately transfer the pump mode from the $F = 2$ manifold to $F = 1$ to switch off the nonlinear coupling. At this stage, we use absorption imaging with a high optical resolution of 1.1 µm to count the number of atoms spin and lattice site resolved [4, 5]. The internal state is resolved by applying a Stern-Gerlach like magnetic field gradient. A short period of time of flight ($\approx$1 ms) is used to reduce the atomic density. During this, the optical lattice remains turned on such that the atomic clouds of each lattice site do not overlap spatially. We image the population within the $F = 2$ and $F = 1$ manifold simultaneously. For this the short pulse of the imaging light (15 µs) is accompanied by repumping light. Then all three involved spin components appear on the same absorption image. Shortly after this (1.2 ms) we take an additional image with the atoms blown away, which acts acts as a reference to correct for fringes and other optical distortions [6]. Details of the imaging procedure and its calibration can be found in reference [5]. A typical single shot absorption image is shown in Fig. 6.9. It shows the outcome when spin exchange was performed for 20 ms.

To reduce the contribution of photon shot noise we count the atom numbers only within the indicated elliptical regions of interest. Thereby the population of each side mode, $|\uparrow\rangle$ and $|\downarrow\rangle$ can be determined in a single shot with an error of ± 4 atoms (which corresponds to one standard deviation) [5]. The magnetic field gradient used for Stern-Gerlach splitting is inhomogeneous over the extent of the optical lattice. This leads to a nonuniform spacing of the two spin components. Ideally, nonlinear time reversal revokes the population transfer caused by spin exchange such that the side modes are empty in the end. To handle this situation, we calibrated each spins position with respect to the pump mode. Since the pump mode is heavily populated in any case, their position can be determined reliably from the absorption image. We

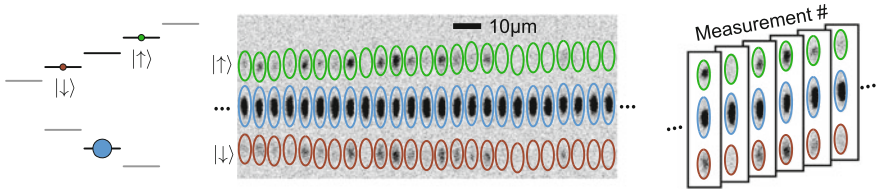

Fig. 6.9 Typical absorption image. Atomic populations of the three involved spin states (indicated in level diagram left) are destructively determined by high resolution absorption imaging. To resolve the internal state, a magnetic field gradient is pulsed on (Stern-Gerlach). During the subsequent time of flight the optical lattice potential remains active. Atom numbers are counted within the elliptical regions. Close to the centre each lattice site is populated by 400–500 atoms, falling off to 200 atoms towards the edges. The outcome of each lattice site is treated as an independent individual measurement (right). The single shot absorption image was obtained after letting resonant spin exchange elapse for 20 ms. The strong number fluctuations observed in adjacent lattice sites are a distinguishing feature of this nonlinear process

use the central region extending over ≈25 lattice sites (as shown) for further analysis. Each lattice site constitutes an independent measurement of the spin dynamics.

The magnetic moments of the $F = 2$ and $F = 1$ sub states are (almost) identical in magnitude. Therefore, after Stern-Gerlach splitting the states $|2, \pm 1\rangle$ and $|1, \mp 1\rangle$ overlap spatially and are not individually resolved. Similar applies to the states $|2, 0\rangle$ and $|1, 0\rangle$ which appear on the same position of the absorption image. We independently checked that the states $|1, \pm 1\rangle$ remain empty during the entire experimental sequence. Therefore, the absorption image consists of the states $|2, \pm 1\rangle$ and the pump mode $|1, 0\rangle$ as indicated in the left panel of Fig. 6.9 and all other spin states remain unpopulated.

6.11 Data Analysis

To characterize the two-mode squeezed vacuum state and its large fluctuations we typically use statistical sample sizes of 600–1000 measurements. The data collection is facilitated by using each of the 25 populated lattice sites. For quantitative analysis we postselect only those experimental runs and lattice sites which have a total atom number in a well defined range. This is necessary as the nonlinear coupling strength depends on the total atom number. This postselection window is typically 50 atoms wide and centred between $N = 400$–550 atoms. Under such conditions the nonlinear coupling strength varies by less than 10%.

6.12 Interleaved Control Measurements

A series of automated control measurements is performed interleaved with the main measurements on spin exchange. Most importantly, these characterize the amount of detection noise. For this we image the atomic cloud after the Stern-Gerlach cleaning procedure. At this stage only the pump mode is populated. On the absorption image, the elliptical regions of the side modes remain empty. The detection noise is determined by the apparent atom fluctuations found when summing these empty regions. This background signal has a Gaussian distribution that is centred at ≈ 0.3 atoms and has a width corresponding to the detection noise of $\sigma = 4$ atoms per spin state. Unless stated otherwise the contribution of this independently characterized detection noise is subtracted for the main data. Similarly, the atom number offset is subtracted. Any specific post selection (e.g. on total atom number, lattice sites) is performed on both, the main data and the control measurements.

Our experiments are performed at a magnetic bias field of $B = 0.9\,\mathrm{G}$ whose major component is along the vertical direction. The magnetic field component along this direction is actively stabilized by means of a fluxgate sensor that is mounted close to the glass cell. The shot-to-shot fluctuations amount to less than 0.1 mG. Long term drifts over the course of several days are compensated by automated Ramsey spectroscopy measurements.

References

1. F. Gerbier, A. Widera, S. Fölling, O. Mandel, I. Bloch, Resonant control of spin dynamics in ultracold quantum gases by microwave dressing. Phys. Rev. A **73**, 041602 (2006), https://doi.org/10.1103/PhysRevA.73.041602
2. A. Widera, F. Gerbier, S. Fölling, T. Gericke, O. Mandel, I. Bloch, Coherent collisional spin dynamics in optical lattices. Phys. Rev. Lett. **95**, 190405 (2005), https://doi.org/10.1103/PhysRevLett.95.190405
3. A. Widera, F. Gerbier, S. Fölling, T. Gericke, O. Mandel, I. Bloch, Precision measurement of spin-dependent interaction strengths for spin-1 and spin-2 87 Rb atoms. New J. Phys. **8**, 152 (2006), http://stacks.iop.org/1367-2630/8/i=8/a=152
4. G. Reinaudi, T. Lahaye, Z. Wang, D. Guéry-Odelin, Strong saturation absorption imaging of dense clouds of ultracold atoms. Opt. Lett. **32**, 3143–3145 (2007), https://doi.org/10.1364/OL.32.003143
5. W. Muessel, H. Strobel, M. Joos, E. Nicklas, I. Stroescu, J. Tomkovic, D.B. Hume, M.K. Oberthaler, Optimized absorption imaging of mesoscopic atomic clouds. Appl. Phys. B **113**, 69 (2013), https://doi.org/10.1007/s00340-013-5553-8
6. C.F. Ockeloen, A.F. Tauschinsky, R.J.C. Spreeuw, S. Whitlock, Detection of small atom numbers through image processing. Phys. Rev. A **82**, 061606 (2010), https://doi.org/10.1103/PhysRevA.82.061606

Part IV
Experimental Results

Chapter 7
State and Process Characterisation

The cornerstone enabling time reversal is the process of parametric amplification which is realized by spin exchange. In this chapter we experimentally characterize the nonlinear process in detail. Emphasis is placed on the generated number fluctuations which are generic to the emerging entangled state. These fluctuations reflect the state's ability for superior phase estimation. Finally, experimental limitations such as particle loss, pump depletion effects, and seeded dynamics are considered.

7.1 Experimental Signatures of Parametric Amplification

Spin exchange leads to peculiar mode correlations of the arising state. In this section we detail these distinctive correlations by comparison to the classical method of distributing atoms among three modes. The pairwise nature of parametric amplification stands in stark contrast to this linear coupling of the levels which cannot introduce particle entanglement.

The mode correlations generated during spin exchange are shown in Fig. 7.1a where the single shot spin populations are plotted. As expected for ideal number correlations, the data points line up along the diagonal indicating $N_\uparrow = N_\downarrow$. The residual width in orthogonal direction is caused mainly by detection infidelities. This becomes apparent when comparing the width to the initially empty state shown in grey. Its isotropic extension is caused exclusively by detection noise. The narrow distribution in $N_\uparrow - N_\downarrow$ is accompanied by a large extension along the diagonal. These fluctuations in $N_\uparrow + N_\downarrow$ are characteristic for the two-mode squeezed vacuum state. Histograms for both mode populations show excellent agreement with a thermal-like number distribution when including detection noise by convolution (indicated in black).

D. Linnemann, *Quantum-Enhanced Sensing Based on Time Reversal of Entangling Interactions*, Springer Theses,
https://doi.org/10.1007/978-3-319-96008-1_7

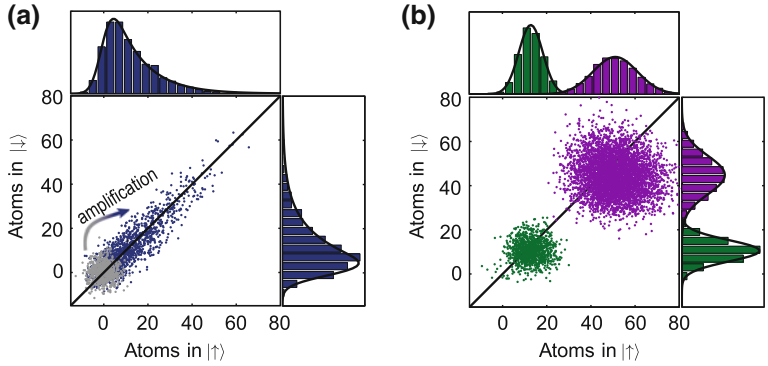

Fig. 7.1 Atom number correlations. **a** Starting from an initial vacuum state (grey) parametric amplification populates the two side modes $|\uparrow\rangle$ and $|\downarrow\rangle$ in a characteristic manner: ideally, the pairwise generation process yields perfectly correlated atom numbers, $N_- = N_\uparrow - N_\downarrow = 0$. In the correlation plot this corresponds to the diagonal line along which the experimental data points line up. The residual spread in N_- is caused by detection noise. Being confined on the diagonal line, large fluctuations in atom number sum $N_+ = N_\uparrow + N_\downarrow$ are exhibited. The population of each mode follows a thermal-like distribution as witnessed by the corresponding histogram. The black lines are fits to thermal distributions also taking into account detection noise by convolution. **b** Atom number distributions obtained when populating the two modes via a classical process, i.e. linear coupling. The green data points correspond to a state with similar average atom number as the one produced by parametric amplification (in panel a). Clearly, the state is concentrated symmetrically around its average population. Its fluctuations are isotropic and result from both, atomic shot noise and detection noise. This is clarified when considering a state with larger atom number such that the atomic shot noise dominates as shown in purple. The individual mode populations follow a Gaussian distribution as shown by the respective histograms

Linear coupling of the three modes cannot generate such distinctive number correlations as exemplified in Fig. 7.1b. Here, starting with all atoms prepared in $|1, 0\rangle$ a resonant rf pulse is used to populate the modes $|1, \pm 1\rangle$. Using short rf pulses only few atoms are transferred to the side modes. The green data points result from a state with the same average atom number of $\langle N_\uparrow \rangle \approx \langle N_\downarrow \rangle \approx 11$ as the state generated by spin exchange. However, as a consequence of atomic shot noise the atom number difference between both modes shows larger fluctuations. This becomes more pronounced when considering a state with higher mode populations as shown in purple. As witnessed by their histograms the mode populations are close to Gaussian. Their width is given by both detection noise and atomic shot noise.

7.2 Nonlinear Coupling Strength

To experimentally determine the nonlinear coupling strength we perform spin exchange for different durations. The average population of the side modes is expected to grow nonlinearly according to $\langle N_\uparrow \rangle = \langle N_\downarrow \rangle = \sinh^2 \kappa t$, where t is the

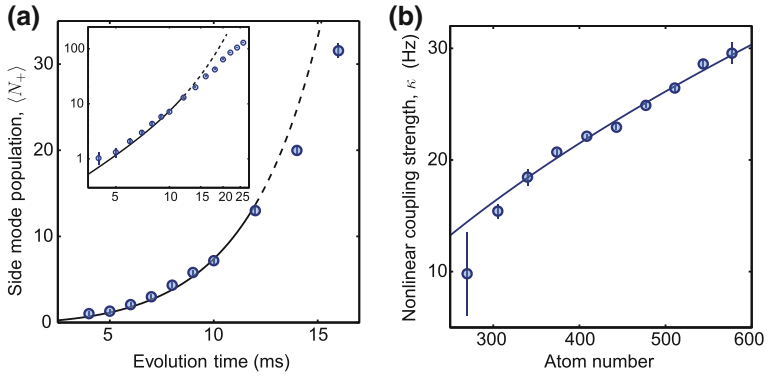

Fig. 7.2 Experimental characterization of the nonlinear coupling strength. **a** For sufficiently short evolution times the undepleted pump approximation remains valid and the side mode growth follows $\langle N_+ \rangle = 2 \sinh^2 \kappa t$ (solid and dashed line). We extract κ by a fit for evolution times up to 12 ms as indicated by the solid line. **b** Postselecting different total atom numbers allows determining the atom number dependence of the nonlinear coupling strength κ. The solid line shows a heuristic square-root-like dependence. Such a behaviour is expected for a trapped mesoscopic BEC. At our atomic densities the system lies in between the range of validity for the Thomas-Fermi regime on the one hand, and the harmonic oscillator regime on the other

evolution time. We use this connection to extract the nonlinear coupling strength κ by a fit. Figure 7.2a shows an exemplary data set. To remain within the validity regime of the undepleted pump approximation we restrict the fit to evolution times shorter than 12 ms (indicated by solid line). For larger durations the side mode populations grows significantly slower (see inset and continuation of the fitted curve shown as the dashed line).

By repeating this procedure for different postselected total atom numbers we extract the atom number dependence of $\kappa = g(N)N$. This atom number dependence of $g(N)$ is caused by the mode function overlap of the BEC's external wave function $g(N) \propto \int \mathrm{d}^3x |\Phi(\boldsymbol{x})|^4$. Panel (b) shows the measured nonlinearity in the range of $N = 280 - 600$. We find an atom number dependence that is compatible with $\kappa \propto \sqrt{N}$ (indicated by the solid line). Such a scaling behaviour is expected for a mesoscopic BEC. This is because it falls into a crossover regime between the region of validity of single-particle (harmonic oscillator) external wave functions and the Thomas-Fermi approximation. In the former case, the mode function overlap would be atom number independent such that $\kappa \propto N$ is expected. In the Thomas-Fermi limit, the mode overlap is $\propto N^{-3/5}$ which leads to a scaling of $\kappa \propto N^{2/5}$. Such an exponent is experimentally indistinguishable from the square root fit which we use for interpolation.

7.3 Atom Loss

The dominant loss mechanism for atoms within the excited hyperfine manifold $F = 2$ are hyperfine changing collisions [1, 2]. In such a collision event at least one of the two atoms relaxes down to $F = 1$ with a corresponding release of energy that allows both atoms to leave the optical trapping potential. As a two-body process this hyperfine relaxation is density dependent. For atoms in state $m_F = i$ with density n_i two-body loss with itself and all other $m_F \neq i$ states must be considered, leading to

$$\frac{\mathrm{d}n_i(\mathbf{r})}{\mathrm{d}t} = -2K_{(i,i)}n_i(\mathbf{r})^2 - \sum_{j\neq i} 2K_{(i,j)}n_i(\mathbf{r})n_j(\mathbf{r}). \tag{7.1}$$

Here, $K_{(i,j)}$ are the loss rates describing collisions between pairs of atoms in state $m_F = i$ and $m_F = j$. Within the single spatial mode approximation we can use our knowledge of the relationship between density $n_i(\mathbf{r})$ and the corresponding atom number N_i. This connection was established in the previous section. Experimentally we find $n_i \propto N_i/\sqrt{N}$. We then obtain

$$\frac{\mathrm{d}N_i}{\mathrm{d}t} = -2K_{(i,i)}\frac{N_i^2}{\sqrt{N}} - \sum_{j\neq i} 2K_{(i,j)}\frac{N_iN_j}{\sqrt{N}}. \tag{7.2}$$

By preparing all atoms in a single component $m_F = i$ in $F = 2$ we can estimate $K_{i,i}$. For such a case $\frac{\mathrm{d}N_i}{\mathrm{d}t} = -2K_{(i,i)}N_i^{3/2}$ is solved by

$$N_i(t) = \left[K_{(i,i)}t + \sqrt{N_i(t=0)}\right]^{-2}. \tag{7.3}$$

Such a loss measurement is shown in Fig. 7.3a. Here, we prepare all atoms into the $m_F = 0$ state and fit the subsequent loss according to Eq. 7.3 (solid blue line). In a similarly manner, the loss coefficient $K_{1,1}$ of $m_F = 1$ is characterized which is due to symmetry arguments identical to $K_{-1,-1}$. With initially only the $m_F = 0$ state populated and all other spin states empty, we observe a small growing population of the $m_F = 1$ state (grey). This is caused by off resonant spin exchange. Especially for long holding times, such spurious effects yield to systematically overestimated loss rates and thereby limit this treatment to small durations <300 ms.

We checked that the loss coefficients are independent of the initial atom number. This is shown in the inset, where $K_{0,0}$ corresponds to the blue data, and $K_{1,1}$ to the red data points. This atom number independence indicates that indeed two-body spin relaxation is the prevailing loss mechanism. In contrast, background gas collisions and off-resonant light scattering of the optical dipole traps are density independent. For these processes, an exponential decay is found. The measured $1/e$-lifetime exceeds 15 s. Single-body loss as well as dipolar losses (which do not necessarily conserve the total angular momentum during collisions) are therefore indiscernible

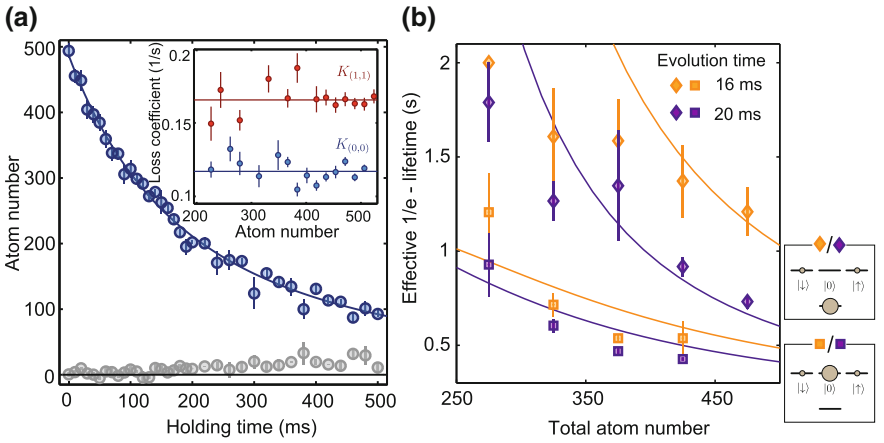

Fig. 7.3 Measurement of loss rates. The dominant source for loss in the excited hyperfine manifold $F = 2$ is a two-body process in which at least one of the scattering atoms relaxes to $F = 1$. The concomitant release of energy suffices to expel one or both atoms from the trap. **a** We assess this process by preparing pure samples in either $|2, 0\rangle$ or $|2, 1\rangle$ (not shown) and observing the subsequent decay (blue). The blue line is a fit to extract the lifetime assuming pure two-body decay. This presumption is checked by confirming that the extracted lifetimes are independent of the initial atom numbers as shown in the inset. Here, the red (blue) data points correspond to extracted loss rates K_{ii} of $|2, 0\rangle$ ($|2, 1\rangle$). Extracting loss rates is compounded by the fact that spurious spin exchange takes place. For the shown case of preparing all atoms in $|2, 0\rangle$ this means that $|2, 1\rangle$ gets populated (grey data). **b** We check the validity of our loss model for the experimentally most relevant case of small side mode populations. These side mode populations are generated by resonant spin exchange for 16 ms (purple) and 20 ms (orange), respectively. The effective $1/e$ life time of the side mode population is shown for the case of the pump mode being held in $F = 2$ (squares) and shelved in $F = 1$ (diamonds). Details of the loss model indicated by the solid lines are explained in the text

on time scales of several 100 ms. These loss mechanisms can thus be neglected for the experiments reported on in this thesis.

Having characterized the intra component loss rates, we follow reference [2] to estimate the remaining loss rates which describe scattering between two different m_F states. For this the knowledge of $K_{1,1}$ and $K_{0,0}$ suffices.

The experiments on time reversal rely on the validity of the undepleted pump approximation. Therefore, the loss of the sparsely populated side modes in presence of a large pump mode is the experimentally most relevant case. We study this situation in Fig. 7.3b. For direct comparison with the main experiments, we use spin exchange to initially populate the side modes and record the subsequent decay of the side modes. Let us first focus on the situation in which the pump mode resides in $F = 2$ (square plot markers). This describes loss during the process of spin exchange. We treat the case in which the pump mode is shelved in $F = 1$ (diamonds) afterwards. With the pump in $F = 2$, the main contribution to atom number loss of the side modes is due to $K_{1,0}$ and $K_{-1,0}$, respectively. However, the loss is not well described by a pure two-body loss model because of the additional albeit weak channels.

We take this into account by heuristically fitting an exponential for short loss times to extract an effective lifetime. We compare this to a numerical simulation which uses the estimated loss coefficients (solid lines). We let spin exchange populate the side modes for 16 ms (orange) and 20 ms (purple) respectively and find reasonable agreement for both evolution times.

During phase imprinting the pump mode is shelved within the $F = 1$ manifold (diamonds). This has a strong influence on the life time of the side modes as the dominant loss mechanism is now absent. We find the remaining loss is best described by $K_{0,1} = K_{0,-1} = 0$ (solid lines). The large deviations for lifetimes exceeding 1 s are caused by residual off-resonant spin exchange.

7.4 Detuning and Comparison to Numerical Simulation

Having experimentally extracted the nonlinear coupling strength κ and its atom number dependence we now proceed with an experimental characterization of the detuning. The difficulties in estimating the detuning from a microscopic point of view have been addressed in Sect. 6.4 where a detailed calculation of all level shifts during microwave dressing was performed. Here, we use the complementary top-bottom approach and extract the detuning from the population dynamics during spin exchange. For this, one could in principle use the detuning dependence of parametric amplification. Taking into account such a detuning by introducing $\delta = \kappa - q$ the side mode's growth can be calculated analytically and is described by

$$\langle N_+ \rangle = \frac{2\kappa^2}{\kappa^2 - \delta^2} \sinh^2(\sqrt{\kappa^2 - \delta^2}t). \tag{7.4}$$

Therefore the population growth depends (only) quadratically on detuning. Being close to resonance we find this dependence to be too weak to use it for an experimental determination of the detuning. The reason for this is that Eq. 7.4 requires the validity of the undepleted pump approximation. Therefore, the dynamic range is restricted to small side mode populations. To circumvent this problem we use the comparison to numerical simulations that take into account pump depletion. As detailed in Sect. 3.7 these numerical simulations rely on the truncated Wigner approximation which is valid up to the point where predominantly atoms from the side mode are scattered back into the pump mode.

We perform such simulations for three different total atom numbers and use the independently characterized coupling strength. Since the detuning arises from level shifts due to microwave dressing and the quadratic Zeeman effect, it is independent on the total atom number. Therefore, for each of the three cases a common detuning is used. We find best agreement to the experimental data for a detuning of $\delta = 2\pi \times 24$ Hz which is shown for all three atom numbers in Fig. 7.4. A different choice of parameter generally improves the agreement only for one particular atom number window, while it leads to significant deviations for the other two cases. The advantage of this procedure is that only one parameter is free and needs to be found.

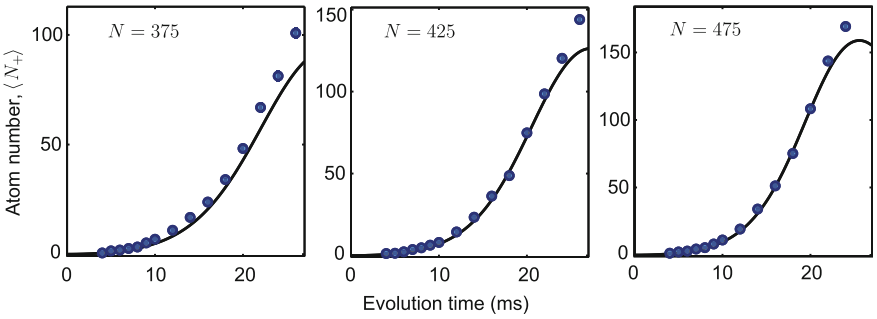

Fig. 7.4 Comparison of the numerical simulation to experimental data. To experimentally characterize the detuning of the spin exchange process we perform numerical simulations (black lines) for three different total atom numbers; $N = (375, 425, 425)$ (from left to right) and compare the results to experimental data. While the nonlinear coupling strength depends on the atom number, the detuning is unique to all three cases. We use the experimentally characterized coupling strength and its atom number dependency to restrict the numerical simulations to a single parameter, i.e. the detuning. Best agreement is found for a detuning of $\delta = 2\pi \times 24\,\mathrm{Hz}$ (black lines). For comparison, the nonlinear coupling strength for the three considered cases is $\kappa = 2\pi \times (20, 23, 25)\,\mathrm{Hz}$

The numerical simulation systematically underestimates the atom number for evolution times exceeding 22 ms. At first sight, this hints towards an underestimated coupling strength, however, we explicitly checked that this behaviour cannot be overcome by additionally adjusting the nonlinear coupling strength. While these simulations include the independently characterized loss the initial atom number is fixed. In the experiment, however, the postselection is done for a range of ± 25 atoms and characterizes the atom number after the spin exchange process took place. This might explain the disagreement at long evolution times. However, for our main experiments which involve evolution times shorter than 16 ms these discrepancies are insignificant.

For long evolution times exceeding 25 ms the growth of the side modes is not just slowed down by pump depletion. As suggested by the results of the numerical simulation for $N = 475$ the population in fact executes oscillations [3]. This is caused by the collisional shifts which are approximately compensated only for small populations which corresponds to short durations. These collisional shifts lead to a dynamically evolving spinor phase—until a phase of π is eventually built up such that time reversal is achieved and the cycle starts again.

7.5 Number Fluctuations

The individual modes making up the two-mode squeezed vacuum state do not possess a mean-field. This means that $\langle\uparrow|\,\hat{a}_\uparrow\,|\uparrow\rangle = 0$ and similarly for mode $|\downarrow\rangle$ [4]. Under such conditions the state's number fluctuations become crucial. With the atom num-

ber imbalance vanishing, $(\Delta N_-)^2 = 0$ the fluctuations in atom number sum are the most distinctive feature of the two-mode squeezed vacuum state. Having shown this in a qualitative manner at the beginning of this chapter we now characterize them quantitatively.

The two-mode squeezed vacuum has thermal-like number fluctuations in each of its constituent modes, $(\Delta N_\uparrow)^2 = \langle N_\uparrow \rangle (N_\uparrow + 1)$ and similarly for $N_\downarrow$. Additionally, both modes are strongly correlated. Due to the covariance of $N_\uparrow$ and $N_\downarrow$ the variance of the atom number sum is twice larger than the combined individual fluctuations, $(\Delta N_+)^2 = 4 \langle N_\uparrow \rangle (N_\uparrow + 1) = \langle N_+ \rangle (\langle N_+ \rangle + 2)$. In Fig. 7.5a we plot the measured variance of N_+ versus this expectation in terms of average number population. For short evolution times (indicated by colour) we find excellent agreement to this undepleted pump theory. Only for durations exceeding $\approx$15 ms pump depletion causes a levelling off. This effect is well captured by numerical simulations which are based on the truncated Wigner approximation (shown as dashed line). These fluctuations are huge compared to Poissonian noise of size $(\Delta N_+)^2 = \langle N_+ \rangle$ which is shown in grey for comparison.

As detailed, the variance of N_+ would only be half as large if the two modes were uncorrelated. These strong mode correlations can also be shown directly. For this the variance of N_- is evaluated, see Fig. 7.5b. For quantum mechanically uncorrelated

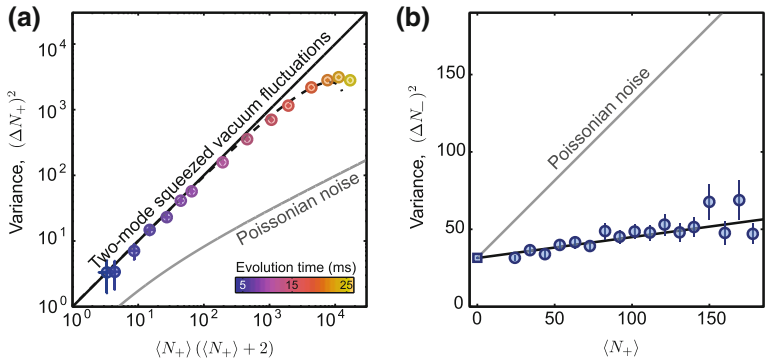

Fig. 7.5 Characteristic atom number fluctuations. **a** The two-mode squeezed vacuum state features thermal-like fluctuations when considering the summed side mode population, $N_+ = N_\uparrow + N_\downarrow$. These excess fluctuations satisfy $(\Delta N_+)^2 = \langle N_+ \rangle (\langle N_+ \rangle + 2)$ which is drawn as the diagonal line. For sufficiently short evolution times (encoded in colour) we find excellent agreement to this ideal expectation. For longer evolution times a large fraction of pump atoms is scattered into the side modes such that the undepleted pump approximation eventually ceases to be valid. This effect is well captured by a numerical simulation (shown as dashed line). Redistributing atoms among three modes in a classical process leads to Poissonian noise which is indicated as the grey line for comparison. **b** Ideally, each side mode's population exhibits perfect correlations due to the pairwise scattering process. To quantify these correlations experimentally we evaluate $(\Delta N_-)^2$ and compare it to the respective Poissonian limit. The Poissonian noise corresponds to $(\Delta N_-)^2 = \langle N_+ \rangle$ (indicated as grey line). We find suppressed fluctuations by 8.5 dB. The squared plot marker denotes an independent measurement of the detection noise. This variance contribution due to detection noise was subtracted for the data in panel **a**)

populations we expect binomial statistics to be valid, leading to $(\Delta N_-)^2 = \langle N_+ \rangle$ which is shown in grey. From a linear fit to the data (black line) we deduce that the fluctuations are suppressed by a factor of 7 (8.5 dB) compared to this classical level [5, 6]. An independent measurement of the detection noise (square plot marker) defines the line's offset. Ideally, the two-mode squeezed vacuum state fulfils $(\Delta N_-)^2 = 0$ irrespective of $\langle N_+ \rangle$.

These distinctive coherent number fluctuations of the two-mode squeezed vacuum state have far reaching implications for phase sensing. We cover these in the next section.

7.6 Number Fluctuations and Phase Dependence

There is a common argument that connects a state's coherent number fluctuations to its sensitivity towards phase changes: in order to be sensitive to a phase imprint of φ_- the probe state needs to have fluctuations of N_- that sample this phase. A similar relation holds for sensitivity with respect to the sum phase φ_+ which accordingly requires fluctuations of N_+. Often this relationship is expressed by the heuristic uncertainty relation of phase and complementary number fluctuations, which reads $(\Delta N_\pm)^2(\Delta\varphi_\pm)^2 > 1$. Therefore, the ability to precisely estimate a phase imprint relies on large coherent number fluctuations. The large fluctuations of the summed side mode population N_+ inherent to the two-mode squeezed vacuum can therefore be considered to be the underlying resource for quantum-enhanced measurements. On the other hand, spin exchange leaves the atom number imbalance N_- unaltered. As a direct consequence, the process is insensitive to the phase difference φ_- which corresponds to the Larmor phase.

It is important to note that the fluctuations of the *probe* state, i.e. the state that experiences the phase shift, are crucial. In this thesis' introduction, a scheme in which the two-mode squeezed vacuum state is fed into a conventional passive SU(2) interferometer is discussed. Here, loosely speaking, the first beam splitter converts the initial state's fluctuations of the atom number sum N_+ into fluctuations of the associated atom number difference N_-. Therefore, precise measurements of φ_- can be performed.

The potential of a probe state to perform quantum-enhanced phase measurements can be characterized by the quantum Fisher information F, which conceptually builds on the associated classical object as employed in statistics and parameter estimation. Adopted to a metrology setting, the *classical* Fisher information quantifies how well a linear phase imprint can be estimated on grounds of probability distributions [7–9]. If a measurement prescription is characterized by a large classical Fisher information then already minute phase imprints yield readily distinguishable output distributions which corresponds to a high phase sensitivity. The quantum Fisher information eliminates the device dependence. It quantifies the metrological usefulness, i.e. the phase sensitivity of a probe state under the assumption that the optimal readout is employed. Furthermore, the quantum Fisher information is often applied to com-

pare various quantum states [10, 11]. Within this paradigm, the single shot phase sensitivity is connected to the quantum Fisher information F via the Cramér-Rao bound that states $(\Delta\varphi)^2 \geq F^{-1}$. This inequality is valid for linear phase imprints; in the following we call the operator that generates the phase shift $\hat{Q}$. For pure states the Fisher information is given by the variance of this phase shift generating operator and thus reads $F = 4(\Delta\hat{Q})^2$. Within this framework the above heuristic argumentation connecting fluctuations to sensitivity can be tightened and formalised: the operator generating linear spinor phase shifts is given by $\hat{K}_z$. Consequently, the quantum Fisher Information of the two-mode squeezed vacuum state $|r, \varphi\rangle$ is given by $F = 4(\Delta Q)^2 = \langle r, \varphi| (\Delta N_+)^2 |r, \varphi\rangle$. Finally, the Cramér-Rao bound states that the phase sensitivity fulfils

$$(\Delta\varphi_+)^2 \geq [\langle N\rangle_+ (\langle N\rangle_+ + 2)]^{-1} \tag{7.5}$$

where the lower bound agrees with the ultimate Heisenberg limit. The nonlinear readout saturates this bound [12]—which is the subject of later chapters. Therefore, the coherent number fluctuations inherent to the two-mode squeezed vacuum state are the resource for quantum-enhanced interferometry.

7.7 Effects of Pump Depletion

In light of pump depletion the perfect agreement between the sum variance on the one hand, and the average population on the other hand might come as a surprise. In particular since the severe effects of pump depletion are clearly visible in the population growth for evolution times exceeding 15 ms, as shown in Fig. 7.2. However, the relationship between $(\Delta N_+)^2$ and $\langle N_+\rangle$ that is distinctive for the two-mode squeezed vacuum state remains to a good approximation intact for evolution times < 20 ms.

Therefore, the main effect pump depletion is causing can be divided into two separate periods of time: for short evolution times, parametric amplification remains a good approximation—only the nonlinear coupling strength $\kappa = gN_0$ is (dynamically) reduced. While this leads to a reduced growth rate of the side modes, the emerging state still shares the essential features of the two-mode squeezed vacuum state. This is reflected in the relationship between average population and the respective number fluctuations.

Only for longer evolution times this effective description breaks down and the generated state significantly deviates. This becomes most evident when considering the full number distribution of N_+ which is shown in Fig. 7.6. Here for short evolution times ($t = 14$ ms) the thermal-like distribution arises. The black line is the expectation of a two-mode squeezed vacuum state for the directly observed average population (indicated by dark coloured bin). Therefore, the black line is not a fit to the data but exploits the fact that the two-mode squeezed vacuum state is fully characterized by a single parameter, e.g. its average value. This relationship breaks down as the evolution time proceeds. We use this comparison to assess the effect of pump depletion. For

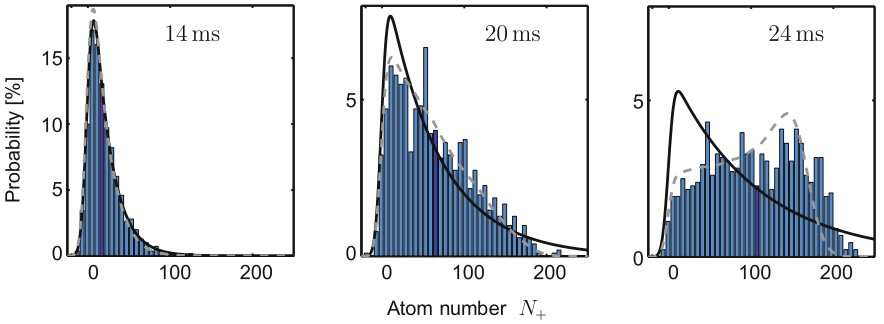

Fig. 7.6 Breakdown of the undepleted pump approximation. The atom number distribution of the two-mode squeezed vacuum state is completely described by a single parameter, e.g. its average mode population. Here, we show the full atom number distribution of N_+ obtained after three different evolution times under spin exchange. The respective average value is indicated as the dark coloured histogram bin. Based on this value the expected thermal-like distribution is shown in black. While we find perfect agreement for an evolution time of $t = 14\,\mathrm{ms}$, significant deviations show up for longer evolution times. Here the measured atom number histogram cannot be described by a thermal-like distribution. At this stage the undepleted pump approximation breaks down and the analogy to parametric amplification is invalidated. The grey dashed line shows the results of a numerical calculation that reproduces the characteristics of the data

$t = 20\,\mathrm{ms}$ the distribution that would correspond to the measured average value does not fit to the shape of the experimental histogram that resembles a triangle. For even longer evolution times we observe an almost uniform distribution that does not even share the characteristic skew of the thermal-like distribution [13]. At this stage, the state wraps around the Bloch sphere and explores the curvature of the sphere as indicated in Fig. 3.5. This causes the departure from the two-mode squeezed vacuum. For all evolution times we find reasonable agreement to our numerical simulation which is shown as the grey dashed line.

7.8 Influence of a Seed

We aim at performing spin exchange with initially empty side modes [14–16]. Under such circumstance the quantum nature of the process is most pronounced as the two-mode squeezed vacuum state with its large coherent fluctuations emerges.

Let us consider the consequences if one side mode is instead populated initially. We assume that this spurious population follows Poissonian fluctuations. In Sect. 4.6 the analogy between the amplification of vacuum fluctuations and spin exchange was developed. Within this framework the characteristic two-mode squeezed vacuum fluctuations that arise during amplification, stem exclusively from the spontaneous process. If, hypothetically, the spontaneous process were absent the amplification would not add extra noise. Therefore, the resulting state of spin exchange

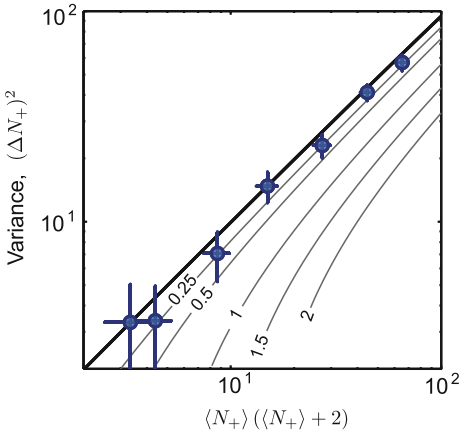

Fig. 7.7 Dependence of the atom number fluctuations on initial seeds. Measurements of the atom number sum and its fluctuations can be used to bound the size of a minute seed that might have triggered the spin exchange initially. For this we replot the data of Fig. 7.5 restricted to small side mode populations $\langle N_+\rangle < 9$. In this range, depleted pump and loss effects can be neglected. The extremal atom number fluctuation of $(\Delta N_+)^2 = \langle N_+\rangle\,(\langle N_+\rangle + 2)$ (bold solid line) are obtained only for a vanishing seed. The grey lines show the expected atom number fluctuations for the indicated seed size. Here the seed size corresponds to the average atom number that is in each of the two side modes. The same result is obtained for unequal partitioning as long as the total size remains equal. Therefore a seed of 1 atom could also correspond to 2 atoms in one mode while the other mode is empty. We find best agreement to our experimental data if we assume an initial seed of 0.25 atoms; On grounds of this analysis we can exclude seeds greater than 0.5 atoms

is a combination of the amplified initial state, and a two-mode squeezed vacuum state contribution. If the spontaneous process prevails, one has on top of the largely fluctuating two-mode squeezed vacuum state a small admixture of a coherent state. Therefore, the initial coherent population reveals itself in reduced number fluctuations. We exploit this connection to experimentally assess the size of a potential seed in a regime where absorption imaging cannot be used unambiguously, i.e. for average mode populations < 0.5 atoms. Thereby we probe an initial seed via the ensuing spin exchange dynamics. For this we compare the measured number fluctuations of N_+ to the extremal value of $(\Delta N_+)^2 = \langle N_+\rangle\,(\langle N_+\rangle + 2)$ which corresponds to the spontaneous contribution. In Fig. 7.7 this limit amounts to the solid black line. The experimental data and its exposition is identical to Fig. 7.5. However, here we restrict ourselves to small atom numbers; then the discussion is model independent as the influence of loss and pump depletion can be neglected. The grey lines show the predicted number fluctuations for various seed sizes. For instance, the line labelled 1 reflects a seed with 1 atom per side mode; portioning the—in total—2 atoms differently among the two modes yields equivalent results. We find the experimental data to lie somewhat consistently below the bound of the two-mode squeezed vacuum state. Best agreement is found when assuming a seed of size 0.25 atom. Seed sizes larger than 0.5 atoms can be excluded on this basis.

References

1. J. Söding, D. Guéry-Odelin, P. Desbiolles, F. Chevy, H. Inamori, J. Dalibard, Three-body decay of a rubidium Bose-Einstein condensate. Appl. Phys. B **69**, 257–261 (1999)
2. S. Tojo, T. Hayashi, T. Tanabe, T. Hirano, Y. Kawaguchi, H. Saito, M. Ueda, Spin-"dependent inelastic collisions in spin-2 Bose-Einstein condensates". Phys. Rev. A **80**, 042704 (2009). https://doi.org/10.1103/PhysRevA.80.042704
3. M.-S. Chang, Q. Qin, W. Zhang, L. You, M.S. Chapman, Coherent spinor dynamics in a spin-1 Bose condensate. Nat Phys **1**, 111–116 (2005). https://doi.org/10.1038/nphys153
4. S.A. Haine, S.S. Szigeti, M.D. Lang, C.M. Caves, Heisenberg-limited metrology with information recycling. Phys. Rev. A **91**, 041802 (2015). https://doi.org/10.1103/PhysRevA.91.041802
5. E.M. Bookjans, C.D. Hamley, M.S. Chapman, Strong quantum spin correlations observed in atomic spin mixing. Phys. Rev. Lett. **107**, 210406 (2011), https://doi.org/10.1103/PhysRevLett.107.210406
6. B. Löcke, J. Peise, G. Vitagliano, J. Arlt, L. Santos, G. Tóth, C. Klempt, Detecting multiparticle entanglement of Dicke States. Phys. Rev. Lett. **112**, 155304 (2014). https://doi.org/10.1103/PhysRevLett.112.155304
7. G. Tóth, I. Apellaniz, Quantum metrology from a quantum information science perspective. J. Phys. A Math. Theor. **47**, 424006 (2014). https://doi.org/10.1126/science.1250147
8. L. Pezzé, A. Smerzi, M. K. Oberthaler, R. Schmied, and P. Treutlein, Non-lassical states of atomic ensembles: fundamentals and applications in quantum metrology (2016), arXiv:1609.01609
9. H. Strobel, W. Muessel, D. Linnemann, T. Zibold, D.B. Hume, L. Pezzé, A. Smerzi, M.K. Oberthaler, Fisher information and entanglement of non-Gaussian spin states. Science **345**, 424–427 (2014). https://doi.org/10.1126/science.1250147
10. F. Fröwis, Lower bounds on the size of general Schrödinger-cat states from experimental data. J. Phys. A: Math. Theor. **50**, 114003 (2017), http://stacks.iop.org/1751-8121/50/i=11/a=114003
11. F. Fröwis, P. Sekatski, W. Dör, N. Gisin, and N. Sangouard, Macroscopic quantum states: measures, fragility and implementations (2017), arXiv:1706.06173
12. M. Gabbrielli, L. Pezzé, A. Smerzi, Spin-mixing interferometry with bose- einstein condensates. Phys. Rev. Lett. **115**, 163002 (2015). https://doi.org/10.1103/PhysRevLett.115.163002
13. C.S. Gerving, T.M. Hoang, B.J. Land, M. Anquez, C.D. Hamley, M.S. Chapman, Non-equilibrium dynamics of an unstable quantum pendulum explored in a spin-1 Bose-Einstein condensate. Nat. Commun. **3**, 1169 (2012). https://doi.org/10.1103/PhysRevLett.115.163002
14. C. Klempt, O. Topic, G. Gebreyesus, M. Scherer, T. Henninger, P. Hyllus, W. Ertmer, L. Santos, J.J. Arlt, Parametric Amplification of Vacuum Fluctuations in a Spinor Condensate. Phys. Rev. Lett. **104**, 195303 (2010). https://doi.org/10.1103/PhysRevLett.104.195303
15. R.J. Lewis-Swan, K.V. Kheruntsyan, Sensitivity to thermal noise of atomic Einstein-Podolsky-Rosen entanglement. Phys. Rev. A **87**, 063635 (2013). https://doi.org/10.1103/PhysRevA.87.063635
16. B.E. Anderson, B.L. Schmittberger, P. Gupta, K.M. Jones, P.D. Lett, Optimal phase measurements with bright- and vacuum-seeded SU(1,1) interferometers. Phys. Rev. A **95**, 063843 (2017). https://doi.org/10.1103/PhysRevA.95.063843

Chapter 8
Quantum-Enhanced Sensing Based on Time Reversal

Having characterized the building block of spin exchange and the nascent entangled state we now detail the interferometric sequence that arises when two periods of spin exchange are performed in sequence. In this section we study the symmetric case where initial entangling and subsequent nonlinear readout are matched in length. First, we study the particular case of time reversal and present its connection to noiseless amplification. We then continue with the full phase dependence and experimentally assess the quantum-enhanced performance. We explicitly demonstrate a phase sensitivity that beats the classical limit. We conclude with describing the noise tolerance of the presented interferometry scheme which will be revisited in the following chapter. The content of this chapter is published in reference [1].

8.1 Time Reversal

Having established that the fluctuations of N_+ are idiosyncratic for the two-mode squeezed vacuum we now present the complete scheme for disentangling readout via time reversal. This scheme is divided into three parts; entangled state generation, phase interrogation, and finally, a matched period under time reversal to disentangle the state. Such a tripartite time sequence is shown in Fig. 8.1a where the variance of N_+ is plotted as a time trace: first, evolution under the nonlinear spin exchange Hamiltonian generates the entangled state (time frame indicated by red arrow). During this initial entangled state preparation the variance experiences a drastic build-up (up to 8 ms). Subsequently, spin exchange is stopped to allow for linear phase interrogation. This interrogation time is chosen such that a dynamic spinor phase of π accumulates. The second period t_2 of spin exchange then proceeds with negative coupling strength (see blue arrow). Therefore the fluctuations are revoked. We find a pronounced minimum for approximately matched evolution times $t_1 \approx t_2$. Ideally, at

D. Linnemann, *Quantum-Enhanced Sensing Based on Time Reversal of Entangling Interactions*, Springer Theses,
https://doi.org/10.1007/978-3-319-96008-1_8

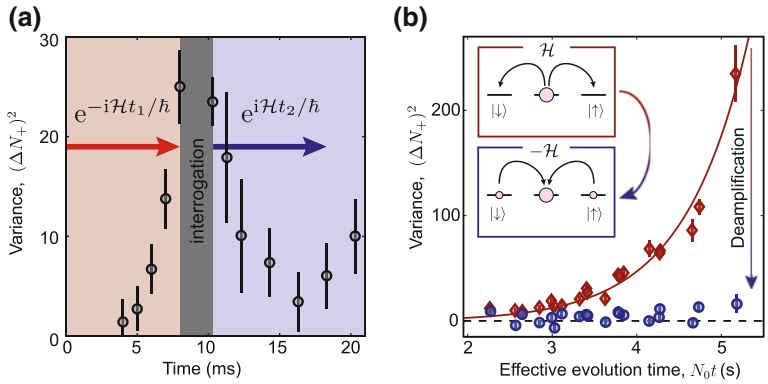

Fig. 8.1 Disentangling with nonlinear time reversal. **a** The nonlinear readout scheme is divided into three parts. During the first period an entangled state is generated (red arrow): the time trace of the characteristic variance $(\Delta N_+)^2$ shows a drastic increase as quantum correlations are built up. During the interrogation stage (grey) nonlinear spin exchange is stopped. With a spinor phase of π being accumulated the ensuing period of spin exchange revokes the fluctuations generated during the first period. We find a pronounced minimum close to the matched case of equal evolution times, $t_1 \approx t_2$. This setting is studied in more detail in panel **b**: here the entanglement and subsequent disentanglement is probed for different strengths of the nonlinear process, i.e. by tuning κt. For this the side mode variance $(\Delta N_+)^2$ before (red diamonds) and after time reversal (blue) is shown. The red line shows the expected behaviour in undepleted pump approximation. Over the entire range of nonlinear couplings we find good reversion to the initial state (dashed)

this point the second period of spin exchange reverses the effect of the first such that the well-known separable initial state is recovered. For longer evolution times the process of entanglement generation starts all over again concomitant with growing fluctuations.

In the following we investigate the balanced situation of two equally long periods of spin exchange. In panel (b) the variance after the first (red diamonds) and second (blue circles) period of spin exchange is shown, respectively. By postselecting experimental realizations with different total atom numbers the effective nonlinear coupling strength is varied additionally to choosing evolution times in the range of $t_1 = t_2 = 7$–10 ms. For the full range of experimental parameters we find good reversion to the initial state with vanishing atom number (dashed line). The red solid line is a fit to the expected variance increase within undepleted pump approximation.

8.2 Noiseless Amplification

Within the amplification framework the time reversal readout can be understood as noiseless amplification. To see this we first have to clarify in what sense amplification usually adds spurious noise [2, 3]. For this we consider a single mode, say $|\uparrow\rangle$ with average atom number $\langle N_\uparrow^{\text{in}} \rangle$. In the process of spin exchange the atom num-

ber of this mode gets amplified to $\langle N_{\uparrow}^{\text{out}} \rangle = \cosh^2(\kappa t) \langle N_{\uparrow}^{\text{in}} \rangle + \sinh^2(\kappa t)$ as shown in Sect. 4.6. Here, the term $\sinh^2(\kappa t)$ describes the effect of spontaneous amplification, i.e. amplification of vacuum fluctuations. This is responsible for a degradation of signal-to-noise during amplification. To see this we look at the atom number variance of this single mode [4]. It is given by

$$(\Delta N_{\uparrow}^{\text{out}})^2 = \cosh^4(\kappa t)(\Delta N_{\uparrow}^{\text{in}})^2 + (N_{\uparrow}^{\text{in}} + 1)\sinh^2(\kappa t)\cosh^2(\kappa t). \tag{8.1}$$

In the large gain and population limit the signal-to-noise ratios read: $S_{\text{in}}/S_{\text{out}} = S_{\text{in}} + 1$ where S_{in} denotes the signal-to-noise ratio for the input mode, $S_{\text{in}} = (N_{\uparrow}^{\text{in}})^2/(\Delta N_{\uparrow}^{\text{in}})^2$ and a similar definition holds for mode $|\uparrow\rangle$. For Poissonian mode population at the input the signal-to-noise ratio is thereby bisected. This is usually referred to when saying that the noise figure increases by at least 3 dB during amplification [2].

While we used the specific spin exchange Hamiltonian for this derivation the argument is general. It goes back to Haus and Caves [5, 6] who recognized that quantum amplification cannot be realized by simply substituting mode operators like $\hat{a} \rightarrow G\hat{a}$ where $|G|^2$ would correspond to the amplifier's gain. Instead, quantum mechanics forces the introduction of additional degrees of freedom for the amplifier—otherwise the bosonic commutation relations could not be retained. Such internal modes deteriorate the signal via their spontaneous amplification [2].

For the spin exchange an extra degree of freedom is given by the other side mode, i.e. $|\downarrow\rangle$. The 3 dB noise limit on amplification can be surpassed by using entanglement [7, 8]. For this the mode to be amplified ($|\uparrow\rangle$) needs to be entangled with the amplifier's internal mode ($|\downarrow\rangle$). In the spin exchange setting this is naturally the case. Under such conditions the amplification is noiseless. This is because the spontaneous term $\sinh^2(\kappa t)$ which degrades the output signal is removed by destructive interference between the two entangled modes.

As we start the interferometric sequence with initially empty side modes we probe this destructive interference in its purest form. Therefore, the absorption of fluctuations which is enabled by entanglement makes noiseless amplification possible. In light of this amplification framework we can now reinterpret the results shown in Fig. 8.1b: in fact, the variance obtained after the initial entangling reflects the quantum mechanically required spurious noise during amplification. This corresponds to Eq. 8.1 when no input signal is applied. Therefore the measurement originally used to characterizes the generation of the entangled state also represents the minimal amount of noise that is added during amplification. This noise level can only be surpassed by using entanglement. This is demonstrated by the subsequent time reversal. Here almost no spurious noise is added during the final amplification process and the noise limit of amplification is clearly surpassed. In this scheme the first period of spin exchange is used to generate entanglement with respect to the amplifier's internal mode. For actual amplification purposes the signal that shall be amplified has to be mixed with this entangled state. This could readily be achieved by applying a microwave pulse to either of the side modes in between both periods

of spin exchange. A analogous scheme has recently been realized with entangled photons [7]. This noiseless amplification during readout is an important feature of the interferometric sequence which we will detail in the following chapter.

8.3 Interferometry Fringe

With time reversal being reached for the particular phase setting $\varphi = \pi$ we now study the nonlinear readout scheme for arbitrary phase imprints. After a spinor phase imprint of φ the nonlinear readout implements the mode transformation

$$\begin{pmatrix} a_\uparrow \\ a_\downarrow^\dagger \end{pmatrix} \to \begin{pmatrix} \cosh \kappa t & \mathrm{e}^{\mathrm{i}\varphi} \sinh \kappa t \\ \mathrm{e}^{-\mathrm{i}\varphi} \sinh \kappa t & \cosh \kappa t \end{pmatrix} \begin{pmatrix} a_\uparrow \\ a_\downarrow^\dagger \end{pmatrix}. \tag{8.2}$$

Applying this transformation to the two-mode squeezed vacuum state yields an interferometry fringe that is given by

$$\langle N_+ \rangle = \langle N_+^{\text{inside}} \rangle (\langle N_+^{\text{inside}} \rangle + 2)(1 + \cos \varphi) \equiv \mathcal{V}(1 + \cos \varphi). \tag{8.3}$$

Here $\left\langle N_+^{\text{inside}} \right\rangle$ denotes the average atom number of the initial two-mode squeezed vacuum state that acts as the probe state. This state is generated by the first period of spin exchange and constitutes the quantum resource for phase sensing. The nonlinear coupling strength (and duration) for both periods of spin exchange are matched. Otherwise evolution under the time reversed generation process at phase $\varphi = \pi$ would not yield complete cancellation. We will study this nonbalanced scheme in a later chapter.

Experimentally, we detail the occurrence of an interferometry fringe in Fig. 8.2. In panel (a) a time trace of the side mode population during the interferometric sequence is shown. The first period of spin exchange ends after 8 ms as indicated by the vertical grey line. At this point different spinor phases are imprinted. For this, microwave dressing is stopped, and the pump mode is shelved in $|1, 0\rangle$ to quickly interrupt spin exchange. Holding the atoms for a variable time (which is not shown in the figure) realizes different spinor phases. Then spin exchange is continued by swapping the pump back to $|2, 0\rangle$ and reactivating microwave dressing. The solid lines denote the results of numerical simulations without any free parameters. After 8 ms (indicated by the dashed rectangle) the average side mode population constitutes the interferometry fringe as shown in panel b (note the common plot markers). The black line is a sinusoidal fit, while the horizontal grey line indicates the average side mode population $\left\langle N_+^{\text{inside}} \right\rangle$ generated by the first period of spin exchange.

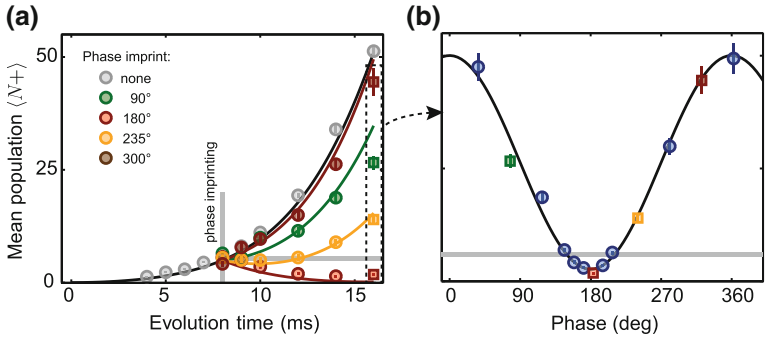

Fig. 8.2 Side mode populations for different phase imprints. **a** Average side mode population $\langle N_+ \rangle$ during the interferometric sequence. The first period of spin exchange lasts for 8 ms. At this point (indicated by the vertical grey line), different spinor phases are imprinted (see legend) before spin exchange is continued for another 8 ms. Time reversed dynamics is obtained for a phase imprint of π (red). All other shown phase imprints lead to an amplified output signal. Solid lines show the result of numerical simulations. **b** The characteristic interferometry fringe is obtained in the balanced case of equal durations, $t_1 = t_2$ (square plot markers in panel a). The horizontal grey line denotes the average side mode population after the first period of spin exchange

8.4 Population Distribution

The state leaving the interferometric sequence is a two-mode squeezed vacuum state. In Fig. 8.3 we show experimentally obtained histograms of the summed side mode populations N_+. The black lines are fits to the expected thermal distribution also taking into account detection noise by convolution with a Gaussian of appropriate width. The red histogram on the left shows the probe state inside the interferometer. Its average atom number ($\langle N_+^{\text{inside}} \rangle = 2.8$) is indicated by the dark coloured bin. At this small average population the width of the histogram is predominantly caused by detection noise. The blue histograms are recorded at the output of the interferometer for different applied spinor phase imprints inside. They show the skewed population distributions characteristic of the two-mode squeezed vacuum state. With the individual distributions being widespread, their average value (indicated by the dark coloured histogram bin) remains constrained to the grey shaded area. A zoom-in into this grey shaded area reveals the interferometry fringe (lower panel). The black line is a sinusoidal fit which agrees with the results of numerical simulations. The average atom number of the probe state inside the interferometer is denoted by the horizontal red line. The intrinsic amplification of the nonlinear readout scheme becomes apparent when comparing this level to the maximal fringe size as indicated.

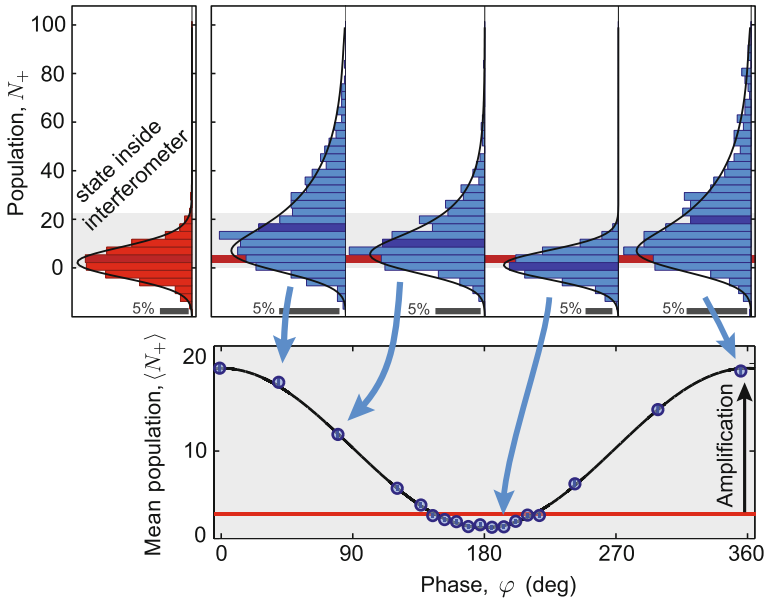

Fig. 8.3 Full counting statistics of the time reversal sequence. Experimental population distributions of N_+ at different stages of the interferometer: the red histogram shows the population within the interferometer. Its average value is indicated by the red horizontal line. The grey scale bar denotes a frequency of 5%. For all phase imprints the population distributions recorded at the output of the interferometer (blue) follow a thermal-like distribution. The black lines are fits to thermal distributions also taking into account Gaussian detection noise. Each histograms contains about 750 experimental realizations. The respective average values (indicated by the dark coloured bins) give rise to the interferometry fringe which is shown in the lower panel. Note that the lower panel is a zoom-in into the grey shaded area

8.5 Variance Fringe

The fluctuations of the interferometry fringe follow directly from the fact that the output state is two-mode squeezed vacuum. The variance of N_+ reads

$$(\Delta N_+)^2 = \langle N_+ \rangle \left(\langle N_+ \rangle + 2\right) = 2\mathcal{V}(1 + \cos\varphi) + [\mathcal{V}(1 + \cos\varphi)]^2. \tag{8.4}$$

This relationship leads to a non-sinusoidal atom number variance: the output signal has two Fourier components with the effect of a flattening close to the fringe minimum at spinor phase setting $\varphi = \pi$. Therefore close enough to the point of complete time reversal the variance remains levelled. The measured fringe of the atom number sum variance $(\Delta N_+)^2$ as depicted in Fig. 8.4 and clearly shows this nonsinusoidal fringe. The black solid line is the expectation within undepleted pump theory. Here based on the measured interferometry fringe of $\langle N_+ \rangle$ the variance expectation $(\Delta N_+)^2 = \langle N_+ \rangle \left(\langle N_+ \rangle + 2\right)$ is plotted. The deviations at the fringe maxima are caused by pump

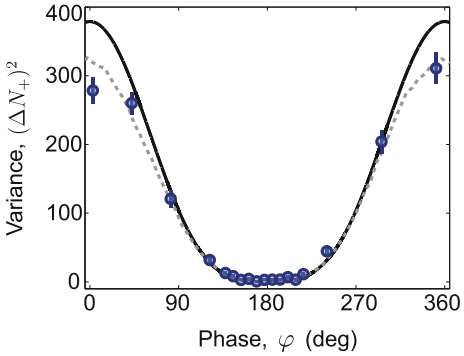

Fig. 8.4 Variance fringe. Fringe of the atom number sum variance recorded at the output. The phase dependence is non-sinusoidal: in the vicinity of the dark fringe at $\varphi = \pi$, the variance is significantly flattened resembling a bathtub curve. The black line shows the expected behaviour in undepleted pump approximation. This is not a fit to the data but instead takes the average atom number as input. Significant deviations are found only at the maxima where pump depletion limits the variance growth. The grey dashed line denotes a numerical simulation. Close to the dark fringe both methods describe the data similarly well

depletion. This effect is well captured in the numerical simulation (dashed grey line). Close to the minimum, pump depletion is negligible and both theory lines coincide. Error bars of the variance are estimated using the jackknife method. In this resampling technique, the error of the variance is determined by the impact it makes if any single observation is omitted. The combination of both, a flattened variance and a sinusoidal average output signal as shown in Fig. 8.3 allows for improved phase sensitivity. We elaborate on this in the next section.

8.6 Quantum-Enhanced Phase Sensitivity

By virtue of the nonlinear readout the spinor phase is mapped onto the first moment of the output distribution, i.e. the average atom number. Consequently, the phase sensitivity can be estimated by employing error propagation onto this average output signal [9, 10],

$$(\Delta\varphi)^2 = \frac{(\Delta N_+)^2}{|\mathrm{d}\langle N_+\rangle/\mathrm{d}\varphi|^2}. \tag{8.5}$$

Remarkably, this simple procedure is optimal as it saturates the Cramér-Rao bound [11]. High phase sensitivities correspond to small errors $(\Delta\varphi)^2$ on the inferred phase with the classical bound being given by $(\Delta\varphi)^2 = \left\langle N_+^{\mathrm{inside}}\right\rangle^{-1}$. On a phenomenological level this limit can be surpassed because the atom number variance of the output signal remains levelled close to the fringe minimum. At the same time the output

fringe is sinusoidal and magnified by the interferometer's intrinsic amplification. The combination of both effects yields a phase sensitivity given by

$$(\Delta\varphi)^2 = \frac{1}{1-\cos\varphi}\left[\frac{2}{\langle N_+^{\text{inside}}\rangle(\langle N_+^{\text{inside}}\rangle+2)} + (1+\cos\varphi)\right]. \tag{8.6}$$

The optimal working point is at spinor phase $\varphi = \pi$ which corresponds to the time reversal setting. Here a phase sensitivity at the ultimate Heisenberg limit is attained, $(\Delta\varphi)^2 = \langle N_+\rangle\,(\langle N_+ + 2\rangle)^{-1}$. When leaving this working point phase sensitivity degrades. Quantum-enhanced performance is obtained only within a phase window given by $\varphi = \pm\arccos\left(-\langle N_+\rangle/(\langle N_+\rangle + 2)\right)$. Therefore, the larger the size of the probe state, $\langle N_+\rangle$, the smaller the region of quantum-enhanced performance gets [10].

Figure 8.5 details the experimental procedure to extract the phase sensitivity. Panel (a) shows the average atom number $\langle N_+\rangle$ in close vicinity of the dark fringe. We determine the slope of the signal by a sinusoidal fit (black solid line). Since pump depletion limits the growth of the side mode population at the fringe's maximum this fit takes into account only the data points close to the minimum. We investigate and justify this fitting procedure below. Based on this fit the expected shape of the associated number variance is estimated. The result is shown as the solid black line in panel (b). We find perfect agreement when allowing for an offset of 4 atoms^2 that displaces the expected variance curve vertically. This heuristic offset takes into account the experimentally nonideal reversion to vacuum. For a two-mode squeezed vacuum state this variance corresponds to an average mode population of 0.65 ± 0.05 atoms per side mode. The independently characterized detection noise (which amounts to 33 atoms^2 in $(\Delta N_+)^2$) is indicated by the dotted horizontal line.

The resulting phase sensitivity is shown in panel (c). For this we evaluate the measured atom number variance at each phase setting and divide it by the derivative of the output signal which in turn is obtained from the fit as detailed above. At spinor phase $\varphi = \pi$ a division by zero is encountered. However on both sides of the divergence we find experimental phase sensitivities that surpass the Standard Quantum Limit (SQL, indicated by the grey bar). The black solid line shows the phase sensitivity that is expected from the fits of the atom number $\langle N_+\rangle$ and the variance, respectively. The width of the divergence at phase $\varphi = \pi$ is caused by the residual fluctuations found at the fringe minimum. In contrast, the dashed line shows the phase sensitivity if reversibility were ideal and no offset in variance is included. In the inset the phase sensitivity over the full phase range 0–2π is shown. High phase sensitivity which surpasses the Standard Quantum Limit is reached only in vicinity of the dark fringe where (partial) time reversal occurs. At other working points only poor sensitivity is found. We find good agreement to the theory over almost two orders of magnitude.

The value of the SQL and Heisenberg limit, respectively, are determined by directly measuring the phase sensing average atom number inside the interferometer. For these measurements we omit the second period of spin exchange. Similar to the control measurements used to independently characterize the detection noise we perform these runs interleaved with the measurements of the full interferomet-

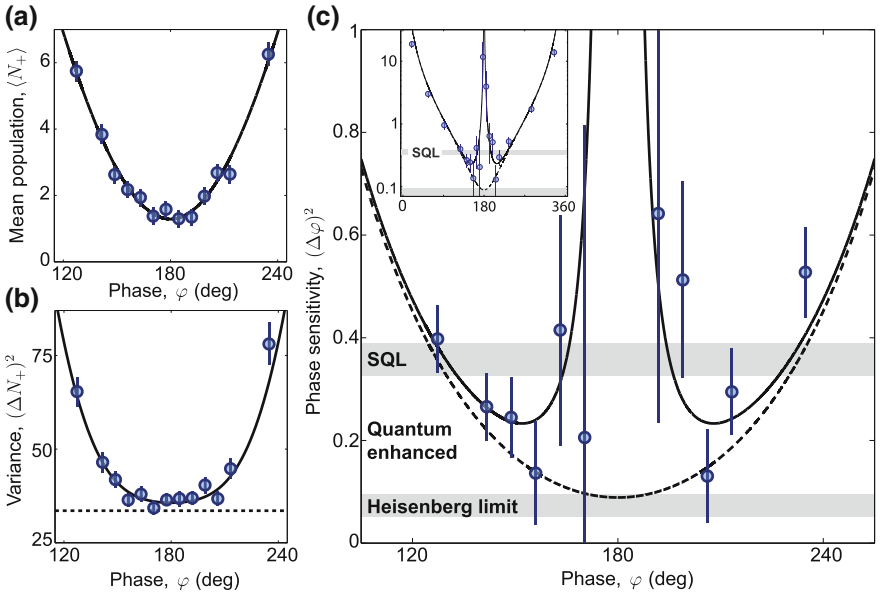

Fig. 8.5 Quantum-enhanced phase sensitivity. The phase sensitivity is estimated by applying Gaussian error propagation onto the average atom number $\langle N_+ \rangle$. **a** The derivative of the output signal is determined by a sinusoidal fit (black line). To limit spurious effects of pump depletion we restrict the fit to the vicinity of the fringe minimum. The corresponding variance is shown in panel (**b**). The dotted line indicates the contribution of detection noise which amounts to 33.5 ± 1.3. The fringe shows the characteristic levelling-off close to spinor phase π. The black line denotes the expected variance in undepleted pump theory. We find good agreement when allowing for an atom variance offset (as shown in panel a) which takes into account the nonideal reversibility. **c** Phase sensitivity. The Standard Quantum Limit (denoted by the grey bar, width corresponds to two s.d.) is surpassed in close vicinity of the fringe minimum. The dashed line denotes the undepleted pump theory which attains the Heisenberg limit (grey bar), while the black lines includes additional fluctuations due to the nonideal reversibility which leads to a divergence at spinor phase π. The SQL and Heisenberg limit, respectively, are determined by independent measurements of the atom resource inside the interferometer. The inset shows the phase sensitivity over the full phase range; over two orders of magnitude we find good agreement to theory

ric sequence. The width of the grey bars reflect the uncertainty in determining this average atom number $\left\langle N_+^{\text{inside}} \right\rangle = 2.8 \pm 0.2$.

We choose such small probe sizes to ensure that during the nonlinear readout the pump is not significantly depleted. By recording the entire fringe, we demonstrate the nonlinear readout in its idealised form of an SU(1,1) interferometer. Note that for phase sensing applications the limitation on small probe sizes is relaxed significantly. This is because the optimal working point is close to time reversal where pump depletion is negligible. In such situations, the probe size can be increased by an order of magnitude—until eventually pump depletion in the preparation step (and not during readout) limits the generation of an entangled state.

8.7 Fringe Enhancement and Noise Suppression

In this section we study the underlying working principle of the balanced interferometer in more detail. During the nonlinear readout the output fringe's size gets magnified while the fluctuations at the point of time reversal remain suppressed. In the previous section we identified this interplay as the key feature which enables quantum-enhanced phase sensitivity. Here we systematically study this interplay for

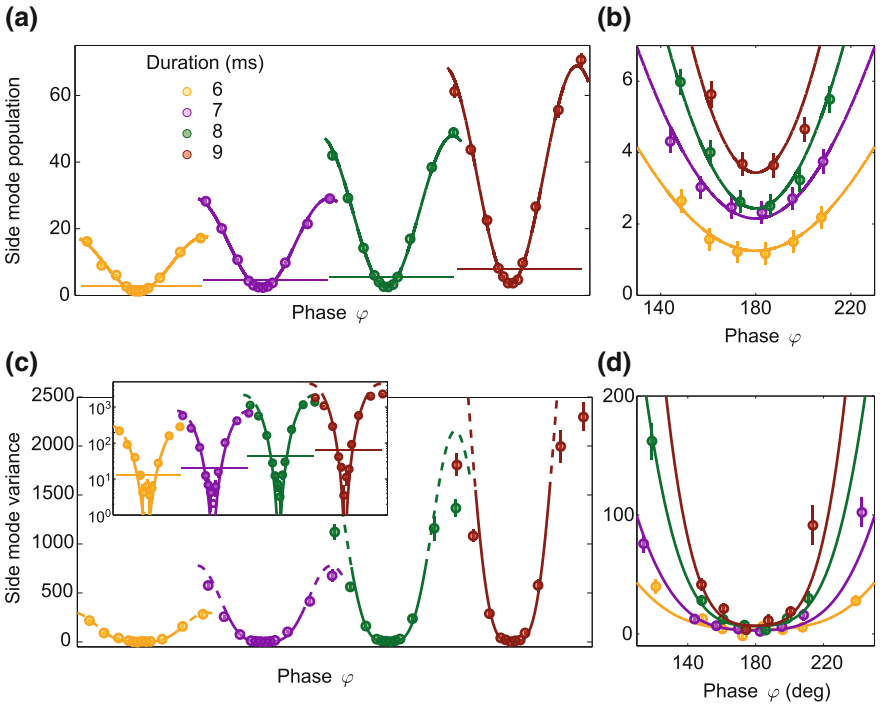

Fig. 8.6 Fringe enhancement and noise suppression. **a** Output fringes obtained for different durations of spin exchange as indicated by colour. For illustrative reasons the individual fringes are displaced and drawn next to each other. The atom number generated by the first period of spin exchange is indicated by the respective horizontal line. Starting from this level, the second period of spin exchange amplifies the atom number in a nonlinear fashion. Thereby the overall fringe size is drastically enhanced easing detection. For each case, both periods of spin exchange have equal duration such that time reversal to the initial vacuum state is expected at the minima. Solid lines are sinusoidal fits. **b** Zoom-in into the fringe minima. Experimentally, best reversibility is found for short durations of spin exchange. **c** Atom number variance of the output fringe. While at the maxima the variance grows massively, the flattened region around the dark fringe becomes compressed for longer durations under spin exchange. Starting from the average side mode population (shown in panel a), the solid lines indicate the expected variance in undepleted pump approximation. The inset shows the data semi-logarithmically, highlighting the suppression of fluctuations down to single quanta level. **d** Zoom-in into the fringe minima. We find the phase dependence of the variance to be well described within undepleted pump theory (solid lines). We merely allow for a phase-independent noise offset to take into account the imperfect reversibility

a wider range of nonlinear couplings; in particular, we explore the regime of larger spin exchange durations.

Figure 8.6a shows the output fringe obtained for different durations of spin exchange, ranging between 6–9 ms as indicated. For clarity, the fringes are displaced horizontally. Technically, the phase of each fringe is scanned by an identical holding period that ranges between 0–2 ms. Clearly, the fringe size increases drastically for larger durations of spin exchange. Going from 6 to 9 ms (a mild increase of 50%) magnifies the fringe by a factor of four. The solid lines are sinusoidal fits. The horizontal lines denote the average atom number within the interferometer. Experimentally, we find a less perfect reversibility for long durations. The corresponding fringe minima are shown in panel (b). We investigate this theoretically not expected behaviour at a later point in time. The fringes of the atom number variance are shown in panel (c). Here the solid lines correspond to the expected behaviour within undepleted pump approximation. The variance fringe grows drastically in size when extending the duration under spin exchange. Consequently, the phase window for which a flattened variance is found becomes narrower; thereby, the region of quantum-enhanced phase sensitivity shrinks accordingly as mentioned above. The inset shows the data in logarithmic scale. The horizontal bar denotes the level of fluctuations generated by the first period of spin exchange. Compared to this level, we find significantly reduced fluctuations close to the fringe minima. Panel (d) shows a common zoom-in into the minimum of each variance fringe. We find perfect agreement to the undepleted pump theory. This excellent agreement to theory motivates us to estimate the phase sensitivity in an indirect manner by using these fitted curves. We detail this procedure in the next sections.

8.8 Determining the Derivative of the Output Signal

A crucial part in determining the phase estimation is the experimental determination of the output signal's slope. Ideally, the visibility of the fringe $\mathcal{V}$ and thus the signal's slope is given by the number of atoms inside the interferometer,

$$\mathcal{V} = 2\langle N_+^{\text{inside}}\rangle(\langle N_+^{\text{inside}}\rangle + 2) \tag{8.7}$$

Experimentally, however, the fringe visibility is reduced by both, pump depletion that affects the fringe maximum, and incomplete reversion at the minimum, respectively. In Fig. 8.7 we experimentally assess the connection between fringe visibility and average probe atom number. We employ two fitting methods to estimate the slope of the signal. To compare both methods we use the inferred value of the probe atom number as a common reference. Finally we compare the respective fitting result to the directly measured average atom number of the probe state which is plotted on the y-axis. For this procedure we consider balanced interferometry sequences with durations of spin exchange ranging between 6–10 ms. Additionally, we include different total atom numbers in the analysis to extend the dynamic range to $\langle N_+^{\text{inside}}\rangle = 1 - 10$.

Examples of the underlying interferometry fringes are shown in Fig. 8.6a. The theory expectation (Eq. 8.7) is represented by the black diagonal line in Fig. 8.7a. The red data shows the result if the entire fringe is fitted with one sinusoidal function. Since pump depletion strongly modifies the output fringe this yields a severely underestimated slope of the signal. This is exemplified in panel (b) which shows the extreme case of $\langle N_+ \rangle = 12$ (rightmost point in panel a) corresponding to 10 ms of spin exchange. Evidently, the data cannot be described by such a single sinusoidal fringe (red). In particular the signal's slope close to the fringe minimum is underestimated massively (see inset). To capture the slope more accurately we restrict the sinusoidal fit to the minimum (indicated by solid blue line). The dashed line shows the continuation of this sinusoidal fit and thus the influence of pump depletion.

Going back to panel (a) the atom number extracted by this fitting method is shown in blue. While it yields better agreement to the theory expectation the slope is still underestimated which is caused by the residual atom number found in the minimum. Remarkably, both fitting methods underestimate the probe atom number by a fixed (relative) portion. The two dashed line indicate this linear trend. Fitting the minimum underestimates the average atom number inside the interferometer by $\approx$15% regardless of the nonlinear coupling strength employed. Therefore, pump depletion and imperfect reversibility cannot be treated in a threshold-like manner

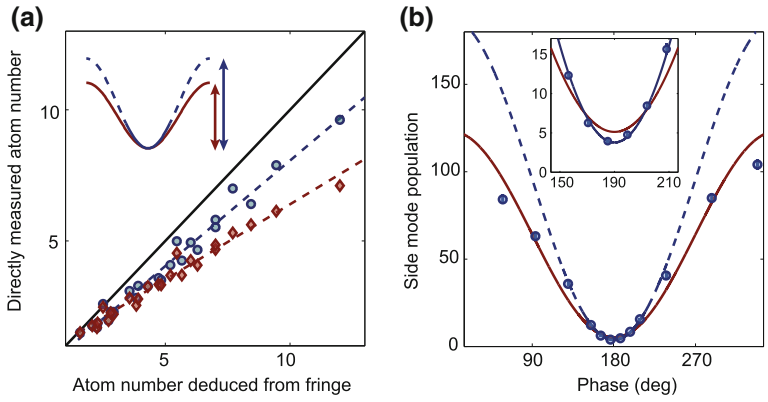

Fig. 8.7 Output fringe and atom number inside. Comparison of the directly measured average side mode population within the interferometer (y-axis) and the inference from the output fringe (x-axis). Agreement between the methods corresponds to the black diagonal line. Taking into account the entire fringe amounts to taking the overall fringe height as a measure (red). Because pump depletion limits the growth predominantly at the maxima this procedure systematically underestimates the atom number. If only the minimum of the fringe is fitted (blue) a more accurate result is obtained. In this case, the atom number is underestimated because of imperfect reversion at the fringe minimum which reduces the curvature. **b** To illustrate the deviation from a sinusoidal fringe in the clearest manner, we show an exemplary fringe for the longest experimentally studied spin exchange durations (10 ms) and largest total atom numbers (550). Clearly, the sinusoidal fit (red) barely reflects the data. In particular, it clearly underestimates the fringe's curvature around the minimum (see inset). A fit that only takes into account the data in close vicinity of the minimum is shown in blue

which modifies the slope only when a specified atom number $\langle N_+ \rangle$ is exceeded. Since the probe atom number is never overestimated, the fitting procedure provides a experimentally reliable method that estimates the fringe's curvature in a conservative manner.

8.9 Indirect Estimation of the Phase Sensitivity

In Sect. 8.6 we experimentally characterized the phase sensitivity in a model independent way. For this the spinor phase was sampled with high resolution. For the more coarsely grained data presented in the previous Sect. 8.7 the good agreement to the undepleted pump theory permits us to estimate the phase sensitivity in an indirect manner. For this purpose, we assume that close to the fringe minimum the shape of the variance follows the undepleted pump theory. The nonideal reversibility is taken into account by including an additional offset. This variance offset is determined directly from the experimental data (see Fig. 8.6 d) and corresponds to the experimentally observed minimal variance. In Fig. 8.8 we plot this variance offset found at the fringe minimum versus the size of the fringe. The colour coding is in accordance with Fig. 8.6, blue data corresponds to 10 ms of spin exchange. For each

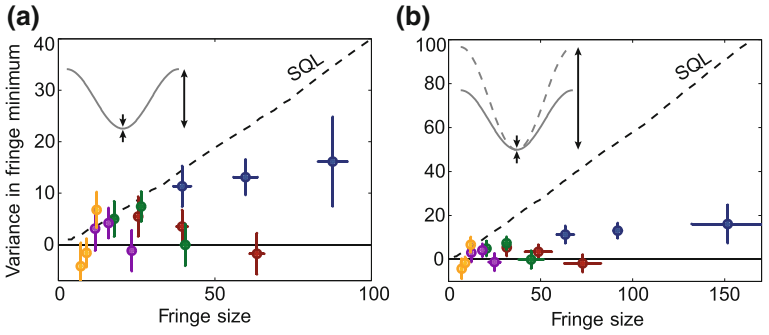

Fig. 8.8 Indirect estimation of the phase sensitivity. From the comprehensive data presented in Fig. 8.6 the phase sensitivity can be estimated. Since the experimental phase increment is too coarse to allow for an analysis akin to Sect. 8.6 we use a more indirect way to assess the phase sensitivity. For this the variance obtained at the minimum is plotted versus the size of the output fringe. The latter is extracted by fitting either the entire fringe data set (panel a), or, more accurately, by taking into account only the minimum (panel b). In either case, the dashed lines indicates the amount of spurious noise that is tolerated by the time reversal sequence to still operate at the Standard Quantum Limit (SQL). For this we assume that the spurious noise adds to the variance fringe, whose functional form (phase dependence) is otherwise left unchanged. Even when underestimating the slope of the signal (left panel) sub-shot noise performance is expected for sufficiently long evolution times. Colour coding is similar to Fig. 8.6 and used to indicate the duration under nonlinear evolution (blue corresponds to 10 ms). Additionally, runs with different total atom numbers (375, 425, 475) are postselected

duration we postselect three different total atom numbers in the range of 350–500. In panel (a) the fringe size is estimated by fitting the overall fringe. Therefore, this plot summarises the variance found in the fringe minimum (y-axis), and the overall fringe size (x-axis) as indicated in the inset. As shown in the previous section, a more accurate way to estimate the slope of the signal is by considering only the data close to the dark fringe. Such a determination of the fringe size is performed in panel (b). In both panels the dashed line indicates the excess variance for which a phase sensitivity at the Standard Quantum Limit (SQL) is retained. Therefore, we infer phase sensitivities that surpass the SQL for a wide range of parameters. The comparison to panel (a) elucidates the robustness of this improvement.

8.10 Residual Atom Number in Minimum

In this section we take a closer look at the residual atom number found in the fringe minimum. As shown in the inset of Fig. 8.6b best reversibility is achieved for short durations t of spin exchange. Additionally, we empirically find a strong dependence on the total atom number. Combining these two findings, the residual atom number behaves similar to $\propto N^2 t$. Figure 8.9a shows this behaviour. Over a wide range of spin exchange durations as indicated in colour and different total atom numbers the data points coalesce to a common trend.

On grounds of the numerical simulation this behaviour is unaccounted for. In particular, particle loss cannot be held responsible for the imperfect reversibility. To explain this imperfection, loss rates 50 times larger than the observed ones would be needed. In principle, a source might be phase jitter which yields to a washing out of the fringe as indicated in the inset of panel (b). However, this leads to inconsistencies which we investigate further in Fig. 8.9b. Here the amount of phase jitter $\Delta\varphi$ which would explain the observed residual atom number is plotted. We find this value to be nearly atom number independent. This is because the overall size of the output fringe is given by $\sinh^4 \kappa t$ and thus shares the proportionality with $\propto N^2$. This atom number independence is evidence that suggests a exogenous origin. However, we find this assumption contradicted by the different amount of phase noise that is inferred for each evolution time. Even worse, for longer durations of spin exchange the amount of phase noise is reduced.

Being unable to explain this finding, we finally checked that the effect of atom number dependent collisional shifts is negligible. In principle, because we postselect experimental runs in a finite atom number window such collisional shifts could lead to dephasing. We detail the sensitivity to collision shifts in the next section.

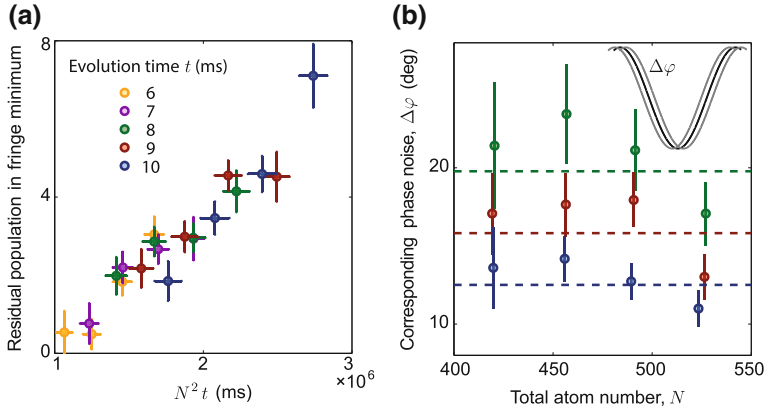

Fig. 8.9 Residual population in fringe minimum. **a** Atom number offset at the minimum of the fringe for different durations of the nonlinear spin exchange t (indicated by colour) and different total atom numbers N. Heuristically, we find that the residual atom number scales similar to $\propto N^2 t$ (x-axis). As detailed in the text, a proportionality with respect to N^2 hints at phase jitter as a possible cause. However, in panel **b** we exemplify that phase jitter (as shown in the inset) cannot be held responsible. Here, the spinor phase jitter $\Delta\varphi$ (one s.d.) that is needed in order to fully explain the residual atom number at the fringe minimum is calculated and the result plotted versus the total atom number N. The dominant source of (putative) spinor phase fluctuations is the microwave dressing, therefore the phase jitter should be worse for long periods of spin exchange. However, panel **b** shows the opposite trend. We therefore conclude that the residual atom number at the fringe minima is not caused by phase jitter

8.11 Characterization of Collisional Shifts

The collisional interactions lead to an energy shift of the pump mode with respect to both side modes. Therefore, these shifts contribute to the dynamic spinor phase rotation during interrogation such that the fringe frequency is altered. In Fig. 8.10 we show interferometry fringes obtained for different postselections on total atom numbers, ranging from $N = 300$ (red) to $N = 500$ (green). For illustrative clarity the fringes are displaced vertically. To make the collisional interactions visible we extend the duration of phase evolution up to 55 ms. After this hold time the collisional shifts lead to a significant dephasing of the fringes. The additional change in fringe visibility is caused by the atom number dependence of the nonlinear coupling strength. In fact, both, the collisional shifts as well as the nonlinear coupling strength describing population transfer are identical, given by $\hbar\kappa$ as stated above. In panel (b) we compare the measurement of both effects: the coloured data shows the measured fringe frequency as a function of atom number. In contrast, the grey diamonds and the solid line represents the atom number dependence found for the nonlinear coupling as plotted in Fig. 7.2. Both measurements agree when adding to the latter a frequency offset which corresponds to the detuning of the microwave π-pulses

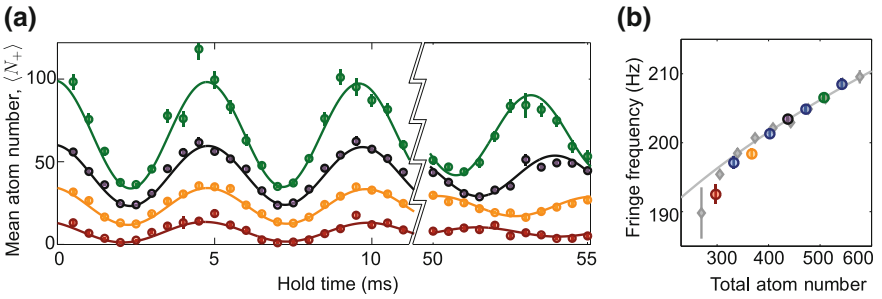

Fig. 8.10 Measurement of the collisional shifts. **a** Interferometry fringes obtained for different total atom numbers (indicated by colour, and identical to panel b). For illustrative reasons the corresponding fringes are displaced vertically by 10 atoms. The hold time under which the spinor phase dynamically evolves ranges up to 55 ms. Eventually, the collisional shifts lead to a dephasing of the fringes as shown in the right panel. **b** The coloured data points show the frequency of the output fringes shown in panel (a) versus total atom number. For comparison, the grey diamonds (and solid line) represent the data of Fig. 7.2, in which the nonlinear coupling strength κ is determined via the nonlinear population growth. Excellent agreement between both results is found when the latter is offset by $2\pi \times 180\,\mathrm{Hz}$ which corresponds to the detuning $\delta_{\mathrm{mw}} = 2\pi \times 90\,\mathrm{Hz}$ of the microwave π-pulse used for pump shelving

used for pump mode shelving. Based on this perfect agreement we deduce that the microwave detuning is $\delta_{\mathrm{mw}} = 2\pi \times 90\,\mathrm{Hz}$.

8.12 Immunity Towards Detection Noise

As motivated in this thesis' introduction the nonlinear time reversal scheme is particularly robust towards detection infidelities. This is because at the point of highest phase sensitivity, the entangled probe state is disentangled which facilitates robust readout. In this section we quantitatively compare the performance of different interferometry schemes when spurious detection noise is added.

A passive interferometer using N uncorrelated particles performs at best at the Standard Quantum Limit, $(\Delta\varphi)^2 = 1/N$. The interferometry fringe is recovered by measuring the atom number imbalance. To assess the phase sensitivity error propagation on the average atom number imbalance suffices. Allowing for additional technical detection noise the optimal working point is at the steepest slope of the signal, i.e. the point of vanishing imbalance. Quantifying the detection noise by an additional variance of Δ_{det} we obtain a phase sensitivity of

$$(\Delta\varphi)^2 = \frac{1}{N} + \frac{\Delta_{\mathrm{det}}}{N^2} \tag{8.8}$$

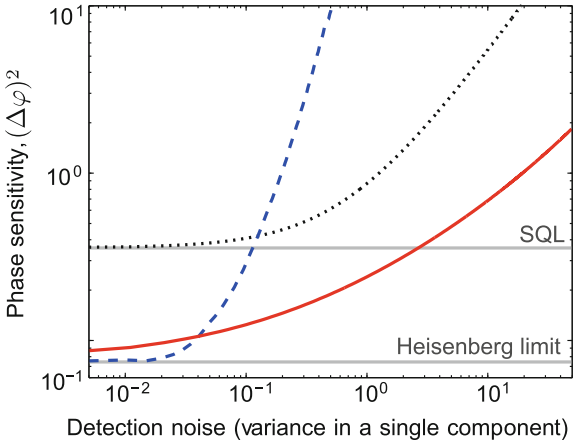

Fig. 8.11 Sensitivity towards detection noise for different interferometry schemes. Using an uncorrelated state (black dotted) in a passive interferometer allows reaching the Standard Quantum Limit (SQL) of phase sensitivity. If detection noise is added, the achievable phase sensitivity diminishes in an asymptotically linear fashion. Using a maximally entangled probe state (blue dashed) in such an interferometer, allows in principle to attain the ultimate Heisenberg limit. However, for this, accurate detection is indispensable. Already small detection noise contributions on the order of 0.1 atoms^2 in variance prevent reaching quantum-enhanced sensitivities. The nonlinear detection scheme combines the advantages of both mentioned techniques: it attains the Heisenberg limit but is also robust with respect to detection noise as it resembles the unentangled state behaviour for large detection noise

This behaviour is shown in Fig. 8.11 as the dotted black line. For this, a probe state of size $N = 2.8$ is chosen to be consistent with the experimentally realized case in Sect. 8.6.

The phase sensitivity of such an SU(2) interferometer can be improved when using the two-mode squeezed vacuum state at its input. However, to exhaust this quantum resource, accurate single-particle readout is essential since the full atom number correlations of the output signal need to be analysed. This is typically achieved by evaluating the atom number *parity* Π. This observable is assigned $+1$ if the single shot output atom number (at one output port) is even, and -1 for an odd atom number detected. In Fig. 8.12a we show simulated atom number distributions recorded at one output port of the interferometer. Similar histograms were introduced in this thesis' introduction. We use a two-mode squeezed vacuum state with average atom number $N = 2.8$. The black histograms correspond to the ideal case of vanishing detection noise, while the red distribution is obtained when detection noise of 0.3 atoms^2 in variance is included. For both cases, panel (b) shows the average parity as a function of applied phase shift. For the ideal case (black) an average parity signal of $+1$ is reached at phase $\pi/2$. At this working point, highest phase sensitivity (at the Heisenberg limit) is reached. Retuning to the histograms, this corresponds to the lowest panel at which only even atom numbers are detected. Highest sensitivity is reached at this point, because already a minute phase change causes the population of odd

atom numbers. At this stage, the additional detection noise of 0.3 atoms^2 appears to be insignificant (red). However, quantum-enhanced phase sensitivity is lost at this stage. The results of this calculation are shown in Fig. 8.11 as the blue dashed line. For this simulation the entire atom number distribution is used. Using a more sophisticated analysis of the data, quantum-enhanced phase sensitivity can be maintained for slightly larger detection noises. Such an analysis is routinely done in practical applications. Here, only experimental realizations are postselected, for which the detected atom number falls into a well-specified window around the integers. However, if this binning threshold is too small, too many realizations are discarded which deteriorates the phase sensitivity. In Fig. 8.13c the trade off between postselection and phase sensitivity is shown. By optimization, a phase sensitivity barely at the SQL can still be attained at a detection noise of 0.3 atoms^2.

The linear readout is characterized by a threshold behaviour as shown in Fig. 8.11: as long as the detection noise is sufficiently small such that no ambiguities arise when determining the single shot parity, the phase sensitivity remains close to the Heisenberg limit. However, when the detection noise exceeds this level, the parity cannot be evaluated in a single shot and the output signal therefore ceases. The output fringe cannot be recovered by averaging more experimental realizations. At this point phase sensitivity degrades extremely fast and is even inferior than interferometry

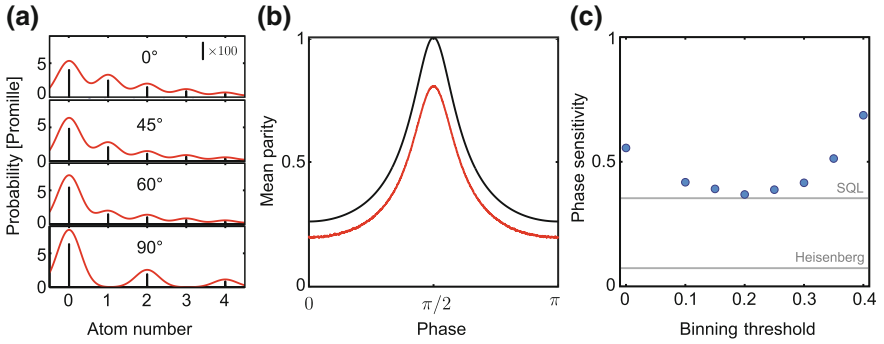

Fig. 8.12 Parity detection of the two-mode squeezed vacuum state **a** Using the two-mode squeezed vacuum state in a passive SU(2) interferometer requires accurate measurements of the parity signal. Simulations are performed for a probe state with average atom number $\langle N \rangle = 2.8$. The ideal output histograms (atom number detected at one output port) for four phase settings are shown in black. Highest phase sensitivity is reached at phase $\pi/2$ where the output signal consists of even atom numbers (lowest histogram). The red lines show the corresponding histogram when detection noise of $\Delta = 0.3$ atoms^2 in variance is added. Although the overlap of even and odd atom numbers might seem insignificant, quantum-enhanced phase sensitivity is lost (see main text). The average parity signal corresponding to these histograms is shown in panel (**b**). Here, the red line corresponds to the case of finite detection noise while black is the ideal theory prediction. Post processing the raw data of the histograms (panel a) can be used to improve the phase sensitivity. Here, measurement outcomes that do not lie within a specified binning window are discarded. The phase sensitivity shows a pronounced minimum at which the SQL can barely be reached for $\Delta \approx 0.3$ (for details see text)

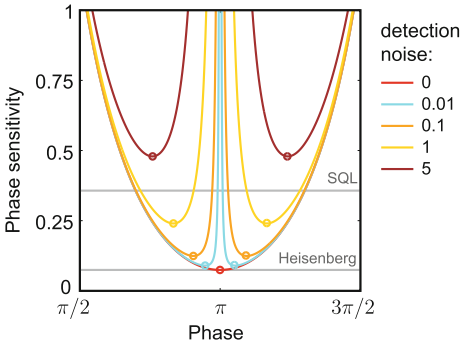

Fig. 8.13 Shift of the optimal working point. The ideal SU(1,1) interferometer features highest phase sensitivity at phase $\varphi = \pi$ (red). However, when additional noise is added during the detection process the optimal working point (indicated by circle) is shifted. The legend specifies the amount of detection noise (in variance)

with uncorrelated particles (black dotted). Therefore, using an entangled state in this situation is not just not better than using a robust classical states, but instead worse: the linear readout relies crucially on accurate detection.

The nonlinear readout scheme combines the advantages of both aforementioned techniques: the detection robustness of uncorrelated particles with the quantum-enhancement sensitivity of entangled particles. Due to the (dis-) entangling prior to detection, the phase sensitivity is mapped onto the easily detectable first moment: the atom number distribution follows a thermal-like distribution which is characterized entirely by its average atom population. In contrast to linear readout, there is no fine grained structure which has to be resolved. Therefore, when detection noise is added the output fringe can be averaged down—no matter how large the noise is. However, the optimal working point depends on the magnitude of the detection noise as demonstrated in Fig. 8.13. Taking this into account, the phase sensitive shown as the red line in Fig. 8.11 can be reached. For small detection noise, the Heisenberg limit is asymptotically attained. For larger noise the phase sensitivity degrades mildly in a fashion comparable to the separable state.

References

1. D. Linnemann, H. Strobel, W. Muessel, J. Schulz, R.J. Lewis-Swan, K.V. Kheruntsyan, M.K. Oberthaler, Quantum-enhanced sensing based on time reversal of nonlinear dynamics. Phys. Rev. Lett. **117**, 013001 (2016). https://doi.org/10.1103/PhysRevLett.117.013001
2. A.A. Clerk, M.H. Devoret, S.M. Girvin, F. Marquardt, R.J. Schoelkopf, Introduction to quantum noise, measurement, and amplification. Rev. Mod. Phys. **82**, 1155–1208 (2010). https://doi.org/10.1103/RevModPhys.82.1155
3. P.D. Nation, J.R. Johansson, M.P. Blencowe, F. Nori, Colloquium: Stimulating uncertainty: Amplifying the quantum vacuum with superconducting circuits. Rev. Mod. Phys. **84**, 1–24 (2012). https://doi.org/10.1103/RevModPhys.84.1
4. R. Boyd, G. Agarwal, W. Davis, A. Gaeta, E. Nagasako, M. Kauranen, Quantum noise characteristics of nonlinear optical amplifiers. Acta Phys. Polonica A **1**, 117–126 (1994)
5. H.A. Haus, J.A. Mullen, Quantum noise in linear amplifiers. Phys. Rev. **128**, 2407–2413 (1962). https://doi.org/10.1103/PhysRev.128.2407

6. C.M. Caves, Quantum limits on noise in linear amplifiers. Phys. Rev. D **26**, 1817–1839 (1982). https://doi.org/10.1103/PhysRevD.26.1817
7. J. Kong, F. Hudelist, Z.Y. Ou, W. Zhang, Cancellation of internal quantum noise of an amplifier by quantum correlation. Phys. Rev. Lett. **111**, 033608 (2013). https://doi.org/10.1103/PhysRevLett.111.033608
8. J. Xin, H. Wang, J. Jing, The effect of losses on the quantum-noise cancellation in the SU (1, 1) interferometer. Appl. Phys. Lett. **109**, 051107 (2016)
9. B. Yurke, S.L. McCall, J.R. Klauder, SU(2) and SU(1,1) interferometers. Phys. Rev. A **33**, 4033 (1986). https://doi.org/10.1103/PhysRevA.33.4033
10. A.M. Marino, N.V. Corzo Trejo, P.D. Lett, Effect of losses on the performance of an SU(1,1) interferometer. Phys. Rev. A **86**, 023844 (2012). https://doi.org/10.1103/PhysRevA.86.023844
11. M. Gabbrielli, L. Pezzè, A. Smerzi, Spin-mixing interferometry with bose- einstein condensates. Phys. Rev. Lett. **115**, 163002 (2015). https://doi.org/10.1103/PhysRevLett.115.163002

Chapter 9
Interferometry Beyond Exact Time Reversal

In this chapter we study the situation that arises when the two durations of spin exchange do not match in length. If the nonlinear readout is shorter than the initial entangled state preparation only an incomplete time reversal can be carried out. Consequently, the probe state does not get fully disentangled and only partial absorption of fluctuations is achieved. In the opposite case the duration of the nonlinear readout is prolonged. This overcompensating regime is the most interesting as it provides benefits for approaching a Heisenberg-limited phase sensitivity in presence of technical fluctuations. This relies on the noiseless amplification that allows magnifying the output signal to an extent that spurious noise can be rendered less significant.

First we analyse this nonbalanced scheme in more detail and discuss its beneficial features before we proceed with the experimental results. Finally we experimentally assess the phase sensitivity and demonstrate its improvement under realistic conditions.

9.1 Partial and Overcompensating Time Reversal

In this section we study the nonbalanced case theoretically. First, we consider the output signal and derive its form. For this we note that the output signal is a sinusoidal fringe. This follows directly from the mode transformations (Eq. 4.3) being linear. The maximum of this fringe occurs for spinor phase setting $\varphi = 0$ where both periods of nonlinear dynamics add up. This is equivalent to (resonant) spin exchange for the combined duration $t_1 + t_2$. At this point the atom number reads $\langle N_+ \rangle = 2\sinh^2(\alpha + \beta)$. Here, we combined the nonlinearity and evolution time under spin exchange to $\kappa t_1 \equiv \alpha$ and $\kappa t_2 \equiv \beta$. On the other hand, at the minimum of the fringe both periods partly compensate. The atom number is then identical to performing spin exchange

D. Linnemann, *Quantum-Enhanced Sensing Based on Time Reversal of Entangling Interactions*, Springer Theses,
https://doi.org/10.1007/978-3-319-96008-1_9

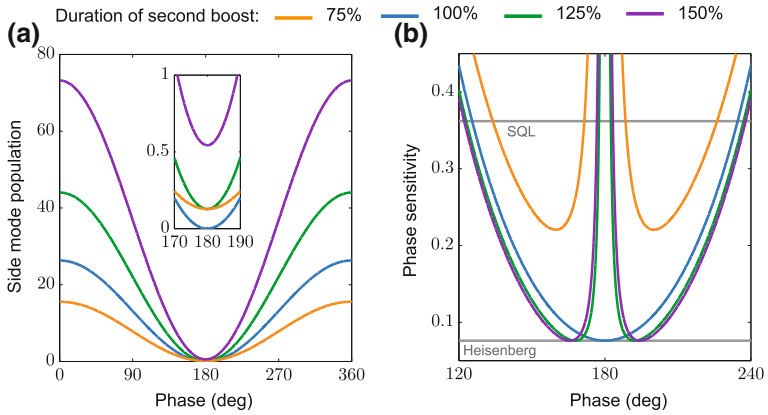

Fig. 9.1 Unbalanced interferometry (theory) **a** Simulated output fringe for four different durations of nonlinear readout as indicated by colour. The first nonlinear process is fixed in length (= 100%) and generates a probe state with $\langle N_+^{\text{inside}} \rangle = 2.8$. The orange and green curve show the resulting fringe if the readout is shortened or extended by 25%, respectively. While the fringe size is greatly influenced the atom number found in the minimum is identical for both cases (inset). Extending the readout by 50% (purple) amplifies the fringe by almost a factor of three at the expense of a growing atom number offset found at the minimum. **b** Simulated phase sensitivity. The blue curve shows the symmetric case for which the Heisenberg limit is attained at the dark fringe (180°). The shortened nonlinear readout (orange) achieves poorer phase sensitivity. This is a consequence of both, the smaller overall fringe size and the remaining atom number (and its corresponding fluctuations) at its minimum. In contrast the enlarged nonlinear readout (green and purple, respectively) reaches the Heisenberg limit. In this case the remaining atom number in the fringe minimum is fully compensated for by the enlarged output fringe. Depending on the duration of the nonlinear readout the optimal working point shifts.

with only the surplus time $\langle N_+ \rangle = 2\sinh^2(\alpha - \beta)$. From these two limiting cases the form of the entire fringe follows to be

$$\langle N_+ \rangle = \left(\sinh^2(\alpha+\beta) - \sinh^2(\alpha-\beta)\right)(1+\cos\varphi) + 2\sinh^2(\alpha-\beta). \tag{9.1}$$

Figure 9.1a shows the expected output fringe for four exemplary cases. Compared to the symmetric case ($\alpha = \beta$, indicated in blue), the overall fringe size is diminished for a shortened readout ($\beta < \alpha$, orange) and magnified for prolonged readouts ($\beta > \alpha$, green and purple). Consequently, by performing an extended nonlinear readout the slope of the signal is magnified,

$$\mathrm{d}\langle N_+ \rangle / \mathrm{d}\varphi = -\left(\sinh^2(\alpha+\beta) - \sinh^2(\alpha-\beta)\right)\sin\varphi. \tag{9.2}$$

The price for this enhanced output signal is a concomitant increased noise level. Since the state at the output is two-mode squeezed vacuum, the corresponding variance fringe is given by

$$(\Delta N_+)^2 = \langle N_+ \rangle (\langle N_+ \rangle + 2) \tag{9.3}$$

which directly reflects the magnified output fringe. In particular, at the fringe minimum a residual average atom number of $\langle N_+ \rangle = 2\sinh^2(\alpha - \beta)$ with a corresponding variance of $(\Delta N_+)^2 = \sinh^2(2(\alpha - \beta))$ is found. The inset of Fig. 9.1a shows this residual atom number that is left in the minimum. The balanced case of $t_1 = t_2$ is shown in blue. Only here, a perfectly dark fringe is recovered.

The magnified slope of the output signal and its collateral additional fluctuations are intimately connected and increase in lock step such that Heisenberg limited phase sensitivity is retained. The resulting phase sensitivity is shown in Fig. 9.1b. Only for a shortened nonlinear readout stage the Heisenberg limit is inaccessible (orange). While for the balanced case Heisenberg-limit phase sensitivity is reached at π the prolonged nonlinear readout attains the same limit. However, since the fringe minimum is not dark the working point of this prolonged time reversal sequence is shifted. In fact, Heisenberg limit phase sensitivity is attained at phase settings

$$\varphi = \pm 2 \arctan\left(\sqrt[4]{\frac{\sinh^4(\alpha+\beta) + \sinh^2(\alpha+\beta)}{\sinh^4(\alpha-\beta) + \sinh^2(\alpha-\beta)}}\right). \tag{9.4}$$

This remarkable result provides a practical path towards noise resilient phase estimation. This is because the slope of the output fringe can, in principle, be magnified ad libitum. Albeit pump depletion will eventually limit amplification of the *entire* fringe, the interferometer's best working point is still in close vicinity of the fringe minimum where depletion effects remain negligible.

9.2 Advantage of Overcompensating Time Reversal

The enhanced slope of the signal makes a larger amount of noise tolerable. This is demonstrated in Fig. 9.2a which shows the phase sensitivity for four readout durations in presence of additional detection noise. The first period of parametric amplification is fixed and generates a probe state with average population of $\langle N_+^{\text{inside}} \rangle = 2.8$. We choose the amount of detection noise such that the performance of the balanced interferometer (blue) is declined to the Standard Quantum Limit. This case is similar to the one discussed in Sect. 8.12. Additionally, we show the phase sensitivity for extended nonlinear readout. A significant better phase sensitivity is attained already when the readout is prolonged by 25% as witnessed by the green curve. For larger durations of the nonlinear readout the Heisenberg limit is asymptotically reached.

In panel (b) we show the best attainable phase sensitivity as a function of additional technical noise. In Sect. 8.12 we argued that the balanced time reversal offers exceptionally high tolerance of detection noise when compared to linear readout schemes. Here, the advantage of the amplified nonlinear readout becomes manifest. Being able to a posteriori amplify the output signal the noise immunity can be improved further. This fact is collaborated by the complementary graph of Fig. 9.2c. Here the best achievable phase sensitivity is plotted versus the duration of the nonlinear readout.

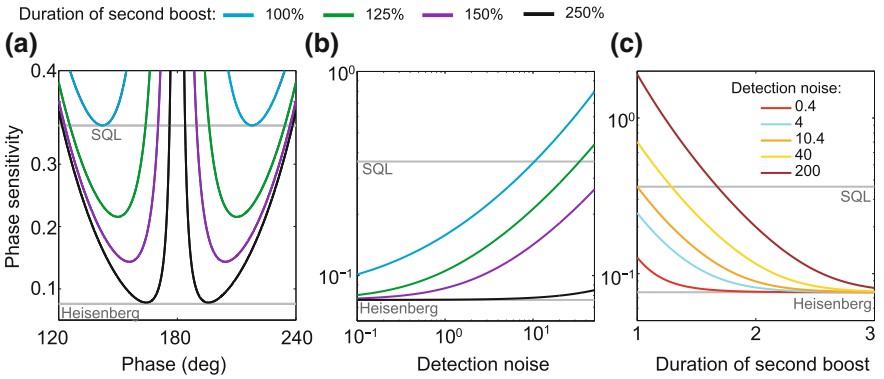

Fig. 9.2 Noise resilience of unbalanced interferometry (theory). Panels **a** Phase sensitivity in presence of detection noise for four different durations of nonlinear readout (indicated by colour, legend on top). For all three panels, the first boost is fixed in length ($\equiv 100\%$) and generates a probe state with $\langle N_+^{\text{inside}} \rangle = 2.8$. Additional detection noise is added and fixed in strength such that the phase sensitivity of the symmetric interferometer (blue) is deteriorated up to the Standard Quantum Limit (SQL). Extended nonlinear readout improves the attainable phase sensitivity such that the Heisenberg limit is asymptotically reached. **b** Phase sensitivity attained at the optimal working point for different amounts of detection noise. Extending the nonlinear readout makes a larger portion of additional detection noise tolerable. The complementary plot of this situation is depicted in panel (**c**). It depicts the best attainable phase sensitivity versus the nonlinear readout's duration. This highlights that under any amount of detection noise (see legend) Heisenberg-limited phase sensitivity is asymptotically reached for sufficiently long nonlinear readout

By employing sufficiently long nonlinear readout any amount of noise added can eventually be tolerated such that phase estimation approaching the ultimate Heisenberg limit is recovered.

9.3 Experimental Nonbalanced Time Reversal

To study the unbalanced nonlinear readout we perform spin exchange for $t_1 = 8\,\text{ms}$. After scanning the spinor phase we vary the length of the second period of nonlinear evolution in the range of $t_2 = 1$–$12\,\text{ms}$. Figure 9.3a shows the output fringes of $\langle N_+ \rangle$ for each duration of the nonlinear readout. For illustrative clarity the fringes are plotted next to each other. Clearly, the overall fringe size increases as the readout is prolonged (note the logarithmic scale). At the same time, the atom number in the respective minimum of the fringe is minimal in the case of balanced interferometry (blue). This fringe minimum is studied in more detail in the following panels b) and c) where the atom number variance found at the minimum is plotted versus the duration of the nonlinear readout. We show the result for two postselected total atom numbers N as indicated. The red data point shows the outcome of omitted nonlinear readout. Here a variance of $\langle N_+^{\text{inside}} \rangle = 29$ and $38\,\text{atoms}^2$ is detected, respectively,

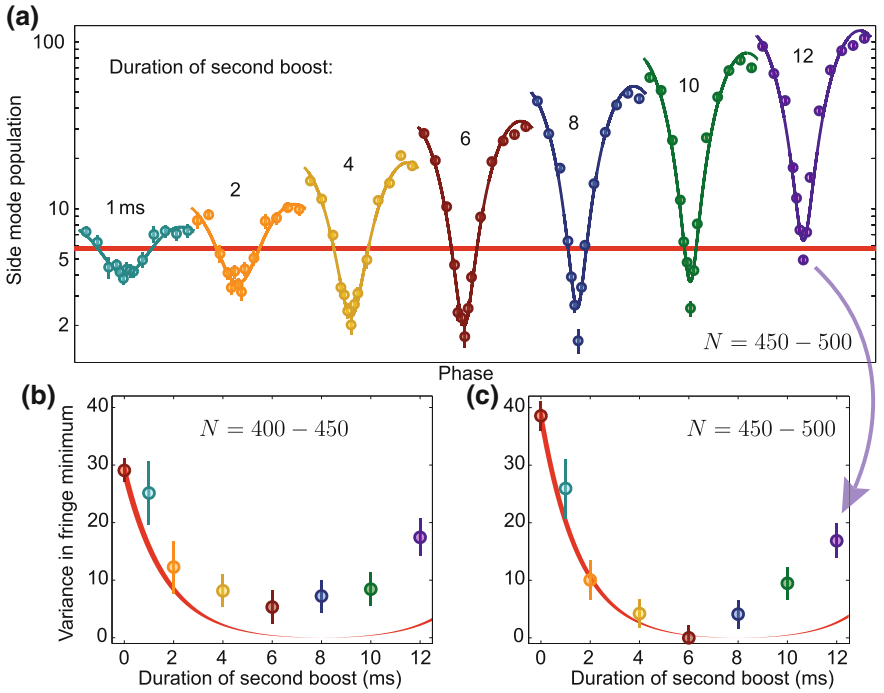

Fig. 9.3 Unbalanced interferometry. **a** Interferometry fringes of $\langle N_+ \rangle$. The first period of spin exchange is fixed at $t_1 = 8$ ms while the second period is varied between $t_2 = 1 - 12$ ms as indicated. For the sake of clarity, the fringes are drawn horizontally displaced. While overall size of the output fringe increases, the atom number found in the minimum is minimal for the balanced case of $t_1 \approx t_2$. The red denotes the measured average atom number of the probe state. **b**, **c** Atom number variance $(\Delta N_+)^2$ found in the corresponding fringe minimum versus duration of the nonlinear readout. Panels b) and c) show the result for different total atom numbers as indicated. Starting from the measured fluctuations of the probe state, the red line indicates the expectation within undepleted pump theory. Ideally, the fluctuations are completely absorbed at $t_1 = t_2$. Experimentally, we find a pronounced minimum for slightly shorter durations of the nonlinear readout

which corresponds to the probe state. Starting from this level, the fluctuations are reduced successively. The red lines indicate the theoretical expectation in undepleted pump approximation. Ideally, perfect time reversal is expected at the balanced case of $t_1 \approx t_2$ where the fluctuations are fully absorbed. For longer durations of nonlinear readout the atom number fluctuations increase again. Experimentally, we find minimal fluctuations for slightly shorter durations. As detailed in the previous section, the excess atoms found at the minimum lead to additional fluctuations. The reason for this nonideal reversion to the initial state remains unclear so far. We can, however, use the prolonged nonlinear readout to learn more about these fluctuations. This is because, if the nonideal reversibility is caused by a deteriorated probe state, a prolonged nonlinear readout could not improve the achievable phase sensitivity. On the other hand, if technical fluctuations prevail the phase sensitivity would indeed

improve. Therefore, this experimental setting might be a realistic testing bed to study the improvement of the practically achievable phase sensitivity in the presence of noise.

9.4 Phase Sensitivity

To experimentally estimate the phase sensitivity for the prolonged readout we restrict ourselves to a small phase range around the respective fringe minimum. Here, pump depletion is negligible and the slope of the output signal can be determined reliably by a sinusoidal fit. Figure 9.4a shows the average atom number in close vicinity of the minimum. The initial period of spin exchange was 8 ms and we postselect atom numbers in the range of 400−450. Clearly, both, the offset level as well as the slope increase with prolonged nonlinear readout. Panel (b) shows the corresponding atom

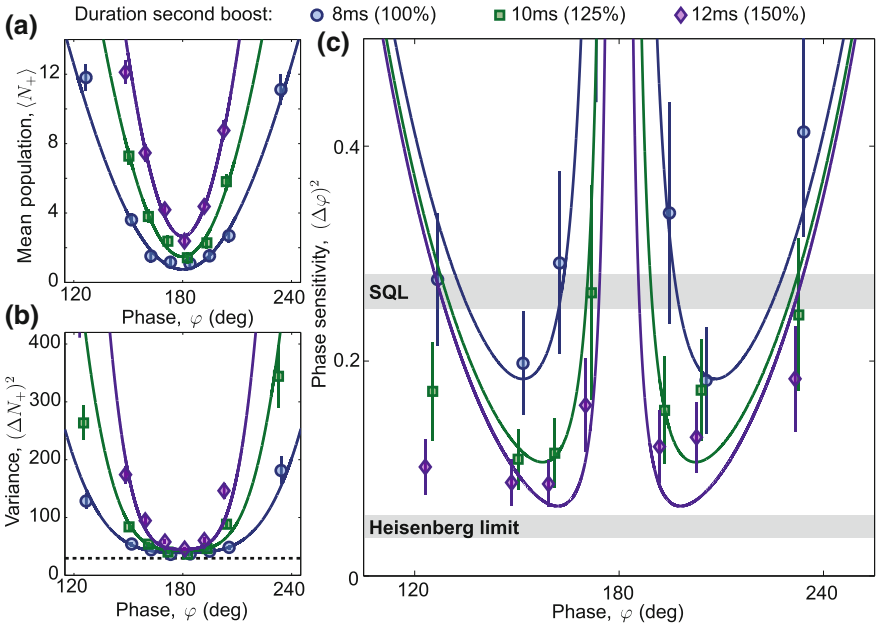

Fig. 9.4 Experimental phase sensitivity with prolonged nonlinear readout. The duration of the first period of spin exchange is fixed at 8 ms. Panel **a** shows the average atom number close to the fringe minimum for three durations of nonlinear readout. Clearly, larger durations increase the slope of the signal. However, as a trade-off the atom number found in the fringe minimum is enlarged. **b** Corresponding atom number variance. The solid lines indicate the expected signal when taking the average atom number as a basis. Additional (technical) fluctuations are taken into account by allowing for an offset. **c** Resulting phase sensitivity. In the symmetric case (blue) the Standard Quantum Limit is only just surpassed. This is a consequence of additional fluctuations that prevent ideal reversion to vacuum at the fringe minimum. For longer durations of the nonlinear readout the phase sensitivity is significantly improved. The solid lines denote the expected phase sensitivity of the corresponding fit shown in panel **a**)

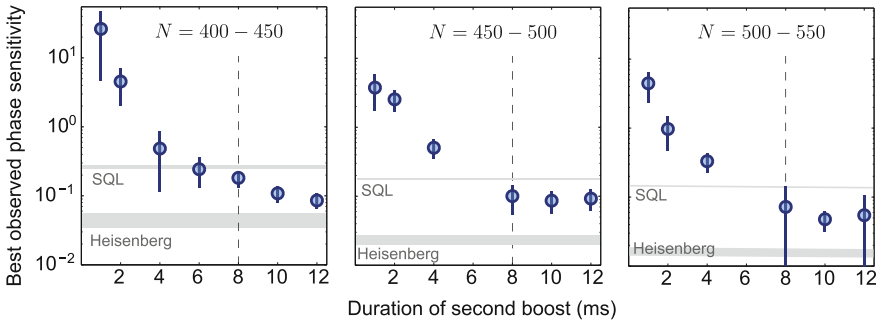

Fig. 9.5 Best observed phase sensitivity with prolonged nonlinear readout. Phase sensitivity versus duration of the nonlinear readout for three different total atom numbers. The phase sensitivity is determined by the procedure detailed in Fig. 9.4c. Here, we plot the best directly observed phase sensitivity. For each atom number the Standard Quantum Limit and the corresponding Heisenberg limit are shown. The matched nonlinear readout is indicated by the vertical dashed line. For short durations only poor phase sensitivities are reached. For all atom numbers best phase sensitivity is found for slightly prolonged nonlinear readout

number variance. The solid lines amount to the theoretical expectation that follows from the measured average atom number, see Eq. 9.3. Employing error propagation similar to the balanced case studied above yields the phase sensitivity that is shown in panel (c). As a consequence of the additional noise the balanced interferometer (blue) performs only just below the Standard Quantum Limit. However, by employing the prolonged nonlinear readout better phase sensitivities are reached. Remarkably, already an elongation of 25% in duration yields a significantly better sensitivity (green). The solid lines take into account the fitted average population (panel a) and the expected variance (panel b).

We repeat this analysis for different total atom numbers. Thereby, the nonlinearity of both periods of spin exchange is symmetrically altered. In Fig. 9.5 the experimentally best observed phase sensitivity is plotted versus the duration of the nonlinear readout. The symmetric case of $t_1 = t_2 = 8\,\mathrm{ms}$ is indicated by the vertical dashed line. As expected for shortened readout the phase sensitivity is massively deteriorated. For longer readout the phase sensitivity is slightly improved. It is important to note that these data points correspond to the best *directly* observed phase sensitivity at one specific spinor phase without interpolation. For each of the three different total atom numbers, the phase sensitivity behaves similar to the one shown in Fig. 9.4c. In this Figure, we find error bars that overlap significantly for a single spinor phase setting. However, the common trend taking into account the entire phase dependence points at an improvement. This improvement under prolonged readout suggests that technical fluctuations play an important rôle in the nonideal reversion to the initial state as discussed in Sect. 8.10. Because of the varying total atom numbers the probe state features different populations which implies different levels of the SQL and Heisenberg limit, respectively, as indicated in each panel.

Chapter 10
Nonlinear Time Reversal as a Diagnostic Tool

Thus far we have presented the advantages of nonlinear readout with respect to performing quantum-enhanced phase measurements. Besides this metrology setting the nonlinear readout provides benefits also for other applications. In this section we employ the nonlinear readout as a versatile tool to efficiently extract information of a probe state. In this view, the nonlinear readout is an autonomous building block to characterize its input state. Before we employ the nonlinear readout as an EPR entanglement witness we remain within the interferometry line of thinking and present a measurement of phase damping. Usually such phase damping is considered a deficiency caused by technical imperfections. It might, however, also be caused by intrinsically quantum mechanical effects that are connected to questions of phase diffusion in Bose-Einstein condensates.

10.1 Phase Damping

In this section we investigate the damping of the interferometry fringe when the phase interrogation is extended to long durations. Figure 10.1 shows such a measurement. We find significant phase damping for holding times exceeding 50 ms. During the hold time the pump atoms are shelved within the $F = 1$ manifold. Therefore loss of both, the pump as well as the side modes during phase evolution is strongly suppressed. Loss is thus not responsible for the fringe damping. This is further demonstrated in the inset of Fig. 10.1: while the phase dependent signal gets damped, the single shot outcomes (shown in grey) exhibit high visibility—even after 150 ms when the averaged signal shows no phase dependence at all.

As detailed in the previous chapters the collisional shifts lead to a varying fringe frequency (Sect. 8.11). In principle, the averaging of runs with different total atoms

D. Linnemann, *Quantum-Enhanced Sensing Based on Time Reversal of Entangling Interactions*, Springer Theses,
https://doi.org/10.1007/978-3-319-96008-1_10

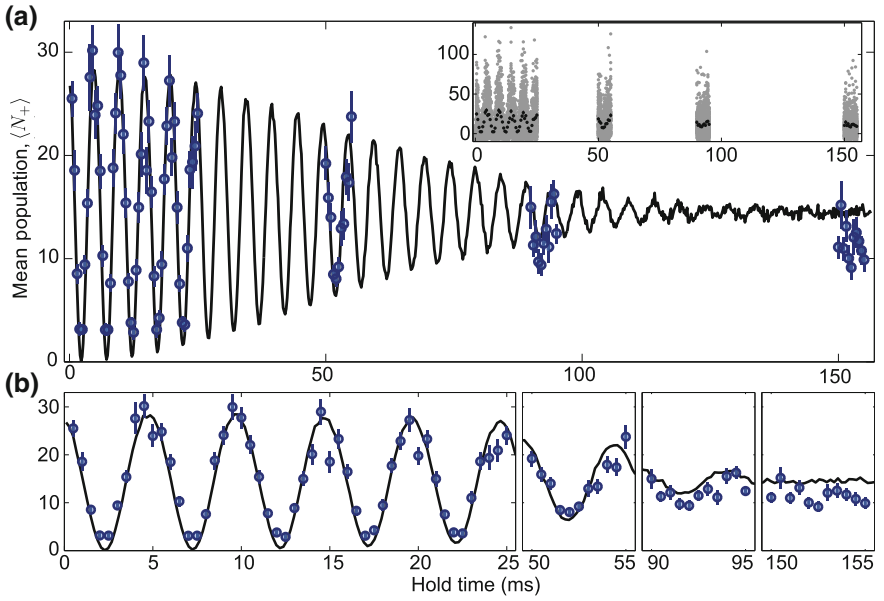

Fig. 10.1 Fringe damping of the nonlinear readout. **a** Output fringe versus holding times. We find significant damping on time scales of 50–100 ms. After 150 ms no phase dependent signal at all is recovered any more (see panel b) for a zoom-in). The black solid line denotes the result of a numerical simulation whose details are described in the main text. Since the pump atoms are shelved in $F = 1$ during holding, the damping is dominantly caused by phase scrambling. The single shot outcomes show only small loss of visibility (grey data in inset)

number could therefore yield to a washing out of the fringe. For this measurement we postselect total atom numbers in the window 380–420. We checked that the damping is not caused by a too wide postselection window.

In the numerical simulations that are based on the truncated Wigner approximation such damping is absent. To reproduce the data we heuristically supplement the simulation with a phase randomization procedure. For this we take an initial phase distribution ϕ that is Gaussian. For each run we then draw a phase from either $\phi \times \sqrt{t_{\mathrm{hold}}}$, or $\phi \times t_{\mathrm{hold}}$ where t_{hold} indicates the hold time during which the phase dynamically evolves. In the first case the phase variance grows linearly in time which is called diffusive. In contrast, the second case describes a ballistic regime meaning that the variance growth is quadratically in time. We find best agreement to the experimental data for the quadratically growing phase variance. In Fig. 10.1 the result of this numerical simulation is shown as the solid line. Simulations incorporating the diffusive phase scrambling behaviour predict instead an envelope that shrinks too slowly for short hold times while at the same time predicting too high visibility at long times.

In a linear interferometry scheme, pure dephasing yields a loss of contrast that eventually converges to the centre of the original fringe. The numerical simulation

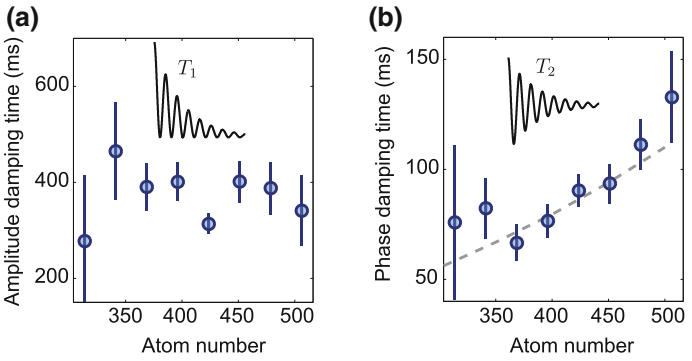

Fig. 10.2 Fringe damping for different atom numbers. **a** Coefficient T_1 (see Eq. 10.1 for a definition) versus total atom number. This parameter captures amplitude damping as indicated in the inset. We find no pronounced dependence on atom number. In contrast, panel **b** shows the coefficient T_2 which describes phase damping as illustrated in the inset. Here, we find longer coherence times for larger atom number. This trend can be reproduced by a numerical simulation by making the phase spread atom number dependent. The grey dashed line shows the result of such a simulation. Here, we take the phase uncertainty (s.d.) to be inversely proportional to atom number

reproduces such a curve. However, in the experiment the contrast as well as the average side mode population eventually shrink. Such a pattern corresponds to additional amplitude loss. In the language of nuclear magnetic resonance, one routinely distinguishes between two relaxation times, the so-called T_1 and T_2 time [1, 2]. The former entails amplitude damping, while the latter describes pure dephasing. In this spirit we fit the experimental data to

$$\langle N_+ \rangle \propto \mathrm{e}^{-t_{\mathrm{hold}}/T_1}(1 + \mathrm{e}^{-t_{\mathrm{hold}}/T_2} \cos \omega t_{\mathrm{hold}}) \tag{10.1}$$

in order to separate both effects from each other.

The results of this fitting procedure are summarized in Fig. 10.2 where the two fit parameters T_1 and T_2 are plotted against total atom number. By postselecting runs with different total atom numbers, both, the pump as well as the side mode population (via the larger nonlinear coupling strength) are enlarged. While the amplitude damping (described by T_1) is constant over the entire range of atoms numbers, we find a strong atom number dependence of T_2. To reproduce this trend by the numerical simulation we make the phase uncertainty atom number dependent. The grey dashed line shows the result when the phase uncertainty (standard deviation) is made inversely proportional to the atom number. The data point at 400 atoms corresponds to the curve shown in Fig. 10.1 which is taken as a reference. We conclude that a larger condensate maintains its phase relation over longer periods and thus supports high visibility fringes for longer hold times.

The particular atom number dependence of T_2 presents a promising result. In fact, it is indicative that indeed phase jitter of the highly populated pump mode is probed by the sparsely populated side modes. Such a situation is ideally suited for investigating

fundamental aspects of phase diffusion, e.g. the temperature dependence. Note that if the decaying contrast were caused by decoherence of the entangled probe state, one would expect the opposite trend: a more fragile entangled state as the number of atoms (and thus also the size of the entangled state) is increased. Technical fluctuations on the other hand are expected to be atom number independent.

The reasons for the appreciable amplitude damping remain unclear. In fact, from the independently conducted relaxation measurements as presented in Sect. 7.3 we expect that less than 1% of the atoms get lost during phase interrogation. The numerical simulations use these loss rates. This would correspond to T_2 times exceeding 1 s which is markedly different from the observed damping. In the direct time series (Fig. 10.1) this discrepancy becomes visible as the different offset level the fringes converge to at long hold times.

10.2 Witnessing EPR Entanglement

The nonlinear readout can be employed to efficiently gather information about the probe state. In quantum optics balanced homodyne detection is *the* standard tool for such state characterization. We presented the method in detail above. It builds on the mode transformation implemented by a phase shift in conjunction with a regular beam splitter. Generalising to the nonbalanced case ($\theta \neq \pi/2$) this transformation reads

$$\begin{pmatrix} a_\uparrow \\ a_\downarrow \end{pmatrix} \to \begin{pmatrix} \cos\theta & \mathrm{e}^{\mathrm{i}\varphi}\sin\theta \\ -\mathrm{e}^{-\mathrm{i}\varphi}\sin\theta & \cos\theta \end{pmatrix} \begin{pmatrix} a_\uparrow \\ a_\downarrow \end{pmatrix}. \tag{10.2}$$

In a very similar manner the mode transformation performed during the nonlinear readout can be used to characterize a state, i.e.

$$\begin{pmatrix} a_\uparrow \\ a_\downarrow^\dagger \end{pmatrix} \to \begin{pmatrix} \cosh\kappa t & \mathrm{e}^{\mathrm{i}\varphi}\sinh\kappa t \\ \mathrm{e}^{-\mathrm{i}\varphi}\sinh\kappa t & \cosh\kappa t \end{pmatrix} \begin{pmatrix} a_\uparrow \\ a_\downarrow^\dagger \end{pmatrix}. \tag{10.3}$$

For the class of states which are similar to two-mode squeezed vacuum this nonlinear readout is particularly efficient. This is because for these states the nonlinear readout amounts to (partial) time reversal. In this section we use the nonlinear readout as an entanglement witness [3, 4]. Prima facie this might seem redundant, as beating the Standard Quantum Limit of phase estimation already proves that the probe state was entangled. However, the two-mode squeezed vacuum state is the prototypical state that shows a very particular form of quantum correlations—namely entanglement that is of the so-called Einstein-Podolsky-Rosen type [5]. This name derives from the famous paper in which the triumvirate presents an apparent paradox, that questions the completeness of quantum mechanics [6]. In particular Einstein refused the concept of a probabilistic theory and saw in it merely a lack of a more detailed description. Ironically however, contrary to their intention the authors did not show

a shortcoming of the quantum mechanics framework but what soon after was recognized as an essential feature, namely entanglement.

The paradox involves two particles whose position (X_1 and X_2, respectively) and momentum (Y_1 and Y_2) exhibit perfect correlations. Such a scenario is quantum mechanically valid. The authors assumed that the two particles could not influence each other when being spatially separated. Then one could measure the position of the first particle (X_1) *exactly* and—because of the perfect correlations—infer the position of the second with any desirable precision. A similar inference could subsequently be done with the particle's momentum. However, as complementary observables the Heisenberg uncertainty relation has to apply which poses a lower bound on the achievable precision of momentum and position. Therefore, it seems that the Heisenberg uncertainty relation is violated. Nowadays the two fallacious assumptions that lead to this apparent paradox are known as locality and counterfactual definiteness.

Generalizing the argument to also apply to nonideal correlations one refers to the EPR argument when the following inequality is satisfied [5, 7]

$$\Delta(X_\uparrow - gX_\downarrow)\Delta(Y_\uparrow + gY_\downarrow) < 1 \tag{10.4}$$

Here we already adopted the scenario to the case where the rôle of the two distinct particles is played by spin modes $|\uparrow\rangle$ and $|\downarrow\rangle$. In this case the particle's position and momentum correspond to mode quadratures [8, 9]. Moreover, we have introduced a scaling factor g which can be chosen to optimally compare the two modes by rescaling one with respect to the other [5]. Atomic EPR-entanglement was first demonstrated in [10] using linear readout [11].

We now show that the nonlinear readout can be used to evaluate this inequality. To this end we calculate the average atom number $\langle N_\uparrow \rangle$ that is obtained in mode $|\uparrow\rangle$ after the nonlinear readout took place

$$\begin{aligned}\langle N_\uparrow\rangle + 1/2 = \cosh^2(\beta)\langle a_\uparrow^\dagger a_\uparrow + 1/2\rangle + \sinh^2(\beta)\langle a_\downarrow^\dagger a_\downarrow + 1/2\rangle + \\ \cosh(\beta)\sinh(\beta)(\mathrm{e}^{-\mathrm{i}\varphi}\langle a_\downarrow a_\uparrow\rangle + \mathrm{e}^{\mathrm{i}\varphi}\langle a_\uparrow^\dagger a_\downarrow^\dagger\rangle)\end{aligned} \tag{10.5}$$

All quantities on the right hand side refer to the initial state. In particular the anomalous moments $\langle a_\downarrow a_\uparrow\rangle$ and $\langle a_\uparrow^\dagger a_\downarrow^\dagger\rangle$ appear which quantify the strong inter mode correlations. Our aim is to connect these correlations to the EPR argument. For this we insert the definition of the mode quadratures (as defined in Chap. 4) and arrive at

$$\begin{aligned}\frac{\langle N_\uparrow\rangle + 1/2}{\cosh^2(\beta)} = \langle X_\uparrow^2 + Y_\uparrow^2\rangle/2 + \tanh^2(\beta)\langle X_\downarrow^2 + Y_\downarrow^2\rangle/2 + \\ \tanh(\beta)\left(\cos(\varphi)(\langle X_\uparrow X_\downarrow\rangle - \langle Y_\uparrow Y_\downarrow\rangle) - \sin(\varphi)(\langle X_\uparrow Y_\downarrow\rangle) + \langle X_\downarrow Y_\uparrow\rangle\right)\end{aligned} \tag{10.6}$$

In the following we assume that the individual quadratures are centred at vacuum, i.e. $\langle X_\uparrow \rangle = 0$ and similarly for the other modes. For the two-mode squeezed vacuum state this is fulfilled. For other probe states this can be achieved by first displacing the state accordingly. At the spinor phase setting $\varphi = \pi$ where time reversal is achieved this simplifies to

$$\frac{\langle N_\uparrow \rangle + 1/2}{\cosh^2(\beta)} = \mathrm{var}(X_\uparrow - gX_\downarrow)/2 + \mathrm{var}(Y_\uparrow + gY_\downarrow)/2 \equiv D \tag{10.7}$$

Here we used the scaling factor $g = \tanh \beta$. The right hand side is known as the Duan criterium [12]; $D < 1$ signals mode inseparability. The stronger EPR inequality Eq. 10.4 is satisfied for $D < 1/2$. This follows immediately from noticing that $XY \leq (X^2 + Y^2)/2$ [5].

To experimentally evaluate the Duan criterium one merely has to compare two average atom numbers [3, 4]. The first is the atom number $\langle N_\uparrow \rangle$ leaving the nonlinear readout when it is applied to the entangled state in question. The second needed quantity is $\cosh^2 \beta$ which corresponds to $\langle N_\uparrow \rangle + 1$ when vacuum is fed to the same nonlinear readout stage. This is equivalent to the average atom number found after a single period of spin-exchange. Therefore, in the measurements on symmetric nonlinear readout the amount by which the minimum of the fringe falls below the atom number of the probe state inside the interferometer signals EPR entanglement. This procedure should be compared to measuring mode quadratures for which a experimentally more demanding fluctuation analysis is needed.

The scaling factor g can be adjusted by varying the length of the nonlinear readout. For an ideal two-mode squeezed vacuum state that is generated by parametric amplification with nonlinearity α the optimal scaling factor reads $g = \tanh(2\alpha)$ [7]. This corresponds to the situation where the nonlinear readout is twice as long as the initial entangling. Ideally, at this point the Duan criterium reads $D = 1/\cosh(2\alpha)$.

Our experimental results are shown in Fig. 10.3. Here we evaluate the Duan criterium for varying durations of the nonlinear readout. The entangled state was generated by 8 ms of spin exchange. The two horizontal lines indicate the region of witnessed inseparability $D < 1$ and EPR entanglement $D < 1/2$, respectively. The error bars reflect the statistical uncertainty in measuring the average atom number after the nonlinear readout. The lowest value[1] of $D = 0.28 \pm 0.02$ is found for the symmetric case where the duration under entangling and nonlinear readout is identical (indicated by the vertical dashed line). In view of the optimal scaling factor g this behaviour is unexpected. To investigate this further the inset shows the result of a numerical simulation which qualitatively resembles the data.

[1] At this stage the summed side mode population with vacuum input at the nonlinear readout is $\langle N_+ \rangle = 5.5 \pm 0.1$ which is reduced down to $\langle N_+ \rangle = 1.1 \pm 0.15$ with the EPR entangled state. The stated error bars are statistical. Systematic shifts as large as ± 1 atom can be tolerated to still violate the Duan criterium. For this purpose we treated the worst case in which the true atom number after the nonlinear readout with vacuum at its input is overestimated by one atom—while the other quantity is underestimated by one atom.

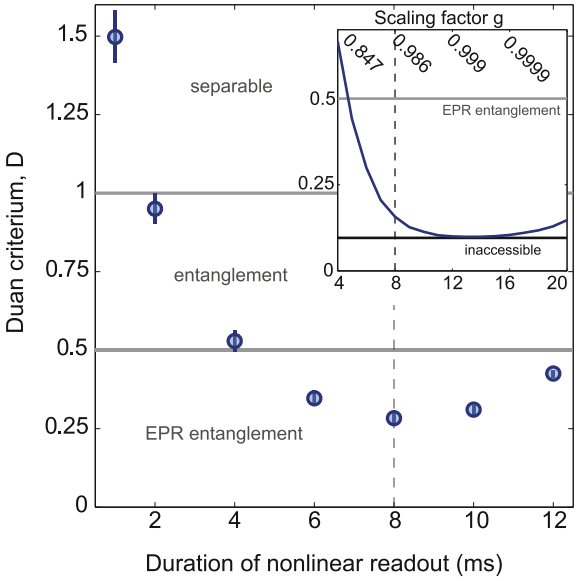

Fig. 10.3 Witnessing EPR entanglement with nonlinear readout. Experimentally inferred value of the Duan criterium D versus duration of the nonlinear readout. Mode inseparability is signalled by $D < 1$. The stronger EPR entanglement is witnessed by $D < 1/2$. Both limits are indicated by horizontal lines. Initially, a probe state that exhibits EPR correlations is generated by performing spin exchange for 8 ms. By changing the duration of the subsequent nonlinear readout different scaling factors g are realized. We find a lowest value of $D \approx 0.3$ when performing nonlinear readout for 8 ms which corresponds to the symmetric case of time reversal. The error bars take into account the statistical uncertainty in determining the average atom number. The inset shows the result of a numerical simulation. Ideally, the probe state could violate the Duan criterium up to $D = 0.1$ (black line). In the lossless case this value is reached at 16 ms of nonlinear readout which is twice as long as the initial entangling. However, the interplay of loss and a scaling factor (indicated on top axis) that quickly approaches unity yields an optimum for slightly shorter durations

The black horizontal line shows the minimally attainable value of the Duan criterium $D = 0.1$. Ideally this value would be reached for a subsequent nonlinear readout of 16 ms. However, atom loss and a quickly unity approaching scaling factor g cause a pronounced minimum for slightly shorter durations. The axis on top shows the respective scaling factor g. It approaches unity rapidly as the duration of nonlinear readout is prolonged.

References

1. L.M. Vandersypen, I.L. Chuang, NMR techniques for quantum control and computation. Rev. Mod. Phys. **76**, 1037 (2005)
2. M. Nielsen and I. Chuang, *Quantum Computation and Quantum Information* (Cambridge University Press, 2000)

3. E. Flurin, N. Roch, F. Mallet, M.H. Devoret, B. Huard, Generating entangled microwave radiation over two transmission lines, Phys. Rev. Lett. **109**, (2012), https://doi.org/10.1103/PhysRevLett.109.183901
4. E. Flurin, *The Josephson Mixer, a Swiss army knife for microwave quantum optics*, PhD thesis, Ecole Normale Supérieure, Paris (2014)
5. M. Reid, P. Drummond, W. Bowen, E.G. Cavalcanti, P.K. Lam, H. Bachor, U.L. Andersen, G. Leuchs, Colloquium: the Einstein-Podolsky-Rosen paradox: from concepts to applications, Rev. Mod. Phys. **81**, 1727 (2009)
6. A. Einstein, B. Podolsky, N. Rosen, Can quantum-mechanical description of physical reality be considered complete? Phys. Rev. **47**, 777 (1935)
7. M. Reid, Demonstration of the Einstein-Podolsky-Rosen paradox using nondegenerate parametric amplification, Phys. Rev. A **40**, 913 (1989)
8. S.L. Braunstein, P. van Loock, Quantum information with continuous variables, Rev. Mod. Phys. **77**, 513–577 (2005), https://doi.org/10.1103/RevModPhys.77.513
9. C. Weedbrook, S. Pirandola, R. García-Patrón, N.J. Cerf, T.C. Ralph, J.H. Shapiro, S. Lloyd, Gaussian quantum information, Rev. Mod. Phys. **84**, 621–669 (2012), https://doi.org/10.1103/RevModPhys.84.621
10. J. Peise, I. Kruse, K. Lange, B. Lücke, L. Pezzé, J. Arlt, W. Ertmer, K. Hammerer, L. Santos, A. Smerzi, C. Klempt, Satisfying the Einstein-Podolsky-Rosen criterion with massive particles, Nat. Commun. **6**, 8984 (2015), https://doi.org/10.1038/ncomms9984
11. C. Gross, H. Strobel, E. Nicklas, T. Zibold, N. Bar-Gill, G. Kurizki, M.K. Oberthaler, Atomic homodyne detection of continuous-variable entangled twin-atom states, Nature **480**, 219 (2011), https://doi.org/10.1038/nature10654
12. L.-M. Duan, G. Giedke, J.I. Cirac, P. Zoller, Inseparability criterion for continuous variable systems, Phys. Rev. Lett. **84**, 2722 (2000)

Chapter 11
Outlook

In this thesis we presented a nonlinear readout scheme which leverages time-reversed dynamics. In the context of applied quantum technologies, such a nonlinear readout technique addresses the detection problem that arises when employing highly entangled probe states. For the experimental implementation, we utilise spin exchange interactions in a mesoscopic atom cloud which—in a first step—lead to an entangled spin state. We demonstrated that the underlying interactions can be controlled comprehensively, which promotes spin exchange to the central building block of our experimental model system. In particular, the entangling interactions can be time reversed and used to disentangle a state by revoking its nonclassical correlations in order to allow for feasible detection.

To show this explicitly, we constructed an interferometric sequence which incorporates this nonlinear readout. It is also known under the name SU(1,1) interferometer. In this scheme, phase imprints are measured by the effect they have on the reversibility during time reversal. Perfect time reversal back to the initial state is only achieved if the entangled probe state remains unperturbed. Instead, accumulated phases during interrogation prevent such reversibility—a working principle that resembles the Loschmidt Echo [1]. We characterized the phase sensitivity experimentally and verified that quantum-enhanced performance is achieved by merely detecting average spin populations. This mapping onto readily detectable first moments stands in contrast to using linear readout which usually requires technically-challenging single particle detection with high fidelity. Our experiments therefore provide a direct example of how nonlinear transformations that build on particle interactions, widen the spectrum of highly entangled states that are useful with present-day detection technology.

Our experimental results are consistent with theoretical predictions. The scheme is capable of exhausting the quantum resource by detecting solely mean atom numbers—in principle, up to the fundamental Heisenberg limit of phase sensitivity.

D. Linnemann, *Quantum-Enhanced Sensing Based on Time Reversal of Entangling Interactions*, Springer Theses,
https://doi.org/10.1007/978-3-319-96008-1_11

Spin exchange can be understood as parametric amplification. Initially empty spin states get populated spontaneously via the amplification of vacuum noise such that a heavily fluctuating probe state emerges. This state's inherent fluctuations are the essential resource for superior phase sensing. While a posteriori amplification cannot enhance phase sensitivity since it cannot differentiate between signal and noise, we demonstrated that amplified noise to start with enables quantum-enhanced phase measurements. In contrast, vacuum noise entering a passive interferometer is detrimental as it limits the achievable phase sensitivity [2]. An additional amplification stage can be used to magnify the output state to ease detection even further. We investigated this scheme of an active interferometer and showed that quantum-enhanced performance is not only maintained but improved in realistic, viz noisy environments. This noiseless amplification is enabled by the nonclassical correlations present during readout. Therefore, the resource entanglement is used twice in this scheme, during interrogation for improved phase sensitivity, and during readout for noiseless amplification.

Furthermore, detached from these interferometry applications, we employed the nonlinear readout as an instrument to study phase damping, and as an entanglement witness to detect correlations of the Einstein-Podolsky-Rosen type in the atomic cloud. For the latter applications, the absorption of fluctuations down to single atom level is crucial.

Several aspects of the work described in this thesis call for further investigations. In this chapter we provide an outlook by highlighting a few ideas in more detail: the technique of time reversal allows to measure out-of-time-ordered correlators (OTOC). Such correlators have recently been identified as a key diagnostics into questions of how initially well-localized information is spread such that isolated quantum many-body systems effectively lose the memory of their initial condition and eventually thermalise. This process is referred to as scrambling of quantum information. We first introduce the main idea behind such correlators and show that the nonlinear readout as demonstrated in this thesis in fact implements such an object. Subsequently, we present an experimentally feasible method to extend the nonlinear time reversal beyond the undepleted pump approximation. We detail how scrambling of quantum information can be accessed experimentally, when applying this extended time reversal scheme to measure OTOCs in more general situations.

Besides this field of topics which is centred at OTOCs and their application we also detail perspectives of the interferometric line of thinking. Recently, theoretical investigations into the SU(1,1) interferometer were centred at increasing the side mode population. Finally, we discuss how the measurements on phase spreading can be complemented and detail how nonlinear readout can be used for state tomography and reconstruction of the covariance matrix.

11.1 Out-of-Time-Ordered Correlators

Inverting the sign of a nonlinear Hamiltonian facilitates measurements of out-of-time ordered correlators (OTOC). Being related to what is called the butterfly effect in chaotic systems they describe the impact of a (minute) perturbation onto the ensuing dynamics [3, 4]. These correlators are connected to time reversal because the perturbation's impact is quantified by a gedankenexperiment in which the arrow of time is inverted. Recently, these correlation functions have attracted significant theoretical and experimental attention [5–8]. In this section we introduce OTOCs and explain their connection to the nonlinear readout stage.

For two commuting operators $\hat{W}$ and $\hat{V}$ the out-of-time-ordered correlator is given by

$$F(t) = \left\langle \hat{W}_t^\dagger \hat{V}^\dagger \hat{W}_t \hat{V} \right\rangle. \tag{11.1}$$

where $\hat{W}_t$ is the time evolved operator of $\hat{W}$, i.e. $\hat{W}_t = \mathrm{e}^{\mathrm{i}\mathcal{H}t/\hbar}\hat{W}\mathrm{e}^{-\mathrm{i}\mathcal{H}t/\hbar}$. Such a correlation function describes the overlap of two states $\langle\Psi_1|\Psi_2\rangle$ which differ in their ordering of the two operators $\hat{V}$ and $\hat{W}_t$: $|\Psi_1\rangle = \hat{W}_t\hat{V}\,|\mathrm{init}\rangle$ and $|\Psi_2\rangle = \hat{V}\hat{W}_t\,|\mathrm{init}\rangle$ where $|\mathrm{init}\rangle$ is a suitable initial state. Both operators act at different time: operator $\hat{V}$ for $t = 0$, and $\hat{W}_t$ for, say, a later time $t > 0$. However, then the chronological order and the order of application do not agree for state $|\Psi_2\rangle$. Therefore, the state $|\Psi_2\rangle$ describes a hypothetical setting in which time runs backwards. In contrast, for time ordered correlation functions operators for later times stand to the left of operators for earlier times.

Being related to different operator orderings, OTOCs measure the commutator between $\hat{W}_t$ and $\hat{V}$. Initially, both operators commute per definitionem. However, the Hamiltonian $\mathcal{H}$ introduces quantum correlations such that both operators fail to commute eventually. This emerging non-commutativity is measured by the real part of the OTOC,

$$\mathrm{Re}\,F(t) = 1 - \left\langle \left| [\hat{W}_t, V] \right|^2 \right\rangle. \tag{11.2}$$

As the concept of OTOC relies on the notion of time reversal there is a natural connection to the experiments reported on in this thesis. Here, we show that the output of the time reversal sequence is in fact a measurement of an out-of-time-ordered correlator. For this we note that the state at the output of the time reversal sequence reads

$$|\Psi\rangle = \mathrm{e}^{\mathrm{i}\mathcal{H}t}\mathrm{e}^{-\mathrm{i}\hat{K}_z\varphi}\mathrm{e}^{-\mathrm{i}\mathcal{H}t}\,|\mathrm{vac}\rangle\,. \tag{11.3}$$

Here, the first period of spin exchange is described by the action of $\mathrm{e}^{-\mathrm{i}\mathcal{H}t}$ acting onto the initial state with empty side modes $|\mathrm{vac}\rangle$. Subsequently, a spinor phase rotation of φ is employed before a second period under spin exchange follows. Inspired

by reference [7] we define $W = \mathrm{e}^{-\mathrm{i}\hat{K}_z\varphi}$ which is the operator generating the spinor phase rotation. We introduced this operator which belongs to the SU(1,1) framework in Chap. 5. Then the above Eq. 11.3 can be written as

$$|\Psi\rangle = \mathrm{e}^{\mathrm{i}\mathcal{H}t} W \mathrm{e}^{-\mathrm{i}\mathcal{H}t} |\mathrm{vac}\rangle = W_t |\mathrm{vac}\rangle . \tag{11.4}$$

Measurements of the side mode population are formally described by $\langle\Psi| \hat{K}_z |\Psi\rangle$. Writing this out yields

$$\langle N_+\rangle \propto \langle \mathrm{vac}| \hat{W}_t^\dagger \hat{K}_z \hat{W}_t |\mathrm{vac}\rangle \propto \langle \mathrm{vac}| \hat{W}_t^\dagger \hat{K}_z \hat{W}_t \hat{K}_z |\mathrm{vac}\rangle . \tag{11.5}$$

In the last step we used that the initial vacuum state $|\mathrm{vac}\rangle$ is an eigenstate of $\hat{K}_z$. At time $t = 0$ the two operators $\hat{W}_t$ and $V \equiv \hat{K}_z$ commute as required. Therefore, determining the side mode population leaving the SU(1,1) interferometer is tantamount to measuring the above OTOC. However, within the undepleted pump approximation the output state is a two-mode squeezed vacuum. This state is exhaustively described by a single parameter, e.g. its average mode population. In this idealised framework measurements of OTOCs can therefore not provide additional information. This situation changes drastically when leaving the undepleted pump approximation.

11.2 Time Reversal Beyond Undepleted Pump Approximation

In this section we present a path towards realising time reversal without imposing the undepleted pump approximation. The spin exchange Hamiltonian consists of two parts, the elementary scattering event as governed by $\mathcal{H}_{\mathrm{SCC}}$ and attached collisional energy shifts described by $\mathcal{H}_{\mathrm{el}}$. Within this thesis we inverted the former part by controlled phase imprints—a method that relies on the fact that the nonlinear coupling strength $\kappa = gN_0$ is given in an effective way by the phase (and magnitude) of the pump mode. Since the collisional shifts are not affected by such phase imprints they are compensated by other means, i.e. by invoking the undepleted pump approximation.

Due to their intimate connection both Hamiltonian terms depend identically on the microscopic nonlinearity g which in turn is related to the microscopic scattering details, in particular all possible s-wave scattering channels. Consequently, the microscopic coupling strength for spin exchange within the $F = 2$ and $F = 1$ manifold have opposite signs: while $F = 1$ is ferromagnetic ($g < 0$), the effective three level system embedded in $F = 2$ features antiferromagnetic interactions with $g > 0$. This provides a way to invert the full many body Hamiltonian without relying on the undepleted pump approximation: initially spin exchange is performed within $F = 1$. Then after swapping all three involved states to $F = 2$ a subsequent period of spin exchange continues with opposite sign of the nonlinearity—thereby realising time

reversal. However, the coupling strength's magnitude for spin exchange in $F = 2$ is an order of magnitude larger than for $F = 1$. To compensate for the different coupling strengths in $F = 2$ and $F = 1$ the external detuning can be adjusted. This is necessary because the spin exchange resonance condition $q = gN_0$ depends on the associated coupling strength. This can be achieved by changing the strength of microwave dressing. Alternatively, for some applications it might suffice to achieve time reversal—ceteris paribus—by transferring only one-tenth of the pump population to $F = 2$ such that both effective coupling strengths are equal in magnitude and differ only by the sign. One has to keep in mind, though, that this changes the total atom number of the system under consideration.

11.3 Scrambling of Quantum Information

Driven classical systems can exhibit chaotic behaviour. In such a situation the knowledge of the initial condition is readily lost. In closed quantum systems, in contrast, information cannot be lost—which leads to questions about how isolated systems equilibrate or eventually thermalise. Scrambling describes how information is distributed to the many degrees of freedom of a quantum system. Then a measurement that is restricted to a sub part of the entire system cannot retrieve the information any more. Such information scrambling is connected to the growth of entanglement [9]. Measurements of OTOCs are to a large extent motivated by assessing such scrambling behaviour of quantum many-body systems. Therefore, being able to perform time reversal beyond the undepleted pump approximation opens up a route to studying how information is delocalised. Here we follow reference [10] and adopt their findings to our experimental system.

A first prerequisite is a system that features chaotic behaviour. Spin exchange allows for such chaotic dynamics which arises when the detuning q is driven periodically [11, 12]. In classical chaotic systems the Lyapunov exponent quantifies how two initially close trajectories subsequently diverge in an exponential fashion. In quantum mechanics the notion of chaos is linked to the decay of the Loschmidt echo (which corresponds to the Lyapunov exponent) [13]. This Loschmidt echo is given by $\langle \text{init}|e^{i\mathcal{H}_1 t}e^{-i\mathcal{H}_2 t}|\text{init}\rangle$. It therefore describes the overlap between the two states starting from the same initial state $|\text{init}\rangle$ but governed by slightly different Hamiltonians $\mathcal{H}_1$ and $\mathcal{H}_2 = \mathcal{H}_1 + \delta\mathcal{H}$ where $\delta\mathcal{H}$ is considered a weak perturbation. This Loschmidt echo, which corresponds to a time ordered correlation function, and its dynamic decay can be compared to the respective decay of the OTOC. The signature of many-body scrambling is a slowed down decay of the OTOC and a particular dependence on the number of degrees of freedom. More details can be found in reference [10].

11.4 Interferometry Within the Depleted Pump Regime

When it comes to improving a measurement's precision the use of entanglement is usually the ultima ratio. Evidently, it is imperative in situations in which the attainable precision is bounded by quantum effects. Similarly, we take for granted that there are severe limitations on the size of the resource. If this were not the case one could readily achieve higher precision by employing more atoms. Regarding the latter point, however, there are various scenarios conceivable: in some situations the size of the probe state is ultimately limited. This might for instance arise when the impact of the probe atoms onto the sample needs to be minimised [14, 15]. In such situations a small yet highly sensitive probe state is desirable. Then, the amplifying nonlinear readout is the optimal scheme because the side modes are only sparsely populated but nonetheless perform phase sensing at the ultimate Heisenberg limit. In other fields of application, however, the *total* number of atoms—and not the ones used for sensing—are the limiting factor. For such situations the presented nonlinear readout is not ideally suited because a large portion of atoms is held back in the pump mode. While these atoms enable the parametric amplification they are not used for the actual phase interrogation.

Recent theoretical works reexamine the here presented atomic SU(1,1) interferometer with the aim to achieve quantum-enhanced performance also for these applications, i.e. with respect to the total number of employed atoms. In reference [16] the authors find sub-shot noise phase sensitivities also when going deep into the depleted pump regime of spin exchange. In contrast, the authors of reference [17] study a slightly adjusted scheme in which spin exchange is supplemented with linear coupling. Thereby the phase sensing atom number in the side mode is enlarged and quantum-enhanced phase sensitivity is predicted.

11.5 Phase Spreading

The arguments put forward in this section are based on references [18–20]. In Section 10.1 we demonstrate that the nonlinear readout can be employed as a tool to study phase damping. Such phase damping has been observed in a variety of experiments, more recently e.g. in reference [21], by splitting a condensate into two equal parts. This splitting introduces relative number fluctuations which in turn impose a phase uncertainty of the initial state. Collisional interactions then lead to a growing phase uncertainty in time. This explanatory approach ignores finite temperature effects [18]. Their importance, however, is clarified by the failure of a zero-temperature theory [22] which takes into account collisional interactions to reproduce the phase spreading found in experiments [23]. The rôle of the noncondensed fraction is the subject of more recent theoretical investigations [20].

To facilitated the study of such fundamental aspects of phase spreading, effects due to collisional interactions should be minimized. Therefore, the unequal atom

distribution of the amplifying nonlinear readout might come as an advantage. This is because the sparsely populated side modes can be used to probe the phase uncertainty of the large pump mode without significantly disturbing it.

11.6 State Tomography, Extension to Many Spatial Modes

In Sect. 10.2 we employed the nonlinear readout as an EPR entanglement witness. In a similar fashion, the nonlinear readout can be used as an autonomous building block to partly reconstruct a state's covariance matrix [24, 25]. This matrix is used widely in quantum optics to characterize quantum states in the Gaussian regime. In this regime, the states are exhaustively described by their mean quadratures and their (mutual) (co-) variances. Furthermore, it might be used for more general state tomography [26]. Such tomographic reconstruction techniques are presented in references [27–29] and build on the symmetry of the SU(1,1) mode transformations.

Going beyond the single spatial mode treatment, we believe that the high degree of experimental control qualifies the nonlinear readout for the characterization of entanglement in spatially-extended Bose-Einstein condensates [30–32]. Recently, we implemented a steerable laser beam with which different parts of the atomic cloud can be addressed. With this technique available, the nonlinear readout might be performed with spatially nonuniform parameters.

References

1. T. Macri, L. Pezzé, A. Smerzi, Loschmidt Echo for quantum metrology (2016), arXiv:1604.04246
2. M. Takeoka, K.P. Seshadreesan, C. You, S. Izumi, J.P. Dowling, Fundamental precision limit of a Mach-zehnder interferometric sensor when one of the inputs is the vacuum (2017), arXiv:1705.09506
3. D.A. Roberts, B. Swingle, Lieb-Robinson bound and the butterfly effect in quantum field theories, Phys. Rev. Lett. **117**, 091602 (2016)
4. M. Campisi, J. Goold, Thermodynamics of quantum information scrambling, Phys. Rev. E **95**, 062127 (2017)
5. J. Li, R. Fan, H. Wang, B. Ye, B. Zeng, H. Zhai, X. Peng, J. Du, Measuring out-of-time-order correlators on a nuclear magnetic resonance quantum simulator (2016), arXiv:1609.01246
6. K.X. Wei, C. Ramanathan, P. Cappellaro, Exploring localization in nuclear spin chains (2016), arXiv:1612.05249
7. M. Gärttner, J.G. Bohnet, A. Safavi-Naini, M.L. Wall, J.J. Bollinger, A.M. Rey, Measuring out-of-time-order correlations and multiple quantum spectra in a trapped-ion quantum magnet, Nat. Phys. **13**, 781–786 (2017), https://doi.org/10.1038/nphys4119
8. E.J. Meier, J. Ang'ong'a, F.A. An, B. Gadway, Exploring quantum signatures of chaos on a Floquet synthetic lattice (2017), arXiv:1705.06714
9. M. Gärttner, P. Hauke, A.M. Rey, Relating out-of-time-order correlations to entanglement via multiple-quantum coherences (2017), arXiv:1706.01616
10. B. Swingle, G. Bentsen, M. Schleier-Smith, P. Hayden, Measuring the scrambling of quantum information, Phys. Rev. A **94** (2016), https://doi.org/10.1103/PhysRevA.94.040302

11. J. Kronjäger, K. Sengstock, K. Bongs, Chaotic dynamics in spinor Bose- Einstein condensates, New J. Phys. **10**, 045028 (2008)
12. J. Cheng, Chaotic dynamics in a periodically driven spin-1 condensate, Phys. Rev. A **81**, (2010), https://doi.org/10.1103/PhysRevA.81.023619
13. A. Goussev, R.A. Jalabert, H.M. Pastawski, D.A. Wisniacki, Loschmidt echo, Scholarpedia **7**, 11687 (2012)
14. M.A. Taylor, J. Janousek, V. Daria, J. Knittel, B. Hage, H.-A. Bachor, W.P. Bowen, Biological measurement beyond the quantum limit, Nat. Photon **7**, 229–233 (2013)
15. F. Wolfgramm, C. Vitelli, F.A. Beduini, N. Godbout, M.W. Mitchell, Entanglement-enhanced probing of a delicate material system. Nat. Photon **7**, 28–32 (2013)
16. M. Gabbrielli, L. Pezzé, A. Smerzi, Spin-mixing interferometry with bose- einstein condensates. Phys. Rev. Lett. **115**, (2015), https://doi.org/10.1103/PhysRevLett.115.163002
17. S.S. Szigeti, R.J. Lewis-Swan, S.A. Haine, Pumped-Up SU(1,1) Interferometry, Phys. Rev. Lett. **118**, (2017), https://doi.org/10.1103/PhysRevLett.118.150401
18. A. Sinatra, Y. Castin, E. Witkowska, Nondiffusive phase spreading of a Bose-Einstein condensate at finite temperature. Phys. Rev. A **75**, 033616 (2007)
19. A. Sinatra, Y. Castin, Genuine phase diffusion of a Bose-Einstein condensate in the microcanonical ensemble: A classical field study, Phys. Rev. A **78**, 053615 (2008)
20. A. Sinatra, Y. Castin, E. Witkowska, Coherence time of a Bose-Einstein condensate, Phys. Rev. A **80**, (2009), https://doi.org/10.1103/PhysRevA.80.033614
21. T. Berrada, S. van Frank, R. Bücker, T. Schumm, J.-F. Schaff, J. Schmiedmayer, Integrated Mach-Zehnder interferometer for Bose-Einstein condensates, Nat. Commun. **4** (2013)
22. A. Sinatra, Y. Castin, Binary mixtures of Bose-Einstein condensates: Phase dynamics and spatial dynamics, Eur. Phys. J. D **8**, 319–332 (2000)
23. D.S. Hall, M.R. Matthews, C.E. Wieman, E.A. Cornell, Measurements of relative phase in two-component bose-einstein condensates, Phys. Rev. Lett. **81**, 1543–1546 (1998) https://doi.org/10.1103/PhysRevLett.81.1543
24. E. Flurin, N. Roch, F. Mallet, M.H. Devoret, B. Huard, Generating entangled microwave radiation over two transmission lines, Phys. Rev. Lett. **109** (2012), https://doi.org/10.1103/PhysRevLett.109.183901
25. E. Flurin, *The Josephson Mixer, a Swiss army knife for microwave quantum optics*, PhD thesis, Ecole Normale Supérieure, Paris (2014)
26. A.I. Lvovsky, M.G. Raymer, Continuous-variable optical quantum-state tomography. Rev. Mod. Phys. **81**, 299–332 (2009) https://doi.org/10.1103/RevModPhys.81.299
27. G.S. Agarwal, J. Banerji, Reconstruction of SU(1,1) states, Phys. Rev. A **64** (2001), https://doi.org/10.1103/PhysRevA.64.023815
28. G.M. D'Ariano, E. De Vito, L. Maccone, SU(1,1) tomography, Phys. Rev. A **64**, (2001) https://doi.org/10.1103/PhysRevA.64.033805
29. E. Knyazev, K.Y. Spasibko, M. Chekhova, F.Y. Khalili, Quantum tomography enhanced through parametric amplification (2017), arXiv:1708.03820
30. L.E. Sadler, J.M. Higbie, S.R. Leslie, M. Vengalattore, D.M. Stamper-Kurn, Spontaneous symmetry breaking in a quenched ferromagnetic spinor Bose-Einstein condensate, Nature **443**, 312–315 (2006), https://doi.org/10.1038/nature05094
31. G.I. Mias, N.R. Cooper, S.M. Girvin, Quantum noise, scaling, and domain formation in a spinor Bose-Einstein condensate. Phys. Rev. A **77**, 023616 (2008)
32. S.R. Leslie, J. Guzman, M. Vengalattore, J.D. Sau, M.L. Cohen, D.M. Stamper-Kurn, Amplification of fluctuations in a spinor Bose-Einstein condensate, Phys. Rev. A **79** (2009), https://doi.org/10.1103/PhysRevA.79.043631

Appendix A
Spin Exchange in $F = 2$

In this section we discuss spin exchange within the $F = 2$ hyperfine manifold taking into account all five sublevels. In the main text, an effective three level system that is embedded within $F = 2$ is considered. Here we justify this simplified description in more detail. We present the full Hamiltonian for spin exchange within $F = 2$ and identify all spin exchange processes among the five involved levels. In particular we investigate the spurious processes that lead out of the effective three level system. To this end we derive the relative coupling strength and the associated spin exchange detuning for each scattering process. Finally, we employ a numerical calculation to examine under which conditions the effective three-level description remains valid.

Due to the five magnetic sublevels of $F = 2$ a slight change of notation is in order. In the following, we call $\hat{a}_i$ the annihilation operator, and N_i the population of the mode $m_F = i$ with $i = 0, \pm 1 \pm 2$.

A.1 Scattering Potential

In this section we treat the scattering of two atoms each having spin $F = 2$. This is a continuation of the theory developed in the main part, Sect. 3.2. In direct analogy to Eq. 3.2 the scattering potential for two $F = 2$ atoms can be written in the following way

$$V = a_0 \mathcal{P}_0 + a_2 \mathcal{P}_2 + a_4 \mathcal{P}_4 \tag{A.1}$$

In contrast to the aforementioned $F = 1$ case, an additional scattering channel with combined spin $F = 4$ exists. This quintet channel is described by the scattering length a_4. This scattering potential can be reformulated in a microscopic way

$$V = c_0 + c_1 \mathbf{F}_1 \cdot \mathbf{F}_2 + 5 c_2 A_2^\dagger A_2 \tag{A.2}$$

D. Linnemann, *Quantum-Enhanced Sensing Based on Time Reversal of Entangling Interactions*, Springer Theses,
https://doi.org/10.1007/978-3-319-96008-1

Here, A_2 is the annihilation operator for a spin singlet. It can be expressed in terms of Clebsch-Gordan coefficients as $A_2 = \sum_{i,j} \langle F = 0, 0 | F_1 = 2, i, F_2 = 2, j \rangle \hat{a}_i \hat{a}_j$. Note that the factor of 5 is missing in reference [1]. The coefficients are given by $(c_0, c_1, c_2) = (\frac{4a_2+3a_4}{7}, \frac{a_4-a_2}{7}, \frac{3(a_4-a_2)-7(a_2-a_0)}{35})$ [1–3]. Spin exchange is driven by the terms described by coefficients c_1 and c_2, respectively [4]. Thus the nonlinear coupling strength follows from both, singlet-triplet and quintet-triplet scattering length differences.

A.2 Full Hamiltonian

Expanding the scattering potential in terms of individual mode operators, one arrives at the Hamiltonian

$$\begin{aligned}\mathcal{H} \propto\, & c_0 \left((N_{-1} + N_0 + N_1)^2 + (N_{-2} + N_2) \right) + \\ & c_2 \left(2a_0 a_0 a_2^\dagger a_{-2}^\dagger - 2a_0 a_0 a_1^\dagger a_{-1}^\dagger - 4a_2 a_{-2} a_1^\dagger a_{-1}^\dagger + 4N_2 N_{-2} + 4N_1 N_{-1} + N_0(N_0 - 1) \right) + \\ & c_1 (2\sqrt{6} a_0 a_{-2} a_{-1}^\dagger a_{-1}^\dagger + 2\sqrt{6} a_0 a_2 a_1^\dagger a_1^\dagger + 2\sqrt{6} a_2 a_{-1} a_1^\dagger a_0^\dagger + 2\sqrt{6} a_0 a_{-1} a_1^\dagger a_{-2}^\dagger + 4 a_2 a_{-2} a_1^\dagger a_{-1}^\dagger + \\ & 6 a_0 a_0 a_1^\dagger a_{-1}^\dagger + (6N_0 - 1)(N_1 + N_{-1}) + (N_1 - N_{-1})^2 + 4N_{-2}(N_{-2} - 1) + 4N_2(N_2 - 1) + \\ & (8N_{-1} - 4N_1 - 4N_2)N_{-2} + (8N_1 - 4N_{-1} - 4N_{-2})N_2) \end{aligned} \tag{A.3}$$

Here the colour coding is in accordance with Fig. A.1 to indicate the elementary spin exchange processes. Each of the coloured terms includes the corresponding hermitian conjugate which is omitted in the formula for clarity. We detail these at a later point. Let us first consider the particular case of vanishing populations in states $m_F = \pm 2$. Then, the Hamiltonian simplifies to

$$\begin{aligned}\mathcal{H} \propto\, & -c_2 \left(2a_0 a_0 a_1^\dagger a_{-1}^\dagger + \text{h.c.} + (2N_0 + 1)(N_1 + N_{-1}) \right) + \\ & c_1 \left(6a_0 a_0 a_1^\dagger a_{-1}^\dagger + \text{h.c.} + (6N_0 - 1)(N_1 + N_{-1}) \right) \end{aligned} \tag{A.4}$$

for this we added the term $c_2((N_1 - N_{-1})^2 - N^2)$ which is a constant for the effective three level system. For large pump mode populations one thus arrives at

$$\mathcal{H} = (6c_1 - 2c_2) \left(a_0 a_0 a_1^\dagger a_{-1}^\dagger + \text{h.c.} + N_0(N_1 + N_{-1}) \right) \tag{A.5}$$

which is similar to the $F = 1$ case, Eq. 3.4 except for a different microscopic nonlinear coupling strength.

A.3 All Possible Spin Exchange Processes

Within $F = 2$ there are several possible elementary spin exchange processes. The only requirement is the conservation of magnetization. Figure A.1 shows all processes in the underlying energy landscape of the quadratic Zeeman shift. The respective processes are colour coded to facilitate comparison with the Hamiltonian terms, Eq. A.3. The nonlinear coupling strength can thereby directly be read off. For instance, the desired spin exchange process $2 \times |0\rangle \leftrightarrow |1\rangle + |-1\rangle$ has the coupling strength, $6c_1 - 2c_2 = [(12(a_4 - a_2) + 7(a_2 - a_0)]/35$. In Table A.1 we list all possible spin exchange processes with their respective coupling strength. For the numerical value in terms of scattering length differences we resort to reference [3]. There, using spin exchange the scattering length differences are measured to be $c_1 \approx 1\, a_B$ and $c_2 \approx -0.1\, a_B$ where a_B denotes the Bohr radius. Compared to the $F = 1$ case, the coupling strength for spin exchange in $F = 2$ is by a factor ~9 larger.

Additionally, we state the spin exchange detuning (in units of $q\, B^2 = 2\pi \times 60\,\mathrm{Hz}$) of the particular process. The underlying energy shifts as generated by the magnetic

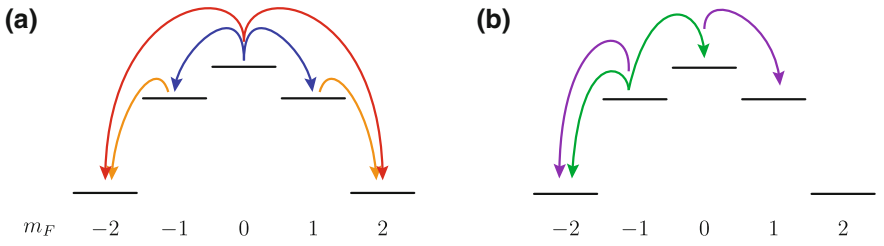

Fig. A.1 Overview of all spin exchange channels in the $F = 2$ manifold. For reference we reproduce Fig. 6.5. **a** Symmetric spin exchange couplings. **b** Asymmetric processes. For the sake of clarity only half of the allowed channels are shown. For a complete accounting, one has to consider the additional processes which arise under the interchange $m_F \rightarrow -m_F$

Table A.1 Coupling strength and spin exchange detuning for spurious spin exchange channels. In the left column all channels that leave the effective three level system are listed. The coupling strength is read off from the Hamiltonian. Its numerical value in units of Bohr radii a_B is based on reference [3]. The remaining two columns state the spin exchange detuning in units of $q_B B^2$ when dispersive microwave dressing is applied and turned off, respectively

Process	Coupling	Scattering length difference (a_B)	Dressing off	Dressing on
$2 \times \|0\rangle \leftrightarrow \|-1\rangle + \|+1\rangle$	$6c_1 - 2c_2$	5.8	1	0
$2 \times \|0\rangle \leftrightarrow \|2\rangle + \|-2\rangle$	$2c_2$	−0.30	4	1.5
$\|1\rangle + \|-1\rangle \leftrightarrow \|2\rangle + \|-2\rangle$	$4(c_1 - c_2)$	3.6	3	3
$2 \times \|\pm 1\rangle \leftrightarrow \|\pm 2\rangle + \|0\rangle$	$2\sqrt{6}c_1$ 4.9	2	1.5	
$\|0\rangle + \|\pm 1\rangle \leftrightarrow \|\mp 1\rangle + \|\pm 2\rangle$	$2\sqrt{6}c_1$ 4.9	1	1.5	

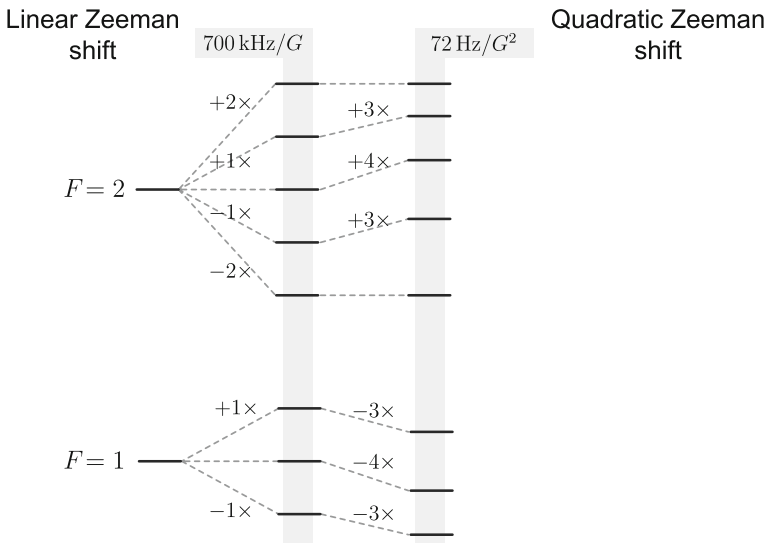

Fig. A.2 Level shifts of Rubidium-87 in a magnetic field. The linear Zeeman effect shifts the atomic levels proportional to their magnetic quantum number m_F. The shift between adjacent levels amounts to 700 kHz/G as shown in the left column. The quadratic Zeeman effect shifts the magnetic sublevels proportional to $(4 - m_F^2)$. Therefore, only the $m_F = \pm 2$ states are not subjected to this level shift. Adjacent levels are shifted by 72 Hz/G^2 (right column)

bias field are detailed in Fig. A.2. To assess the spin exchange detuning we distinguish between the case of activated and deactivated microwave dressing. To this end we assume that microwave dressing merely shifts the $m_F = 0$ component to be in resonance with $m_F = \pm 1$ which is a reasonable approximation.

A.4 Numerical Simulation of the Full $F = 2$ Hamiltonian

From the previous section we deduce that the description in terms of an effective three level system is valid because of the large detuning to the $|2, \pm 2\rangle$ states. In this section we investigate the region of validity and the robustness of the effective three level approximation. For this we numerically simulate spin exchange among all five levels taking the full $F = 2$ Hamiltonian. For this purpose we resort to the truncated Wigner approximation. We start with 400 atoms prepared in $|0\rangle$ and all other states empty. The numerical value of the coupling strength is fixed at $\kappa = 2\pi \times 25$ Hz which is slightly larger than the experimentally extracted value. While we tune the spin exchange process $2 \times |2, 0\rangle \leftrightarrow |2, 1\rangle + |2, -1\rangle$ into resonance, the energy detuning to the states $|2, \pm 2\rangle$ is left as a free parameter. We call this detuning q_2. The energy landscape is summarised in the inset of Fig. A.3b. In the experiment this detuning

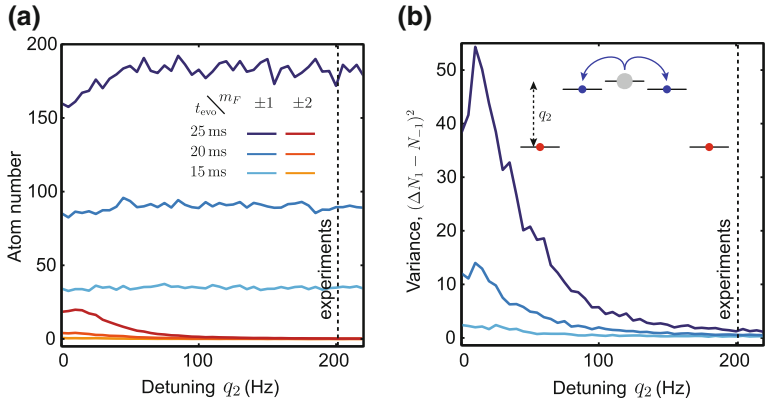

Fig. A.3 Full $F = 2$ spin exchange simulation. **a** Simulated mode populations treating the full $F = 2$ Hamiltonian. The process $2 \times |0\rangle \leftrightarrow |1\rangle + |-1\rangle$ is tuned into resonance by shifting the pump mode in energy. The states $|\pm 2\rangle$ are detuned from the pump by amount q_2 (see inset of panel b). In the experiment this detuning depends on the quadratic Zeeman shift and amounts to $q_2 = 2\pi \times 200\,\text{Hz}$. This value is indicated by the vertical dashed line. We use a coupling strength of $\kappa = 2\pi \times 25\,\text{Hz}$ and let spin exchange evolve for $t_{\text{evo}} = 10$, 15, and 20 ms (see legend). We find significant population of the $|\pm 2\rangle$ states only for a detuning $q_2 < 50\,\text{Hz}$ and evolution times $t_{\text{evo}} > 20\,\text{ms}$. **b** Variance of the atom number difference $N_1 - N_{-1}$ versus detuning q_2. For the effective three level treatment, this atom number difference between the states $|\pm 1\rangle$ vanishes. Significant deviations are found for detuning $q_2 < 100\,\text{Hz}$ and large evolution times $t_{\text{evo}} > 20\,\text{ms}$. At the detuning where the experiments are performed the effect is negligible

is determined by the quadratic Zeeman shift and amounts to $q_2 \approx 2\pi \times 200\,\text{Hz}$. In panel (a) we plot the summed spin population of either $|2, \pm 1\rangle$ (blue) or $|2, \pm 2\rangle$ (red) found after a variable time of spin exchange ranging up to 25 ms (see inset) well above the experimentally employed time scales. A population of the $|2, \pm 2\rangle$ levels (with a concomitant decrease in levels $|2, \pm 1\rangle$) occurs only for detunings that fall below $q_2 = 2\pi \times 50\,\text{Hz}$. The experimental value is indicated by the vertical dashed line. At this stage any population outside the effective three level system encompassing the $|2, \pm 1\rangle$ levels is negligible. In panel (b) we go one step further than average mode populations and also consider fluctuations which are a more sensitive probe: the variance of $N_1 - N_{-1}$ is plotted versus the detuning q_2. Ideally, the variance vanishes for all durations of spin exchange (colour coding identical to panel a). The influence of the spurious additional levels $|2, \pm 2\rangle$ shows up predominantly for long durations of spin exchange exceeding 20 ms. For shorter durations and at the detuning employed in the experiments a insignificant contribution is found.

A.5 External Trap Levels

Thus far we investigated the closedness of the effective spin-1 system solely with respect to spin dynamics—and did not take into account any interplay with exter-

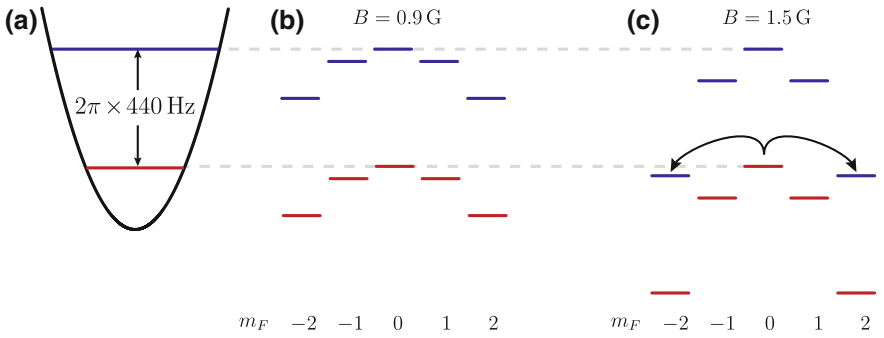

Fig. A.4 Spin exchange among external modes. **a** Harmonic trap in transversal direction of the optical waveguide potential. **b** At a magnetic bias field of $B = 0.9$ G—as employed in the experiments—the higher lying trap levels (blue) are out of reach for spin exchange. This situation changes at higher magnetic bias fields as exemplified in panel c). Here, spin exchange starting from the pump mode in $m_F = 0$ might lead to population of the $m_F = \pm 2$ states that belong to a higher trap level as indicated

nal dynamics. This is valid for sufficiently small magnetic bias fields. If, however, the energy shifts caused by the quadratic Zeeman shift are comparable to trap frequencies, spin exchange might populate higher lying trap modes [5]. We explain this in Fig. A.4. Our spin exchange experiments are performed at a magnetic field of $B = 0.9$ G. At a transversal trap frequency of $2\pi \times 440$ Hz the higher lying state of the harmonic potential (depicted in panel a) is inaccessible. Besides the large detuning the spin exchange coupling strength suffers from a reduced mode overlap to the excited trap states. Therefore, the effective spin-1 description remains valid. However, this situation changes drastically if the magnetic bias field is increased. Panel (c) shows the quadratic Zeeman shifts arising at $B = 1.5$ G. Here, spin exchange into a higher lying trap mode becomes possible as indicated. Such and similar processes might invalidate the effective spin-1 system at larger magnetic bias fields.

Appendix B
Technical Details

B.1 Accounting of the Level Shifts Due to Microwave Dressing

To assess the level shifts exerted by the microwave dressing, we first detail the radiation characteristics of our microwave antenna, i.e. the relative strength of the three microwave polarizations. For this we start from state $|1, 0\rangle$ and measure the on-resonance Rabi frequency for the three direct microwave transitions to $|2, -1\rangle$, $|2, 0\rangle$, and $|2, 1\rangle$. We find Rabi frequencies of $\Omega_{(\pi,\sigma_-,\sigma_+)} = 2\pi \times (4.9, 3.3, 3.1)$ kHz. Therefore, the microwave antenna radiates polarizations with relative strength (in Rabi frequency) $\pi : \sigma_+ : \sigma_- = 1{:}0.74{:}0.8$; here, the different line strengths of the respective microwave transitions have been eliminated. Therefore, the energy shift of the $|2, 0\rangle$ level results from three contributions due to the off-resonant microwave coupling to all $F = 1$ sub states. However, because of the large first order Zeeman shift, the dominant dispersive energy shift is caused by microwave coupling of $|2, 0\rangle \leftrightarrow |1, 0\rangle$. Each of the two side modes $|2, \pm 1\rangle$ is shifted in energy by two off-resonant couplings.

The microwave that is used for dressing is power stabilized via a servo loop. This ensures reproducibility on the time scale of several weeks. However, as a side effect, the levelling mechanism leads to power drifts during the microwave pulse. We have observed power reductions amounting to 20% in Rabi frequency on the time scale of milliseconds. However, all stated Rabi frequencies are measured via resonant Rabi flopping with short pulse durations $500 < \mu$s. We find agreement among a series of measurements only, if we heuristically reduce the Rabi frequencies of each polarization by 15%.

We will now detail these independent measurements from which we infer the spin exchange detuning. The first is described in Fig. 6.4 where fringes of the non-linear readout are investigated for different detuning used for dispersive microwave dressing. Independently, the effective detuning can be estimated on basis of the side mode population growth during a single period of spin exchange. For this we

D. Linnemann, *Quantum-Enhanced Sensing Based on Time Reversal of Entangling Interactions*, Springer Theses,
https://doi.org/10.1007/978-3-319-96008-1

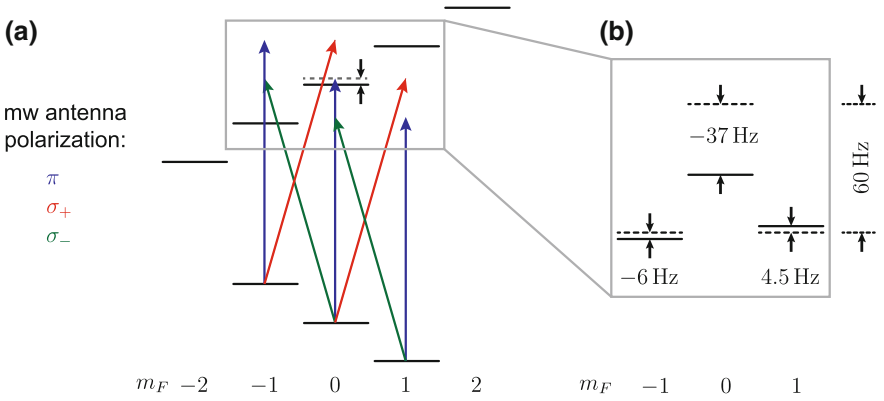

Fig. B.1 Overview of the energy shifts exerted by microwave dressing. **a** We perform microwave dressing $\delta = 2\pi \times 110\,\mathrm{kHz}$ blue detuned to the transition $|1,0\rangle \leftrightarrow |2,0\rangle$. Coupling due to this transition generates the dominant energy shift. Additional energy shifts arise due to all other possible couplings as indicated. **b** Inferred energy shifts of the effective three level system. The dashed levels represent the energy landscape due to the quadratic Zeeman effect. Microwave dressing shifts the levels from the dashed to the solid line

performed numerical simulations as discussed in the main part (see Sect. 7.4). Finally, to find the spin exchange resonance condition in the first place, we typically scan the microwave detuning δ at constant power and record the side mode population after a fixed evolution time. In such spectroscopic measurements, the onset of spin exchange—corresponding to $q = 0$—is witnessed by a sudden and rapid growth of the side mode population. Experimentally, we find this point at a detuning of $\delta = 2\pi \times 70\,\mathrm{kHz}$. All these three measurement are in agreement with the microscopic calculation of energy shifts if we assume the above introduced power drop (Fig. B.1).

B.2 Spatial Gradients of the Microwave Dressing

To assess the microwave gradients over the extent of the atomic cloud we perform resonant Rabi flopping. Eventually, different parts of the cloud dephase due to the spatial gradient of the on-resonance Rabi frequency. Expressed in Rabi frequency, the gradients of each polarization amount to $(\pi, \sigma_+, \sigma_-) = (0.03\%, 0.15\%, -1.3\%)$ over $100\,\mu\mathrm{m}$. Therefore, the gradient of the associated energy shift is dominated by the σ_- polarization. This gradient amounts to less than 1 mHz over $100\,\mu\mathrm{m}$.

B.3 Spatial Gradients

In this section we show that spatial gradients are indiscernible for the experiments on spin exchange and interferometry. Thereby, we justify the usage of all lattice sites to increase the statistical sample size irrespective of their spatial position along the one-dimensional array. With spin exchange being magnetically insensitive to first order we argued above that the dominant source of spatial gradients is the microwave dressing. Here, we assess spatial gradients (regardless of the source) by their effective action onto spin exchange. First, we investigate a potential spatial dependence of the nonlinear coupling strength κ. For the interferometry measurements a spatially constant spinor phase is important which is assessed in the second part.

In Fig. B.2a we evaluate the nonlinear coupling strength for each lattice site separately. For this, we take the average atom number population of every individual lattice site as a reference and use experimental runs for which the on-site atom number falls into a narrow window of $\pm 5\%$. The spatial position along the one-dimensional lattice is colour encoded. As the coupling strength depends on the total atom number it is highest in the centre of the atomic cloud ($\approx 60\,\mu$m) and falls off towards both edges. To asses gradients the coupling strength for similar total atom numbers but at

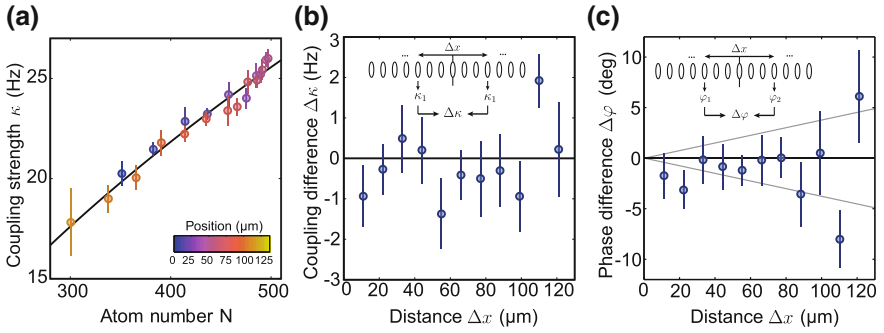

Fig. B.2 Spatial gradients. **a** Spin exchange coupling strength κ evaluated at each individual lattice site. The spatial position along the one-dimensional lattice site is indicated in colour. The atomic density is highest at the centre of the atomic cloud (at $\approx 60\,\mu$m) and falls off towards both edges. With the nonlinear coupling strength being intrinsically density dependent a spatial gradient can be estimated by comparing lattice sites with similar atom number that are close to the left and right edge of the cloud, respectively. **b** To assess spatial gradients quantitatively we evaluate the coupling strength difference between pairs of lattice sites that are taken symmetrically from the centre (see inset). Going outwards step-by-step we increase the distance between the compared lattice sites while their respective atom number remains equal. Plotting the difference in coupling strength versus the baseline shows a flat behaviour and thus no spatial gradients are discernible. Similarly, a potential spatial gradient of the spinor phase imprint can be characterized (panel c). For this the phase offset of the interferometry fringes is evaluated at pairs of lattice sites separated in space by Δx (see inset). Plotting the phase difference versus their spatial distance shows a flat profile. For comparison the two grey lines indicate the expected behaviour if the nonlinear coupling strength κ had a spatial variation of 1 Hz/100 μm

different edges of the cloud should be compared. This is done quantitatively in panel (b). Starting at the centre of the atomic cloud we compare the extracted coupling strength of both adjacent lattice sites. These two lattice sites have equal atom numbers and are separated in space by two lattice sites (11 μm). Going further towards the edges in this symmetrical fashion, lattice sites with equal atom number but larger spatial separation are compared with each other. Thereby the atom number dependence is cancelled and a spatial gradient would show up as a linear slope. Even when comparing the two outermost lattice sites separated by 120 μm we find no indication for a spatial gradient.

In a similar manner we characterize eventual spatial gradients of the spinor phase. The spinor phase might have a spatial variation because of two reasons; first, the dependence could be inherited from a spatially varying nonlinear coupling strength. In this case, a spinor phase gradient builds up during the spin exchange period. Finally, a spinor phase variation could be caused by spatially inhomogeneous phase accumulation during the interrogation period. To evaluate such gradients we compare the SU(1,1) interferometry fringes of two lattice sites with similar atom number. In panel (c) the phase difference of the two interferometry fringes is plotted versus the separation of the two considered lattice sites. We find no indication for gradients. For comparison the two grey lines indicate the expected behaviour if the nonlinear coupling strength κ had a spatial variation of 1 Hz/100 μm.

Appendix C
Notation and Mathematics

In this chapter we summarise essential formulas and mathematical notations used throughout this thesis.

C.1 SU(2) Schwinger Boson Representation

The Schwinger Boson representation describes a method to construct spin operators in terms of Fock states which describe bosonic modes. Describing a (fictious) spin, these operators satisfy the rotational SU(2) symmetry.

Spin-1/2
We first treat the spin-1/2 case. To this end we combine the two bosonic mode operators to a vector, $\boldsymbol{a} = \begin{pmatrix}\hat{a}_\uparrow & \hat{a}_\downarrow\end{pmatrix}^t$. Then the Schwinger Boson representation is given by the Jordan map

$$\hat{J}_i = \boldsymbol{a}^\dagger \frac{\sigma_i}{2} \boldsymbol{a}. \tag{C.1}$$

Here σ_i denote the Pauli matrices which read

$$\sigma_x = \begin{pmatrix}0 & 1\\ 1 & 0\end{pmatrix} \quad \sigma_y = \begin{pmatrix}0 & -\mathrm{i}\\ \mathrm{i} & 0\end{pmatrix} \quad \sigma_z = \begin{pmatrix}1 & 0\\ 0 & -1\end{pmatrix}. \tag{C.2}$$

Written out this yields the spin operators as stated in Eq. 2.1.

Spin-1
The above procedure can be extended to three bosonic modes. For this purpose we combine the three mode operators in the following vector, $\boldsymbol{a} = \begin{pmatrix}\hat{a}_\uparrow & \hat{a}_0 & \hat{a}_\downarrow\end{pmatrix}^t$. In this case the Jordan map reads

$$\hat{S}_i = \boldsymbol{a}^\dagger s_i \boldsymbol{a} \tag{C.3}$$

D. Linnemann, *Quantum-Enhanced Sensing Based on Time Reversal of Entangling Interactions*, Springer Theses,
https://doi.org/10.1007/978-3-319-96008-1

where s_i denotes matrices which describe a spin-1. They are given by

$$s_x = \frac{1}{\sqrt{2}}\begin{pmatrix}0&1&0\\1&0&1\\0&1&0\end{pmatrix} \quad s_y = \frac{\mathrm{i}}{\sqrt{2}}\begin{pmatrix}0&-1&0\\1&0&-1\\0&1&0\end{pmatrix} \quad s_z = \begin{pmatrix}1&0&0\\0&0&0\\0&0&-1\end{pmatrix}. \tag{C.4}$$

This yields the spin operators as defined in Eq. 2.6.

C.2 SU(3) Schwinger Boson Representation

To fully describe the three bosonic modes $\hat{a}_\uparrow$, $\hat{a}_0$, and $\hat{a}_\downarrow$ a treatment within the SU(3) symmetry group is appropriate [6, 7]. Similarly to the above description in terms of spin operators that satisfy the rotational SU(2) symmetry, the Schwinger Boson representation can be generalized to the present case of SU(3) [8]. To do so, we introduce Cartesian coordinates, $a_x = (\hat{a}_\downarrow - \hat{a}_\uparrow)/\sqrt{2}$, $a_y = \mathrm{i}(\hat{a}_\downarrow + \hat{a}_\uparrow)/\sqrt{2}$, $a_z = \hat{a}_0$ and use the following vector notation $\boldsymbol{a} = (a_x, a_y, a_z)$. Then the Jordan map reads

$$\hat{L}_i = \boldsymbol{a}^\dagger \frac{\lambda_i}{2} \boldsymbol{a}$$

where the eight matrices λ_i are named after Gell-Mann. They read

$$\lambda_1 = \begin{pmatrix}0&1&0\\1&0&0\\0&0&0\end{pmatrix} \quad \lambda_2 = \begin{pmatrix}0&-\mathrm{i}&0\\\mathrm{i}&0&0\\0&0&0\end{pmatrix} \quad \lambda_3 = \begin{pmatrix}1&0&0\\0&-1&0\\0&0&0\end{pmatrix} \quad \lambda_8 = \frac{1}{\sqrt{3}}\begin{pmatrix}1&0&0\\0&1&0\\0&0&-2\end{pmatrix}$$
$$\lambda_4 = \begin{pmatrix}0&0&1\\0&0&0\\1&0&0\end{pmatrix} \quad \lambda_5 = \begin{pmatrix}0&0&-\mathrm{i}\\0&0&0\\\mathrm{i}&0&0\end{pmatrix} \quad \lambda_6 = \begin{pmatrix}0&0&0\\0&0&1\\0&1&0\end{pmatrix} \quad \lambda_7 = \begin{pmatrix}0&0&0\\0&0&-\mathrm{i}\\0&\mathrm{i}&0\end{pmatrix} \tag{C.5}$$

Here the unusual ordering facilitates the comparison with the Pauli matrices: the first three matrices λ_i are just the Pauli matrices σ_i with the third column and row filled up with zeros. Therefore, these three matrices describe SU(2) subspaces within SU(3). In a similar fashion, the matrices $\{\lambda_4, \lambda_5\}$ and $\{\lambda_6, \lambda_7\}$ contain Pauli matrices. In either case, to complete the SU(2) subspace a diagonal matrix with elements as contained in L_3 and L_8 is needed. We describe these arising SU(2) subspaces now in more detail.

The eight operators L_i satisfy the commutator relations $\left[\hat{L}_i, \hat{L}_j\right] = \mathrm{i} f_{ijk} \hat{L}_k$ with the structure constants f_{ijk}. The nonvanishing structure constants are given in the following Table [8]:

ijk	123	147	156	246	257	345	367	458	678
f_{ijk}	1	1/2	−1/2	1/2	1/2	1/2	−1/2	$\sqrt{3}/2$	$\sqrt{3}/2$

From this table one can identify all SU(2) subspaces of SU(3), e.g. $\{S_1, S_2, S_3\}$ and $\{S_2, S_5, S_7\}$. It is important to note that in order to complete the SU(2) subspace of L_4 and L_5 one has to construct a linear superposition of operators L_3 and L_5 as motivated above. The coefficients of this superposition can be read off from from the commutator relations. Therefore, we have the two particularly important SU(2) subspaces: $\{L_4,L_5,(\sqrt{3}L_8 + L_3)/2\}$ and $\{L_6,L_7,(\sqrt{3}L_8 - L_3)/2\}$.

Explicitly, all eight operators read

$$
\begin{aligned}
2L_1 &= \mathrm{i}(a_\uparrow a_\downarrow^\dagger - a_\downarrow a_\uparrow^\dagger) && \equiv \hat{Q}_{xy} \\
2L_2 &= a_\downarrow a_\downarrow^\dagger - a_\uparrow a_\uparrow^\dagger && \equiv -\hat{S}_z \\
2L_3 &= -a_\uparrow a_\downarrow^\dagger - a_\downarrow a_\uparrow^\dagger \\
2L_4 &= \frac{1}{\sqrt{2}}(a_0 a_\downarrow^\dagger + a_\downarrow a_0^\dagger - a_\uparrow a_0^\dagger - a_0 a_\uparrow^\dagger) && \equiv \hat{Q}_{xz} \\
2L_5 &= \frac{\mathrm{i}}{\sqrt{2}}(-a_0 a_\downarrow^\dagger + a_\downarrow a_0^\dagger - a_\uparrow a_0^\dagger + a_0 a_\uparrow^\dagger) && \equiv \hat{S}_y \\
2L_6 &= \frac{\mathrm{i}}{\sqrt{2}}(-a_0 a_\downarrow^\dagger + a_\downarrow a_0^\dagger + a_\uparrow a_0^\dagger - a_0 a_\uparrow^\dagger) && \equiv \hat{Q}_{yz} \\
2L_7 &= -\frac{1}{\sqrt{2}}(a_0 a_\downarrow^\dagger + a_\downarrow a_0^\dagger + a_\uparrow a_0^\dagger + a_0 a_\uparrow^\dagger) && \equiv -\hat{S}_x \\
2L_8 &= \frac{1}{3}(a_\downarrow a_\downarrow^\dagger - 2a_0 a_0^\dagger + a_\uparrow a_\uparrow^\dagger)
\end{aligned}
$$

Here, we identify the operators $\hat{L}_i$ to spin operators $\hat{S}_i$ and $\hat{Q}_{ij}$ denote quadrupole operators that are introduced in reference [9]. Using the operators $\hat{s}_+ = (\hat{a}_\uparrow + \hat{a}_\downarrow)/\sqrt{2}$ and $\hat{s}_- = (\hat{a}_\uparrow - \hat{a}_\downarrow)/\sqrt{2}$ the two SU(2) subspaces discussed above can be written in the particular elegant form stated in the main text:

$$
\begin{aligned}
2L_6 \equiv -F_y &= -(a_0^\dagger s_+ - a_0 s_+^\dagger)/\mathrm{i} \\
2L_7 \equiv -F_x &= -(a_0^\dagger s_+ + a_0 s_+^\dagger) \\
\sqrt{3}L_8 - L_3 \equiv -F_z &= -(a_0^\dagger a_0 - s_+^\dagger s_+)
\end{aligned}
$$

$$
\begin{aligned}
2L_4 \equiv -G_x &= -(a_0^\dagger s_- + a_0 s_-^\dagger) \\
2L_5 \equiv G_y &= (a_0^\dagger s_- - a_0 s_-^\dagger)/\mathrm{i} \\
\sqrt{3}L_8 + L_3 \equiv -G_z &= -(a_0^\dagger a_0 - s_-^\dagger s_-)
\end{aligned}
$$

C.3 Input-Output Relation for Bilinear Hamiltonian

Every Hamiltonian that is at most quadratic in bosonic field operators performs a mode transformation according to

$$\begin{pmatrix} a_\uparrow \\ a_\downarrow \end{pmatrix} \to A \begin{pmatrix} a_\uparrow \\ a_\downarrow \end{pmatrix} + B \begin{pmatrix} a_\uparrow^\dagger \\ a_\downarrow^\dagger \end{pmatrix} + \gamma. \tag{C.6}$$

Since this transformation needs to keep the bosonic commutator relations intact, the matrices are required to fulfil: $AB^t = BA^t$ and $AA^\dagger = BB^\dagger + 1$ [10, 11]. Possible parametrisations for SU(2) and SU(1,1) are given by (with $\gamma = 0$)

$$A = \begin{pmatrix} \cos\theta & e^{\mathrm{i}\varphi}\sin\theta \\ -e^{-\mathrm{i}\varphi}\sin\theta & \cos\theta \end{pmatrix} \quad \text{and} \quad B = 0 \qquad \text{for} \quad \mathrm{SU}(2) \tag{C.7}$$

$$A = \begin{pmatrix} \cosh r & 0 \\ 0 & \cosh r \end{pmatrix} \quad \text{and} \quad B = \begin{pmatrix} 0 & e^{\mathrm{i}\varphi}\sinh r \\ e^{-\mathrm{i}\varphi}\sinh r & 0 \end{pmatrix} \quad \text{for} \quad \mathrm{SU}(1,1) \tag{C.8}$$

With these relations any combination of elements, e.g. the complete interferometric sequence can be built up.

C.4 Special Unitary Group, SU(2) and SU(1,1)

The name SU(n) refers to the special unitary group. In matrix representation this group applies to n dimensional unitary matrices U that have determinant of unity. For SU(2) a possible parametrization of all allowed matrices reads

$$U = \left\{ \begin{pmatrix} \cos\theta & e^{\mathrm{i}\varphi}\sin\theta \\ -e^{-\mathrm{i}\varphi}\sin\theta & \cos\theta \end{pmatrix} \middle| \varphi \in [0, 2\pi), \vartheta \in [0, \pi) \right\}. \tag{C.9}$$

Since this is identical to the mode transformation of a passive interferometer its name affix SU(2) is justified.

The SU(n) group can be generalized by weakening the unitarity property: instead of stipulating that $U^\dagger U = 1_n$ (unitarity, 1_n denotes unity matrix of size n) one merely requires that $U^\dagger A U = A$. Here A is a diagonal matrix with the first k entries being $(+1)$ and the l next entries being (-1) with $n = k + l$. This property is called pseudo-unitarity. Matrices of this form satisfy the generalized special unitary group, encoded by SU(k, l). For the special case of SU(1,1) the matrix A reads $A = \mathrm{diag}(1, -1)$. In this framework the SU(2) group corresponds to the specific case SU(2,0). All possible matrices can be parametrized by

$$U = \left\{ \begin{pmatrix} \cosh r & e^{\mathrm{i}\varphi} \sinh r \\ e^{-\mathrm{i}\varphi} \sinh r & \cosh r \end{pmatrix} \middle| \varphi \in [0, 2\pi), r \in [0, \infty) \right\}. \tag{C.10}$$

Therefore the mode transformation of parametric amplification are described by the SU(1,1) group.

References

1. D.M. Stamper-Kurn, M. Ueda, Spinor Bose gases: Symmetries, magnetism, and quantum dynamics. Rev. Mod. Phys. **85**, 1191 (2013), https://doi.org/10.1103/RevModPhys.85.1191
2. J. Kronjäger, C. Becker, P. Navez, K. Bongs, K. Sengstock, Magnetically tuned spin dynamics resonance. Phys. Rev. Lett. **97**, 110404 (2006), https://doi.org/10.1103/PhysRevLett.97.110404
3. A. Widera, F. Gerbier, S. Fölling, T. Gericke, O. Mandel, I. Bloch, Precision measurement of spin-dependent interaction strengths for spin-1 and spin-2 87 Rb atoms. New J. Phys. **8**, 152 (2006), http://stacks.iop.org/1367-2630/8/i=8/a=152
4. H. Schmaljohann, M. Erhard, J. Kronjäger, M. Kottke, S. van Staa, L. Cacciapuoti, J.J. Arlt, K. Bongs, K. Sengstock, Dynamics of $F = 2$ spinor bose-einstein condensates. Phys. Rev. Lett. **92**, 040402 (2004) https://doi.org/10.1103/PhysRevLett.92.040402
5. C. Klempt, O. Topic, G. Gebreyesus, M. Scherer, T. Henninger, P. Hyllus, W. Ertmer, L. Santos, J.J. Arlt, Multiresonant spinor dynamics in a bose-einstein condensate. Phys. Rev. Lett. **103**, 195302 (2009), https://doi.org/10.1103/PhysRevLett.103.195302
6. T. A. Tóth, *Quadrupolar Ordering in Two-Dimensional Spin-One Systems*, PhD thesis, Ecole Polytechnique Fédérale de Lausanne (2011)
7. V. Corre, T. Zibold, C. Frapolli, L. Shao, J. Dalibard, F. Gerbier, Spin-1 condensates at thermal equilibrium: A SU (3) coherent state approach. EPL **110**, 26001 (2015)
8. S.M. Davidson, A. Polkovnikov, SU(3) semiclassical representation of quantum dynamics of interacting spins. Phys. Rev. Lett. **114**, 045701 (2015)
9. C.D. Hamley, C.S. Gerving, T.M. Hoang, E.M. Bookjans, M.S. Chapman, Spin-nematic squeezed vacuum in a quantum gas. Nat. Phys. **8**, 305 (2012). https://doi.org/10.1038/nphys2245
10. S.L. Braunstein, P. van Loock, Quantum information with continuous variables, Rev. Mod. Phys. **77**, 513–577 (2005), https://doi.org/10.1103/RevModPhys.77.513
11. C. Weedbrook, S. Pirandola, R. García-Patrón, N.J. Cerf, T.C. Ralph, J.H. Shapiro, S. Lloyd, Gaussian quantum information. Rev. Mod. Phys. **84**, 621–669 (2012), https://doi.org/10.1103/RevModPhys.84.621